INVESTIGATION OF WATER DRAINAGE THROUGH AN ALPINE GLACIER BY TRACER EXPERIMENTS AND NUMERICAL MODELING

A dissertation submitted to the

SWISS FEDERAL INSTITUTE OF TECHNOLOGY ZURICH

for the degree of
Doctor of Natural Sciences

presented by

THOMAS SCHULER

Dipl. Hydr. Universität Freiburg im Breisgau

born 19. March 1971

in Bühl/ Baden (Germany)

accepted on the recommendation of

Prof. Dr. H.-E. Minor, examiner

Dr. U. H. Fischer, co-examiner

Dr. G. H. Gudmundsson, co-examiner

Dr. L. N. Braun, co-examiner

2002

Contents

List of Figures

List of Tables

List of Symbols

Symbol	Meaning	Unit
Chapter 2		
Q_G	ground heat flux	$\mathrm{W\,m^{-2}}$
Q_H	flux of sensible heat	$\mathrm{W\,m^{-2}}$
Q_L	flux of latent heat	$\mathrm{W\,m^{-2}}$
Q_M	flux of latent energy for melting	$\mathrm{W\,m^{-2}}$
Q_N	flux of net radiation	$\mathrm{W\,m^{-2}}$
Q_R	precipitation heat flux	$\mathrm{W\,m^{-2}}$
Chapter 3		
$a_{\mathrm{snow/ice}}$	radiation coefficient for snow or ice	$\mathrm{m^2\,W^{-1}\,mm\,h^{-1}\,{}^\circ C^{-1}}$
c	tracer concentration	ppb
c_0	background tracer concentration	ppb
d_{debris}	reduction factor to account for debris cover	
h_{s}	water stage	m
I	potential clear-sky solar radiation	$\mathrm{W\,m^{-2}}$
k	conductivity calibration coefficient	$(\mathrm{kg\,m^{-3}})/(\mu\mathrm{S\,mm^{-1}})$
L	electrical conductivity	$\mu\mathrm{S\,mm^{-1}}$
L_0	background electrical conductivity	$\mu\mathrm{S\,mm^{-1}}$
m	mass of injected tracer	kg
M	hourly melt rate	$\mathrm{mm\,h^{-1}}$
MF	melt factor	$\mathrm{mm\,h^{-1}\,{}^\circ C^{-1}}$
Q	discharge	$\mathrm{m^3\,s^{-1}}$
T	air temperature	$^\circ$C
t	time	s
τ	time	s

Chapter 4

A	cross-sectional area	m^2
c	tracer concentration	ppb
$c_{\text{m/im}}$	tracer concentration in the mobile/ immobile region	ppb
D	hydrodynamic dispersion coefficient	$\text{m}^2\,\text{s}^{-1}$
m	mass of injected tracer	kg
t	time	s
Q	discharge	$\text{m}^3\,\text{s}^{-1}$
v	velocity	$\text{m}\,\text{s}^{-1}$
x	distance in flow direction	m
β	fraction of mobile region	
ω	first-order kinetic rate coefficient	s^{-1}

Chapter 5

A_{w}	cross-sectional area occupied by water	m^2
c	tracer concentration	ppb
d_{norm}	normalized tracer load	h^{-1}
D	hydrodynamic dispersion coefficient	$\text{m}^2\,\text{s}^{-1}$
F	fluorescence	FU
$F_{\text{s/0}}$	fluorescence of a sample/ reference	FU
m	mass of injected tracer	kg
m_{s}	mass of injected salt	kg
m_{model}	virtual tracer mass in the transport model	
M	fraction of recovered tracer mass	
n	temperature exponent of Sulphorhodamine B, $n_{\text{SRB}} = -0.029$	$°\text{C}^{-1}$
Q	discharge	$\text{m}^3\,\text{s}^{-1}$
Q_{in}	supraglacial discharge	$\text{m}^3\,\text{s}^{-1}$
Q_{pro}	average proglacial discharge	$\text{m}^3\,\text{s}^{-1}$
r^2	coefficient of determination	
t	time	s
$T_{\text{s/0}}$	temperature of a sample/ reference	$°\text{C}$
v	velocity	$\text{m}\,\text{s}^{-1}$
β	fraction of mobile region	
ω	first-order kinetic rate coefficient	s^{-1}

Chapter 6

a, b, c	denote arbitrary terms	
A	cross-sectional area	m^2
A_{eff}	effective cross-sectional area of an inclined moulin	m^2
A_{inc}	cross-sectional area of an inclined moulin	m^2
$A_{\text{m/c}}$	cross-sectional area related to melting/ closure	m^2
A_{moulin}	cross-sectional area of the moulin	m^2
A_{w}	cross-sectional area occupied by water	m^2
B	flow law coefficient	$\text{Pa}^{-3}\,\text{s}{-}1$
c_{t}	pressure melting coefficient	$\text{K}\,\text{J}^{-1}\,\text{m}^3$
c_{w}	specific heat of water	$\text{J}\,\text{K}^{-1}\,\text{kg}^{-1}$
C	ratio to which the perimeter is wetted	
d	number of local losses	
E	energy	J
E_{m}	energy available for melt	J
E_{t}	energy related to a change in pressure melting point	J
f	friction factor in Equation (6.9)	
f_{bottom}	friction factor of a conduit bottom	
f_{com}	composite friction factor	
f_{i}	friction factor of an ice-walled conduit	
F_{T}	turbulent resistance parameter	$\text{s}^2\,\text{m}^{-5}$
g	gravitational acceleration	$\text{m}\,\text{s}^{-2}$
h	water pressure (expressed in hydraulic head)	m
h^*	ice-overburden pressure (expressed in hydraulic head)	m
h_{i}	ice thickness	m
h_{max}	maximum filling height in a moulin	m
h_{moulin}	water level in the moulin	m
H	total hydraulic potential (expressed in hydraulic head)	m
ΔH_{loc}	local loss of hydraulic potential	m
i	number of equations (subscript)	
k	roughness coefficient in Equation (6.11)	$\text{m}^{1/3}\,\text{s}^{-1}$
k_{bottom}	roughness coefficient of a conduit bottom	$\text{m}^{1/3}\,\text{s}^{-1}$
k_{com}	composite roughness coefficient	$\text{m}^{1/3}\,\text{s}^{-1}$
k_{i}	roughness coefficient of an ice-walled conduit	$\text{m}^{1/3}\,\text{s}^{-1}$
L_{f}	latent heat of fusion	$\text{kJ}\,\text{kg}^{-1}$
n	flow law exponent	
p_{w}	water pressure	Pa
Q	discharge	$\text{m}^3\,\text{s}^{-1}$
Q_{conduit}	discharge through main conduit	$\text{m}^3\,\text{s}^{-1}$
$Q_{\text{in/out}}$	net discharge into/ out of the moulin	$\text{m}^3\,\text{s}^{-1}$
$Q_{\text{low/up}}$	lower/ upper limit of discharge variation	$\text{m}^3\,\text{s}^{-1}$
Q_{max}	maximum open-channel discharge	$\text{m}^3\,\text{s}^{-1}$
Q_{sub}	subglacial discharge	$\text{m}^3\,\text{s}^{-1}$

real	subscript to denote a real value as opposed to a modeled one	
r_r	relative roughness	
R	radius	m
R_h	hydraulic radius	m
$R_\mathrm{L/T}$	linear/ turbulent resistance	$\mathrm{s\,m^{-2}}$
R_P	resistance of a rigid pipe	$\mathrm{s\,m^{-2}}$
R_R	resistance of a Röthlisberger channel	$\mathrm{s\,m^{-2}}$
Re	Reynolds-number	
t	time	s
T	period of discharge variations	d
U	perimeter	m
U_w	wetted perimeter	m
$\overline{v}$	mean velocity	$\mathrm{m\,s^{-1}}$
V_m	volume produced by melting	$\mathrm{m^3}$
x	distance in flow direction	m
X, Y	denoting left and right hand side of Equation (6.16)	
z	elevation of the glacier bed	m
z_bottom	elevation of the moulin bottom	m
z_tracer	elevation of the tracer in the moulin	m
α	opening angle	π
γ	constant introduced in Equation (6.5), $\gamma = c_\mathrm{t} c_\mathrm{w} \rho_\mathrm{w}$	
ε	objective function	
ϵ	infinitesimally small time constant	s
ν	kinematic viscosity of water	$\mathrm{m^2\,s^{-1}}$
ξ	coefficient of hydraulic head loss	
ξ_loc	coefficient of local head loss	
Φ	angle of inclination	°
$\rho_\mathrm{w/i}$	density of water/ ice	$\mathrm{kg\,m^{-3}}$
ω	angular velocity	$\mathrm{s^{-1}}$

Chapter 7

B	body force vector	N
c_μ	constant in eq. 7.6	
D_m	coefficient of molecular diffusion	$\mathrm{m^2\,s^{-1}}$
F	transfer function of a black-box system	
I	input into a black-box system	
k	turbulent kinetic energy	$\mathrm{m^2\,s^{-2}}$
m, n	denoting different time steps	
O	output from a black-box system	
p	fluid pressure	Pa
t	time	s
v	fluid velocity vector	$\mathrm{m\,s^{-1}}$
v_0	inlet velocity	$\mathrm{m\,s^{-1}}$
δt	time scale for Reynolds-averaging	s
ϵ	turbulence dissipation rate	$\mathrm{m^2\,s^{-3}}$
μ	molecular viscosity	$\mathrm{Pa\,s}$
μ_T	turbulent viscosity	$\mathrm{Pa\,s}$
ρ	fluid density	$\mathrm{kg\,m^{-3}}$
τ	time	s
Φ	an arbitrary quantity	
Ψ	a scalar	

Abstract

In this thesis, the water flow through and from Unteraargletscher, an alpine glacier in the Bernese Alps, Switzerland, is investigated with particular emphasis on the internal plumbing and its behavior in time.

To quantify water input to the glacial hydrological system during the ablation season 1999, a distributed temperature index melt model including potential clear-sky solar radiation was applied to Unteraargletscher. Model parameters were determined by calibrating calculated melt with ablation measurements. Discharge was measured in the proglacial stream for 18 days until the station was destroyed by an outburst flood. Comparison of modeled melt and measured discharge reveals an imbalance which suggests that water was stored in or beneath the glacier during this period. The culminating outburst flood presumably released this en- or subglacially stored water and may be related to a change in the configuration of the glacial drainage system as inferred from measurements of subglacial water pressure.

The morphology of the drainage system and its diurnal variability were investigated by conducting series of tracer tests over a number of discharge cycles during the ablation season 2000. Dye injections into a moulin were repeated at intervals of a few hours and were accompanied by simultaneous measurements of discharge of supraglacial meltwater draining into the moulin and bulk runoff in the proglacial stream. Records of dye concentration were analyzed using an appropriate transport model. Results of this analysis reveal a large diurnal variability in terms of transit velocity and dispersion coefficients. Furthermore, the obtained velocity-discharge and velocity-dispersion relationships display pronounced hystereses, thereby inhibiting the use of conventional evaluation techniques.

A time-dependent and physically-based model of subglacial water flow is used to investigate the observed variations of transit velocity. It is found that the ability of a Röthlisberger-channel to adjust its size to the prevailing hydraulic conditions contributes to hysteresis of the velocity-discharge relationship. Additionally, the model results further suggest that such hysteresis can be caused also by retardation of water due to inflow modulation at the junction of a tributary moulin and a main conduit.

Further, we studied the relation between conduit cross-section and tracer dispersion with numerical tracer experiments. The velocity field for steady flow through a given conduit geometry is calculated using a commercial flow solver. Tracer transport is represented by a scalar volume which is advected by the velocity field. Experiments were conducted for several scenarios by varying flow velocity and conduit geometry. Results show that a functional dependence of dispersion on the hydraulic radius of the conduit exists but it is weak. Further, it is found that the dispersion coefficient is strongly affected by changes in roughness. This suggests, that a dynamical conduit geometry can account for the observed velocity-dispersion hysteresis, especially, if the evolution of the conduit involves also roughness changes. Additionally, the effect

of inflow modulation on tracer dispersion is found to provide an equivalent explanation of the observed hysteretic behavior.

Zusammenfassung

In der vorliegenden Abhandlung wird der Wassertransport durch und der Abfluss vom Unteraargletscher in den Berner Alpen, Schweiz, untersucht. Dabei wird besondere Aufmerksamkeit dem internen Abflusssystem und seiner zeitlichen Entwicklung gewidmet.

Um den Wasserinput in das Gletscherabflusssystem während der Ablationsperiode 1999 zu quantifizieren, wurde ein flächenverteiltes Schmelzmodell auf den Unteraargletscher angewendet. Dieses Modell basiert auf einem Temperatur-Index Verfahren, das auch die potentielle Solarstrahlung mit einschliesst. Die Parameter des Modells wurden mit einer Kalibrierung der berechneten Schmelze anhand von Ablationsmessungen bestimmt. Der Wasserabfluss im Gletscherbach wurde über eine Periode von 18 Tagen aufgezeichnet, bis die Messstation von einer Flutwelle zerstört wurde. Die Bilanz von berechneter Schmelze und gemessenem Abfluss ist unausgeglichen, was auf eine Wasserspeicherung während dieser Periode in oder unter dem Gletscher hinweist. Dieses intra- oder subglazial gespeicherte Wasser wurde vermutlich in einem anschliessenden Wasserausbruch, der die Flutwelle im Gletscherbach erzeugte, wieder freigesetzt. Dieser Ausbruch wird mit einer Neukonfigurierung des Gletscherabflusssystems, die von Messungen des subglazialen Wasserdrucks abgeleitet wurde, in Verbindung gebracht.

Die Morphologie des Abflusssystems und dessen tageszeitliche Variabilität wurde mit Serien von Tracerversuchen untersucht, die über einige Abflusstageszyklen während der Ablationsperiode 2000 durchgeführt wurden. Dabei wurden die Tracereingaben in eine Gletschermühle in Intervallen von wenigen Stunden wiederholt. Gleichzeitig wurde der Abfluss im supraglazialen Bach, der in die Mühle entwässert, ebenso wie der Gesamtabfluss im proglazialen Fluss gemessen. Die erhaltenen Datenreihen der Tracerkonzentrationen wurden mit einem geeigneten Transportmodell ausgewertet. Die Resultate dieser Analyse weisen einen ausgeprägten Tagesgang der Abstandsgeschwindigkeiten und der Dispersionskoeffizienten auf. Die daraus abgeleiteten Geschwindigkeits-Abfluss- und Geschwindigkeits-Dispersions-Beziehungen zeigen jeweils eine deutliche Hysterese. Dieser Umstand verhinderte eine weitere Auswertung mittels konventioneller Verfahren.

Ein zeitabhängiges und physikalisch basiertes Modell subglazialer Abflussprozesse wurde eingesetzt, um die beobachteten Variationen der Abstandsgeschwindigkeiten zu untersuchen. Es ergab sich, dass die Eigenschaft eines Röthlisberger-Kanals, seine Grösse an die vorherrschenden hydraulischen Bedingungen anzupassen, zur Hysterese der Geschwindigkeits-Abfluss-Beziehung beiträgt. Zudem geben die Modellergebnisse zu erkennen, dass eine solche Hysterese ebenfalls durch eine Regulierung des Zuflusses aus einer Gletschermühle in einen Hauptkanal verursacht werden kann.

Des weiteren wurde die Beziehung zwischen dem Kanalquerschnitt und der Tracer-Dispersion mit numerischen Tracerexperimenten untersucht. Dabei wurde zuerst mit einem kommerziellen Programm das stationäre Geschwindigkeitsfeld durch eine gegebene Kanalgeometrie berechnet. Der Tracertransport wurde daraufhin simuliert mittels einem Skalarvolumen, das mit

diesem Geschwindigkeitsfeld advektiert wird. Experimente für mehrere Szenarien wurden durchgeführt, indem die Fliessgeschwindigkeit oder die Kanalgeometrie geändert wurden. Die Ergebnisse zeigen, dass zwar ein funktionaler Zusammenhang zwischen der Dispersion und dem hydraulischen Radius des Kanals besteht, dieser aber schwach ist. Ausserdem stellte sich heraus, dass der Dispersionskoeffizient stark von Rauhigkeitsänderungen beeinflusst wird. Diese Ergebnisse deuten an, dass eine dynamische Kanalgeometrie für die beobachtete Geschwindigkeits-Dispersions Hysterese verantwortlich gemacht werden kann, besonders, wenn die Entwicklung des Kanals mit einer Rauhigkeitsänderung einhergeht. Zudem wurde gezeigt, dass eine Zufluss-Regulierung einen ähnlichen Effekt auf die Tracerdispersion hat und somit eine äquivalente Erklärungsmöglichkeit für die beobachtete Hysterese bietet.

Chapter 1

Introduction

Zuletzt wollten zwei oder drei stille Gäste sogar einen Zeitraum grimmiger Kälte zu Hülfe rufen und aus den höchsten Gebirgszügen, auf weit ins Land hinausgesenkten Gletschern, gleichsam Rutschwege für schwerste Ursteinmassen bereitet, und diese auf glatter Bahn, fern und ferner hinausgeschoben im Geiste sehen. Sie sollten sich, bei eintretender Epoche des Auftauens, niedersenken und für ewig in fremdem Boden liegen bleiben. Auch sollte sodann durch schwimmendes Treibeis der Transport ungeheurer Felsblöcke von Norden her möglich werden. Diese guten Leute konnten jedoch mit ihrer etwas kühlen Betrachtung nicht durchdringen. Man hielt es ungleich naturgemäßer die Erschaffung einer Welt mit kolossalem Krachen und Heben, mit wildem Toben und feurigem Schleudern vorgehen zu lassen.

J. W. Goethe, Wilhelm Meisters Wanderjahre, 1829

1.1 Significance of glacial hydrology

1.1.1 Glacier dynamics

An early intimation that erratic boulders might be indicative of a major climate change came from the poet Goethe. The possibility of such boulders being of glacial origin was a pioneering thought at the time when it was mentioned in his novel *Wilhelm Meisters Wanderjahre*. Goethe quite reasonably believed that a vast amount of ice was required to explain the observed distribution of boulders by glacial transport and he inferred the existence of a considerably colder period in the past (Goethe, 1829). Today, there is little doubt about the existence of such ice-ages but the current discussion in the context of global climate change concentrates on the mechanism of ice sheet collapse by sudden discharges of ice at the termination of a glacial period. Similar changes between states of rapid and slow motion of ice-masses is today observed as switching on and off of ice streams (e.g. the Siple Coast ice streams in Antarctica), as pulsating flow of surging glaciers (e.g. Variegated Glacier, Alaska) and as short term "speed-up events" of alpine glaciers.

Variations in glacier motion are to a great extent associated with changes in conditions at the interface between ice and the underlying bed (Paterson, 1994). It is generally accepted that the

subglacial hydrological system has a strong influence on basal conditions as high subglacial water pressures lead to a decoupling of the glacier from its bed thereby promoting basal sliding (Boulton et al., 1974; Bindschadler, 1983; Iken et al., 1983; Iken and Bindschadler, 1986; Kamb and Engelhardt, 1987; Hooke et al., 1989). At the same time high subglacial water pressures can also cause the sediment comprising the bed to weaken enabling sediment deformation (Boulton and Jones, 1979; Boulton and Hindmarsh, 1987; Iverson et al., 1995; Fischer et al., 1999; Fischer and Clarke, 2001; Fischer et al., 2001).

Elevated basal water pressures result from the inability of the subglacial drainage system to discharge water at the same rate as it is supplied to the system from the glacier surface. This situation can arise at the beginning of the ablation season when rapid melting of the winter snowpack causes a sudden influx of large amounts of meltwater to an inefficient winter drainage system.

In response to high subglacial water pressures, hydraulic and mechanical instabilities can result which then lead to a reorganization of the subglacial drainage system (e.g. Gordon et al., 1998; Stone and Clarke, 1996) or periods of enhanced glacier motion (e.g. Iken et al., 1983; Kamb and Engelhardt, 1987; Kavanaugh and Clarke, 2001). These velocity increases are often accompanied by anomalous vertical surface velocities of the order of $10 \, \text{cm} \, \text{d}^{-1}$ (Iken et al., 1983; Mair et al., 2001). Surface uplifts were initially interpreted to result from water storage at the bed. Measurements of vertical and horizontal strain suggest that temporal variations in the strain-rate regime may also contribute to the observed surface uplifts (Gudmundsson, 1996).

The subsequent establishment of stable hydraulic and mechanical conditions at the glacier bed is often marked by a sudden release of the subglacially backed-up water and an increased suspended-sediment flux (e.g. Anderson et al., 1999; Barrett and Collins, 1997; Collins, 1998; Humphrey et al., 1986).

The same processes are used to explain glacier surging (Raymond, 1987; Kamb et al., 1985; Humphrey et al., 1986; Kamb, 1987; Humphrey and Raymond, 1994; Björnsson, 1998). For a given constellation of bed roughness, ice rheology, glacier geometry and hydraulic conditions, an inefficient drainage system may be stable enough against water pressure perturbations. In this way, high subglacial water pressures and thereby increased basal motion can be maintained over some time. The surge is terminated when the subglacial drainage morphology switches to a hydraulically more efficient structure.

1.1.2 Glacial discharge

Besides its glacier-dynamical aspects, the internal plumbing of a glacier is also of significance for hydrological purposes. In many regions, glaciers provide substantial water supply to the surrounding lowlands which benefit notably from the compensating effect of glaciers, releasing meltwater typically during periods of precipitation deficit (Röthlisberger and Lang, 1987). However, regions in vicinity to glaciers are also vulnerable to floods caused by sudden outbursts of stored water from the glacier itself or from ice- or moraine-dammed lakes. Therefore, accurate estimates of the volume and timing of glacial runoff is required for water resource and risk management purposes. Such tasks include flood control and prediction, efficient water management and design and operation of hydroelectric facilities and protective installations. Special consideration is given to these issues as most glaciers world-wide decrease in volume due to global climate change (e.g. WGMS, 1999).

Assessing a possible future evolution of glacial water resources and risks related to glacial discharge requires models which describe the relevant processes. A variety of methods to calculate discharge from glaciers has been developed (e.g. Fountain and Tangborn, 1985; Hock, 1998). Efforts have been undertaken to simulate the melt process accurately but the water transfer through the glacier is mostly represented by a black-box model based on a linear reservoir approach (e.g. Mader and Kaser, 1994; Braun and Aellen, 1990; Baker et al., 1982) thereby neglecting the dynamic nature of a glacial drainage system.

Another shortcoming of a black-box approach is that it cannot provide meaningful insight into the system when detailed or distributed information is required. For instance, subglacial water pressures are of particular concern where water is tapped from under the glacier for hydropower purposes (e.g. Vivian and Bocquet, 1973; Hagen et al., 1983; Jansson et al., 1996) or where water should be drained from mines underneath a glacier (Melvold et al., 2002).

1.2 Techniques of investigation

Because of the inaccessibility of the bed, hydraulic conditions and processes prevailing beneath glaciers are difficult to study and therefore our present understanding of subglacial hydrology is incomplete. The character of the subglacial drainage system and its physical parameters have to be deduced from experimental techniques in conjunction with theoretical considerations. Experiments using tracer methods have made a major contribution to the understanding of water flow beneath glaciers (Röthlisberger and Lang, 1987) and are thus considered to provide the best data for determining the structure of subglacial drainage systems (Hooke, 1989). The relatively simple procedures required mean that tracer techniques are ideal for temporally intensive and spatially extensive investigations (Nienow, 1993). Tracer tests provide general characteristics of the water flow path, the rate at which water flows through the glacier and the extent to which the water is delayed during its passage through the system (e.g. Behrens and others, 1975).

Tracer techniques have been used to elucidate the nature and the seasonal evolution of the drainage system beneath a number of glaciers including Haut Glacier d'Arolla (Nienow, 1993; Nienow et al., 1996c, 1998) and Storglaciären (Hooke et al., 1988; Seaberg et al., 1988; Hock and Hooke, 1993; Kohler, 1995). Repeated dye tracing experiments at Haut Glacier d'Arolla showed that both the transit velocity and the degree of tracer dispersion changed over the course of the summer suggesting that the hydrological system changed from an initial inefficient configuration to a more efficient one over large parts of the glacier bed.

Seaberg et al. (1988), Fountain (1993) and Kohler (1995) developed conceptual models of subglacial drainage to infer hydraulic conditions from tracer tests. However, the interpretation of such tracer tests using a physically based model of subglacial drainage has not been attempted to date. Such a model would enable the identification of the governing processes and the determination of the contribution of individual mechanisms. As such, the information yield of tracer tests would be significantly enlarged.

1.3 Study area: Unteraargletscher

This study was performed on Unteraargletscher, a temperate valley glacier situated in the Bernese Alps, Switzerland (Fig. 1.1). Already in the first half of the 19th century, Unteraar-
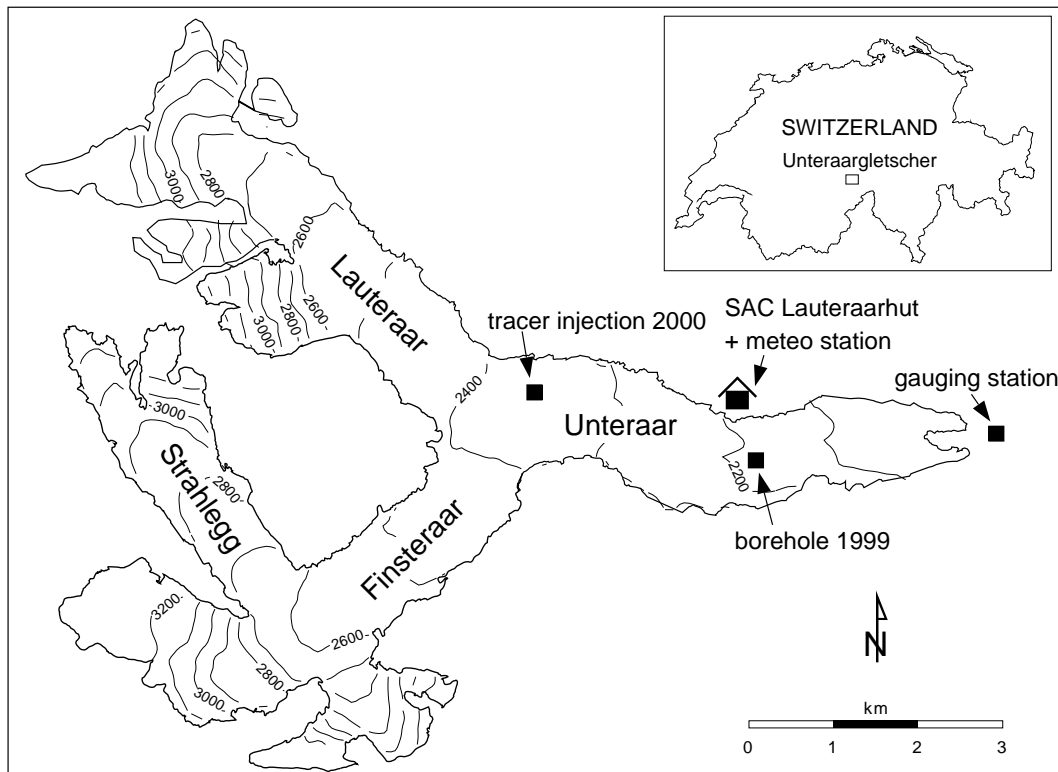
Figure 1.1: *Map of Unteraargletscher showing the location of the Lauteraarhut and the sites of various glaciological, meteorological and hydrological measurements conducted during the field-campaigns 1999 and 2000. Inset shows the location of the study area in the Bernese Alps, Switzerland.*

gletscher was object of scientific investigations by Franz Josef Hugi and Louis Agassiz (Hugi, 1830, 1842; Agassiz, 1840, 1847). Their pioneering work contributed substantially to our present understanding of glaciers. Since the 1920s systematic measurements of changes in surface elevation and displacement have been conducted (Flotron, 1924 to date). A comprehensive list of references to work related to Unteraargletscher can be found in Zumbühl and Holzhauser (1988, 1990). Today, Unteraargletscher belongs to the most comprehensively studied glaciers in the Alps.

Unteraargletscher is the common tongue of the two tributaries Lauteraar- and Finsteraargletscher (Fig. 1.1). From the confluence zone at $\sim$2400 m above sea level (a.s.l.), Unteraargletscher extends about 6 km eastwards with a mean width of 1 km and a slope of approximately $4°$. The entire system of glaciers covers an area of $26\,\text{km}^2$. The present terminus, $\sim$1.5 km from Lake Grimsel, is at an elevation of 1950 m a.s.l, and the headwalls of the accumulation basins are surrounded by peaks up to 4274 m a.s.l. Despite the lack of detailed mass balance measurements, the present equilibrium-line altitude is estimated at $\sim$2800 m a.s.l. based on a comparison with other glaciers in the area and on an analysis of aerial photographs (Gudmundsson, 1994).

A prominent feature of Unteraargletscher is the large ice-cored medial moraine which is formed by the convergence of the lateral moraines of Lauteraar- and Finsteraargletscher. The debris cover is typically 5 to 15 cm thick. At the confluence zone the medial moraine is between 10 and 20 m high and $\sim$100 m wide. With distance downglacier it grows to a maximum height of 50 m and width of 300 m before it gradually spreads out and merges with the marginal morainic debris

in the terminus region. Smaller medial moraines on the southern side of Unteraargletscher are the result of Finsteraargletscher being fed by Strahleggletscher and a number of smaller tributaries. In contrast, there are no tributaries that feed large amounts of ice to Lauteraargletscher and, thus, the northern side of Unteraargletscher is nearly debris-free.

For simplicity we refer in the remainder of this study to the entire system of glaciers (Fig. 1.1) as "Unteraargletscher". The catchment area of Unteraargletscher is embedded in the central massif of the Alps, namely the Aare-massif (Labhart, 1992). This formation belongs to the varascic basement and consists of old crystalline gneiss and Aare-granite .

The bedrock topography of Unteraargletscher has been mapped by seismic reflection and radio-echo soundings (Knecht and Süsstrunk, 1952; Sambeth and Frey, 1987b; Funk et al., 1994; Gudmundsson, 1994; Bauder, 2001) (Fig. 1.2a). Two seismic reflectors at different depth have been identified, where the upper one represents the true glacier bed and the lower one the surface of the underlying bedrock. The intervening layer consists of unconsolidated sedimentary material (Sambeth and Frey, 1987a). From the systematic thinning of the sediment layer in up-glacier direction and its final disappearance at the confluence it has been inferred that a transition from bed erosion to sedimentation occurs in down-glacier direction (Gudmundsson, 1994). The glacier bed of Unteraargletscher is U-shaped in transverse direction and is only weakly inclined down-glacier from the confluence area. Maximum ice-thickness of more than $400\,\mathrm{m}$ is observed up-glacier of the junction on both tributaries, Lauteraargletscher and Finsteraargletscher (Fig. 1.2b). From there, the ice-body thins out but at a distance of $1.5\,\mathrm{km}$ from the terminus it is still $\sim 200\,\mathrm{m}$ thick (Funk et al., 1994; Bauder, 2001).

1.4 Objectives

The main goals of this thesis are to gain a better understanding of subglacial drainage, to identify the governing processes and to determine their effects on hydraulic conditions. In detail, these objectives were achieved by:

- studying the water balance of Unteraargletscher prior to a release event with regard to possible subglacial water storage.

- conducting tracer injections in quick succession over a range of different discharges to investigate the morphology of the drainage system and its diurnal variability.

- a careful analysis of the data obtained from tracer tests and accompanying discharge measurements to determine transport parameters.

- developing a physically based, numerical model of subglacial drainage to interpret the experimentally observed variations of transit velocity.

- performing numerical tracer experiments to investigate mechanisms of tracer dispersion and thereby elucidating the behavior of dispersion observed in the experiments.
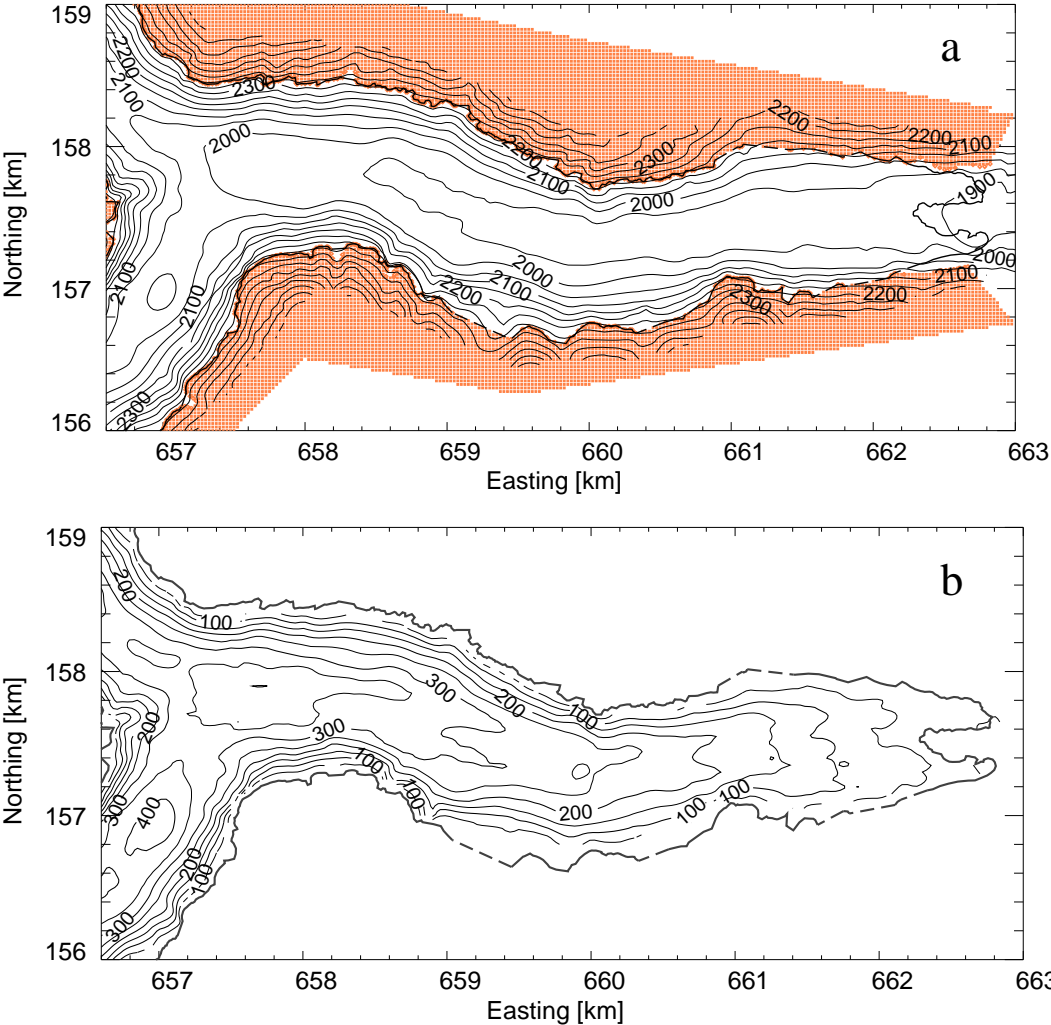
Figure 1.2: *(a) Basal topography and (b) ice-thickness of Unteraargletscher in 1996. Shaded areas denote the surrounding topography which was used for the interpolation (Bauder, 2001).*
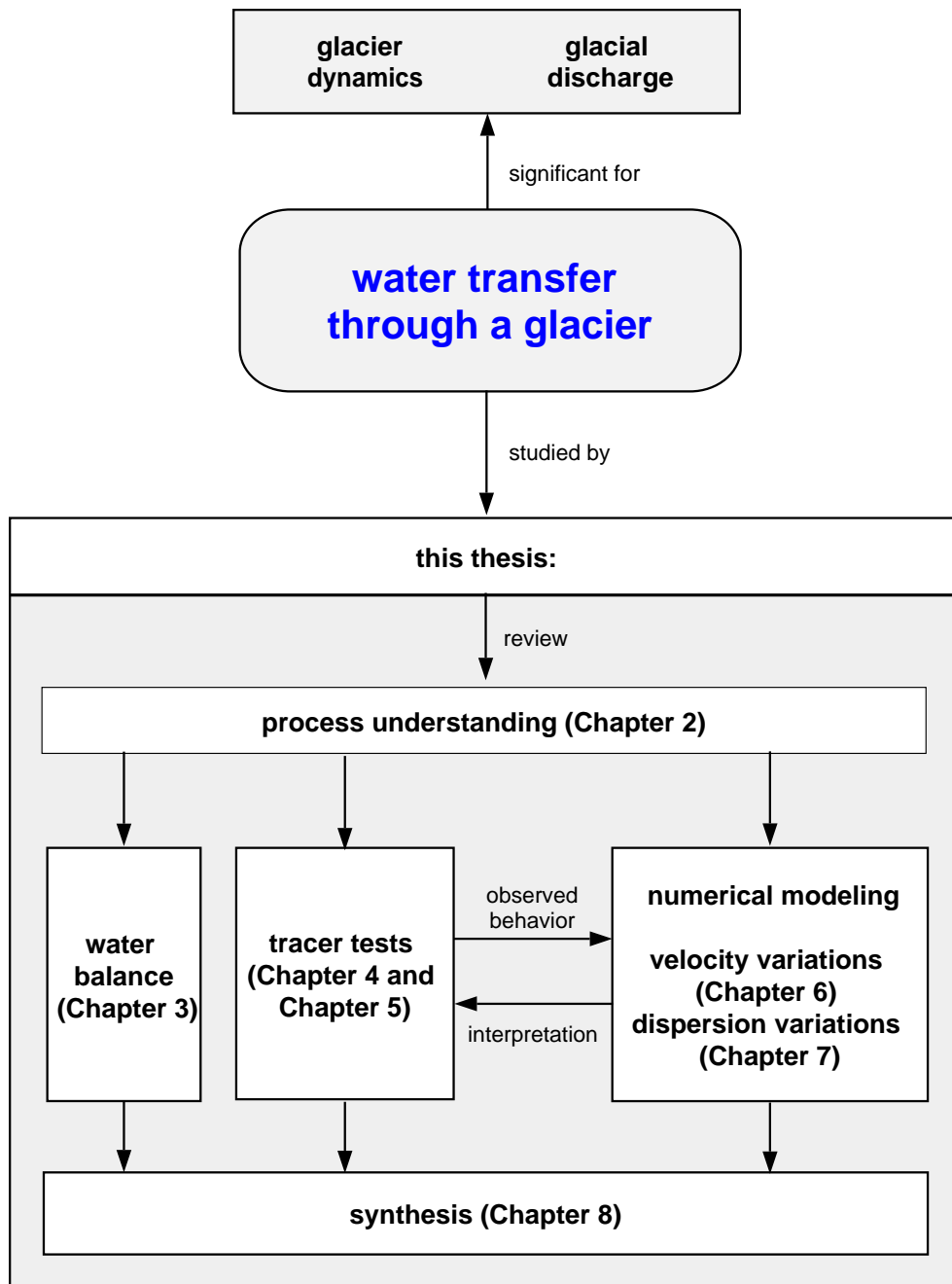
Figure 1.3: *The structure of this thesis.*

1.5   Structure of the thesis

Figure 1.3 sketches the organization of this thesis. Chapter 2 introduces the processes involved in glacier melt and discharge and gives a review of previous work. As such, it provides the background knowledge on which this thesis is based. In Chapter 3, the possibility that water was stored in Unteraargletscher and contributed to a flood event is investigated by balancing water input and output. For this reason, the water input was determined using a melt model and compared to measured discharge. The content of this chapter has recently been published in *Nordic Hydrology* (Schuler et al., 2002). Chapter 4 introduces the principles of tracer tests. Further, models of tracer transport are presented which provide the basis for the evaluation

of the experimental part of this study. Based on theoretical considerations made in Chapter 2 and Chapter 4, appropriately designed tracer experiments were performed at Unteraargletscher. Chapter 5 describes the strategy of data acquisition and subsequent analysis. The implication of the results for subglacial plumbing are discussed. In Chapter 6, a physically based model of subglacial conduit drainage is developed to investigate mechanisms accounting for the observed variation of transit velocity. Similarly, a numerical model of tracer transport is used in Chapter 7 to study the observed behavior of tracer dispersion. The results obtained in this chapter form the substance of a paper which is accepted for publication in *Annals of Glaciology* (Schuler and Fischer, 2002). Finally, the thesis is concluded by Chapter 8 discussing the main findings of the previous chapters with regard to conclusions drawn from other studies.

Chapter 2

Glacial hydrology: a process review

Most of the runoff from the surface of an alpine glacier disappears into the glacier and emerges from under the terminus in one or a few large streams. The interior of the glacier is virtually inaccessible (Röthlisberger and Lang, 1987) and therefore observations of the internal plumbing are difficult to obtain (Hooke, 1989). Hence, the character of the subsurface drainage system has to be deduced from theoretical consideration and indirect experimental techniques such as tracer tests or borehole water level monitoring. In this section, the findings of previous studies of glacial water production and routing are summarized and the significance of glacial hydrology for the motion of glaciers and water resource management are illustrated.

2.1 Runoff generation at the surface

For temperate glaciers, the most important contribution to bulk runoff originates at the glacier surface (e.g. Paterson, 1994; Röthlisberger and Lang, 1987). This water is derived from melting of snow, firn and ice, from rainfall or from inflow of extraglacial water. Additional contributions are provided by meltwater produced internally in the glacier by dissipation of energy related to the flow of ice or water and by basal meltwater caused by the geothermal heat flux. These internal and basal contributions play a minor role in alpine glacial hydrology since they are on the order of only $10^{-2}\,\mathrm{m\,a^{-1}}$ while surface melt rates range from 0.1 to $10\,\mathrm{m\,a^{-1}}$ (Röthlisberger and Lang, 1987). A basic understanding of the melt process at the surface is therefore essential for a comprehensive characterization of runoff which is drained through or beneath a glacier.

2.1.1 Surface energy balance

The balance of all energy fluxes from or towards a glacier surface of unit area is given by

$$Q_N + Q_H + Q_L + Q_G + Q_R + Q_M = 0$$

where Q_N is the net radiation, Q_H is the sensible heat flux, Q_L is the latent heat flux related to phase changes, Q_G is the heat exchange with the ground, Q_R is the heat flux supplied by rain and Q_M is the flux of latent energy available for melt. By convention, energy fluxes directed towards the surface are denoted by a positive sign while those away from the surface carry a negative sign.

9

Net radiation (Q_N)

The net radiation is the difference between radiation directed to or away from the considered surface (Kondratyev, 1965). It can be further subdivided into a shortwave component (ranging from 0.15 to $4\,\mu\text{m}$) which is predominantly of solar origin and into a longwave part of mainly terrestrial origin (4 to $120\,\mu\text{m}$). The global radiation (incoming shortwave radiation) is subject to considerable variability in space and time due to effects of slope, aspect and effective horizon. The reflected part of global radiation is controlled by the shortwave albedo of the surface, therefore increasing the variability of Q_N (Kondratyev, 1965). Thermal emission from the lower atmosphere and the considered surface contribute to Q_N in the longwave spectrum.

Sensible and latent heat (Q_H, Q_L)

The fluxes of sensible and latent energy are proportional to the vertical gradients of air temperature and specific humidity. The exchange of energy in both cases is driven by turbulence in the lower atmosphere. Hence the expressions for both turbulent fluxes are analogous. The magnitude of turbulence depends on wind speed, surface roughness and atmospheric stability (Morris, 1989).

Rain heat flux Q_R **and ground heat flux** Q_G

The energy flux provided by rainfall onto the glacier is determined by precipitation intensity and rain temperature. Vertical exchange of energy between the surface and the underlying glacier ice occurs in winter mainly by heat conduction. Otherwise, percolation of surface meltwater into a permeable medium (snow, firn) and refreezing of that water at a depth where the temperature is below $0°\text{C}$ is the most efficient process to warm up the snow (e.g. Paterson, 1994). However, the surface temperature cannot rise above $0°\text{C}$.

Heat available for melting Q_M

A necessary condition to start meltwater production is a glacier surface at the melting point. Once this condition is met and the budget of all other components provides a surplus of energy, the residual flux Q_M is used for melting.

2.1.2 Importance of energy fluxes

The assumption of the surface of a temperate glacier being at the melting point is appropriate for most alpine glaciers during the ablation season. In this case some terms of the energy balance equation can be neglected. At a temperate glacier surface, Q_G vanishes except for occasional periods of nocturnal freezing (Paterson, 1994) and Röthlisberger and Lang (1987) demonstrated that Q_R is significant only for extreme rainfall events and only on a short time-scale. As opposed to a soil surface or to a surface covered by vegetation, the low temperature of a glacier surface favors the formation of atmospheric stable conditions thereby supressing turbulence. Thus, the turbulent fluxes generally play a minor role for snow and ice melt compared to the flux of net radiation (e.g. Lang and Schönbächler, 1967; Lang *et al.*, 1977). Nevertheless, highest melt

rates coincide with high values of the turbulent fluxes (Hay and Fitzharris, 1988) and the flux of latent energy can be of importance for the short-term variations of melt rates (Lang, 1981). Ohmura (2001) presented an extensive review of energy balance measurements on glaciers and lists the components in their order of significance for meltwater generation. This paper underlines the dominating role of net radiation which the author examined in more detail. On average, longwave incoming radiation is by far the largest energy source, followed by absorbed global radiation. From this follows the pronounced temporal and spatial variability of melt which is characteristic for runoff generation on glaciers. Since longwave incoming radiation and sensible heat flux components are very closely related to air temperature (Lang and Braun, 1990), the course of melt water generation is to a large extent explained by the variation of air temperature (Ohmura, 2001). The resulting pattern of the melt distribution is modulated by the variability of the absorbed global radiation. The amount of incoming shortwave radiation depends on zenith angle, cloudiness and topography whereas the absorption is controlled by surface properties such as albedo and roughness. Albedo of a glacier surface experiences drastic variations which may range from 0.1 for dirty ice to more than 0.9 for fresh snow (Warren, 1982). Many authors reported how snowfall during the ablation season affected meltwater generation (e.g. Hoinkes and Rudolph, 1962; Tronov, 1962). Lang (1966) estimated a 27% reduction of monthly runoff from Hintereisferner due to one snowfall in July.

To summarize, the melt water production is characterized by an enormous temporal variability on a seasonal as well as diurnal time scale which is a consequence of the governing influence of air temperature and absorbed global radiation. Due to its high albedo, the presence of a snow cover on the glacier and the retreat of the snow line during the ablation season introduces further complexity in the temporal and spatial pattern of melt.
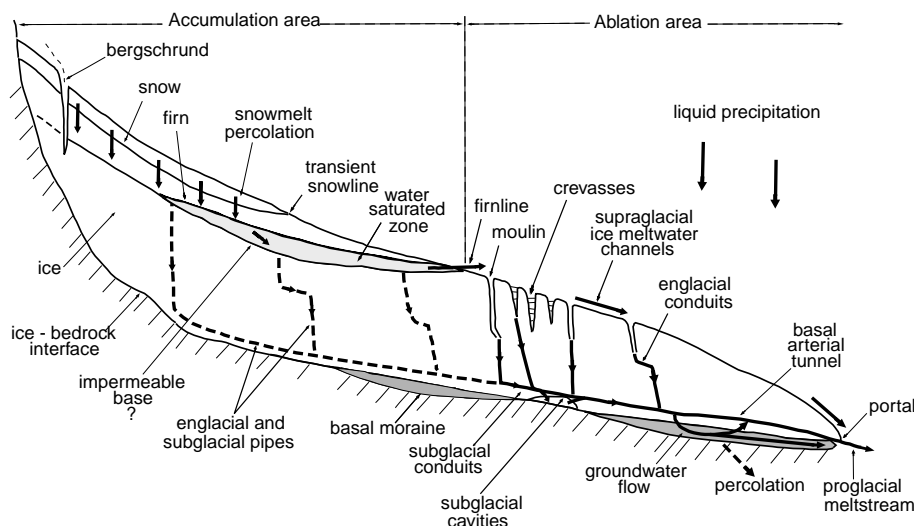
Figure 2.1: *Schematic diagram of supraglacial, englacial and subglacial drainage pathways of a temperate glacier (after Röthlisberger and Lang (1987), taken from Collins (1988)).*

2.2   Water flow through the glacier

Drainage from an alpine glacier takes place in a complex system consisting of numerous elements. Generated at the glacier surface by melting or rainfall, water percolates through the

snow or firn layer in the accumulation zone or where a transient snow cover exists. In the ablation zone where the winter snow cover has disappeared, water flows on bare ice, channelised in supraglacial streams. Crevasses and moulins provide access to the interior of the glacier where the water continues to the glacier bed flowing in conduits, through a network of interconnected cavities or in a permeable basal sediment layer (Röthlisberger and Lang, 1987; Fountain and Walder, 1998).

Figure 2.1 sketches the structure of the principal drainage pathways, their location in the glacier and probable interactions between them. Accordingly, glacier drainage is subdivided into three main parts:

- the flow within the snow-firn layer and along the ice surface

- the transfer to and the passage through the interior of the glacier and

- the subglacial drainage pathways.

For further details of glacial hydrology beyond the discussion presented below, I refer to more extensive reviews (Röthlisberger and Lang, 1987; Hooke, 1989) and the more recently published work of Fountain and Walder (1998) and Hubbard and Nienow (1997).

2.2.1 Firn and supraglacial hydrology

At the onset of the melt period, the glacier is typically covered by a winter snow cover. Where yearly mass gain exceeds mass loss, the snow is transformed into firn, a transitional material in the metamorphism of snow to ice. The hydrological behavior of the snow and firn layers is comparable to a porous aquifer in soil hydrology (Meier, 1973). Gravity drives the percolation of water through unsaturated snow or firn (Colbeck and Davidson, 1973; Ambach et al., 1981) down to a zone of substantially lower permeability where a saturated layer builds up (Ambach et al., 1978; Behrens et al., 1979). Water level monitoring, pumping tests and dye tracer experiments (Schommer, 1977; Ambach and Eisner, 1979; Oerter and Moser, 1982; Fountain, 1989; Schneider, 1999, 2001) reveal that the passage of water through firn is considerably delayed due to a low hydraulic conductivity on the order of $10^{-5}\,\mathrm{m\,s^{-1}}$. Substantial volumes of water are temporarily stored within the firn layer. As a consequence, diurnal variations in melt water runoff are substantially dampened during its passage through the firn (Schneider, 2001).

The firn aquifer is discharged by outflow on the ice surface at the firn line, by drainage into crevasses underneath (Schneider, 2001) or by seepage through the glacier ice through intergranular veins (Röthlisberger and Lang, 1987). The latter process was discussed by Lliboutry (1964), Shreve (1972) and Nye and Frank (1973) but observations reveal that the quantity of intergranuler drainage is probably negligible (Raymond and Harrison, 1975; Lliboutry, 1971, 1996).

In contrast to the firn layer, the bare ice surface has hardly any retention capacity to delay the input of water into the body of the glacier. Penetration of shortwave solar radiation enlarges intergranular veins (Lliboutry, 1971; Brandt and Warren, 1993), but substitution of melted surface ice by ice emerging from the interior of the glacier disables the formation of a deeply weathered crust. Hence, the ice surface remains relatively impermeable (Lliboutry, 1996) and water flows in supraglacial channels that disappear into the glacier (Stenborg, 1973). Large surface streams flowing as far as to the margins or the glacier terminus are only rarely observed (Röthlisberger and Lang, 1987).

2.2.2 Englacial passageways

As mentioned above, several authors considered a general but weak permeability of glacier ice via intergranular veins (Lliboutry, 1964; Shreve, 1972; Nye and Frank, 1973). Shreve (1972) argued that the release of potential energy in the water flowing through such veins would enlarge them to pipes. The visco-plastic property of the surrounding ice would tend to contract such pipes. By applying a balance of ice-overburden pressure and water pressure, Shreve (1972) described the behavior of such pipes. If two flow paths of different size were competing for the same discharge, the larger passage would grow at the expense of the smaller one. Röthlisberger (1972) obtained the same conclusion by balancing closure rate and melt rate. Hence, the englacial conduit system should form an upward branching arborescent network, with tributaries joining into larger passages (Fig. 2.2). There is little doubt on the existence of larger englacial passageways (Raymond and Harrison, 1975; Pohjola, 1994), even though the process initiating their development is not completely understood.

Flow into crevasses and moulins contributes to a much larger extent to the transfer of meltwater to the interior of the glacier than intergranular seepage does. Whereas drainage of water to crevasses from underneath the firn layer is inferred from observations of firn water level (Schommer, 1977; Oerter and Moser, 1982; Schneider, 1999, 2001), it is obvious in the ablation zone (Röthlisberger and Lang, 1987). Crevasses are tensional fractures in the ice capturing supraglacial water when they cut across the surface drainage (Hooke, 1989). Within the ice, the crevasse may intersect englacial passages through which the water drains further into the glacier, thereby enlarging the englacial conduits rapidly. Otherwise, if none of such passages is intersected by the crevasse or if their capacity to drain the water is not sufficient, the crevasse will begin to fill. In this case, the higher density of water compared with ice may promote the downwards propagation of a water filled crack. Robin (1974) and Weertman (1974) proposed hydro-fracturing as the mechanism facilitating inflow of surface water to the glacier bed. Hooke (1984) argued that descending englacial conduits larger than $4\,\mathrm{mm}$ in diameter, experience rates of wall melting in excess of creep closure rates. At a given discharge, the water pressure would drop and finally open channel flow would occur. Then, melting would take place at the bottom and thereby causing the conduit to cut gradually downwards.

Moulins are sink holes in the glacier surface (Röthlisberger and Lang, 1987). Their formation is attributed to the establishment of an efficient drainage mechanism starting from a preferential flow path such as fractures and crevasses. Descends into such moulins (Reynaud, 1987) and mapping structures of ancient moulins as they are exposed at the glacier surface (Holmlund, 1988) revealed that they steeply plunge down into the glacier at least in the uppermost (accessible) few decameters. It remains still unclear whether water draining from the bottom of moulins continues to descend more or less vertically to the glacier bed (Hooke, 1984). From the difference between the cable length and the pressure reading of a pressure transducer which was lowered down a moulin at White glacier, Iken (1972) inferred a gradually decreasing slope with increasing depth of the moulin. From theoretical considerations it was also argued that the lower part of moulins should be tilted down-glacier (Shreve, 1972) or even up-glacier (Röthlisberger and Lang, 1987). However, even though their plumbing is not fully understood, it is evident that such englacial drainage structures facilitate rapid transfer of surface water to the glacier bed.
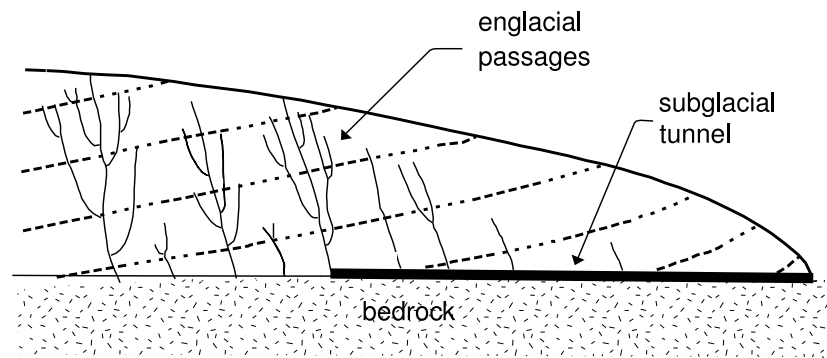
Figure 2.2: *Hypothetical network of arborescent englacial channels. Flow direction is in general perpendicular to contours of fluid potential (dotted lines), (after Shreve, 1985).*

2.2.3 Subglacial hydrology

Alpine glaciers are typically drained by outflow streams emerging from underneath the glacier terminus discharging turbid water (the so called glacial milk). Since the bulk of the runoff is derived from clear surface meltwater, it is obvious that during its passage at least some of the water must have experienced contact with sediments at the glacier bed. Another evidence of hydraulic connections between the glacier surface and the bed was first reported by Mathews (1964) who measured diurnal variations of water pressure at the bed of South Leduc Glacier in response to a diurnally varying meltwater production. Numerous studies following different approaches identified different subglacial flow systems. Dye tracer experiments (Ambach et al., 1972; Lang et al., 1979; Burkimsher, 1983; Brugman, 1986; Fountain, 1993; Nienow et al., 1998; Hock et al., 1999), investigations of the chemical and isotopic composition of bulk discharge (Behrens et al., 1971; Collins, 1979; Oerter et al., 1980; Tranter et al., 1996) as well as borehole water level monitoring (Hodge, 1979; Hantz and Lliboutry, 1983; Iken and Bindschadler, 1986; Stone and Clarke, 1993; Fountain, 1994; Hubbard et al., 1995; Gordon et al., 1998) suggest the existence of several distinct systems. Distinctions between "fast and slow", "low and high resistive" or "arborescent and non-arborescent" systems have been made to categorize subglacial drainage systems. However, these properties can be derived from the geometry of the system. Therefore, in this thesis, we use the geometry as a criterion and distinguish between channelised and distributed drainage systems. Weertman (1972) stated that both types of flow may occur side by side, with the surface-derived water showing a preference for channel flow.

Channelised systems

Once a large englacial conduit reaches the glacier bed it seems implausible that it would disappear. Thus, the arborescent tunnel network is likely to continue along the ice-bed interface towards the glacier terminus (Shreve, 1972; Röthlisberger, 1972). Further, at the transition from a englacial to a subglacial conduit, the channel properties should remain unaltered since the principle of melt enlargement versus creep closure holds unconditionally (Röthlisberger and Lang, 1987). However, specific conditions of the glacier bed have to be taken into account since they affect both, the motion of water and of ice. The impact on subglacial channel characteristics of various factors such as consistence and roughness of the bed, cross-sectional conduit geometry and properties of basal ice was discussed in detail by several authors proposing differ-

ent channel types (Röthlisberger, 1972; Nye, 1973; Hooke, 1984; Hooke et al., 1990; Lliboutry, 1983; Walder and Fowler, 1994) (see Fig. 2.3).

Subglacial conduits as described in the theory of Röthlisberger (1972) are commonly referred to as "Röthlisberger-Channels" or "R-Channels". To compute water pressures in a subglacial channel, Röthlisberger (1972) and Iken and Bindschadler (1986) assumed a semi-circular cross-section but model results consistently underestimated measured water pressures. Therefore, they had to assume an enhanced tunnel closure rate to achieve agreement between modeled and measured water pressures. Lliboutry (1983, 1996) justified an increased deformation of basal ice by enhanced closure rates on the upstream-side of bed obstacles as well as by material properties of basal ice. Hooke (1984) and Hooke et al. (1990) argued that the drag on the bed would prevent a semi-circular tunnel to maintain its shape while closing. Thus, its cross-sectional shape should be broad and low instead. Cutler's (1998) finite element modeling of the evolution of subglacial tunnels due to varying water input supports the assumption of a broad and low conduit shape. Sometimes, such a channel is also referred to as "H-channel" ("Hooke-Channel", in analogy to "Röthlisberger-Channel") even though the underlying idea is a modification of the Röthlisberger theory rather than an independent one.

Nye (1973) suggested continuous subglacial waterways as channels incised into the bed. Their hydraulics were described in detail by Weertman (1972). Studies of recently deglaciated bedrock surfaces provide evidence for the existence of such "Nye-Channels" (Walder and Hallet, 1979; Hallet and Anderson, 1980; Sharp et al., 1989), however, their occurrence is limited to regions of highly soluble carbonate bedrock. Walder and Fowler (1994) and Ng (2000) developed theories of flow in tunnels incised into deformable subglacial sediments, considering melt enlargement and creep-closure of the ice-ceiling as well as erosion and inward creep of the sediment.

Actual subglacial channel geometries in nature are presumably combinations of these basic types. However, all subglacial conduit concepts exhibit an identical feature: the cross-section adjusts in accordance to the hydraulic conditions. The exact geometry of the conduit appears to be of secondary importance considering the many uncertainties which result from the difficult access to the subglacial environment. The most important consequence of a dynamic geometry is the inverse relationship between pressure and discharge under stationary conditions (Röthlisberger, 1972). Hence, conduits carrying higher discharges would capture water from smaller channels, thus, leading to an arborescent network (Röthlisberger, 1972; Shreve, 1972). This finding is supported by the fact that meltwater drains from the glacier in one or a few large streams, whereas numerous tributaries are fed by water entering from the surface through moulins or crevasses (Hubbard and Nienow, 1997). However, steady-state conditions are only approximated for seasonal runoff variations. Instead, channel geometry cannot adjust to short-term fluctuations and water pressure is found to vary in phase with discharge (Spring and Hutter, 1982).

Distributed systems

Some water from the surface is also drained at the glacier bed where or when a channelised system is not available. Additionally, meltwater is also produced at the ice-bedrock interface by frictional heating and geothermal heat. Since a channelised system, if present, is localized only at a small portion of the glacier bed, another mechanism must be responsible for the drainage of water from extensive bed areas. Such flow may occur via water films (Weertman, 1972, 1983),
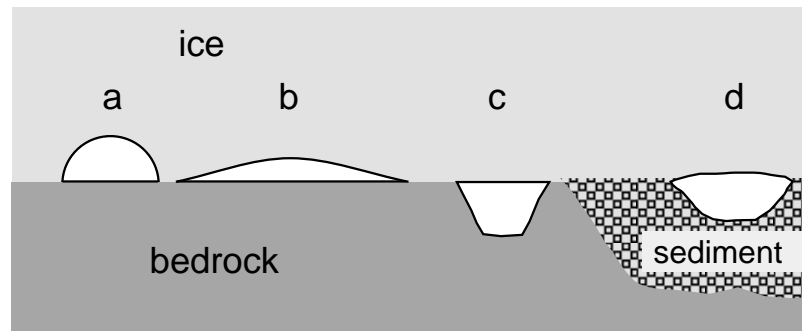
Figure 2.3: *Different types of subglacial channels: (a) semicircular R-channel, (b) broad, low H-channel, (c) Nye-channel, incised into bedrock and (d) canal eroded into subglacial sediment.*

through a permeable sediment layer (Boulton, 1974; Clarke, 1987) or via a network of linked cavities (Walder, 1986; Kamb, 1987).

Water film   Weertman (1972) proposed drainage of basal meltwater as a thin water film. The flow through such a system and hence basal melting due to viscous energy dissipation scale with film thickness. Thus, the system would be unstable against perturbations in layer thickness and formation of channels would result (Walder, 1982). These considerations were developed for a planar, debris-free and impermeable glacier bed. Although actual glacier beds are rough and consist at least partly of a permeable sediment layer the concept may still apply locally, displaying a patchy structure, as it may exist under the Antarctic ice streams (Alley, 1989b).

Sediment bed   Where the bed of the glacier is composed of permeable sediments, water infiltrates into the sediment until saturation and percolation of water through the sediment layer occurs like in a confined porous aquifer (Boulton and Jones, 1979; Boulton and Hindmarsh, 1987; Alley, 1989a). If the meltwater supply exceeds the aquifer drainage capacity, drainage between the ice and the sediment layer must occur, either as a Weertman-type water film (Weertman, 1972; Alley, 1989b) or in canals cut into the sediment as proposed by Walder and Fowler (1994) and Ng (2000). Except for a few cases where the glacier overlies a karstic limestone (Smart, 1983, 1986), the permeability of a hard bed is neglected.

Linked cavities   Mobility of water either through a film or through permeable basal ice (Lliboutry, 1996) is required to sustain regelation-sliding of the glacier (Weertman, 1957). As ice flows over a bedrock obstacle, the increased pressure on the upstream side causes melting. The resultant water is transferred around the obstacle and refreezes on the lee side. If ice flow over a basal obstacle is fast enough, the ice may separate from the bed in the lee of the bump, leaving a cavity (Lliboutry, 1968). Water can find access to the cavity and fill it. If the water is pressurized, it is forced to spread out from the cavity along the glacier bed into neighboring voids, thereby establishing links between them (Walder, 1986; Kamb, 1987). Steady state hydraulics in a network of interconnected cavities was investigated by Walder (1986) and Kamb (1987). Links or orifices are enlarged by energy dissipated by flowing water counteracting the creep-closure of the ice, whereas the size of the cavities is mainly determined by the sliding speed (Fig. 2.4). Empirical evidence for the existence of such a interconnected-cavities configuration was found by proglacial bedrock mapping (Walder and Hallet, 1979; Hallet and
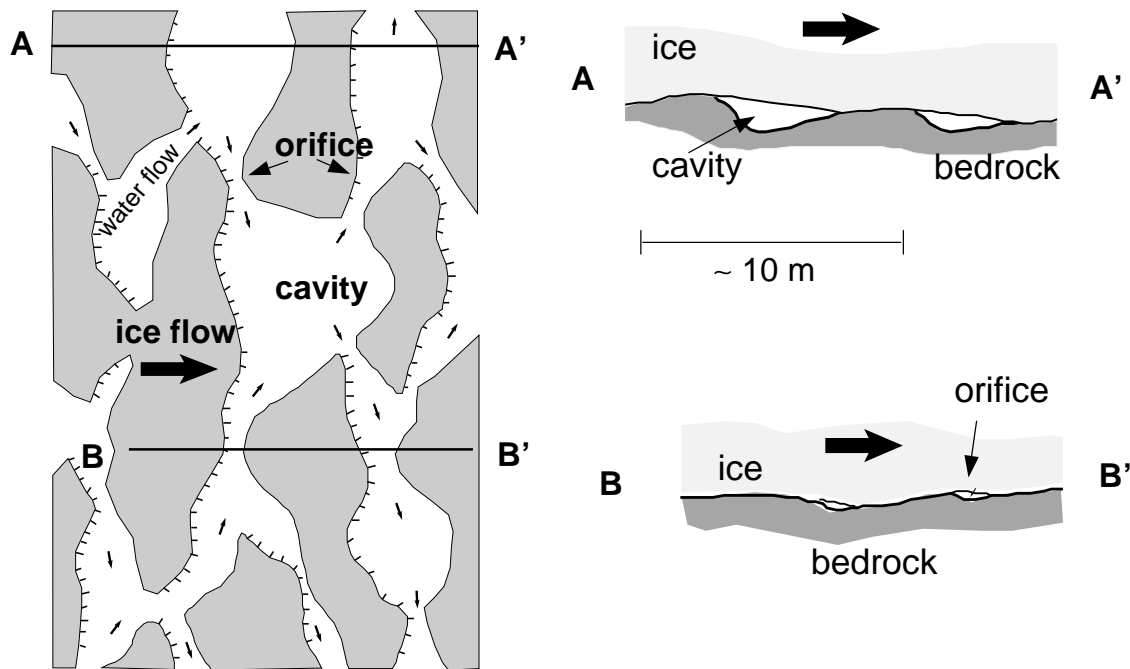
Figure 2.4: *The left part shows a map view of an idealized linked-cavity-network. The dark signature indicates where ice is in contact with the bed, the arrows indicate the direction of basal sliding. The hatched lines indicate where ice separates from the bedrock. Vertical cross-sections along lines AA' and BB' are shown in the right part (taken from Kamb, 1987).*

Anderson, 1980; Sharp et al., 1989). Observations of broadly dispersed or multi-peaked tracer breakthrough-curves a long time after injection into a glacial drainage system, (Lang et al., 1979; Kamb et al., 1985; Brugman, 1986; Nienow et al., 1998; Hock et al., 1999) indicate a distributed or multiply linked system through which water moves slowly.

Several properties of a linked-cavity drainage system are contrary to those of a channelised system. Linked-cavities occur widely distributed on the glacier bed and flow paths are tortuous and partly directed transversely to ice flow (Fig. 2.4). The water pressure scales with the discharge through the system. Thus, the linked-cavity system can remain anastomosing. While analyzing the stability of such linked cavity systems Walder (1986), Kamb (1987) and Fowler (1987) found that once a certain threshold discharge is exceeded, water pressures are higher in a cavity system than in a channelised system, subsequently leading to the collapse into a channelised drainage system. Fowler (1987) pointed out that a rough bed topography always leads to the formation of cavities which may evolve into such a drainage network even though drainage from the glacier is dominated by channels. This coexistence of channelised and distributed drainage systems is probably the most common configuration beneath alpine glaciers.

2.3 Characteristics of glacial runoff

The amount and the course of discharge emerging from an alpine glacier is determined by both the temporal distribution of meltwater production as well as the routing through a complex drainage system. Consequently, runoff is subject to a pronounced temporal variability over a wide range of time scales, integrating variations due to the melting process as well as variations due to the evolution of the drainage system.

2.3.1 Variability due to meltwater generation processes

Longterm variability

From a longterm perspective, a glacier represents a hydrological storage. Most of the annual precipitation falls as snow, thus, it contributes to mass storage rather than directly to runoff (Röthlisberger and Lang, 1987). Hence, the glacier mass balance is equivalent to the storage change component in the glacier's water budget. During times of negative mass balance, water is released from this storage and contributes to runoff. In contrast, a positive glacier mass balance is associated with a cool and wet ablation season, resulting in decreased total runoff. This inverse relationship of glacier runoff and precipitation is referred to as the "compensating effect" (Röthlisberger and Lang, 1987). Through this coupling to the glacier mass balance, the amount of glacial discharge is controlled by climatic variations.

Seasonal variability

The annual cycle of glacier runoff is primarily governed by the course of solar radiation and air temperature. The radiation dependence implies also a large influence by the retreat of the transient snow-line. Subjected to identical meteorological conditions, more meltwater would be produced late in the ablation period when large areas of dark ice are exposed to the surface as compared to the beginning when those areas are covered by high albedo snow. Similarly, as a result of this albedo-effect, a pronounced discharge decline is observed after summer snowfalls (Fig. 2.5) (Röthlisberger and Lang, 1987; Escher-Vetter and Reinwarth, 1994; Braun, 1996).

Diurnal variability

Due to the dominance of meltwater production by solar radiation and air temperature, melting occurs predominantly during the day whereas it is strongly reduced at night. This produces a diurnal hydrograph cycle which is characteristic for the runoff from glaciers. Figures 2.5 and 2.6 demonstrate how this diurnal variation is superimposed to a base flow varying on a seasonal time scale and that high discharges coincide with large diurnal variations (Elliston, 1973; Röthlisberger and Lang, 1987).

2.3.2 Variability due to routing processes

As shown above, water can be transferred through a glacier by different drainage systems. As such, the initial temporal distribution of meltwater supply is modified. The primary hydrological effects of the firn and transient snow-cover is the retention of meltwater and its delay due to slow percolation velocities (Oerter and Moser, 1982; Fountain and Walder, 1998; Schneider, 1999). Consequently, runoff concentration is accelerated as the snow line retreats during the summer season or as the thickness and extend of the firn area is decreased during periods of negative mass balance (Braun, 1996).

Since the geometry of englacial and subglacial drainage configurations is controlled by the rate of discharge as well as by creep-closure of the ice, most passageways decrease considerably in size during winter, when no surface meltwater is produced (Röthlisberger and Lang, 1987). In
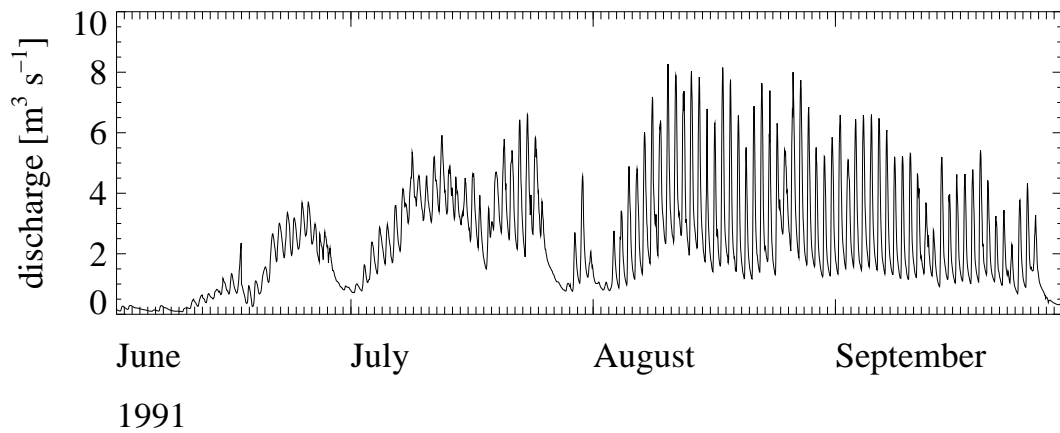
Figure 2.5: *Hydrograph of hourly means of discharge from Vernagtferner as measured during the ablation season June to September 1991, (taken from Escher-Vetter and Reinwarth (1994)).*
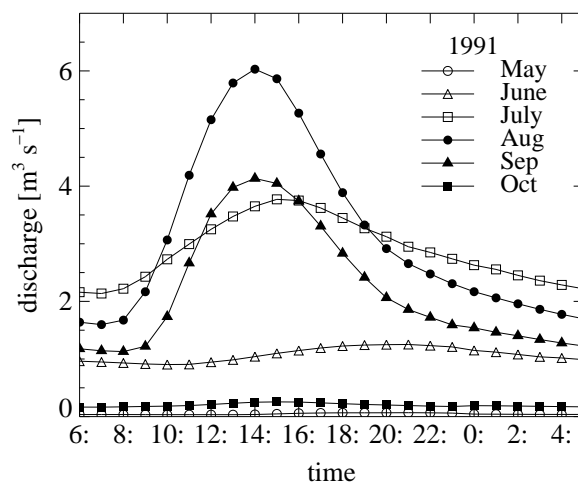
Figure 2.6: *Mean diurnal variation of discharge from Vernagtferner during the ablation season June to September 1991. The faster arrival of peak discharge as the season progresses is clearly noticeable, (taken from Escher-Vetter and Reinwarth (1994)).*

contrast, a cavity system is kept open mainly by basal sliding and only secondarily by melting. Therefore it is likely to persist throughout the winter (Fountain and Walder, 1998) by draining subglacially produced water (Lliboutry, 1983). At the beginning of the melt season the capacity of the basal drainage system is not sufficient to cope with the actual meltwater flux. With increasing discharge the linked cavity system becomes unstable (Walder, 1986; Kamb, 1987; Fowler, 1987) resulting in the formation of hydraulically efficient channels. In response to a progressively rising meltwater supply, the channelised system expands up-glacier over the course of the season (Nienow et al., 1998). The evolution of discharge routing through a glacier is determined by two processes. First, retention decreases due to a reduction in the thickness and extent of the snow and firn cover and second, the en- and subglacial systems develop a higher drainage capacity. Figure 2.6 displays this behavior in the faster arrival of the daily discharge peak as the season progresses (Elliston, 1973; Escher-Vetter and Reinwarth, 1994; Braun, 1996).

Aperiodic variability

Additional runoff variability is induced by discharges of water derived from rainfall onto the glacier surface. Further, water can be stored temporarily in isolated en- or subglacial water pockets and cavities or ice-dammed lakes. The sudden release of such water causes erratic variations in runoff which are not directly triggered by climatic variations (e.g. Luetschg, 1926; Liestøl, 1956; Röthlisberger, 1981; Clarke, 1982; Haeberli, 1983; Bjørnsson, 1998; Anderson et al., 1999).

Chapter 3

Water balance

Balancing the water input with discharge output provides a possibility to investigate the evolution of a glacial drainage system. An imbalance of input and output would indicate temporary storage of water in or beneath the glacier. Subglacial storage of water can be related to the inability of the prevailing drainage system to discharge water at the same rate as it is supplied to the system. This is especially likely to occur at the beginning of the ablation season when large amounts of meltwater are rapidly transferred into an inefficient winter drainage system (Sec. 1.1.1).

During the 1999 summer field season we conducted an extensive field program at Unteraargletscher comprising glaciological, meteorological and hydrological measurements. In this chapter, we want to assess the storage of water in or beneath the glacier early in the melt season, when a rearrangement of the subglacial drainage system and mechanical adjustments at the glacier bed are likely to occur. Meltwater input to the glacial hydrological system was quantified using a temperature index melt model which was calibrated with ablation measurements. Discharge was measured at a gauging station in the proglacial stream. However, 18 days after its installation, the station was destroyed during a flood event which was presumably caused by a rainfall-induced outburst of en- or subglacially stored water. We discuss this outburst flood in light of a significant imbalance of water input and output during the days preceeding the release event and a change in the configuration of the drainage system.

3.1 Methods

3.1.1 Meteorological records

At the Lauteraarhut (Fig. 1.1) we operated an automatic weather station to collect data on air temperature, relative humidity, wind speed, wind direction and precipitation at intervals of 15 minutes. Only the air-temperature and precipitation measurements (Fig. 3.1) are of relevance to the work presented here. Air temperature was measured by a ventilated thermistor (Vaisala T107) and precipitation was measured using a tipping bucket rain gauge (Joss-Tognini). We chose a measurement site beside the glacier rather than directly on the glacier because thermal conditions of the near surface boundary layer adjacent to the glacier are less affected by local processes such as catabatic winds, condensation and evaporation than those on the glacier itself (Lang and Braun, 1990).
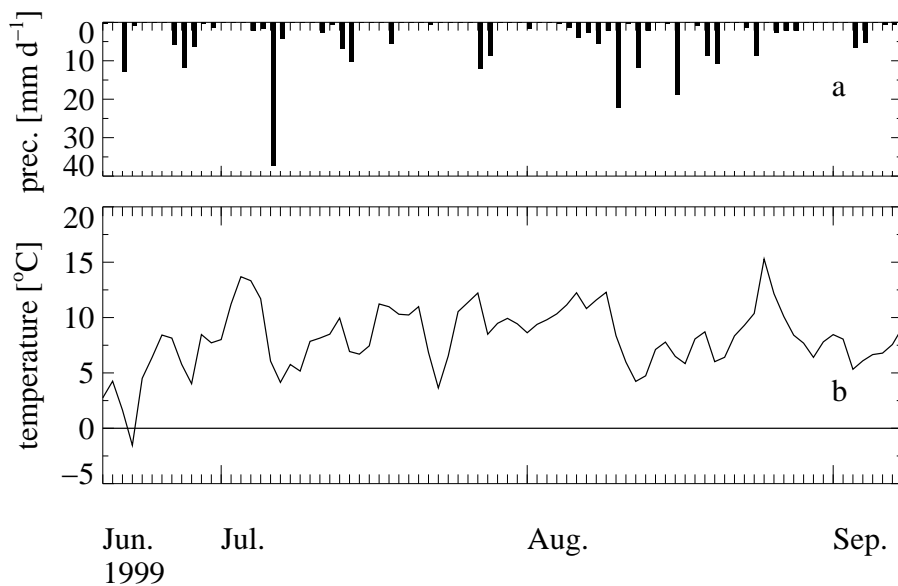
Figure 3.1: *Daily values of (a) total precipitation and (b) mean air temperature as recorded at the Lauteraarhut during the ablation season 1999.*

3.1.2 Determination of surface melt

Water originating from surface melt was the main input into the hydrological system of Unteraargletscher during the period in which the interest of this study is focused on. To quantify this meltwater input, point measurements of ablation were used to calibrate a distributed melt model (Sterr, 2000; Hock, 1999). Liquid precipitation may also contribute to the water input but a quantification of the precipitation over the entire catchment is not performed in this study. The complex spatial distribution of precipitation in a mountainous catchment would require a study on its own. Thus, in the remainder of this thesis the contribution of precipitation is neglected such that the term "input" as used here represents a minimum estimate.

Ablation measurements

Melt was monitored between June and September 1999 at up to 26 ablation stakes distributed across the ablation area of Unteraargletscher (Fig. 3.2) by taking stake readings on four occasions at intervals of 2–5 weeks. However, only at 14 stakes the measurements were performed four times. Nevertheless, for some intervals between individual stake readings the dataset is complete. In addition, the thickness of the snow cover at the beginning of the observation period was measured at four locations at different altitudes. To convert these thickness-measurements into water-equivalent (w.e.) melt, we use a typical density of $500 \, \mathrm{kg \, m^{-3}}$ for wet snow and a density of $900 \, \mathrm{kg \, m^{-3}}$ for ice (Paterson, 1994).

Melt model

Snow and ice melt across the entire glacier was estimated using a distributed temperature-index method developed by Hock (1999) that includes direct clear-sky solar radiation. The method is
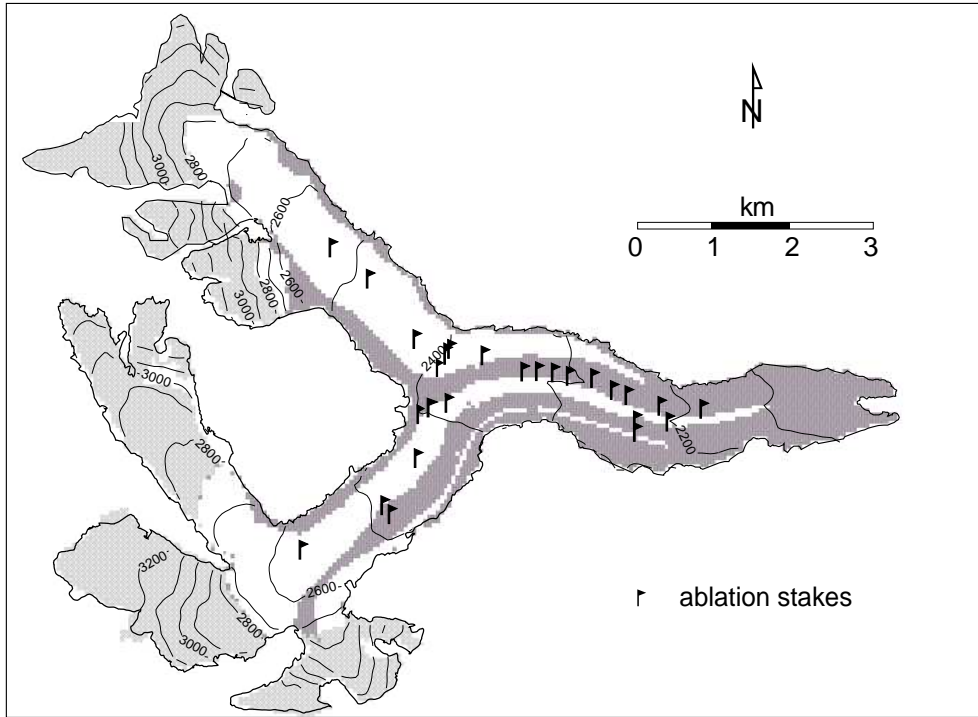
Figure 3.2: *Map of Unteraargletscher showing the locations of the ablation stakes in 1999. Dark shaded areas denote debris cover whereas the firn area is indicated by light shading.*

based on the classical positive degree-day approach (e.g. Braithwaite, 1995) in which calculated melt rates are only a function of positive air temperatures. However, by incorporating a radiation index in terms of potential direct solar radiation, the method also accounts for shading of the glacier due to surrounding topography and allows spatially-variable melt by considering the effects of local slope and aspect of the glacier surface. Hourly melt rates M (mm h^{-1}) are thus calculated as

$$M = \begin{cases} (\mathrm{MF} + a_{\mathrm{snow/ice}}\, I)\, T & : \quad T > 0 \\ 0 & : \quad T \leq 0 \end{cases}, \tag{3.1}$$

(Hock, 1999) where MF is a melt factor (mm h^{-1} °C^{-1}), $a_{\mathrm{snow/ice}}$ is a radiation coefficient different for snow and ice surfaces (m^2 W^{-1} mm h^{-1} °C^{-1}) and T is air temperature (°C). The potential clear-sky solar radiation at the glacier surface I (W m^{-2}) is calculated as a function of solar geometry and topographic characteristics (Hock, 1999).

A spatial variability of melt also arises due to debris that covers large parts of the tongue of Unteraargletscher. To describe the insulating effect of a debris cover, the melt rate calculation (Equation 3.1) was adapted to account for the reduced melt of the underlying ice. Even though the debris cover is far from being uniform in terms of thickness, spatial distribution and rock type, a simple approach was selected in accordance with the generalizing nature of a temperature-index method. A single reduction factor d_{debris} is introduced in the model calculation representing the fraction by which the melt rate of ice is reduced due to a debris cover (Sterr, 2000). Hence, for a debris-covered ice surface and positive air temperatures, hourly melt rates are calculated as

$$M = (\mathrm{MF} + a_{\mathrm{ice}}\, I)\, d_{\mathrm{debris}}\, T. \tag{3.2}$$

Table 3.1: *Model parameters optimized for Unteraargletscher*

Parameter	Value	Unit
Air temperature lapse rate	-0.65	$^\circ\text{C}\,(100\,\text{m})^{-1}$
Melt factor	1.875×10^{-2}	$\text{mm}\,\text{h}^{-1}\,^\circ\text{C}^{-1}$
Radiation factor for ice	0.7×10^{-3}	$\text{m}^2\,\text{W}^{-1}\,\text{mm}\,\text{h}^{-1}\,^\circ\text{C}^{-1}$
Radiation factor for snow	0.5×10^{-3}	$\text{m}^2\,\text{W}^{-1}\,\text{mm}\,\text{h}^{-1}\,^\circ\text{C}^{-1}$
Reduction factor for debris	0.65	-

Rates of snow and ice melt were computed using Equations 3.1 and 3.2 for each gridcell of a $50\,\text{m}$ resolution digital elevation model (DEM) of Unteraargletscher that was constructed from 1998 aerial photographs. To account for the shading of the glacier surface due to surrounding topography, the glacier DEM was embedded within the Swiss 1:25000 digital elevation model DHM25 of the entire surrounding catchment area (L+T, 1993). Slope and aspect angles of each gridcell were directly derived from the DEM. In addition, topographic shading of the glacier was determined for every time step and each gridcell based on the effective horizon and the position of the sun. The melt model further requires a digital model of the glacier surface type beneath the winter snow cover (Hock, 1999). This surface type was prescribed by raster maps, indicating for each gridcell whether the surface was ice, firn or debris (Fig. 3.2). For the purpose of melt rate calculation the model treats firn like snow. Spatial distribution of debris and firn were derived from aerial photographs. A further raster map contains the distribution of the initial snow cover on the glacier which is based on a linear interpolation of snow thickness measurements, ranging from $0.15\,\text{m}\,\text{w.e.}$ at $2200\,\text{m}\,\text{a.s.l.}$ to $0.5\,\text{m}\,\text{w.e.}$ at $2400\,\text{m}\,\text{a.s.l.}$ and $1.0\,\text{m}\,\text{w.e.}$ at $2550\,\text{m}\,\text{a.s.l.}$.

Required input data for the model is air temperature. The temperature recorded at the automatic weather station (Fig. 3.1) was extrapolated and distributed to each gridcell using a linear lapse rate. The melt factor, radiation coefficients for snow and ice, and debris reduction factor are empirical coefficients. Together with the temperature lapse rate, these coefficients are the calibration parameters of the model.

The melt simulations were initialized using model parameters which have been optimized for Storglaciären, Sweden, by Hock (1999). Subsequently, these parameters were adjusted iteratively to achieve maximum agreement between computed and measured melt rates at the ablation stakes (Sterr, 2000). Typically model runs were performed for the period that begins with the start of the temperature record on 19 June and ends on 8 September 1999 when the final ablation stake readings were taken. Parameter optimization involved the visual inspection of plots of simulated and measured melt for three different periods that coincided with the intervals between the ablation stake measurements. Table 3.1 lists the model parameters optimized for Unteraargletscher.

Model performance

The spatial distribution of the calculated melt (Fig. 3.3) compares favorably with what we expect when we bear in mind the effects of topography on shading and potential direct solar radiation. Values of calculated radiation averaged over the entire observation period 19 June to
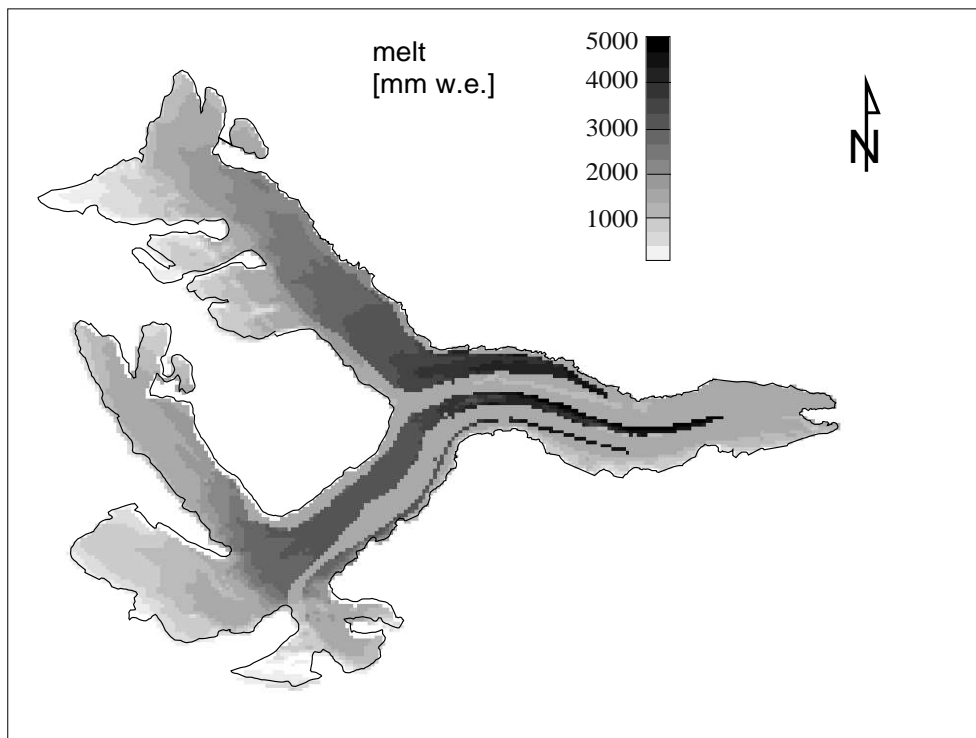
Figure 3.3: *Spatial distribution of the calculated melt* (mm w.e.) *on Unteraargletscher, cumulated over the entire observation period 19 June – 8 September 1999.*

8 September range between a minimum of 17 and a maximum of $314\,\mathrm{W\,m^2}$. Melt on south-facing slopes typically exceeds that on north-facing slopes. In addition, the effect of the debris cover is also clearly visible. The highest melt is calculated for debris-free zones at the northern side of the tongue of the glacier and between the medial moraines. In contrast, calculated melt is drastically reduced in the debris-covered terminus region.

Fig. 3.4 shows simulated and measured melt at 14 ablation stakes distributed across the ablation area of the glacier for the entire observation period (19 June – 8 September). Melt simulation and measurement as a function of time at two stakes are compared in Fig. 3.5. Considering the simplicity of the model, there is good agreement between ablation measurements and melt simulation (Fig. 3.4b). While at some stakes the model overestimates melt, at others ablation is underestimated (Fig. 3.4a). Nevertheless we want to note that a direct comparison of measured melt with that calculated by the model is not without problems because simulations represent the spatial means of $50\,\mathrm{m}$ by $50\,\mathrm{m}$ gridcells, whereas stake measurements refer to an individual point inside each of these areas.

A notable feature in Fig. 3.4a is that melt at higher altitudes is significantly larger than that in the lower reaches of the glacier. The lower melt at lower altitudes reflects reduced ablation due to debris covering much of the tongue of Unteraargletscher as most of the stakes below the confluence zone ($2400\,\mathrm{m\,a.s.l.}$) are located in debris-covered ice (triangles in Fig. 3.4a). The insulating effect of the debris cover is also revealed in plots of melt versus time (Fig. 3.5). Melt at a stake located in debris-covered ice on the medial moraine ((a) in Fig. 3.5) is roughly half as large as that at a stake located $\sim\!150\,\mathrm{m}$ higher in altitude but in debris-free ice ((b) in Fig. 3.5). However, prior to the retreat of the snowline past these two stakes at the end of June, the snowcover at these locations is melted roughly at the same rate.

The performance of the melt model can be further assessed by comparing the simulated retreat
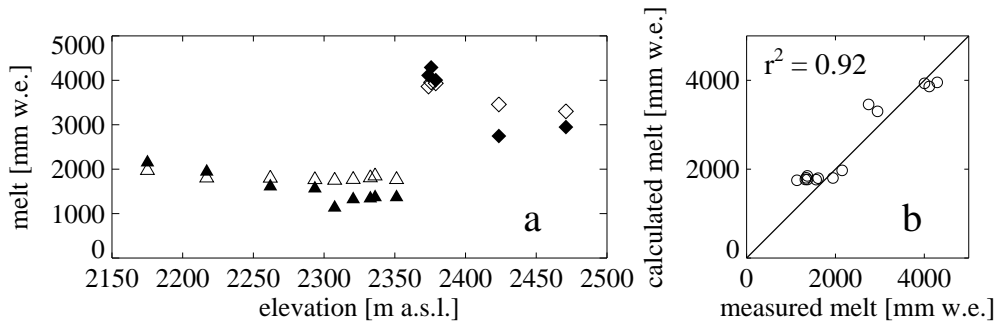
Figure 3.4: *(a) Measured (fi lled symbols) and simulated (open symbols) melt* (mm w.e.) *at 14 ablation stakes for the entire observation period 19 June – 8 September 1999. Diamonds and triangles denote stakes that are located in debris-free and debris-covered ice, respectively. (b) Measured vs simulated melt.*
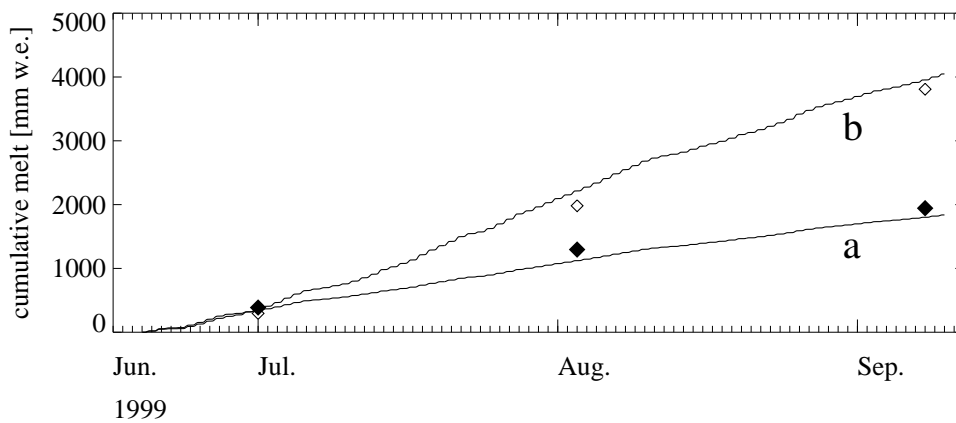
Figure 3.5: *Simulated (solid line) and measured (diamonds) melt (mm w.e.) vs time at (a) a stake located in debris-covered ice on the medial moraine (2217 m a.s.l.) and (b) a stake located in debris-free ice (2376 m a.s.l.).*
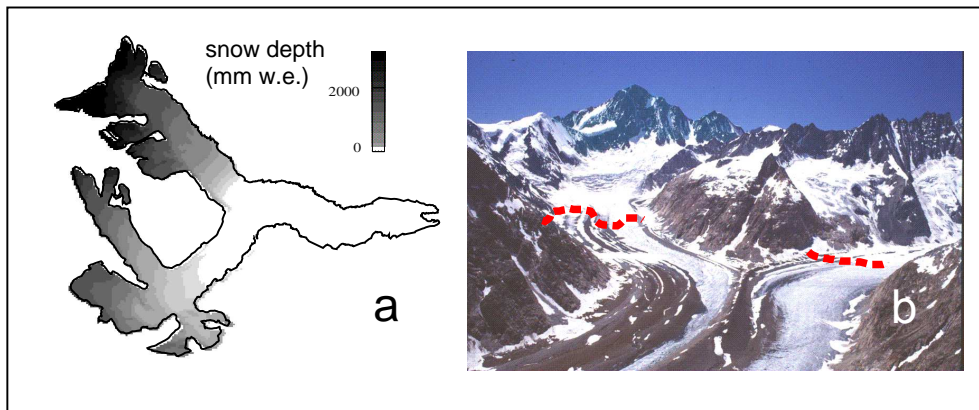
Figure 3.6: *Spatial distribution of the snow cover on Unteraargletscher. (a) Simulated snow depth* (mm w.e.) *on 24 July 1999. (b) Photograph showing the snowline (dashed line) on 26 July 1999 (photograph taken by T. Schuler).*

of the snow line with that observed on the glacier. The close agreement of the location of the snow line as identified on a photograph taken on 26 July (dashed line in Fig. 3.6b) and that as determined from the calculated snow depth distribution on 24 July 1999 (Fig. 3.6a) suggests that the spatial pattern of snow melt is reproduced reasonably well by the model calculations.

3.1.3 Glacial runoff

Stage recording

Most of the glacial runoff exits Unteraargletscher through a single large glacier portal. However, because the proglacial area consists of a flat alluvium, the stream is strongly braided before it reaches Lake Grimsel and single branches change their position frequently by lateral and vertical erosion. Only at a few locations flow is concentrated in a single thread. About $500\,\mathrm{m}$ downstream of the glacier terminus, the stream is incised into a former terminal moraine offering a moderately stable cross-section. All hydrological measurements were performed at this location which is referred to as the gauging site (Fig. 1.1 and 3.7).

Water stage was measured using a vented capacitive pressure transducer (Keller PR-46W) and electrical conductivity was measured with a commercial conductivity probe (Campbell 247). Conductivity readings were corrected for errors resulting from ionisation and temperature effects according to technical instructions by the producer (Campbell, 1994). Both sensors were housed inside a gauging device that consists of two $1.2\,\mathrm{m}$ long concentric PVC cylinders having diameters of 20 and $30\,\mathrm{cm}$. The device was positioned vertically in the stream and fastened to steel pipes that were anchored at the stream bank by a $4.5\,\mathrm{m}^3$ sized gabion filled with boulders (Fig. 3.8). The inner cylinder is closed at its lower end. A set of four $10\,\mathrm{mm}$ diameter holes close to the bottom allows water to pass through the cylinder while at the same time effectively damping high frequency water level fluctuations. The outer cylinder serves as a protection from mechanical damage and reduces the accumulation of sediment within the inner cylinder. Output from both sensors were recorded by a Campbell CR-10 data logger every 5 minutes.
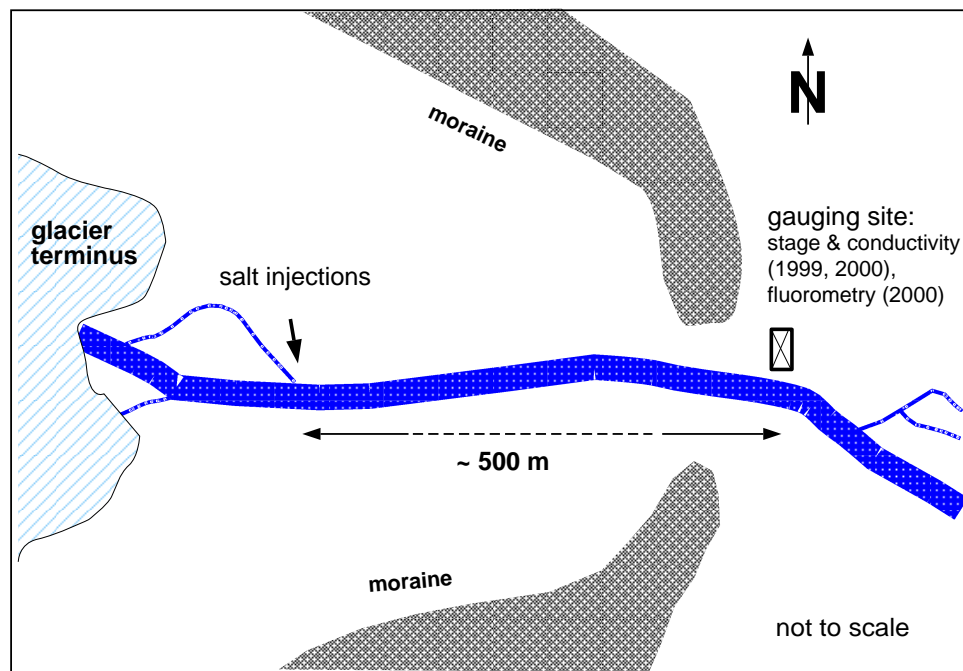
Figure 3.7: *Schematic sketch showing the approximate locations of installations in the proglacial area. Streamflow is towards east.*

Discharge measurements

To relate water stage to glacier runoff 22 individual discharge measurements were performed in the proglacial stream using the tracer-dilution method which is particularly suited to measurements at conditions of highly turbulent flows and unstable stream configurations (Fischer, 1982; Käss, 1998). The method entails the injection of a tracer in the stream and its subsequent detection at an appropriate distance downstream assuming that the tracer is uniformly mixed over the entire cross-section of the stream at the detection point. Additional assumptions are that discharge does not change significantly during the course of a measurement and that there are no sources and sinks of water between the points of tracer injection and detection. For the proglacial stream of Unteraargletscher the minimum flow distance necessary to ensure uniform mixing of the tracer with the stream water was estimated between 200 and $500\,\mathrm{m}$ (Käss, 1998).

We injected amounts of 5 to $10\,\mathrm{kg}$ of solid sodium chloride (NaCl) $\sim 500\,\mathrm{m}$ upstream from the gauging station (Fig. 3.7). We found that the results were unaffected by not dissolving the salt in stream water prior to injection. Following a salt injection, electrical conductivity was recorded at intervals of one second until the entire salt wave had passed the gauging station and conductivity values had essentially returned to the background level. The salt concentration $c\,(\mathrm{kg\,m^{-3}})$ in the stream water is derived from the measured electrical conductivity $L\,(\mu\mathrm{S\,mm^{-1}})$ by applying the linear relationship $c = kL$, where the constant $k = 7.36 \times 10^{-3}\,(\mathrm{kg\,m^{-3}})/(\mu\mathrm{S\,mm^{-1}})$ was determined by calibrating the instrument with solutions of known salt concentration. Discharge $Q\,(\mathrm{m^3\,s^{-1}})$ is then calculated using the mass-balance relationship

$$Q = \frac{m}{\int_0^\tau (c(t) - c_0)\,dt},$$

(3.3)

where m (kg) is the mass of salt injected, τ is the time it takes for the entire salt wave to pass the

Figure 3.8: *The gauging station in June 1999. The terminus of Unteraargletscher can be seen in the background (photograph taken by T. Schuler).*

gauging station, and $c_0 = kL_0$ is the background concentration. The background conductivity L_0 was determined as a linear interpolation of 10 second averages before and after the passage of the salt wave (Fig. 3.9).

Discharge measurements were carried out repeatedly throughout the entire period of stage measurements that extended from 16 June when the stream gauge was installed to 4 July when the data was downloaded for the last time before the gauging station was destroyed. Furthermore, the measured discharges cover the whole range of observed water stages. The stage–discharge relation is obtained using the water stage measurements h_s (m) at the time of the discharge measurement. The resulting rating curve

$$Q = e^{3.82\,h_s} + 1.564 \tag{3.4}$$

is constructed as the best fit to the data points (Fig. 3.10). The exponential form of the rating curve reflects the increasing width of the stream as the water level rises.

3.2   Results

3.2.1   Input into glacial system

The modeled melt rate (Fig. 3.11c) displays pronounced diurnal variations which primarily reflect the distinct daily cyclicity of the direct clear-sky solar radiation. While the calculated melt rates are nearly zero during night time, they peak sharply at mid day when the potential solar radiation reaches its daily maximum. In addition, the daily melt rate maxima are modulated by the general course of the temperature record (Fig. 3.11b). Warm temperatures in early July result in a high meltwater production. The highest melt rate of the entire period of melt simulation (19 June - 8 September), exceeding $40\,\mathrm{m^3\,s^{-1}}$ integrated over the glacier area, is calculated for
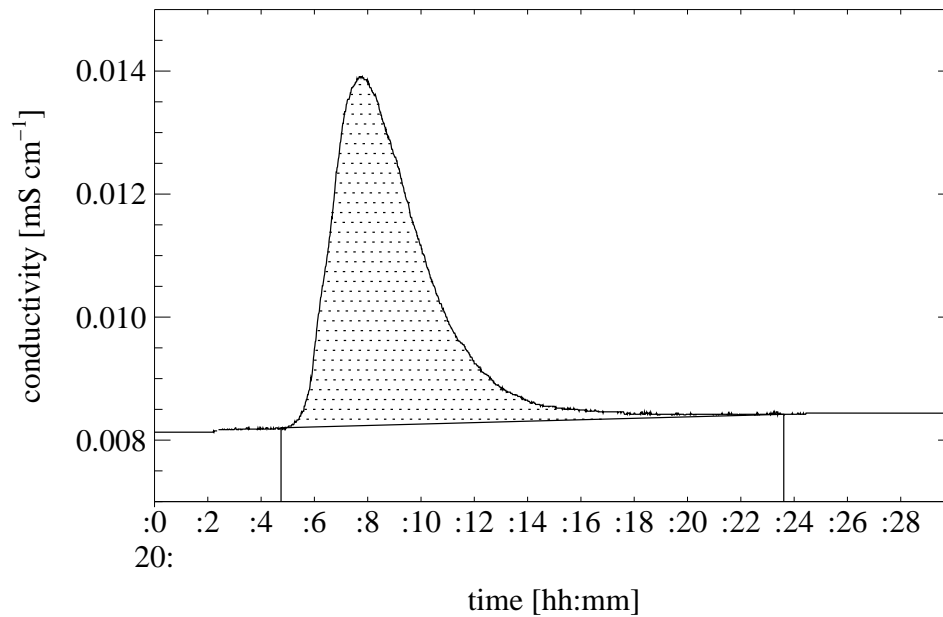
Figure 3.9: *Example of an individual discharge measurement using the salt dilution method. The vertical lines indicate the duration of the tracer passage. The dotted area represents the concentration integral in the denominator of Equation 3.3.*

3 July. Conversely, meltwater production ceases completely during periods with temperatures well below $0°C$ on 21 and 22 June.

To quantify the uncertainty of the melt calculation we determined the standard deviation of simulated melt with respect to measured melt. For the 14 stakes that are available for the entire period, calculated melt deviates from measurements by $\pm390\,\mathrm{mm\ w.e.}$. Taking a mean measured ablation of $2290\,\mathrm{mm\ w.e.}$, this deviation translates into a $\pm17\%$ uncertainty in our melt simulations. The number of stakes available for the shorter intervals between individual ablation measurements is larger but uncertainties are similar varying between $\pm13\%$ and $\pm16\%$. An exception is the two week interval between the first two stake readings where the uncertainty amounts to $\pm44\%$. However, the calculation of this high uncertainty is likely affected by two artifacts. First, measurement and simulation do not refer to the same length of time. The first stake readings were taken on 16 June, three days before the starting date of the model calculation. In effect, we are comparing measured and calculated melt over time intervals that differ in length by $\sim20\%$. Second, during these two weeks at the end of June, the medial moraine became partly snow-free, resulting in a pronounced micro-scale variability of melt due to the discontinuous snow coverage which is not accounted for in the conceptual melt model. Therefore, we disregard the $\pm44\%$ uncertainty determined for this two week interval and accept a generous overall uncertainty of $\pm20\%$ for our melt calculations.

3.2.2 Output from glacial system

The recorded discharge (Fig. 3.11d) varies between 2.8 and $7.6\,\mathrm{m^3\,s^{-1}}$ and shows a diurnal cycle that is characteristic for glacial runoff (Röthlisberger and Lang, 1987). Typically, discharge maxima occur in the early evening followed by discharge minima in the morning of the next
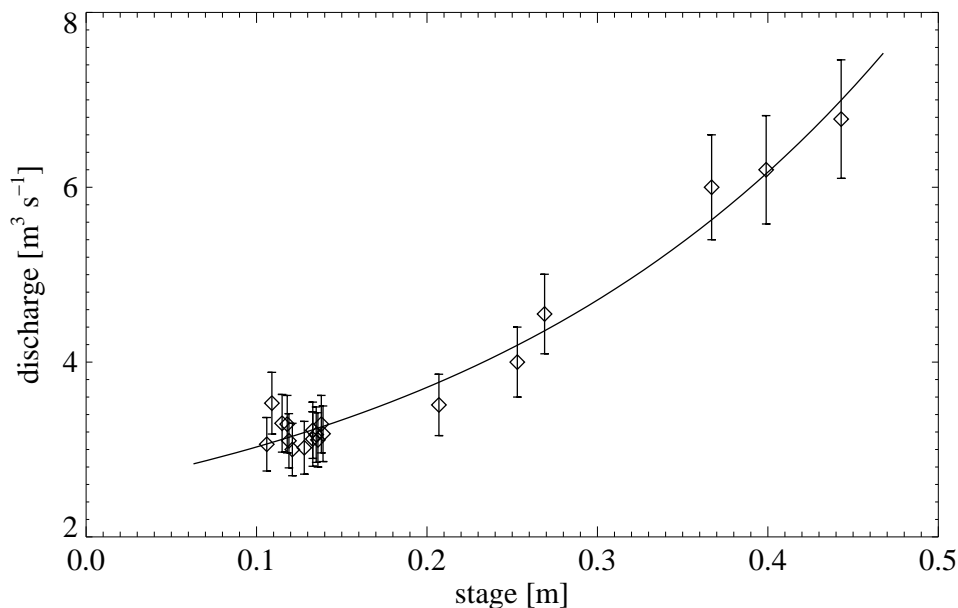
Figure 3.10: *Discharge rating curve for the proglacial stream of Unteraargletscher. Error bars are* ±10%. *The solid line represents Equation 3.4 over the entire range of measured water stages.*

day. Superimposed on these diurnal variations are secondary spikes that can be associated with precipitation events on 21, 26, 27 and 28 June (Fig. 3.11a). In general, we note a period of recession flow lasting from 19 to 25 June followed by an increase in discharge during the second part of the record. Coinciding with increasing discharge the amplitude of the diurnal cycle is also enlarged. Furthermore, towards the end of the period of observation discharge varies less smoothly and the record displays a jagged appearance. These small but rapid fluctuations are attributed to enhanced bed load transport at high discharges.

We believe that the main source of error in our rating curve and discharge measurements stems from the unstable stream configuration due to an unconsolidated nature of the stream bed. In particular, erosion and sedimentation processes within the stream can lead to changes in water level that are unrelated to variations in discharge. A number of discharge measurements at low water stages (cluster of data points in the lower lefthand corner of Fig. 3.10) suggests that discharge measurements can vary by roughly $\pm 0.2 \, \mathrm{m^3 \, s^{-1}}$ for nearly the same water level. For a discharge of $\sim 3 \, \mathrm{m^3 \, s^{-1}}$, this variability corresponds to less than the $\pm 10\%$ accuracy which has been reported for comparable situations (Anderson et al., 1999; Kite, 1994). In contrast, noise in the stage measurements that results from the roughness of the water surface inside the gauging device is considered to be small except maybe at very high discharges. Other sources of error are associated with the calibration of the pressure transducer and the salt-dilution measurements of discharge themselves. As an overall estimate, we assign an uncertainty of $\pm 10\%$ to our discharge measurements.

3.2.3 Water balance

In general, the diurnal variations of glacial runoff from Unteraargletscher reflect those of melt-water input to the glacier. Daily maxima and minima of discharge (Fig. 3.11d) lag behind those
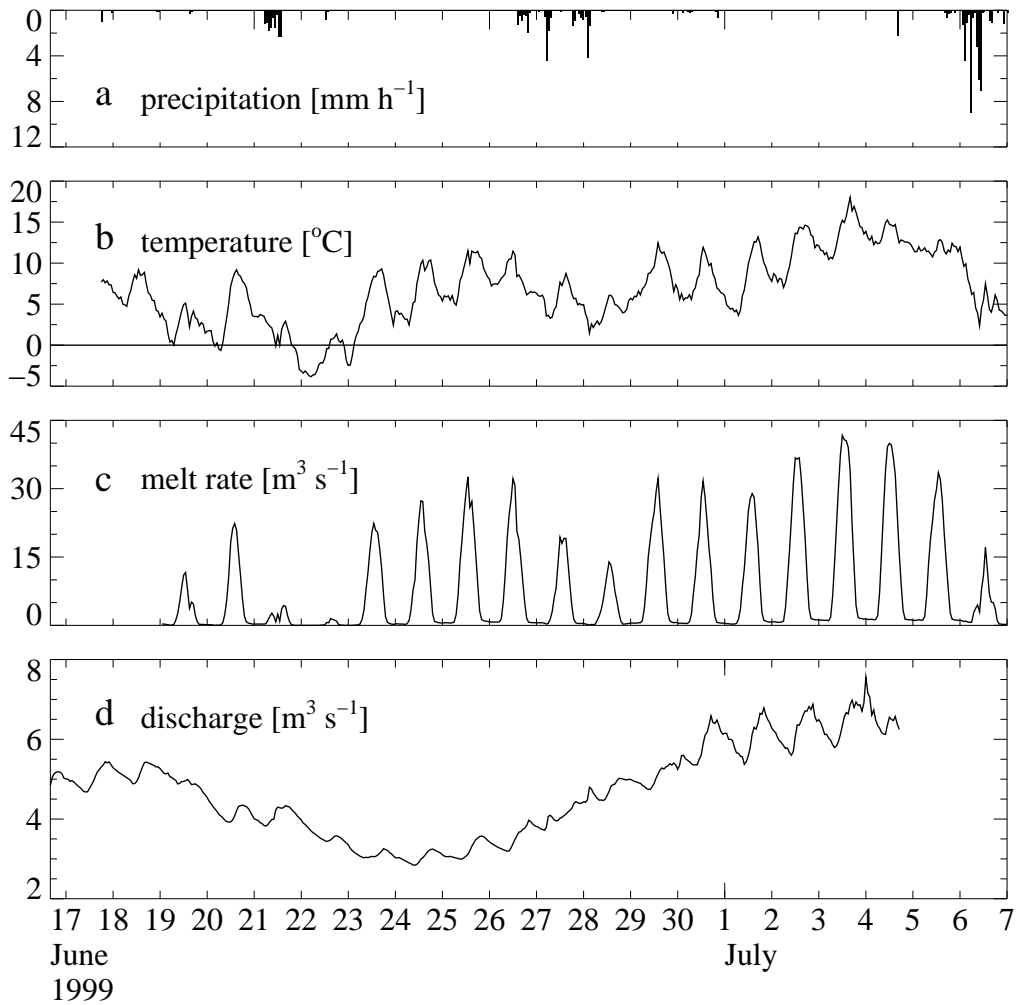
Figure 3.11: *Hourly values of (a) precipitation and (b) air temperature at the Lauteraarhut, (c) modeled melt rate of the entire glacier and (d) discharge in the proglacial stream.*

of melt rate (Fig. 3.11c) and air temperature (Fig. 3.11b) by ∼3–5 hours which suggests that runoff was fed mainly by meltwater. However, for longer-term variations, temporal patterns of surface melt rate and glacial runoff show significant differences. With the arrival of a cold front on 21 June, air temperature dropped drastically to values well below 0°C causing the meltwater production to fall to zero. In response to this reduced meltwater input to the glacier, discharge of water in the proglacial stream started to decline. The return of higher temperatures on 23 June led to an increase in meltwater production. However, discharge remained low for three further days. Subsequently, melt rates remained high and discharge increased until the end of the record.
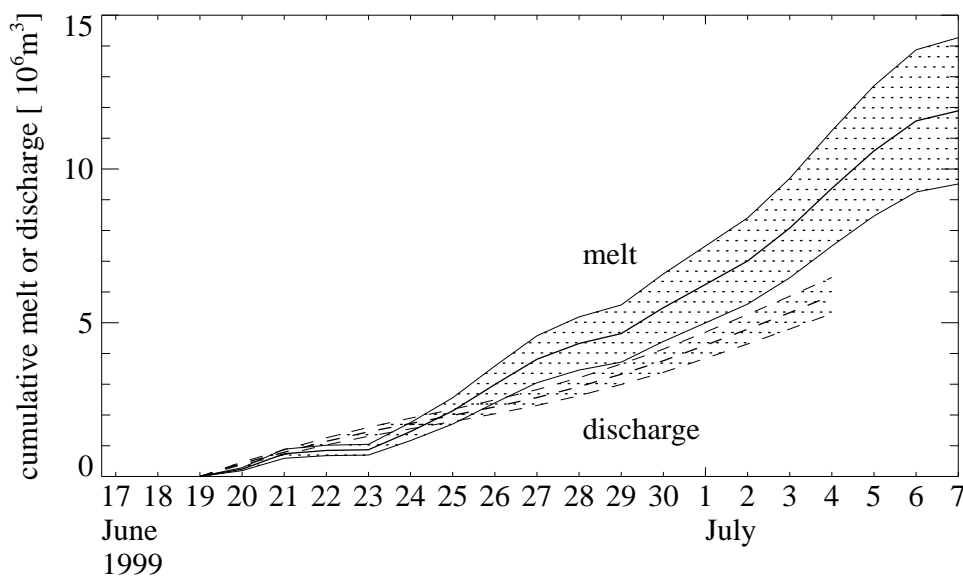
Figure 3.12: *Cumulative melt of the entire glacier (solid line) and cumulative discharge in the proglacial stream (dashed line). The shaded regions show the uncertainties associated with determining melt and discharge (see text for details).*

We illustrate the water balance further in Fig. 3.12 by plotting the cumulative meltwater input and the cumulative discharge. The uncertainties in determining melt or discharge (shaded regions in Fig. 3.12) increase with time due to the cumulative nature of the plot. They are based on the ±10% and ±20% uncertainties in our discharge measurements and melt calculations, respectively. During the first two days of the period shown in Fig. 3.12 meltwater input and discharge output of water were roughly balanced. Due to low temperatures on 21 and 22 June meltwater production essentially ceased. However, discharge in the proglacial stream continued, suggesting that water stored within the glacier was drained during these two cold days. The temperature rise on 23 June marks the start of a recharging period that lasted at least until the end of the discharge record on July 4. Most of this period is characterized by inputs in excess of outputs as more water was produced by melting on the glacier surface than was discharged in the proglacial stream. After taking the uncertainties in determining melt and discharge (shaded regions in Fig. 3.12) into consideration, the surplus of water at the end of the discharge record on 4 July amounts to ∼10^6 m^3 (Fig. 3.12).

3.2.4 Rainfall-induced outburst

Following six days of warm conditions, a storm system brought torrential rainfall to Unteraargletscher in the early morning of 6 July (Fig. 3.11a and b). Nearly $40\,\mathrm{mm}$ of rain was recorded at the Lauteraarhut between 0000 and 1200 hours. In fact, this storm produced the highest continuous rainfall amount during the entire period of observation from 19 June to 8 September (Fig. 3.1a). Coinciding with the intense rain, the discharge of water in the proglacial stream had increased dramatically. As a consequence, our stream gauge was completely destroyed. We estimate that the discharge at mid day of 6 July was between 20 and $30\,\mathrm{m^3\,s^{-1}}$ which corresponds to roughly three times the maximum discharge recorded during the preceeding days. Due to the high discharge the stream bank at our gauging site had been eroded and the stream had changed its course. Furthermore, large chunks of ice (up to $0.8\,\mathrm{m}$ diameter) floated in the stream and were strewn across much of the proglacial area.

3.3 Discussion

In this chapter, we have compared meltwater input and discharge output of water at Unteraargletscher during a two week period prior to a hydraulic release event. This comparison suggests that roughly $10^6\,\mathrm{m^3}$ more water was produced by melting of snow and ice on the glacier than was discharged in the proglacial stream implying that this water was stored in the glacial hydrological system. The water storage may have been in any part of the glacier: within the snow and firn on the glacier surface, within englacial conduits and water pockets, or in cavities and drainage channnels at the bed.

To assess the extent to which water was stored in or beneath the glacier, we have to investigate the capacity of the snowpack covering the glacier to retain water. At the beginning of our measurement program in mid June, we noticed small streamlets and slush areas on the snow surface up to an elevation of at least $2600\,\mathrm{m\,a.s.l.}$ The occurrence of water at the surface is symptomatic for a snow cover which is water saturated. Thus, no further retention of water was possible and any meltwater produced in the region of the glacier below $2600\,\mathrm{m\,a.s.l.}$ must have contributed to either runoff or en- and subglacial storage. For the region of the glacier above $2600\,\mathrm{m\,a.s.l.}$ we do not know the degree of water saturation of the snow cover, rendering it difficult to determine whether meltwater that percolated into the snow was retained or was delivered to the glacier. To simplify our discussion we now focus on the region of the glacier below $2600\,\mathrm{m\,a.s.l.}$ Computation of melt for this region yields a total amount of $\sim 6.5 \times 10^6\,\mathrm{m^3}$ of water for the period from 19 June to 4 July. This amount alone is sufficient to balance the total discharge of water from the glacier during the same period ($\sim 5.9 \times 10^6\,\mathrm{m^3}$). We note, however, that our melt calculation led to a conservative estimate of the water input to the glacial hydrological system because snow melt from the non-glacierized portion of the catchment is not accounted for. Furthermore, the rise in snowline from the terminus to the confluence zone during this period released meltwater that was detained in the snowpack earlier in the season. Therefore, this additional meltwater originating from both the surrounding non-glacierized area and the disappearing snow cover together with the contribution from precipitation in liquid form ($\sim 43\,\mathrm{mm}$ at the Lauteraarhut between 19 June and 4 July), when factored into the water balance, lead to inputs of water in excess of discharge outputs that had to be stored within or at the base of Unteraargletscher.
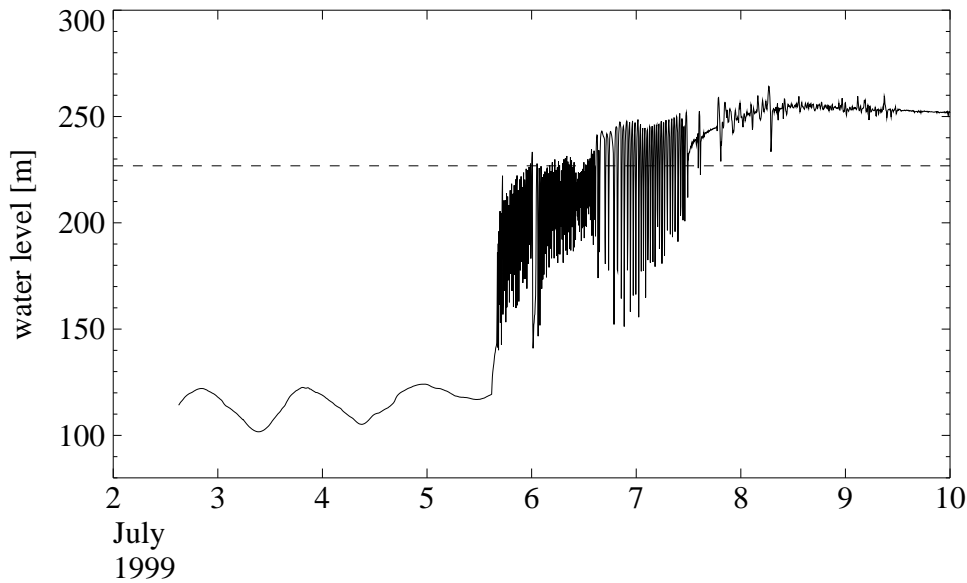
Figure 3.13: *Variations of water level in a 250 m deep borehole drilled to the bed of Unteraargletscher. The dashed line denotes the water level that corresponds to flotation pressure.*

The flood in the proglacial stream that coincided with a severe rain storm early on 6 July presumably reflects the outburst of the water that was stored en- or subglacially during the preceeding days. The large ice chunks that were spewed out and strewn across much of the proglacial area during this event suggest that the peak discharge of water early in the morning was considerably larger than the $20 - 30\,\mathrm{m}^3\,\mathrm{s}^{-1}$ we estimate for mid day of 6 July. However, these chunks were probably not derived subglacially as they can be attributed to a collapse of ice at the glacier portal. Nevertheless, we believe that the outburst flood is related to a change in the configuration of the subglacial drainage system. Support for this suggestion stems from a record of water level fluctuations (Fig. 3.13) in a $250\,\mathrm{m}$ deep borehole drilled through the ice to the bed near the central flowline, roughly $3\,\mathrm{km}$ upglacier from the terminus (Fig. 1.1). Diurnal variations in borehole water level were in phase with those of discharge in the proglacial stream during the days preceeding the release event which suggests that the hole was hydraulically connected to the drainage system. With the onset of precipitation in the afternoon of 5 July (Fig. 3.11a), the water level quickly rose indicating a sudden increase in subglacial water pressure to near flotation level (Fig. 3.13). Subsequently, the water level fluctuated wildly before the borehole lost its connection to the drainage system and filled with water. The fast rise in water pressure is thought to reflect the inability of the drainage network to adapt to the sudden increase in water supply caused by the rain. We conjecture that in response to high basal water pressure, water was forced to spread out at the ice–bed interface thereby altering configurations, dimensions and positions of exisiting drainage pathways. During the course of this basal drainage-system reorganization, the borehole became hydraulically isolated, while the establishment of a hydraulically efficient drainage net elsewhere enabled the fast release of en- and subglacially stored water.

In summary, a warm weather period at Unteraargletscher in late June and early July produced meltwater at a rate greater than the glacial drainage system could transmit. Consequently, water storage in and beneath the glacier increased. This warm period culminated in a storm with intense rain which caused water flow to back up further and subglacial water pressure to rise.

The high water pressure triggered a reorganization of the basal drainage system which in turn led to the release of water that was stored in and beneath the glacier.

Chapter 4

Tracer tests and their analysis

4.1 Principles of tracer experiments

Tracing techniques are widely used in hydrology to investigate manifold issues including determination of ground water trajectories, residence times and also quantitative characterization of drainage systems and measuring discharge rates (see also Sec. 3.1.3). In principle, the technique consists of labelling water at its entry into an unknown system and the subsequent detection of the marker after its passage through that system. An extensive compilation of the development in tracing techniques from first simple applications to modern experiments is found in Käss (1998). Today tracer techniques are important tools for research on virtually inaccessible hydrological systems and processes. In contrast to measurements at an individual point, these methods impart direct information on the flow characteristics integrated from an input location to a site of detection. Therefore, tracer tests have been used quite early as a preferred method for investigating glacial drainage systems. Tracer experiments made a significant contribution to the understanding of glacial hydrology (Röthlisberger and Lang, 1987). Tracing the water that percolates through the firn or flows into moulins or at the bottom of boreholes had substantial implications for the identification of distinct drainage types, delimiting catchments and inferring hydraulic conditions (Fountain and Walder, 1998; Hubbard and Nienow, 1997).

4.1.1 Requirements on tracers

Tracer experiments provide information about hydraulic conditions of a drainage system if the tracer transport is identical to the flow of individual water particles. Today's tracing techniques come close to this ideal. Furthermore, the 'ideal tracer' requires the satisfaction of a number of conditions. The substance should possess optimal dissolubility in water, physical and chemical stability and high resistance against adsorption to the surrounding substratum or the suspended sediments. Besides these primary qualities, tracer should be detectable at low concentration independent of temperature and pH. And further, the natural background concentration should be as low as possible. Additionally, questions as to whether the substance is ecologically harmless, available in the necessary quantity and cost-effective play a role in the choice of an appropriate tracer.

4.1.2   Properties of fluorescent dyes and other tracers

For glacio-hydrological purposes, primarily fluorescent dyes are used as tracers since they meet the mentioned requirements closest. Nevertheless, the use of salt and other substances has also been reported (Stenborg, 1969; Kohler, 1995; Grust et al., 2001).

The use of fluorescent dyes in glacio-hydrological research traces back to the beginning of the 20th century (Forel, 1898; Mercanton, 1916). Initially, the method exploited the extreme coloring properties of such dyes, permitting visible detection (Käss, 1998). Today, this quality becomes irrelevant since modern detection methods are based on fluorometry. A fluorescent molecule has the ability to absorb light at one wavelength and almost instantaneously emit light at a different and longer wavelength. Fluorescence typically occurs about $10^{-8}\,\text{s}$ after the molecule absorbed the exciting light. The wave bands at which light is absorbed or emitted are specific for the fluorescent. Fluorescence intensity is directly proportional to the concentration of fluorescent solutes (Turner, 1997), thereby providing an efficient technology to detect dye tracers. Exploiting the knowledge about excitation and emission wavelength for a specific fluorescent, it became possible to detect dye down to concentrations of $0.01\,\text{ppb}$ (parts per billion). The sensitivity of the fluorometric analysis depends on the efficiency of the dye in converting excitation energy into fluorescence (Smart and Laidlaw, 1977). This property depends on the temperature and water quality of the sample which can affect a dye's fluorescence yield. In general, fluorescence intensity varies inversely with temperature, though this dependence is specific for each dye. Some dye's fluorescence is suppressed considerably at low $p\text{H}$ values. In typical glacial runoff reducing effects on fluorescence due to salinity or presence of fluorescent organic matter can be excluded whereas other factors can be significant. In particular, high suspended sediment concentrations coinciding with high turbidity values are likely to occur in runoff from glaciers and can produce misleading background concentrations. Adsorption of tracer on substratum or suspended sediment surfaces is mainly irreversible and can therefore cause significant dye losses. Some fluorescent dyes are subject to photochemical decay limiting their usage in surface water (Smart and Laidlaw, 1977; Käss, 1998).

NaCl-salt can also be used as a suitable tracer, when fast flowing currents of low conductive water should be labeled (Sec. 3.1.3). The natural background in glacial meltwater is typically low, thus providing a clear tracer signature while the detection is simply achieved via the electrical conductivity at low costs. On the other hand, the low detection sensitivity requires the injection of large quantities, often representing a logistical limitation for an application at remote locations. The use of such tracers is therefore restricted to experiments where low output concentrations are not expected or not of interest.

Knowledge of both, dye tracer properties as well as some physical and chemical characteristics of the investigated flow system is necessary to select the dye appropriate to the experiment. This task sometimes requires pilot investigations.

4.2   Transport models

To interpret the observed tracer-return curves we are faced with a typical inverse problem. The way in which the tracer reappears after passage through an unknown system is determined by the geometry of and the hydraulic conditions prevailing in that system. Visual inspection of the observed return curve can already provide some general information on the configuration of the

drainage system (Hock and Hooke, 1993; Nienow, 1993). The application of more objective methods is required to obtain further insight into system properties. Intrinsically, a tracer return curve represents the residence time distribution of a specific system under given hydraulic conditions (Jury and Roth, 1990). A quantitative evaluation of curve characteristics allows the inference of system properties such as flow velocity and the degree of tracer spreading during transit. Reliable estimates for those quantities can be obtained by carefully fitting parameters of a transport model to the observed data. However, an appropriate choice of the transport model is crucial for a reliable parameter estimate since only correct simulations and predictions of tracer data lead to a legitimate description of system properties (Beven, 2001). In particular, the adopted forward model should be capable of successfully predicting main characteristics of the tracer return curve such as the onset of tracer breakthrough, the time and magnitude of maximum concentration and the duration of concentration recession.

Considering that a tracer return curve represents the response of an unknown and possibly complex system, the use of simple, conceptual models is imperative to avoid under-determination of the problem and therefore equifinality of different solutions and subsequent over-interpretation of the data (Beven, 2001). Furthermore, the following models are strictly valid only for a conservative tracer, a legitimate assumption considering the careful selection of the tracer.

The following transport models, their specific solutions and the parameter optimization procedure are implemented in the software CXTFIT2.1 which was used for estimating the transport parameters. This code is provided by the U. S. Salinity Laboratory and uses a nonlinear least-squares optimization method (Marquardt, 1963) to derive parameters (Toride et al., 1999).

4.2.1 Advection-dispersion model

In the following, we assume that the tracer concentration c is distributed over the entire cross-section of the flow and the width of the system is very small compared to its longitudinal extent. Thence, the tracer transport is regarded as a one-dimensional problem along the flow direction x.

Mainly, the tracer is advected with a transit velocity v which corresponds to the mean flow velocity along the flowpath

$$\frac{\partial c}{\partial t} = -v\frac{\partial c}{\partial x}. \tag{4.1}$$

Assuming a constant and homogeneous velocity field within a labeled water volume, the tracer should reappear at the detection site in a concentration distribution identical to its initial distribution. However, two main processes determine the dispersion of the tracer cloud: molecular diffusion and dispersion. Molecular diffusion is the thermic motion of dissolved components (Brownian motion) and dispersion is due to differential local velocities as well as differential lengths of flow trajectories (see Figure 4.1). Regardless of their different nature, both processes are usually described by a diffusion equation using a single hydrodynamic dispersion coefficient D (Taylor, 1954)

$$\frac{\partial c}{\partial t} = D\frac{\partial^2 c}{\partial x^2}. \tag{4.2}$$

Furthermore, "dispersion" is used synonymously to "hydrodynamic dispersion coefficient". The combined advection-dispersion equation for one-dimensional transport of a conservative tracer is written as

$$\frac{\partial c}{\partial t} = D\frac{\partial^2 c}{\partial x^2} - v\frac{\partial c}{\partial x}. \tag{4.3}$$
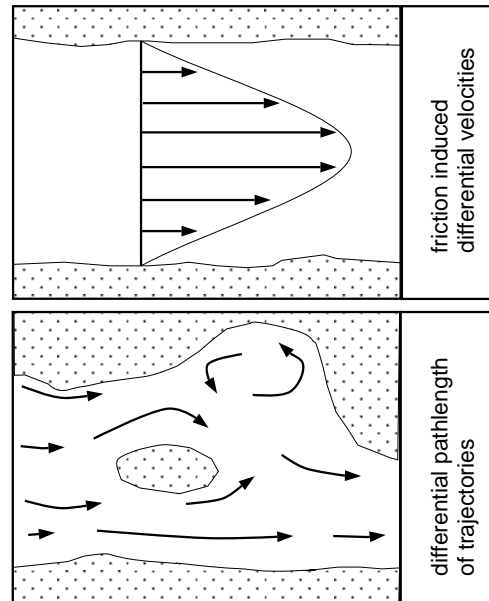
Figure 4.1: *Mechanisms of hydrodynamic dispersion.*

With the initial condition of an instantaneous tracer injection

$$c(x = 0, t) = \frac{m}{Q}\delta(t),$$ (4.4)

where $\delta(t)$ is a Dirac delta function and m is the total mass of tracer injected into the water flux Q, the problem can be solved analytically (Kreft and Zuber, 1978; van Genuchten and Wagenet, 1989; Kinzelbach, 1992). At a distance x_1, the concentration as a function of time is given by

$$c(t) = \frac{m}{Q}\frac{x_1}{(4\pi Dt^3)^{\frac{1}{2}}}\exp(-\frac{(x_1 - vt)^2}{4Dt}).$$ (4.5)

The two transport parameters v and D are obtained by a fitting procedure. Since D characterizes the velocity inhomogeneities in the system, the $c(t)$-solutions of a transport functions are also referred to as the travel time probability function (Jury and Roth, 1990).

4.2.2   Mobile-immobile model

Homogeneous flow conditions as assumed for the advection-dispersion model are rarely found in natural systems. Tracer transport through a glacial drainage system is often affected by storage-retardation processes which lead to a pronounced asymmetry of the return curves characterized by a slowly declining tail (e.g. Brugman, 1986; Seaberg et al., 1988; Willis, 1990; Fountain, 1993; Hock and Hooke, 1993; Nienow 1993). Behavior like this cannot be explained by the advection-dispersion model (Ambach and Jochum, 1973; Seaberg et al., 1988; Hock and Hooke, 1993; Fountain, 1993). This retardation is commonly attributed to temporary storage phenomena. Such a heterogeneous flow regime represents a physical nonequilibrium and is often modeled using a two-region type formulation. In doing so, the total region is subdivided into a mobile and an immobile portion (van Genuchten and Wierenga, 1976) and the solute exchange between the two sub-regions is modeled as a first-order process. The two-region

transport model is then written

$$\beta\frac{\partial c_{\mathrm{m}}}{\partial t} - (1-\beta)\frac{\partial c_{\mathrm{im}}}{\partial t} = D\frac{\partial^2 c_{\mathrm{m}}}{\partial x^2} - v\frac{\partial c_{\mathrm{m}}}{\partial x} \tag{4.6}$$

where

$$\frac{\partial c_{\mathrm{im}}}{\partial t} = \omega(c_{\mathrm{m}} - c_{\mathrm{im}}) \tag{4.7}$$

and

$$c = \beta c_{\mathrm{m}} + (1-\beta)c_{\mathrm{im}}. \tag{4.8}$$

Here, the indices $_{\mathrm{m}}$ and $_{\mathrm{im}}$ denote the mobile and the immobile region, respectively, β represents the fraction of mobile water and ω is a first-order exchange coefficient. Given the same initial condition as in Equation (4.4), the problem can be solved (van Genuchten and Wagenet, 1989) and the transport parameters v, D, ω and β determined by fitting the model to measured data.

4.3 Analyzing results from tracer tests

The transit velocity as determined from tracer tests represents a mean flow velocity averaged spatially over the length of the flowpath and temporally over the residence time of the tracer in the system. The transit velocity varies with water discharge, flow conditions and system geometry, whereas the dispersion coefficient is a function of transit velocity and system resistance (Taylor, 1954). A widely used approach to analyze properties of a subglacial drainage system is therefore to investigate the variation of tracer velocity with discharge and the variation of dispersion with velocity (Collins, 1982; Seaberg et al., 1988; Fountain, 1993; Hock and Hooke, 1993; Kohler, 1995; Nienow et al., 1996c).

4.3.1 Variation of velocity with discharge

The relationship between discharge and velocity has been employed in previous studies to infer whether subglacial drainage occurs in pressurized conduits or in open channels. The underlying idea is based on the continuity consideration $vA = Q$, where A is the average cross-sectional area occupied by the water flow. If a drainage system is completely filled with water, then A would remain constant and an increase in Q would cause directly an increase of v. This behavior would be reflected by a positive, linear relationship in a plot of v versus Q. Furthermore, the slope of a linear vQ-relationship is determined by the hydraulic geometry of the system and provides therefore a measure of system size and resistance (Fig. 4.2a).

In the case of open-channel flow, an increase of Q would be accommodated partly by an increase in A as well as in v and resulting in a curvature of the vQ-relationship (Fig. 4.2a). The characteristic of this curvature is conditioned by the hydraulic radius of the drainage system (Fountain, 1993; Kohler, 1995).
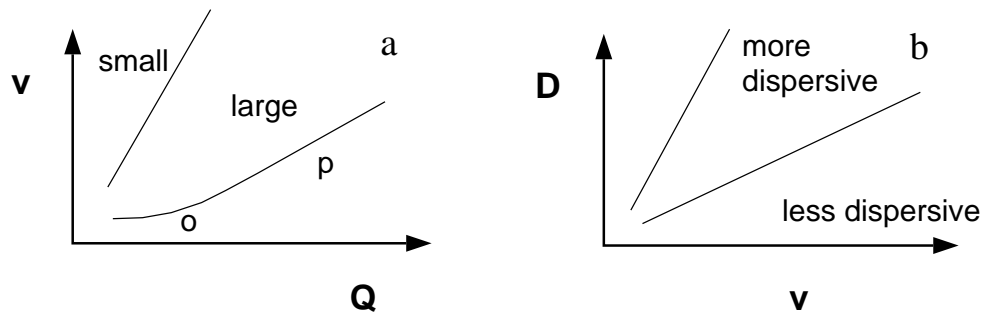
Figure 4.2: *Principles of analyzing results from tracer tests. (a) Velocity-discharge relationships for a small and a large drainage system. "O" and "P" denote the sections where water flows in an open or pressurized system, respectively. (b) Velocity-dispersion relationships for a more and a less dispersive system.*

4.3.2 Variation of dispersion with velocity

Since the dispersion coefficient D has units of $[\mathrm{m^2\,s^{-1}}]$ it is obvious that it depends on the transit time and therefore on the transit velocity v and the length-scale of the system. In a given pipe with a constant roughness and hydraulic radius, it has been found that D is approximately proportional to v (Taylor, 1954). Investigations of the vD-relationship has been used to infer changes in the drainage system from changes in the slope of a linear regression of v on D (Seaberg et al., 1988). As such, a more dispersive system would be characterized by a steeper slope compared to a less dispersive one.

4.3.3 Particularity of a glacial drainage system

A main characteristic of runoff from a glacier is its pronounced variability of water discharge on seasonal and diurnal timescales. In addition, the drainage system adjusts to prevailing hydraulic conditions (Chapter 2). Since the vQ-relationship is determined by the geometry of the system, it is therefore evident that interpretations of flow conditions are invalid if they were made from tracer tests conducted over a time interval long enough to allow system evolution. Values obtained from tracer tests through a conduit whose geometry varies with time would appear in a vQ-plot as a curve whose exact position and shape would be a function of the instantaneous state of the system (Kohler, 1995). Thus, multiple tracer injections at the same location have to be conducted in quick succession to provide a snapshot of the curve (Collins, 1982; Fountain, 1993; Kohler, 1995; Nienow et al., 1996c).

Furthermore, the slope of a vD-relationship depends also on the length scale of the considered flowpath (e.g. Kinzelbach, 1992) . Thus, interpretations of results from tracer injections at different locations of a glacier are doubtful. Consequently, sets of tracer injections at different discharges are required for each individual flow path which is investigated.

In summary, the requirements for a reliable analysis of both velocity-discharge and velocity-dispersion relationships are met if tracer injections into the same flow path are conducted in quick succession over a diurnal discharge cycle.

Chapter 5

Field experiments at Unteraargletscher

In the present study, tracer methods were used for two different purposes: to obtain information on subglacial flow conditions by injections of tracer into a moulin and secondly to measure discharge by salt dilution. Since the latter was already explained in detail in Section 3.1.3, this section focuses primarily on the methods applied in the dye tracer experiments.

5.1 Procedure in the field

Moulins are the most common entry for supraglacial water to the interior of an alpine glacier. To obtain insight into the hydraulics of a major flow path, we conducted tracer tests from a large moulin at the centerline of Unteraargletscher, $4450\,\mathrm{m}$ upglacier of the gauging station (Fig. 1.1). In our experiment design, we followed the arguments discussed in Section 4.3.3. Dye was injected in quick succession over a range of different discharges to obtain a reliable vQ-curve. Such series of tracer injections were performed at intervals of approximately one month over the ablation season 2000.

5.1.1 Tracer experiments

For the experiments at Unteraargletscher, we used sulforhodamine B, a dye which is known to have a high resistance to adsorption. This is a potentially important argument considering the substantial suspended sediment load of glacial runoff (Smart and Laidlaw, 1977; Käss, 1998). Furthermore, the fluorescent property of sulforhodamine B is not reduced in the pH range (Smart and Laidlaw, 1977) which is observed in the proglacial stream of Unteraargletscher. Values ranging from $pH\,6$ to 6.5 as determined by pH-indicator strips label slightly acidic conditions in the proglacial stream as it is expected considering the crystalline mineralogy of the catchment area (Sec. 1.3).

Tracer injection

For convenience, the tracer was weighed and prepackaged in the laboratory. The dye powder was dissolved in distilled water and sealed in labeled PVC bottles of $1\,\mathrm{l}$ volume. The dissolubility of Sulforhodamine B in water is $10\,\mathrm{kg\,m^{-3}}$ at $20°\mathrm{C}$ (Käss, 1998). To accommodate the

Table 5.1: *Tracer injections into the drainage system of Unteraargletscher during the ablation season 2000.*

2–3 August 2000		8–9 September 2000	
time	m [g]	time	m [g]
10h00	100.3	09h18	150.1
12h00	100.2	12h47	100.4
14h00	100.0	14h30	100.3
16h00	100.3	16h00	100.0
18h00	100.2	18h00	100.2
20h00	100.3	20h00	100.2
22h00	100.2	22h00	100.1
00h00	100.4	00h00	100.2
03h00	100.2	03h00	100.4
06h00	100.8	08h00	99.8
08h00	100.1	10h00	99.9
10h00	100.1		

required quantities of 50 to 200 g in a manageable volume, a small amount of ethylenglykol was added to keep sulforhodamine B in suspension. The portions prepared in this way, were poured manually into the supraglacial stream at its entry into the moulin (Fig. 1.1). The input was carried out instantaneously such that the injection time was very short compared to the tracer breakthrough duration.

The injections were conducted in quick succession over an entire diurnal discharge cycle each in August and September 2000, respectively. Table 5.1 lists the time of individual tracer experiments. The injections were accompanied by simultaneous measurements of discharge of supraglacial meltwater draining into the moulin and bulk runoff in the proglacial stream (Table 5.2).

Dye detection

Sulforhodamine B fluorescence was monitored in the proglacial stream at the gauging site using a Turner Model 10-AU field fluorometer. Water was diverted from the stream by a suction-driven siphon consisting of a 15 mm diameter PVC hose of 50 m length. This length was necessary to obtain a gravitational potential ensuring the continuous flow of water in the weakly inclined proglacial area of Unteraargletscher. The Turner 10-AU is a robust filter fluorometer, equipped internally with a temperature probe and a programmable datalogger. A continuous-flow cuvette enables the continuous fluorometry while water is routed through the instrument. To obtain a high resolution dataset, measurements of fluorescence and temperature were performed at 2 s intervals. White noise related to instrument instability (Smart and Zabo, 1997) was rejected by compilation of average values which were recorded by the logger every 10 s. High frequency sampling is required to avoid inaccurate estimates of transport parameters due to an insufficient reproduction of the tracer return curve by coarse measurement intervals (Nienow et al., 1996a). Power was supplied by four 20 W-solar panels charging a 12 V, 110 Ah-sized battery. Previous tests indicated that a fully charged battery ensures the permanent operation
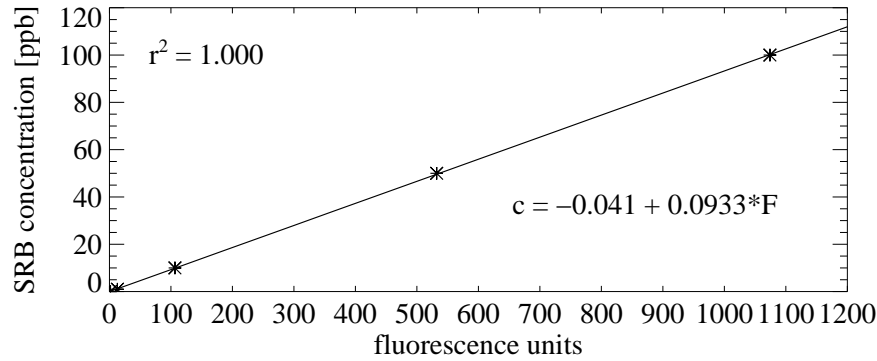
Figure 5.1: *Fluorometer calibration curve for sulforhodamine B (SRB).*

of the fluorometer for about three days. This capacity is adequate to guarantee continuous operation during overnight experiments.

Fluorescence readings were converted into dye concentrations by a calibration function. A set of standard solutions was prepared by progressively diluting an exactly known quantity of dye powder in distilled water to predefined concentrations. The obtained standard concentrations cover the entire range of observations and were used to calibrate the instrument. The flow cuvette of the Turner 10-AU was sealed and standard solutions were injected directly into the flow cell (Turner, 1997). Fluorescence and sample temperature were measured in the fluorometer for each standard. To compensate for temperature variations by which sulforhodamine B is considerably affected (Smart and Laidlaw, 1977; Käss, 1998), we used two complementary methods. First, the fluorometer was calibrated in a cold-room at a temperature close to that expected in the field. And second, we applied an established correction function to the fluorescence records:

$$F_{\text{s}} = F_0 e^{n(T_{\text{s}} - T_0)}, \tag{5.1}$$

where F and T denote fluorescence and temperature and the subscripts $_{\text{s}}$ and $_0$ refer to the sample and a reference, respectively. For sulforhodamine B, the temperature coefficient n equals $-0.029\,^{\circ}\text{C}^{-1}$ (Smart and Laidlaw, 1977; Käss, 1998). After temperature-compensation, a calibration function was derived by linear regression of fluorescence readings F (in fluorescence units) to tracer concentrations c (in ppb) (Fig. 5.1).

5.1.2 Discharge measurements

Discharge time series are required for a quantitative interpretation of tracer experiments. The experience with gauging in the highly dynamic proglacial stream made in 1999 (Chap. 3) shows that continuous discharge recording is impractical. Therefore, we performed individual discharge measurements as described in Section 3.1.3 at short intervals concurrent with the duration of tracer experiments. For this purpose, salt of mass m_{s} was injected into the water and the tracer-dilution method was used to determine the discharge.

The salt dilution method was also used to determine discharge in the supraglacial stream into which the dye tracer was poured. Simultaneous to dye injections, amounts of salt between 0.5 and $1\,\text{kg}$ were injected $\sim 150\,\text{m}$ upstream of where conductivity was recorded. Details are presented in Table 5.2. The 22h00 measurement of September 8, 2000 was not evaluated since

Table 5.2: *Individual discharge measurements carried out at the detection site in the proglacial stream and the injection site on the glacier during the tracer experiments in August and September 2000.*

	gauging site			injection site		
date	time	m_s (kg)	Q (m^{3}s^{-1})	time	m_s (kg)	Q (m^{3}s^{-1})
2 Aug 2000				10h20	0.50	0.190
	12h05	4.87	10.5	12h10	1.00	0.302
	14h05	7.79	11.1	14h05	1.00	0.306
	16h05	6.93	10.3	16h05	1.00	0.270
	18h00	9.74	12.8	18h05	1.00	0.181
	20h00	10.00	13.2	20h05	1.00	0.110
	22h00	6.93	10.7	22h07	0.50	0.065
3 Aug 2000	00h05	6.93	13.4	00h05	0.50	0.072
	03h00	6.93	10.6	03h05	0.50	0.045
	06h00	6.93	9.5	06h06	0.50	0.044
	08h05	6.93	9.2	08h05	0.50	0.101
	10h99	6.93	9.6	09h58	0.50	0.077
8 Sep 2000	10h20	10.00	10.2	10h36	0.50	0.088
	12h35	10.00	12.2	12h30	0.50	0.279
	14h25	10.00	12.9	14h37	0.50	0.345
	16h08	10.00	14.6	16h08	0.50	0.315
	18h04	10.00	14.7	18h05	0.50	0.167
	20h00	10.00	14.0	20h06	0.50	0.051
	22h00	10.00	–	22h06	0.50	0.024
	23h55	10.00	13.6	23h57	0.50	0.013
9 Sep 2000	03h15	10.00	14.3	02h57	0.50	0.012
	06h10	10.00	14.1	07h57	0.50	0.024
	08h15	10.00	14.4	10h09	0.50	0.211
	10h10	10.00	14.6	10h09	0.50	0.211
	13h35	10.00	18.9			

the data record was interrupted before conductivity background levels were reached, leading to an incomplete mass recovery. Two successive injections of first dissolved and than of solid salt were performed around noon of July 6, 2000. It is found that the result is affected by the injection method by less than 3%.

5.2   Data processing

5.2.1   Compilation of a continuous discharge series
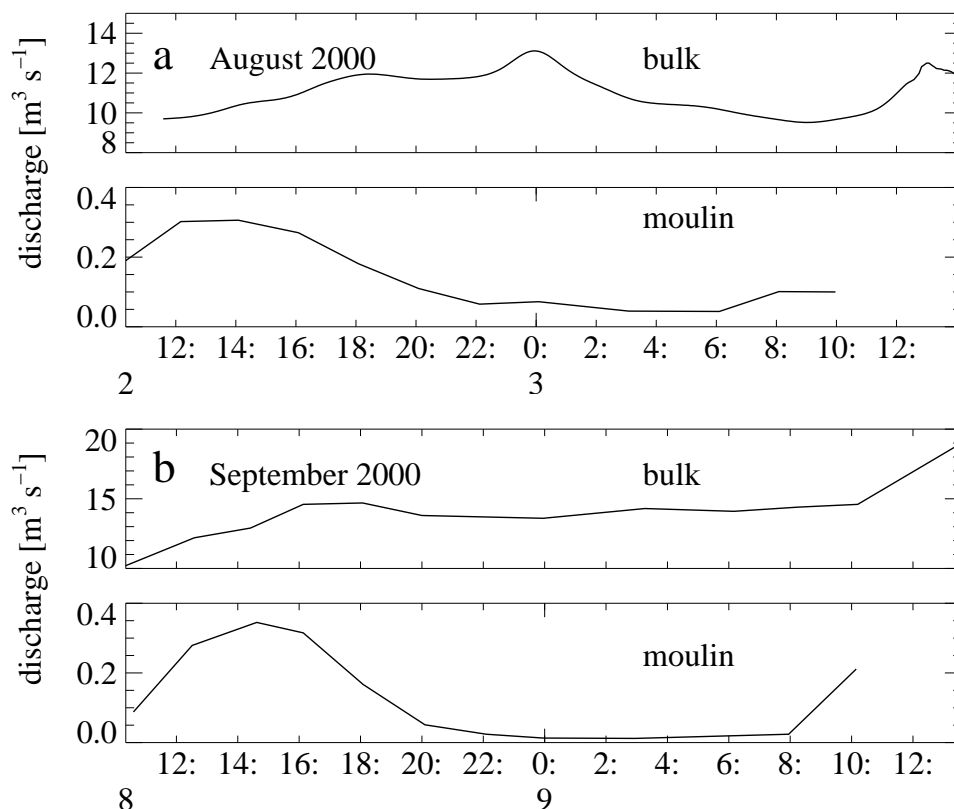
Figure 5.2: *Time series of bulk discharge in the proglacial stream and discharge input into the moulin during the tracer experiments in August (a) and September 2000 (b).*

Quasi-continuous discharge data are necessary to calculate the tracer load based on high frequency fluorescence measurements. To cope with this requirement, we measured stream stage by a KELLER PR-46W pressure transducer at $5\,\mathrm{min}$ intervals in August 2000. Due to failure of the datalogger, a stage record is not available for September 2000.

After removing high frequency fluctuations from the stage record using a Gaussian filter, a rating curve was established by fitting a third degree polynomial to the stage-discharge relationship. In September, the diurnal discharge cycle is well defined by the 13 individual measurements which were linearly interpolated to obtain discharge data in the required temporal resolution.

Figures 5.2a and b show diurnal cycles of input and output discharge concurrent with the tracer experiments. The discharge input into the moulin drains surface meltwater and follows therefore

closely the theoretical course of solar radiation. It displays a clear diurnal cycle with a maximum shortly after solar-noon (the x-axis is in CEST/MESZ) and minimum values just before sunrise. On both dates, supraglacial discharges culminate in the early afternoon with comparable values of about $0.35\,\mathrm{m^3\,s^{-1}}$ which are reduced to $< 0.1\,\mathrm{m^3\,s^{-1}}$ during night.

After having passed the glacial drainage system, bulk discharge in the proglacial stream shows a less pronounced diurnal amplitude. Therefore, low flow discharge stays at a relatively high level and peak discharge occurs in the evening with a delay of approximately 3 hours compared to the maximum of moulin input. This behavior is consistent with observations made in 1999 (Fig. 3.11). The course of bulk discharge in August is roughly cyclic (Fig. 5.2a) whereas that in September is characterized by an increasing trend superimposed on a diurnal variation (Fig. 5.2b). Further, there is a noticeable discharge increase around midnight between 2 and 3 August which rapidly rises to a peak value of $13.1\,\mathrm{m^3\,s^{-1}}$ followed by a similarly rapid decline. The increasing trend of discharge in September coincides with the return of sunny and warm weather after a cold period.

5.2.2 Preprocessing of tracer return curves

To determine transport parameters for individual tracer return curves, the raw concentration data has to be transformed into a form suitable for application of the transport models specified in Section 4.2. To ensure comparability between results from individual tracer tests, this evaluation strategy has to be standardized.

It is advantageous to subdivide the continuous time series of tracer concentration into sections which correspond to individual tests. Therefore, the main concentration peaks were attributed to particular injections, the intermediate minima were identified and then used to separate individual tracer return curves. Apparent background concentration was eliminated from each dataset by a linear interpolation between the onset and the termination of the clearly defined tracer signal. The tracer load $c(t)\,Q(t)$ was calculated to account for dilution of tracer concentration under transient discharge conditions. Here, Q denotes the discharge at the site where the tracer concentration is detected.

Normalizing the tracer load to the mass of injected tracer allows intercomparison of tracer return curves independent of the particular discharge conditions and the applied tracer quantity. Integration of the normalized tracer load yields the tracer recovery rate

$$M = \int\limits_{t_0}^{t_1} \frac{c(t)\,Q(t)}{m}\,\mathrm{d}t. \tag{5.2}$$

The integration limits are finite in natural experiments, thus t_0 and t_1 are given by the times when the tracer concentration rises above and falls below the detection limit. In a perfectly conservative tracer test, $M = 1$. Such recovery rates are rarely obtained from tracer tests in glacial drainage systems indicating a loss of tracer (Fig. 5.3). Such loss can be caused by adsorption of tracer onto the substratum, partial isolation in immobile zones or outflow in concentrations below the detection limit. As such, the estimate of M is subjected to considerable inaccuracies since it accumulates any errors stemming from the determination of tracer concentration, background concentration, mass of tracer injected and discharge. For example, apparent recovery rates even larger than 1 have been reported by Seaberg et al. (1988) who related this erroneous result to shortcomings of their discharge measurement.
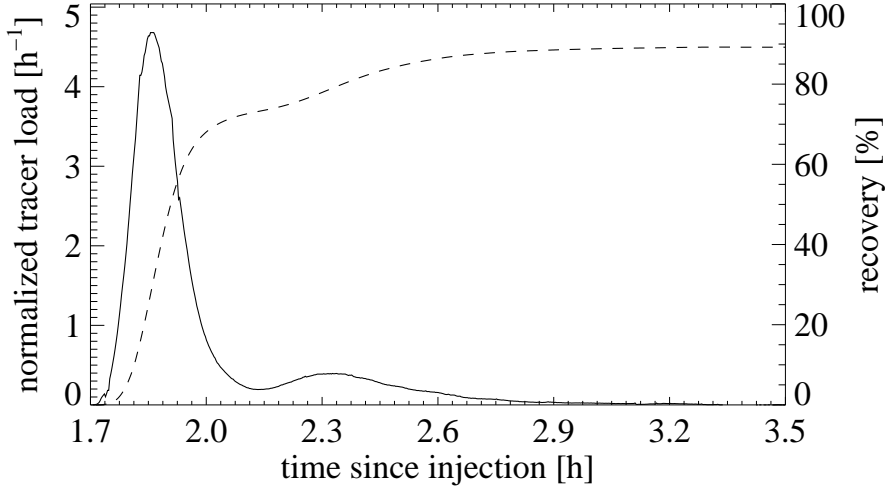
Figure 5.3: *Example of a dye return curve prepared in the described procedure (solid). The dashed line represents the percentage of recovered tracer.*

Due to its susceptibility to inaccuracies, the significance of the recovery rate is limited and therefore, we modify in this study the calculation of normalized tracer load by using the actually recovered tracer mass rather than the injected tracer mass. Then the return curve is expressed in terms of a normalized tracer load d_{norm}:

$$d_{\mathrm{norm}} = \frac{c(t)\,Q(t)}{\int_{t_0}^{t_1} c(t)\,Q(t)\,\mathrm{d}t} \tag{5.3}$$

When rewriting Equation (4.5) in terms of d_{norm}, the right hand side would depend only on the free parameters D and v. Since processes controlling the recovery rate are not implemented in the transport models anyway, the use of d_{norm} does not imply improper assumptions but it simplifies the parameter optimization.

5.2.3 Single-peaked return curves

When single-peaked dye return curves were observed, the relatively simple shape of the curves permits intercomparison of the two transport models and offers thereby the opportunity to validate the approach adopted here.

Advection-dispersion model

Any natural channel geometry would produce a tracer return curve with the falling limb different from the prediction of the advection-dispersion model since tracer retardation processes are not considered in the model formulation (e.g. Hauns et al., 2001). Hence, fitting the parameters of the advection-dispersion model to the entire measured return curve which includes parts not obeying the model equation, would lead to erroneous results (Figure 5.4). Hock and Hooke (1993) proposed therefore to ignore the part of the tail in which concentrations are less than 5-10% of the peak value. However, storage-retardation is a continuous process and is immanent
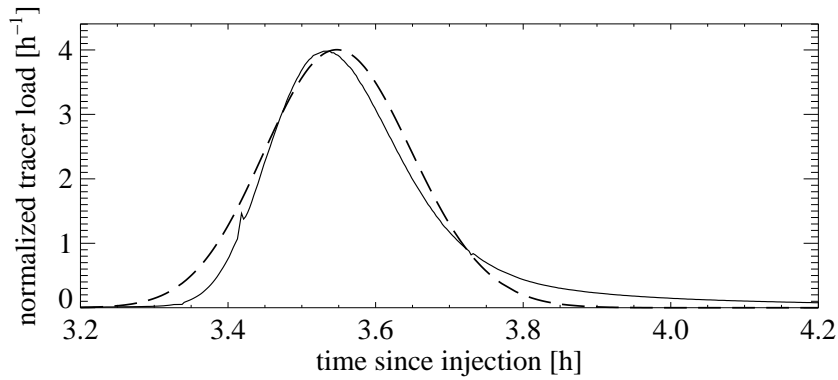
Figure 5.4: *Example of fitting the advection-dispersion model (dashed) to the entire curve of a typical tracer return (solid). The onset of tracer breakthrough, the time and magnitude of maximum concentration and the falling limb are reproduced incorrectly.*
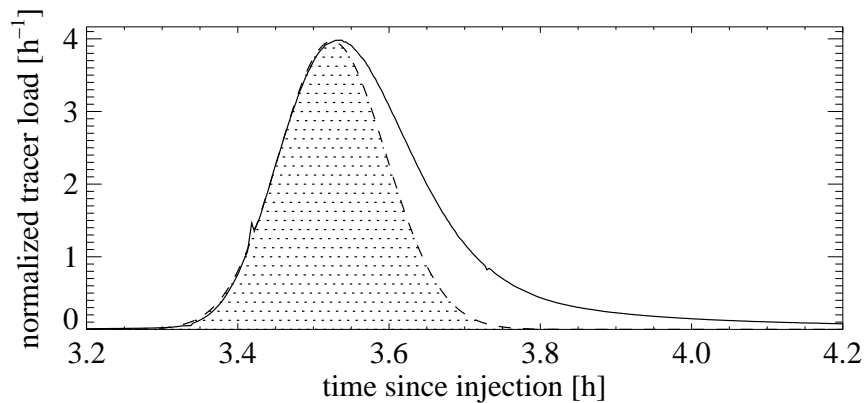
Figure 5.5: *Example of fitting the advection-dispersion model (dashed) to the rising limb of the tracer return curve shown in Figure 5.4 (solid). The integral under the fitted curve (shaded area) corresponds to the value of m_{model}.*

in the entire curve. Nevertheless, tracer transport in a conduit system is by far dominated by advection and dispersion which determine therefore the form of the rising limb. This allows us to consider the influence of storage-retardation only on the falling limb of a return curve. In this study, the following strategy was applied:

1. The model parameters were fitted to the rising limb of the measured curve such that the peak concentration is conserved (Sauty and Kinzelbach, 1988) (Fig. 5.5).

2. The parameters obtained were applied in a forward model stretching over the entire observation period. The area under this modeled curve is generally smaller than under the observed one.

3. The difference of the area under the modeled and the measured curve is used as a parameter to quantify storage-retardation.

The model optimization requires initial guesses for the fitting parameters. Start values for v were obtained by dividing the straight line distance from the injection to the detection site by
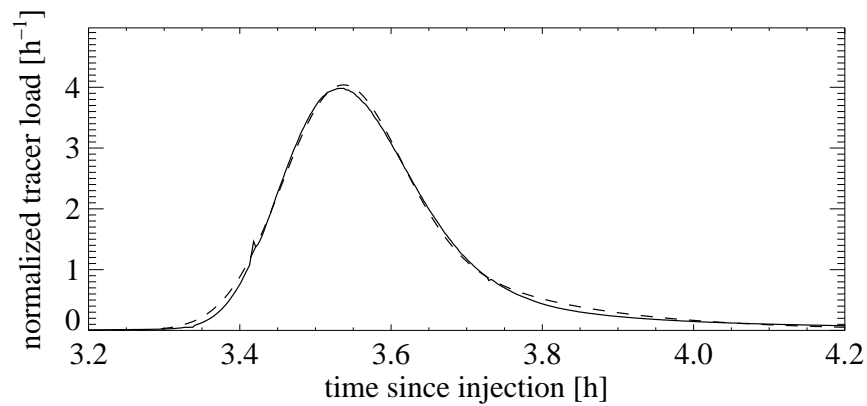
Figure 5.6: *Example of fitting the mobile-immobile model (dashed) to the entire curve of the tracer return shown in Figure 5.4 (solid).*

the time difference between detection of peak concentration and tracer injection. The guess for D turned out to be uncritical for the convergence of the optimization procedure. Since the model describes usually only a part of the observed return curve, it was necessary to adjust the modeled tracer mass m_{model} such that the peak concentration is conserved. By definition $d_{\mathrm{norm}} = 1$ and therefore, m_{model} expresses directly the fraction of the recovered mass which is explained by the model (Fig. 5.5).

Mobile-immobile model

The model was used in the way described by Toride et al. (1999) without further adjustments. The transport model was fitted to the observed concentration curve to obtain estimates of the four parameters v, D, β and ω (Fig. 5.6). Initial values for v and D were chosen as described above, β was set $= 1$ and $\omega = 10^{-4}\mathrm{s}^{-1}$. In contrast to the method described above, m is conserved here, because the model can account for continuous storage-retardation.

5.2.4   Double-peaked return curves

The more complex shape of the multiple-peaked tracer return curves cannot be reproduced by a simple transport model. A double-peaked curve suggests that tracer was transported in parallel through a preferential and a secondary flow path.

Advection-dispersion model

To maintain direct inter-comparability between the experiments, the approach of applying the advection-dispersion model as described for single-peaked curves (Sec. 5.2.3) was also applied to double peaked curves. Hence, only the transport of tracer through the preferential flow path is evaluated and any difference to the observed curve is considered as retardation, regardless of whether secondary peaks occurred or the concentration declined continuously. The finding that more than 75% of the tracer mass had passed the observation point before the onset of a secondary peak strengthens the confidence in the representativity of the method.
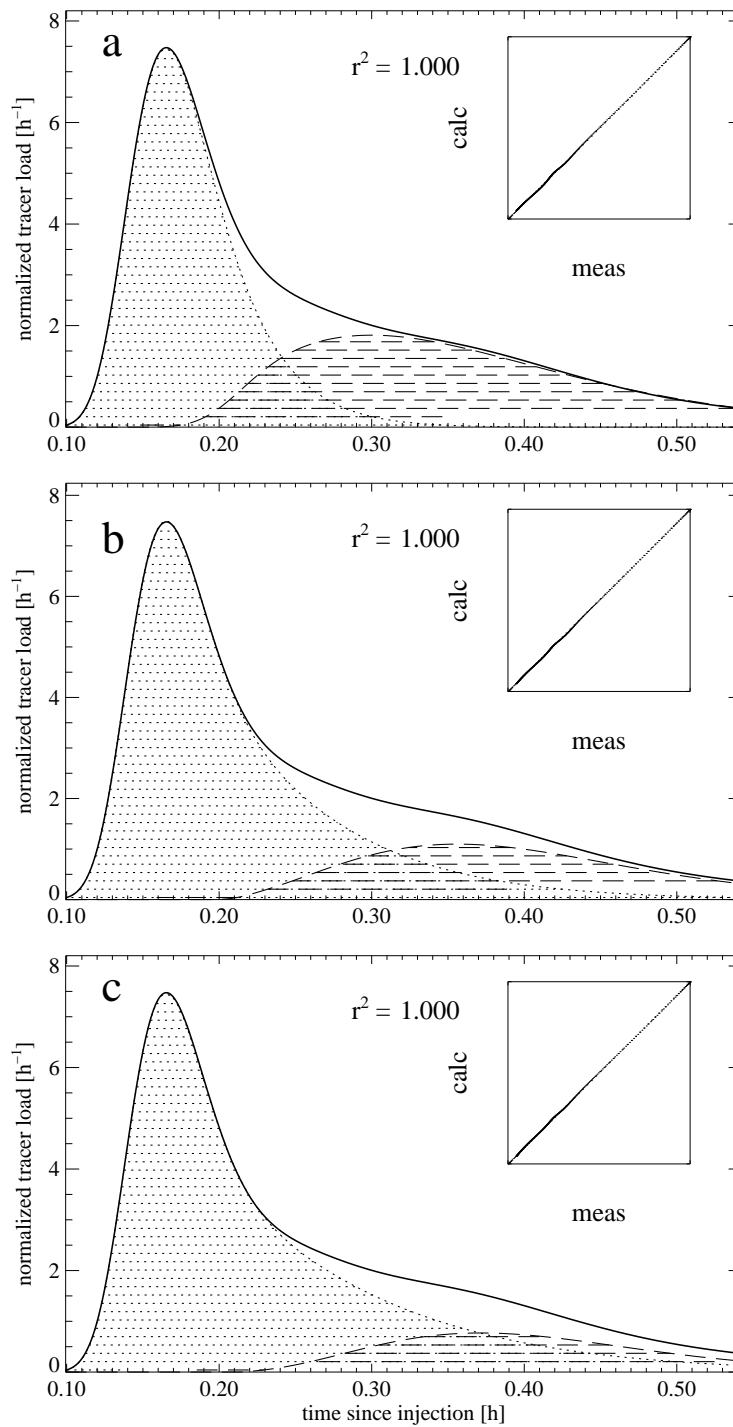
Figure 5.7: *Example of ambiguous parameter determination by describing a complex return curve by the superposition of two mobile-immobile transport models (dotted and dashed). Three obviously different parameter combinations (a, b, c) yield the same perfect match to the data (solid line). The insets show scatter-plots of calculated vs. measured values.*

Mobile-immobile model

To describe the entire curve as a superposition of two individual tracer transits appears to be a promising approach. In contrast to the advection-dispersion model, the mobile-immobile model can account for the tailing of the observed return curves and is therefore the obvious choice here. A step-by-step procedure offers the possibility to disassemble the complex return curves. Alternating optimization and forward modeling should enable the independent determination of parameters for each single peak. However, the method to delimit individual peaks turned out to be crucial for the determination of the transport parameters. Several combinations of different parameter values provide equivalent and therefore ambiguous solutions (Fig. 5.7). Since concatenation of two or more four-parameter models results in equifinality, this approach is not further continued.

5.3 Experiment results

5.3.1 Tracer return
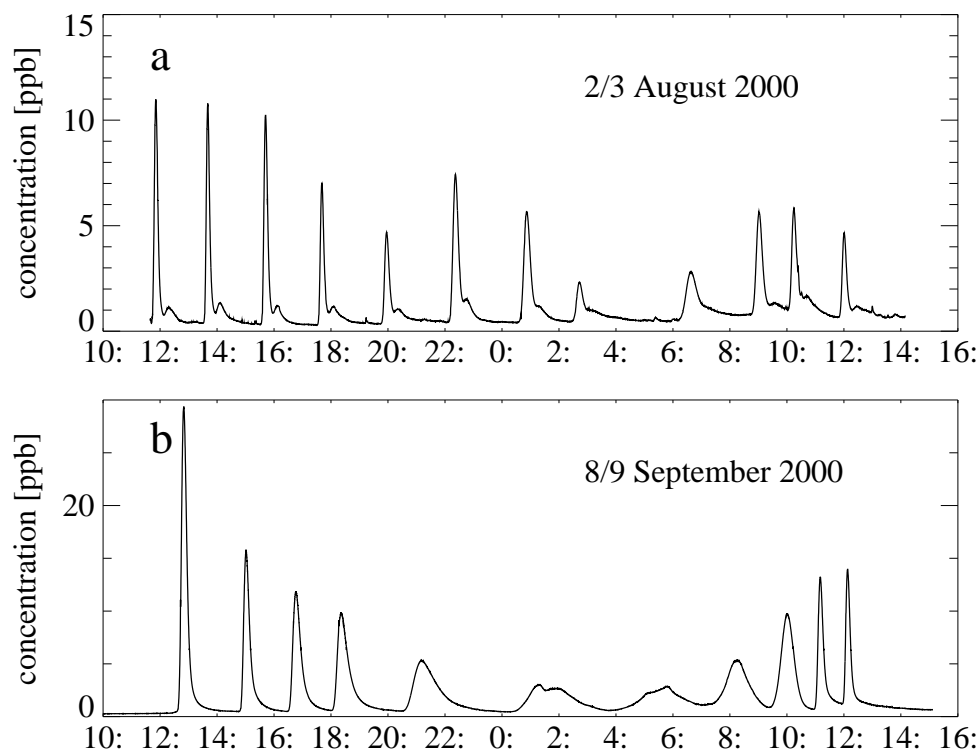
Figure 5.8: *Time series of tracer concentration resulting from succeeding injections of Sulforhodamine B. The experiments cover each an entire diurnal discharge cycle in August (a) and September 2000 (b).*

Figure 5.8 illustrates the tracer concentration observed at the gauging station subsequent to the injection series conducted in August and September 2000. Both series yielded sets of easily separable and independent tracer returns.
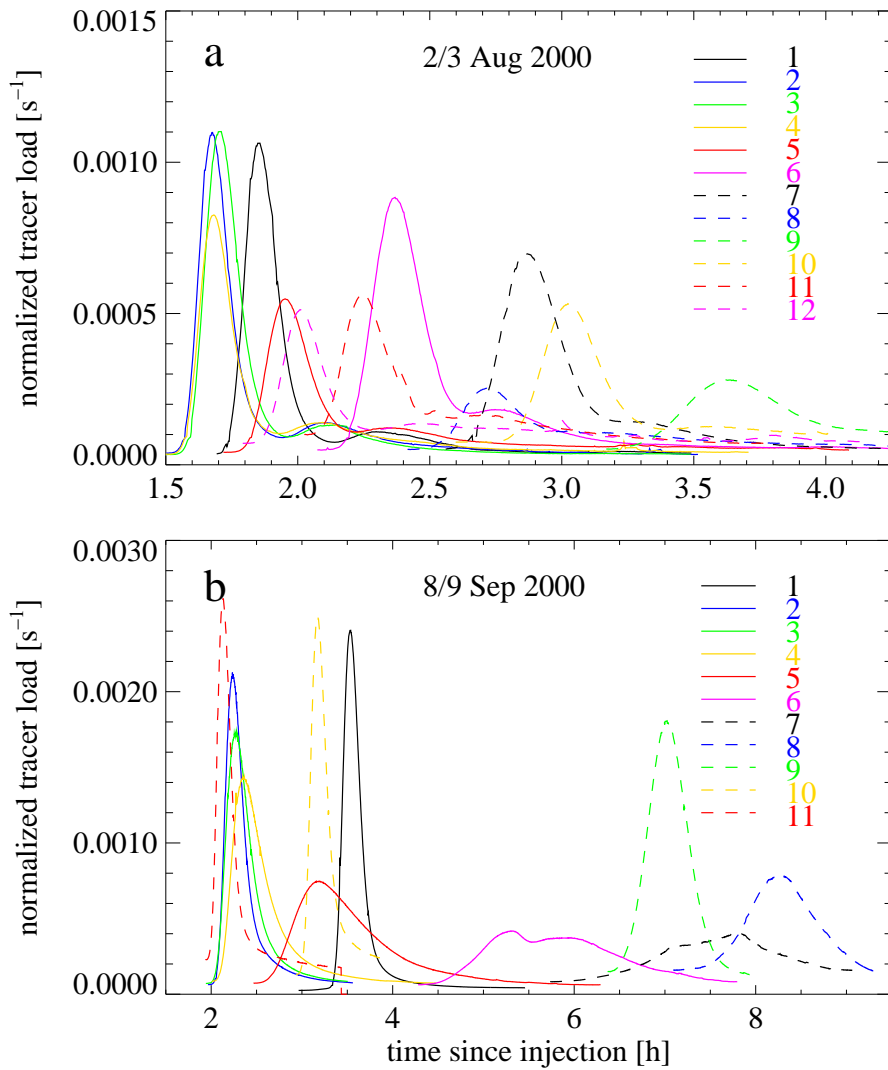
Figure 5.9: *Individual, normalized tracer return curves resulting from the August (a) and September (b) experiments plotted versus time elapsed since injection. Tracer return curves are numbered in order of their injections. Note that the time-axes are scaled differently.*

Return curves resulting from injections in August are characterized by sharply peaked first concentration pulses which are followed by secondary, much lower peaks. During night, the primary breakthroughs are broader such that the secondary peaks are almost not perceivable.

In contrast, September tests return textbook-like, single-peaked concentration curves. Comparable to the August tests, the return curves in September show a systematic variation of tracer spread with broadly dispersed and sometimes irregularly shaped tracer breakthroughs during night and sharp spikes during day.

To better compare the characteristics of individual tracer return curves, the data was processed as explained in Section 5.2.2 and plotted versus time elapsed since the corresponding injection (Fig. 5.9). This illustration reveals a substantial variability in terms of transit time and tracer dispersion. Fastest breakthroughs in August (numbers 2,3 and 4 in Fig. 5.9a) occurred about 1.5 hours after injection whereas maximum concentration after injection number 9 was reached 3.5 hours after injection. With the onset of meltwater discharge in the following morning, transit times returned gradually to their former magnitude. This situation was even more pronounced in September (Fig. 5.9b) when the injection-to-peak-concentration times ranged from approximately 2 hours to more than 8 hours.

The variation of tracer dispersion follows in general the evolution of transit velocity such that a sharply focused signal is associated with a short transit time and vice versa. However, although the September injection number 5 resulted in a return curve with similar timing of maximum concentration as the one belonging to number 10, the width of the curve is obviously very different.

5.3.2   Analysis of return curves

Illustrations of fitting the advection-dispersion model to individual tracer return curves of the August and September experiments are presented in Appendix A.1 and A.2. Figures 5.10 and 5.11 show the derived transport parameters. The top panel in each figure shows discharge into the moulin Q_{in} and discharge in the proglacial stream Q_{pro} associated with each individual tracer transit. $Q_{in}$ was measured at the time of tracer injection and Q_{pro} is the bulk discharge averaged over the time of tracer detection. Due to the unequal temporal spacing of the injections, the horizontal axis in Figures 5.10 and 5.11 cannot be directly translated into a time-axis. Further, by definition Q_{in} and Q_{pro} that belong to a given tracer test are separated in time by the transit of the tracer through the glacier.

August experiment   Input discharge was highest during the third injection and minimal in the early morning when the tenth test was started. In contrast, Q_{pro} is maximal for the sixth tracer parcel which passed the detection site concurrent with the high discharge at midnight (Fig. 5.2a).

The obtained transit velocities vary over a range between 0.34 and $0.75\,\mathrm{m\,s^{-1}}$ following closely the course of Q_{in}. Further, this regime seems to be roughly reflected by the course of dispersion coefficients, a behavior which is expected considering the simple relationship between v and D inferred from theory (Sec. 4.3.2). Values vary from $0.78\,\mathrm{m^2\,s^{-1}}$ at minimum discharge to $1.44\,\mathrm{m^2\,s^{-1}}$ coinciding with maximum velocity. However, this parallel trend seems to be inverted at minimum velocity, where D reaches an outlying value of $1.35\,\mathrm{m^2\,s^{-1}}$. The fraction
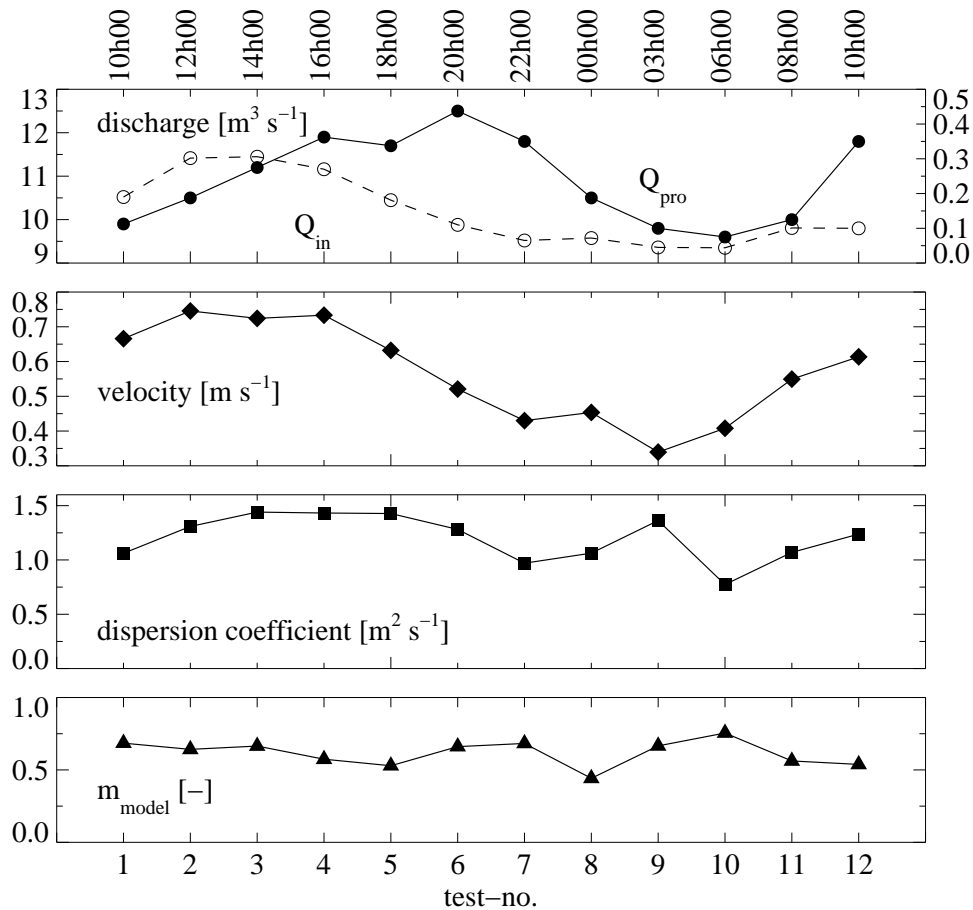
Figure 5.10: *Transport parameters derived from fi tting the advection-dispersion model to individual tracer return curves of the August experiment. The top panel shows input discharge at the time of tracer injection (dashed, right scale) and average output discharge during the time of tracer detection (solid, left scale). The horizontal axis on top refers to the time of tracer injection.*
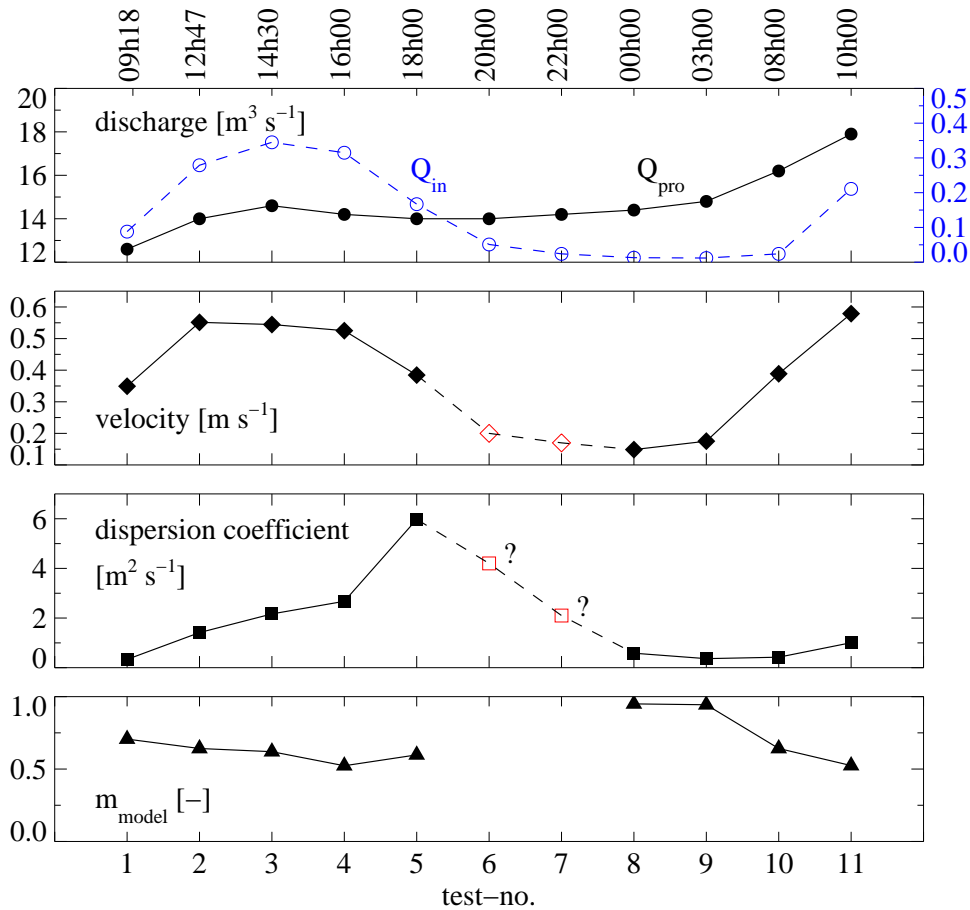
Figure 5.11: *Transport parameters derived from fitting the advection-dispersion model to individual tracer return curves of the September experiment. The top panel shows input discharge at the time of tracer injection (dashed, right scale) and average output discharge during the time of tracer detection (solid, left scale). Red symbols indicate estimated values, see text for details. The horizontal axis on top refers to the time of tracer injection.*

of tracer mass m_{model} which is described by the used model, varies between 0.45 and 0.76 but does not reveal a systematic diurnal course.

September experiment The quality of the data is not continuous in this data set. The anomalous shape of return curves number 6 and 7 in Figure 5.9b cannot be explained by a simple advection-dispersion transport model. Hence, fitting the model to these data would not yield a meaningful parameter determination. However, residence times could be estimated by the median time, when half of the returned tracer had passed the site of detection. Dispersion coefficients were obtained by linear interpolation between the adjacent data points. To emphasize the reduced certainty, these data points are specially signified in Figure 5.11.

In general, the September experiment reveals results similar to the August experiments with regard to the relation of input discharge and transit velocity. However, transit velocities are somewhat smaller than in August and values vary between 0.15 and $0.58\,\mathrm{m\,s^{-1}}$. In contrast, Q_{pro} shows a very distinct picture due to the overall increasing trend as described in Section 5.2.1. Again, dispersion coefficients follow the course of velocity but seem to be retarded with respect to velocity. However, on the declining limb of transit velocity, the dispersion coefficient from

injection number 5 reaches $5.98\,\mathrm{m^2\,s^{-1}}$ whereas D-values during rising or stagnant phases of velocity range from 0.34 to $2.67\,\mathrm{m^2\,s^{-1}}$. Again, as in Figure 5.10 the proportion of tracer mass described by the used model does not show a clear diurnal variation.

A noteworthy observation is obtained from comparing the results of the two experiments in August and September. While discharge during the August experiment varied between 9.5 and $13\,\mathrm{m^3\,s^{-1}}$, the average transit velocity is $0.58\,\mathrm{m\,s^{-1}}$. In contrast, velocities in September are lower with an average value of $0.37\,\mathrm{m\,s^{-1}}$ although discharge (10–$19\,\mathrm{m^3\,s^{-1}}$) was consistently higher than in August.

5.4 Discussion

5.4.1 Experiment design

This section deals with the tracer experiments which were conducted to characterize the hydraulic behavior of a subglacial channel at different stages during the ablation season 2000. Based on theoretical considerations (Sec. 4.3.3), the experiments were designed to account for the fact that a glacial drainage system evolves with time. For this purpose, tracer injections into a moulin were repeated in quick succession over an entire diurnal discharge cycle. The tracer tests were accompanied by measurements of discharge input into the moulin and bulk discharge in the proglacial stream. Results of careful data analysis reveal a pronounced diurnal variability of transit velocity and dispersion coefficient. This finding underlines the difficulty to detect a possible drainage system evolution based on single tracer tests at coarse temporal intervals. For instance, Hasnain et al. (2001) deduced extensive morphological changes in the drainage system from a reduction of transit velocity from ~ 0.4 to $\sim 0.1\,\mathrm{m\,s^{-1}}$ within a period of about 40 days. However, our observations reveal a comparable velocity range within one single day and along one single flow path. There is little doubt that in our case these variations are related to changing hydraulic conditions rather than to extensive changes in the morphology of the drainage system.

5.4.2 Choice of the transport model

Except for two injections during night, the return of tracer during the September experiment occurred in single-peaked concentration curves. This provides the opportunity for an intercomparison of the two transport models proposed in Chapter 4. Figure 5.12 compares the two transport parameters transit velocity and dispersion coefficient determined by the advection-dispersion model and the mobile-immobile model. Both approaches render identical velocity values (Fig. 5.12a) which is not surprising since the estimate of transit velocity is a robust feature for advection-dominated systems. In contrast, there is a slight disagreement concerning the estimate of the dispersion coefficient (Fig. 5.12b). However, deviations are small and appear to be non-systematic. The largest deviation is observed for the somewhat outlying dispersion coefficient of test number 5. Considering the wide range of observed dispersion coefficients, the inaccuracies related to the choice of transport models are insignificant for our results. Hence, we can justify the use of the simplified procedure described in Section 5.2.3 even though it does not explain the entire return curve. In previous studies retardation was either neglected in the transport model formulation (e.g. Seaberg et al., 1988; Hock and Hooke, 1993; Nienow, 1993;
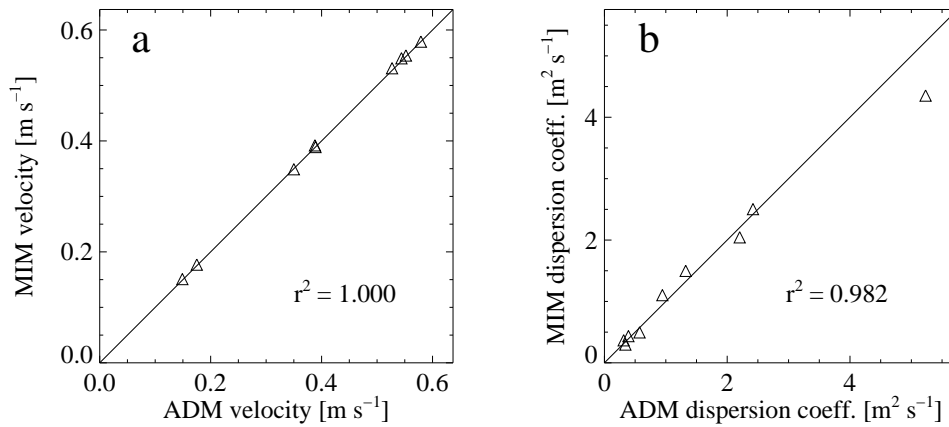
Figure 5.12: *Comparison of the transport parameters transit velocity (a) and dispersion coefficient (b) determined by the advection-dispersion model (ADM) and the mobile-immobile model (MIM). The diagonal line has a slope=1 and represents perfect agreement.*
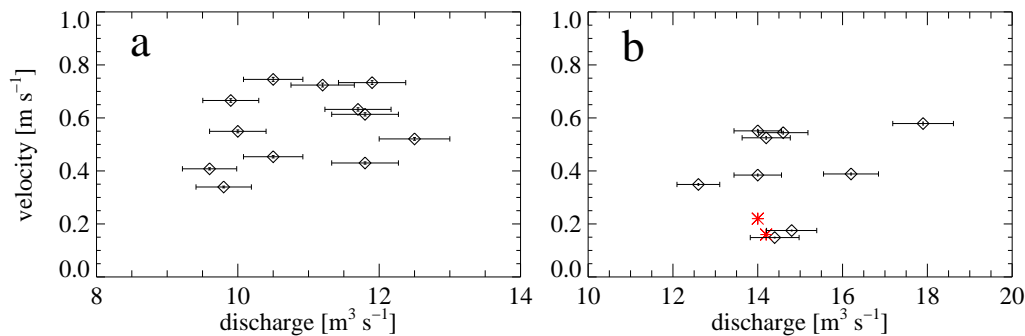
Figure 5.13: *Velocity-discharge plots derived from dye injections in August (a) and September (b) 2000. Horizontal error bars denote the uncertainty of the discharge measurements. Vertical error bars for the velocity are overlapped by the data points.*

Hasnain et al., 2001) and the advection-dispersion model was used inappropriately as shown in Figure 5.4 or storage-retardation was treated separately from advection-dispersion (Brugman, 1986; Willis et al., 1990). Therefore the comparability of dispersion estimates is limited. An attempt to model a continuous advection-dispersion-retardation transport was made by Fountain (1993) but in his formulation retardation is caused by an englacial plunge pool, the size of which was used as a free parameter. In this study, we prefer to conceptualize the retardation process instead of introducing additional assumptions.

5.4.3 Hydraulic implications

Variation of velocity with discharge

Since we have used normalized concentration values to derive transport parameters, absolute tracer concentrations and their inaccuracy are irrelevant for our parameter estimate. Therefore, the accuracy of the transport parameters v and D depends only on the certainty by which the timing of the tracer breakthrough can be determined. For a conservative estimate of this error, we
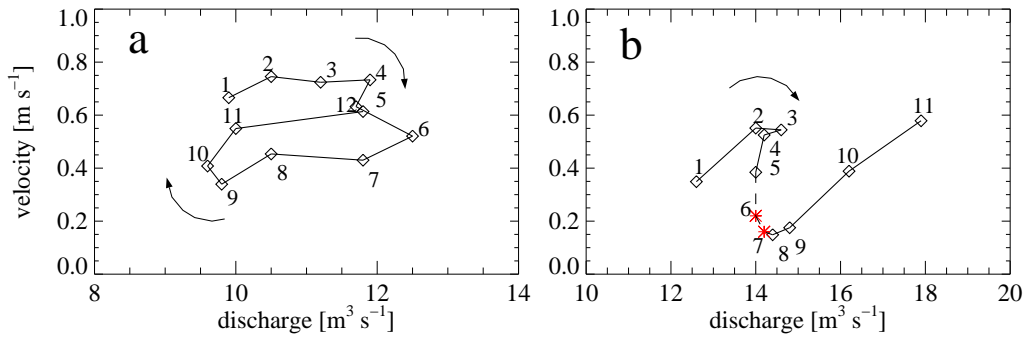
Figure 5.14: *The pattern of velocity-discharge relationships derived from series of dye injections in August (a) and September (b) 2000. The points are numbered according to the chronological order.*

accept a maximum of $\pm 1\,\mathrm{min}$. Recalling that peak concentrations of the fastest breakthroughs occurred about $100\,\mathrm{min}$ after tracer injection, the inaccuracy for both v and D is $\leq 1\%$. In a figure, the error bars for velocity and dispersion would be covered by the plot symbols and are therefore not shown.

The error of our discharge measurements is certainly smaller than the $\pm 10\%$-accuracy which we have attributed to our discharge record in 1999 (Sec. 3.2.2). In 1999 the discharge measurements were performed over a period of more than 2 weeks and a continuous record was constructed from stage measurements. As noted in Section 3.2.2, we believe that the main source of error in 1999 is related to the unstable nature of the unconsolidated stream bed. In contrast, in 2000, the records of discharge are based on measurements which were performed at intervals of about two hours. On this timescale, alterations of the river cross-section which would introduce inaccuracy in our discharge record are much smaller and we accept an error of $\pm 5\%$ as conservative estimate.

After having obtained datasets of discharge, velocity and dispersion coefficients, we proceed to characterize hydraulic conditions using the methodology described in Section 4.3.1. However, the data points in the resulting vQ-relationship appear to be broadly scattered (Fig. 5.13). Hence, a functional relationship is not well defined and its determination as done in previous studies (e.g. Seaberg et al., 1988; Hock and Hooke, 1993; Fountain, 1993; Kohler, 1995) would be highly sensitive to the choice of the function thereby reducing the reliability of the result.

If the chronological order of the data is taken into account, the sequence reveals a conspicuously systematic behavior. Figure 5.14 illustrates how the vQ-relationship follows distinct trajectories through a discharge cycle. In the August series (Fig. 5.14a), transit velocity stays at a high level as discharge increases but features a noticeable drop during the maximum phase of discharge. During discharge minimum, velocity values increase but start the next discharge cycle on a different level. Such a clockwise hysteresis is symptomatic for a velocity signal preceding the discharge signal in phase. Similarly, September results (Fig. 5.14b) show also a non-linear relationship with velocity markedly decreasing during the stagnant discharge phase but subsequently rising in parallel with the increasing discharge.
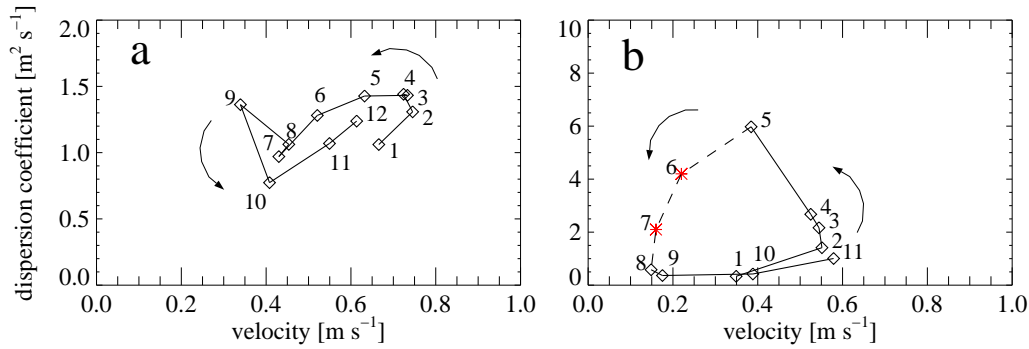
Figure 5.15: *Relationships between velocity and dispersion coefficients derived from series of dye injections in August (a) and September (b) 2000. The points are numbered according to the chronological order.*
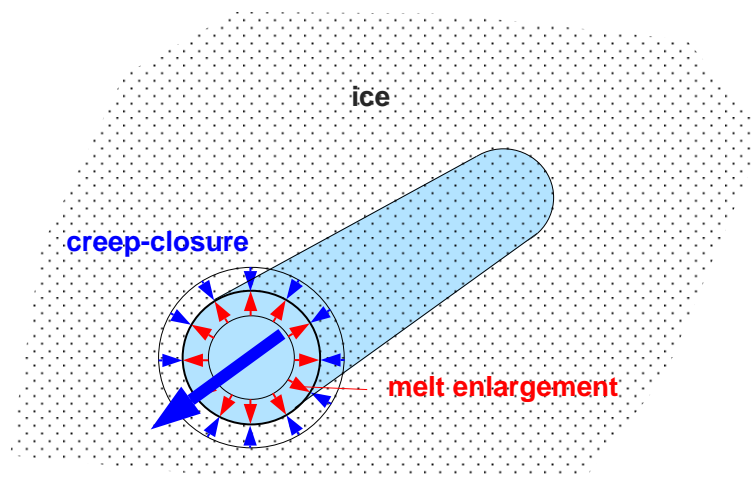
Figure 5.16: *Sketch of a Röthlisberger-type channel with dynamic geometry.*

Variation of dispersion with velocity

Similarly to the vQ-plots in Figure 5.13, the scattering in the interrelation of transit velocity and tracer dispersion inhibits the determination of a reliable functional relationship by linear regression (Sec. 4.3.2). In fact, the vD-relationship exhibits a hysteresis in anti-clockwise direction (Fig. 5.15) such that in both experiments the dispersion coefficient is systematically higher during declining than during increasing velocity. In August (Fig. 5.15a), the D-value at minimum velocity deviates from the otherwise regular hysteresis. The hysteresis of the September experiment (Fig. 5.15b) is more pronounced with strongly increased dispersion coefficients during the falling limb of velocity. However, the dispersion coefficients of the two tracer return curves numbered 6 and 7 are not precisely determined and their positions in the vD-plot are therefore not exactly defined. Nevertheless, the magnitude of transit velocity in these cases is well constrained, thereby supporting the general shape of the hysteresis, regardless of exact dispersion values.

Possible interpretations

Dynamic conduit geometry   Since the slope of a velocity-discharge relationship reflects directly the hydraulic geometry of the drainage system (Sec. 4.3.1), it seems reasonable to associate the hysteretic behavior of our experiments to an corresponding evolution of the flow path.

The short transit time of the tracer in the system and its reappearance in a sharp breakthrough curve suggests flow through an efficient, channelized drainage system. Röthlisberger (1972) postulated channels with a dynamic geometry (Sec. 2.2.2). The size of such a channel is determined by the counteracting processes of melt enlargement due to dissipation of potential energy versus creep-closure of the viscous ice (Fig. 5.16). The consequences of the Röthlisberger-theory for the transit velocity of a tracer is considered in a qualitative model applied to the two observed discharge situations. In response to an increasing discharge, a Röthlisberger channel would be enlarged. On the other hand, when discharge decreases, the water pressure in the channel would decline. This would cause an enhanced closure rate of the conduit and therefore result in a decrease of the channel size. If we compare two channels of different cross-sectional area A, both carrying the same discharge Q, the flow velocity v in the larger one would be smaller since continuity requires $Q = v A$. This mechanism of a Röthlisberger-channel can coherently explain the decrease of velocity during high discharges in August and September as well as the subsequent velocity increase at minimum discharge in August. As a further consequence, the conduit would be larger on the falling than the rising limb of velocity. To explain the observation that dispersion is generally larger during declining that during increasing velocity, we conjecture a positive relationship between conduit size and dispersion, because the decrease of velocity coincides with the enlarged conduit.

Finally, the assumption of an adaptable channel geometry receives additional support by the fact that over the course of one day transit velocities in September were consistently lower than those in August although discharge was higher. An increase of the channel diameter as described by the Röthlisberger-theory could permit the drainage of a larger discharge even at a lower velocity.

In summary, the ability of a Röthlisberger channel to adjust its size to prevailing hydraulic conditions provides a lucid explanation for the observed hysteretic behavior. However, this hypothesis needs to be tested by a quantitative model to investigate whether the physical processes can account for the observed behavior.

Inflow modulation   Besides the above interpretation, there is also an alternative explanatory hypothesis. Figures 5.10 and 5.11 illustrate how transit velocity varies with both the supraglacial and the output discharge during the test series. It is obvious, that the velocity variations were more closely in phase with Q_{in} than with Q_{pro}. This finding might suggest that the obtained velocities are the result of flow through an independent conduit connecting the moulin directly to the glacier terminus. However, such a scenario is highly implausible since dye emerged in the outlet stream which carries a much larger discharge than the supraglacial stream entering the moulin. Thus, it is clear that the moulin acts as a tributary which joined a main conduit before exiting the glacier.

Smart (1990) mentioned "hydraulic damming" due to higher discharge in the main conduit which controls the proportion of tracer entering at the junction of tributary and conduit. However, "hydraulic damming" may not be an appropriate term to describe the process since the water is not blocked at the junction. The pressure conditions in the main channel modulate the inflow from the tributary and we therefore prefer to use the term "inflow modulation". Fountain
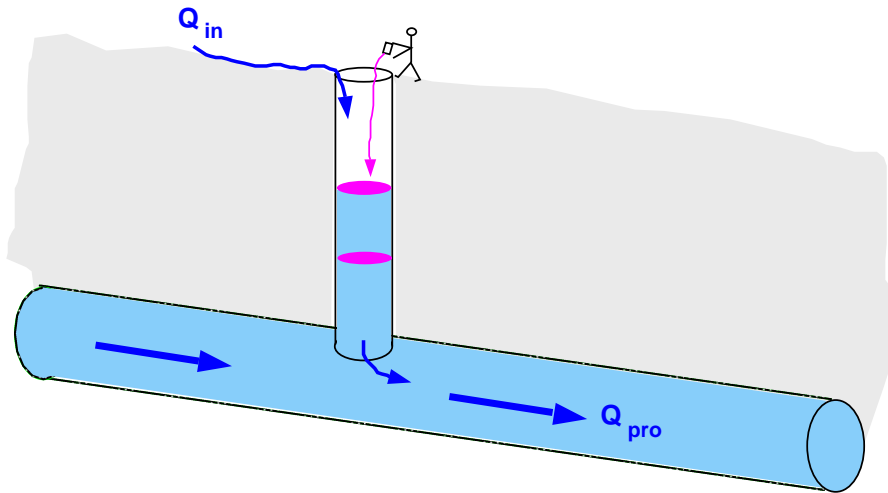
Figure 5.17: *Schematic overview of a two component flow system where flow through the moulin is governed by Q_{in} as well as by the level to which water is backed up.*

(1993) argues that it is unlikely that any of the tracer would be routed from the glacier surface to the main conduit without some effect of this mechanism. Such a two component channelized system was considered by Nienow et al. (1996c) with the transit velocity in the tributary channel controlled by Q_{in} and in the main conduit by Q_{pro}. If the influence of the tributary is large enough, this conceptual idea would be able to explain the hysteretic behavior observed in our experiments (Fig. 5.14). In this case, we postulate that retardation in the tributary must lead to an increase in tracer dispersion to explain the observed variation of dispersion with velocity (Fig. 5.15). This follows from the consistently increased dispersion coefficients during decreasing velocities which are attributed to enhanced inflow modulation.

As above for the assumption of a dynamic conduit geometry, this hypothesis needs to be tested by a quantitative model. Nienow et al. (1996c) described drainage through a combined moulin-conduit system by a two-component model. However, the representation of the hydraulic processes and the coupling between the components is purely conceptual. Nienow et al. (1996c) described the relationship between velocity and discharge in each subsystem by empirical power functions and adjusted two parameters determining each of these functions as well as the partitioning between the two subsystems. With a total of five free parameters for four equations, the problem is underdetermined such that the same result was obtained by different parameter combinations. Hence, it inhibits further insight into the process and can therefore not be used to investigate whether inflow modulation is responsible for the observed behavior.

Chapter 6

Modeling variations of transit velocity

In Chapter 5, it was found that dye injected into a moulin at Unteraargletscher was routed through an efficient, channelized drainage system. The observed velocity-discharge relationships displayed pronounced hystereses. It was suggested that the dynamic geometry of a Röthlisberger-channel could induce such hystereses. An alternative concept proposes that discharge through the moulin might be dammed hydraulically at the junction to a larger conduit, thereby causing the observed behavior.

However, whether conduit evolution happens at a rate fast enough or whether inflow modulation alters the transit time of a tracer sufficiently to explain the observed behavior has to be examined in detail. This chapter aims to tackle this task by numerical modeling of the proposed mechanisms. After a review of existing theories on water flow through subglacial conduits, which go into more detail than the general considerations in Section 2.2.3, we will introduce a our model which we use to study variations of transit velocity with discharge. We first begin by looking at our visualization of the channelized drainage system beneath Unteraargletscher.

6.1   Visualization of channelized drainage

From the results presented above (Ch. 5), it appears that the investigated flowpath is a subglacial channel connected to the tributary moulin through which the tracer was injected. Moulins typically descend steeply towards the glacier bed (Holmlund, 1988) where we expect them to join a conduit. As such, we visualize the conduit as located at the glacier bed and incised into the overlying ice (Fig. 2.3a,b). Similar to the proglacial stream, we conjecture that the bottom of the subglacial conduit consists of coarse sediments and differently sized blocks. The cross-section of the conduit is approximately semi-circular at the terminus of Unteraargletscher but may be rather broad and low below the upper part of the glacier where the ice is thicker (Hooke et al., 1990; Cutler, 1998; Ng, 1998). The shape and size of the cross section are determined by the opposing effects of melt-enlargement due to dissipation of energy and creep-closure due to visco-plastic behavior of the ice-roof (Röthlisberger, 1972). In general, the conduit will principally follow the steepest potential gradient (Shreve, 1972). However, in detail, its course is probably not a direct one but it is most likely meandering and disturbed by intersecting crevasses and the underlying bedrock relief producing bends and breaks. Similarly, we visualize the distribution of the cross-section along the course of the conduit as irregular, characterized by contractions and expansions. Since the water exits Unteraargletscher through a single large glacier portal

(Ch. 3.1.3) while meltwater enters the glacier at numerous locations at the surface, it is obvious that tributary channels join to form a main conduit. Therefore, we believe that the structure of the subglacial conduit system is appropriately described by an upglacier branching arborescent network as proposed by Shreve (1972) and Röthlisberger (1972).

6.2   Background

Originally, the theory of conduit flow through a glacier was developed for englacial conduits which are completely enclosed by ice. In this case, channelised drainage is a flow of a fluid through its solid phase (Spring and Hutter, 1982). The first comprehensive theory was presented by Röthlisberger (1972), who considered an equilibrium state between melt-enlargement and creep-closure. The resulting inverse relationship between water pressure and discharge and its extensive implications for glacial hydrology was already discussed in Section 2.2.3. However, diurnal meltwater input varies on a time scale much shorter than the time needed by such a channel to reach steady-state conditions (Spring, 1980). Therefore, the steady-state assumption is not appropriate for typical glacier drainage situations. This shortcoming was closed by Nye (1976) who presented a time-dependent theory which he then used to explain the hydrograph during a Jökulhlaup (the Icelandic expression for an outburst of a glacier-dammed lake). The theories of Röthlisberger (1972) and Nye (1976) are valid only for straight conduits of circular cross-section that are completely surrounded by ice. Spring (1980) developed therefore a more complex and physically based theory for curved and twisted conduits. However, it is strictly valid only for conduits which are entirely enclosed by ice since any interaction with the glacier bed is neglected. It was shown by Spring (1980), Spring and Hutter (1981) and Spring and Hutter (1982) that the former formulations of Röthlisberger (1972) and Nye (1976) can be derived as special cases from the more general Spring-theory. Spring (1980) also compared two different expressions for frictional head loss: the Manning-Gauckler-Strickler-formula which was used by Röthlisberger (1972) and Nye (1976) and the Darcy-Weisbach-formula. Differences between the two approaches turned out to be slight and in subsequent studies the Darcy-Weisbach form was adopted (Spring and Hutter, 1982; Kohler, 1995; Clarke, 1996). Where the conduit is in contact with the glacier bed some modifications to the theory have to be made. The friction between ice and bed affects the closure of a conduit in such a way that the inward creep of the bottom ice is retarded with respect to the ceiling of the conduit (Hooke et al., 1990). Hence, its resulting cross-sectional shape is wide and low rather than semi-circular. Further effects are related to the interaction between water and glacier bed. As such, the roughness of the bed and the altered cross-sectional shape would increase the resistance for water flow. This in turn alters the water pressure gradient thereby affecting the cross-sectional geometry which is additionally changed by erosion-sedimentation processes of a sedimentary bed. Röthlisberger (1972) argues that these alterations to his theory counteract each other and thus, the assumption of a circular cross-section would not introduce much inaccuracy. As mentioned in Section 2.2.3, modifications to the theory were necessary to explain measured water pressures; calculated pressure values were consistently too low and agreement could be achieved in two ways. One approach was the assumption of an enhanced closure-rate (Röthlisberger, 1972; Iken and Bindschadler, 1986; Lliboutry, 1983) due to material properties of the basal ice. In a second approach a broad and low cross-sectional geometry is proposed (Hooke, 1984; Hooke et al., 1990). Such a geometry is more resistive to water flow, thereby a higher hydraulic gradient is required to drive the flow. Additionally, the closure rate of such a broad low cross-section is larger than that of a semi-circular one. While Hooke et al. (1990) simplified the conduit shape by a segment of

a circle, the problem of closure of an irregularly shaped cross-section was tackled by Cutler (1998) and Ng (1998). Erosion-sedimentation controlled geometry changes were addressed by the work of Walder and Fowler (1994) and Ng (2000) yielding equilibrium results contrary to those of Röthlisberger (1972) for the case of a very thick sediment bed. This case may apply for ice streams (Alley et al., 1987), but where the sediment layer is thinner, a common situation beneath alpine glaciers, sediment creep is limited by enhanced strength of sediment in close vicinity to a channel (Alley, 1992). Therefore, channels are likely to become isolated from the deforming sediment. In this case, the theory for subglacial conduits on a hard bed is again applicable.

6.3 Model theory

Based on the theories considered above, we now formulate expressions which enable us to simulate the behavior of a Röthlisberger-channel for given discharge variations. Such a model should also allow us to derive a physically based relationship between discharge and flow velocity. Since open-channel flow is conceivable in parts of the conduit (Lliboutry, 1983; Hooke, 1984; Fountain, 1993; Kohler, 1995; Nienow et al., 1996c), this possibility will be included in the model as well. Further, aiming for a simulation of our series of tracer experiments, we treat the problem in a spatially distributed formalism for a simplified geometry of Unteraargletscher.

6.3.1 Assumptions

Despite our visualization of an irregularly meandering subglacial conduit of complex cross-sectional shape and size, the model which will be used for our purpose is rather simple. The lack of detailed information on the real course and geometry of the conduit requires that we make the simplest possible assumptions. As such, the following assumptions are included in our model formulation:

1. The conduit is located at the glacier bed and follows the thalweg.

2. The ice is isothermal and at the pressure melting point. This is a typical characteristic of alpine glaciers. Hence, the energy dissipated by the flow of water is entirely available for melting channel walls.

3. The ice is incompressible and isotropic. Therefore, Glen's flow law is appropriate to describe closure-rates.

4. If we consider a uniform distribution of velocity and pressure within the channel cross-section the problem can be reduced to one dimension in flow direction.

5. The contribution to discharge from melting of conduit walls is negligible.

6. The conduit is directed parallel to ice-flow and far-field longitudinal and transverse strain-rates are zero, thus the conduit-axis is stationary.

7. Any thermal energy is produced and consumed locally (within one spatial increment), thus advection of thermal energy into or out of the considered conduit segment is neglected.

8. The conduit has a circular cross-section, i.e. for the computation of closure-rates, we follow Röthlisberger's argument (p. 65) and neglect direct influences from the bed. This simplifies the matter and the analytical expression for closure-rate of a cylinder (Nye, 1953) can be applied.

9. The conduit-axis is straight and effects of curvature, bends and breaks on water flow are not described explicitly.

10. Any kind of head loss is described by a single friction parameter using the Darcy-Weisbach-formula. In doing so, we have to bear in mind that we omit explicit descriptions of curvature of the conduit-axis and irregularities of cross-sectional shape and size which would cause additional local head losses. Thus, our estimate of the friction parameter comprises frictional as well as local losses.

11. The kinetic potential of the flowing water is small compared to the pressure and topographic potentials and can be neglected.

12. Negative water pressure or suction cannot occur. Instead, water would flow under open-channel conditions and fill the conduit partially. In this case, melting occurs only at the wetted part of the conduit perimeter.

6.3.2 Model equations

The assumptions made above enable us to formulate a simplified model that suits our requirements.

Energy dissipation

Water flows down a potential gradient $\partial H/\partial x$, with x defining a length in stream-wise direction. Thereby, the water releases potential energy E. The local hydraulic potential is expressed by

$$H = h + z, \tag{6.1}$$

where h is water pressure expressed in terms of hydraulic head $h = p_\mathrm{w}/\rho_\mathrm{w} g$ with p_w denoting the water pressure, ρ_w the density of water, g the acceleration due to gravity and z is the elevation of the bed relative to a datum. The potential energy released per time t and per unit length $\mathrm{d}x$ is given by

$$\frac{\partial E}{\partial t} = \rho_\mathrm{w} g Q(t) \frac{\partial H}{\partial x} \mathrm{d}x. \tag{6.2}$$

Melt enlargement

This energy is consumed by melting ice at the conduit walls and by maintaining the water at pressure melting conditions. For the considered solid-liquid phase transformation the water pressure and temperature are inversely correlated, thus, the melting condition requires higher temperature as the pressure drops. The temporal evolution of energy E_t required for this process is

$$\frac{\partial E_\mathrm{t}}{\partial t} = c_\mathrm{t} c_\mathrm{w} \rho_\mathrm{w} Q(t) \rho_\mathrm{w} g \frac{\partial h}{\partial x} \mathrm{d}x \tag{6.3}$$

with c_t expressing the change in melting temperature per unit pressure and c_w the specific heat of water.

The energy E_m required per time step to increase the volume V_m of the conduit by melting is written

$$\frac{\partial E_m}{\partial t} = \rho_i L_f \frac{\partial V_m}{\partial t}, \tag{6.4}$$

where ρ_i stands for density of ice and L_f for latent heat of fusion. Expressing $V_m = A_m dx$, where A_m is the cross-sectional area produced by melting and considering the length of the conduit constant in time ($\partial x / \partial t = 0$), we can drop dx from the energy equation $E = E_m + E_t$. Solving for $\frac{\partial A_m}{\partial t}$, we obtain then

$$\frac{\partial A_m}{\partial t} = \frac{\rho_w g}{\rho_i L_f} Q(t) \left((1 - \gamma) \frac{\partial h}{\partial x} + \frac{\partial z}{\partial x} \right), \tag{6.5}$$

where $\gamma = c_t c_w \rho_w$ defines a dimensionless constant.

Creep-closure

Viscoplastic deformation of ice counteracts the growth of subglacial conduits. Nye (1953) derived an analytical solution for the closure rate of a cylindrical tunnel using Glen's flow law:

$$\frac{\dot{R}}{R} = B \left(\frac{\rho_w g}{n} (h^* - h) \right)^n. \tag{6.6}$$

Here, R is the radius of the circular cross-section, the dot indicates derivation with respect to time, B and n are flow law parameters. The ice-overburden pressure expressed in terms of hydraulic head $h^* = \rho_i / \rho_w h_i$ is exerted by ice of the thickness h_i. Simple geometrical considerations reveal $\dot{A}_c = 2\pi R \dot{R}$, where A_c denotes the cross-sectional area closed by creep. By using Equation (6.6) we obtain

$$\frac{\partial A_c}{\partial t} = 2AB \left(\frac{\rho_w g}{n} (h^* - h) \right)^n \tag{6.7}$$

where A denotes the cross-sectional area of the conduit. Finally, to derive an equation describing the change of the conduit cross-section with time, we combine the counteracting expressions for melt enlargement (Equation (6.5)) and creep closure (Equation (6.7)):

$$\frac{\partial A}{\partial t} = \frac{\rho_w g}{\rho_i L_f} Q(t) \left((1 - \gamma) \frac{\partial h}{\partial x} + \frac{\partial z}{\partial x} \right) - 2AB \left(\frac{\rho_w g}{n} (h^* - h) \right)^n. \tag{6.8}$$

Pressurized water flow

With an expression relating the release of hydraulic potential ΔH to discharge Q, our model to describe subglacial drainage is complete. Taking a critical Reynolds-number of about 2300 (Weertman, 1972) for water flow through a pipe, it turns out that even for a very small conduit of $0.1\,\text{m}$ in diameter a velocity higher than $0.05\,\text{m s}^{-1}$ would cause turbulence. Observation yields typically higher velocities (e.g. Lang et al.,1979; Hock and Hooke, 1993; Nienow, 1993; Fountain, 1993). Hence, flow in subglacial conduits carrying significant water quantities is expected to be turbulent.

For turbulent flow through a pipe, the Darcy-Weisbach relation states that:

$$\rho_\mathrm{w} g \frac{\partial H}{\partial x} = \frac{f \rho_\mathrm{w} \overline{v}^2}{8 R_\mathrm{h}}, \tag{6.9}$$

where $\overline{v}$ is the mean flow velocity and R_h the hydraulic radius. The dimensionless friction factor f depends on the wall-roughness and the Reynolds-number. However, this dependence vanishes for high Reynolds-numbers, hence, for simplicity, we use a constant f. We will justify this assumption a posteriori (Sec. 6.8.2). By definition $R_\mathrm{h} = A_\mathrm{w}/U_\mathrm{w}$ with A_w being the area occupied by the water and U_w the wetted conduit perimeter. Recalling that the conduit is pressurized yields $A_\mathrm{w} = A$, $U_\mathrm{w} = U$ and $Q = \overline{v} A$. If solved for Q, Equation (6.9) yields

$$Q = 2 A^{3/2} \left(\frac{2g}{fU} \frac{\partial H}{\partial x} \right)^{1/2}. \tag{6.10}$$

Open-channel flow

Flow conditions through a conduit are pressurized, where discharge exceeds the maximum amount which can be routed under open-channel flow conditions. This threshold can be derived from the Manning-Gauckler-Strickler formula:

$$\overline{v} = k R_\mathrm{h}^{2/3} \left(\frac{\partial z}{\partial x} \right)^{1/2}, \tag{6.11}$$

where k represents a roughness coefficient and water flow is driven by the topographical potential gradient $\partial z/\partial x$. For a completely filled conduit $R_\mathrm{h} = 1/2 \, (A/\pi)^{1/2}$ and the corresponding non-pressurized discharge is

$$Q_\mathrm{max} = k \left(\frac{\partial z}{\partial x} \right)^{1/2} 2^{-2/3} \pi^{-1/3} A^{4/3}. \tag{6.12}$$

We adopt this value as the threshold between pressurized and open-channel flow. Where open-channel flow takes place, the conduit is only partially filled. In this case melt enlargement occurs only along the wetted perimeter of the conduit. However, we assume that the circular shape of its cross-section persists and consequently the Nye (1953)-solution for creep-closure holds. Thus Equation (6.8) becomes

$$\frac{\partial A}{\partial t} = C \frac{\rho_\mathrm{w} g}{\rho_\mathrm{i} L_\mathrm{f}} Q(t) \frac{\partial z}{\partial x} - 2AB \left(\frac{\rho_\mathrm{w} g}{n} h^* \right)^n, \tag{6.13}$$

where $C = U_\mathrm{w}/U$ is a correction factor that represents the ratio of wetted perimeter U_w to total perimeter U. For the cross-sectional area occupied by water A_w in a partially filled circular conduit of radius R, the following relation applies:

$$A_\mathrm{w} = \frac{R^2}{2} \left(\alpha - \sin \alpha \right) \tag{6.14}$$

where the angle α is defined as shown in Figure 6.1. From the simple continuity relation $Q = \overline{v} A_\mathrm{w}$, Equation (6.11) and the definition of $R_\mathrm{h} = A_\mathrm{w}/U_\mathrm{w}$ we obtain

$$Q = k \left(\frac{\partial z}{\partial x} \right)^{1/2} U_\mathrm{w}^{-2/3} A_\mathrm{w}^{5/3}. \tag{6.15}$$
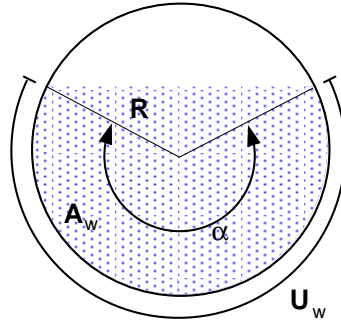
Figure 6.1: *Cross-section of a partly-filled circular conduit. The shaded area represents the area occupied by the water, A_{w}.*

Substituting Equation (6.14) and $\alpha = U_{\mathrm{w}}/R$ yields

$$Q^{3/5}k^{-3/5}\Big(\frac{\partial z}{\partial x}\Big)^{-3/10}\frac{2}{R^2} = U_{\mathrm{w}}^{-2/5}\Big(\frac{U_{\mathrm{w}}}{R} - \sin\frac{U_{\mathrm{w}}}{R}\Big). \qquad (6.16)$$

This equation cannot be solved analytically for U_{w}. Figure 6.2 illustrates that the relation of discharge and filling depth in a partly filled circular conduit is not unique for high filling levels. At such a high filling level, U_{w} increases faster with filling depth than A_{w}. In consequence, when water fills the conduit to 92%, a slightly larger discharge is drained than that at higher filling levels. This point marks the transition to pressurized flow when the filling depth in a partly filled conduit increases. In contrast, the transition from pressurized to open-channel flow takes place at a discharge which corresponds to complete filling (Chow, 1988; Hager, 1995). We recall that we treat this transition by a single value Q_{max} (Equation (6.12)) instead of two different thresholds for opening and closing. However, the resulting error in the calculated pressures is of the order of 10^{-5}m for typical values of A (5–$10\,\mathrm{m^2}$). We neglect this inaccuracy because it is small compared to typical hydraulic head variations which are of the order of several meters.

The value of U_{w} was iterated by finding the zero of an objective function $\varepsilon = X - Y$, where X stands for the left hand side and Y for the right hand side of Equation (6.16). Ambiguous solutions where avoided by starting the approximation of U_{w} from zero. In doing so, we will always approach the physical meaningful solution first.

Computation of flow velocity

When the water flow through the conduit is pressurized, mean flow velocity can easily be obtained from

$$\overline{v} = \frac{Q}{A}. \qquad (6.17)$$

To determine $\overline{v}$ in the case of open-channel flow, A in Equation (6.17) has to be replaced by A_{w}. Once U_{w} is determined, A_{w} follows from Equation (6.14) using $\alpha = U_{\mathrm{w}}/R$.
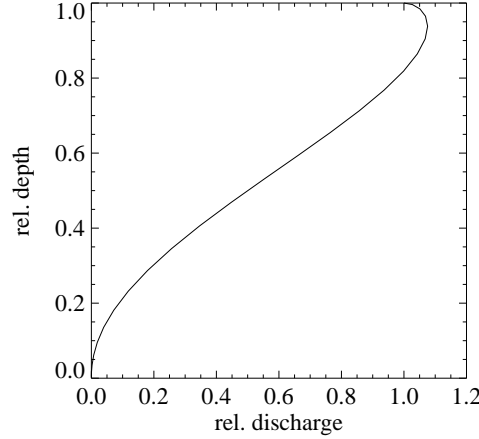
Figure 6.2: *The discharge through a partly filled circular conduit as a function of filling depth. The values are normalized with respect to those that correspond to complete filling.*

6.4 Model implementation

6.4.1 Flow resistors

So far, we derived expressions describing water flow and the evolution of the conduit geometry. To integrate these equations we formulate a scheme for numerical computation. For this purpose, we follow the formulation of Clarke (1996) defining a hydraulic analogue to Ohm's law in electricity for both linear as well as nonlinear flow resistances. Water discharge is driven by the release of hydraulic potential ΔH through a hydraulic system exerting a resistance towards flow. The passage of water is obstructed by friction on the system boundaries, thus, the resistance is governed by roughness elements, the geometry of the system and the type of flow. Linear resistance R_L is characterized by a H-Q-relationship:

$$\Delta H = Q R_\mathrm{L} \tag{6.18}$$

and is associated with laminar flow. In contrast, turbulent flow obeys power-law relations of the form:

$$\Delta H = Q^2 F_\mathrm{T}, \tag{6.19}$$

with F_T denoting a resistance parameter. We may define a nonlinear resistance that increases linearly with discharge $R_\mathrm{T} = Q F_\mathrm{T}$ and consequently we obtain:

$$\Delta H = Q R_\mathrm{T}. \tag{6.20}$$

Using this formalism, expressing Q by Equation (6.10) and using $U = 2(\pi A)^{1/2}$ (since we consider a circular cross-section) yields

$$R_\mathrm{T} = \frac{\pi^{1/4}}{2 A^{5/4}} \Big(\frac{f \, \Delta x \, \Delta H}{g} \Big)^{1/2}. \tag{6.21}$$

In contrast to a linear resistor R_L which is a function of geometry only, a turbulent resistor R_T depends on geometry, roughness and the applied hydraulic potential difference ΔH and is therefore nonlinear.

It is useful to consider an element of a fixed length Δx. All spatially dependent processes are assumed to be constant on this length scale. This implies that the potential gradient $\Delta H / \Delta x$ and the conduit cross-section A are constant along the element and consequently, the partial differential Equations (6.8) and (6.10) become ordinary.

Finally, we obtain the equations describing turbulent flow through a Röthlisberger-channel, represented by an element with resistance R_R. This system is described by Equations (6.20)

$$\Delta H = Q R_\mathrm{R}$$

and Equation (6.21)

$$R_\mathrm{R} = \frac{\pi^{1/4}}{2A^{5/4}} \Big(\frac{f \, \Delta x \, \Delta H}{g} \Big)^{1/2}$$

combined with Equation (6.8) if flow is pressurized

$$\frac{\mathrm{d}A}{\mathrm{d}t} = \frac{\rho_\mathrm{w} g}{\rho_\mathrm{i} L_\mathrm{f}} Q(t) \Big((1 - \gamma) \frac{\Delta h}{\Delta x} + \frac{\Delta z}{\Delta x} \Big) - 2AB \Big(\frac{\rho_\mathrm{w} g}{n} (h^* - h) \Big)^n.$$

For open-channel flow the system is determined by

$$\Delta H = \Delta z$$

and Equation (6.13)

$$\frac{\mathrm{d}A}{\mathrm{d}t} = C \frac{\rho_\mathrm{w} g}{\rho_\mathrm{i} L_\mathrm{f}} Q(t) \frac{\Delta z}{\Delta x} - 2AB \Big(\frac{\rho_\mathrm{w} g}{n} h^* \Big)^n.$$

In the latter case, we omit the explicit expression for the resistance of an open conduit since the calculation of H is trivial with $h = 0$.

This formulation is consistent with Clarke's (1996), except for the hydraulic potential which is used here as the driving force instead of hydraulic head, enabling us to consider inclined conduits.

6.4.2 Numerical scheme

In this section, we aim to model variations of transit velocity due to changing hydraulic conditions along the flow path. This is achieved by investigating the water pressure distribution along a R-channel in response to a given discharge. The approach requires a linear arrangement of flow resistors to obtain the desired longitudinal resolution by considering the topographies of glacier surface and glacier bed. In discretized form, the system of equations describing turbulent flow through a Röthlisberger-channel contains i algebraic equations describing the drop of hydraulic head over a spatial increment Δx:

$$h_i - h_{i-1} = (z_{i-1} - z_i) + Q^2 \frac{\pi^{1/2} f \, \Delta x}{4g A_i^{5/2}} \tag{6.22-a}$$

if flow is pressurized, otherwise

$$h_i = 0 \tag{6.22-b}$$

and i ordinary differential equations describing the temporal evolution of the conduit cross-section. For pressurized flow

$$\frac{\mathrm{d}A_i}{\mathrm{d}t} = \frac{\rho_\mathrm{w} g}{\rho_\mathrm{i} L_\mathrm{f}} Q(t) \Big((1 - \gamma) \Big(\frac{\Delta h}{\Delta x} \Big)_i + \Big(\frac{\Delta z}{\Delta x} \Big)_i \Big) - 2A_i B \Big(\frac{\rho_\mathrm{w} g}{n} (h_i^* - h_i) \Big)^n \tag{6.23-a}$$
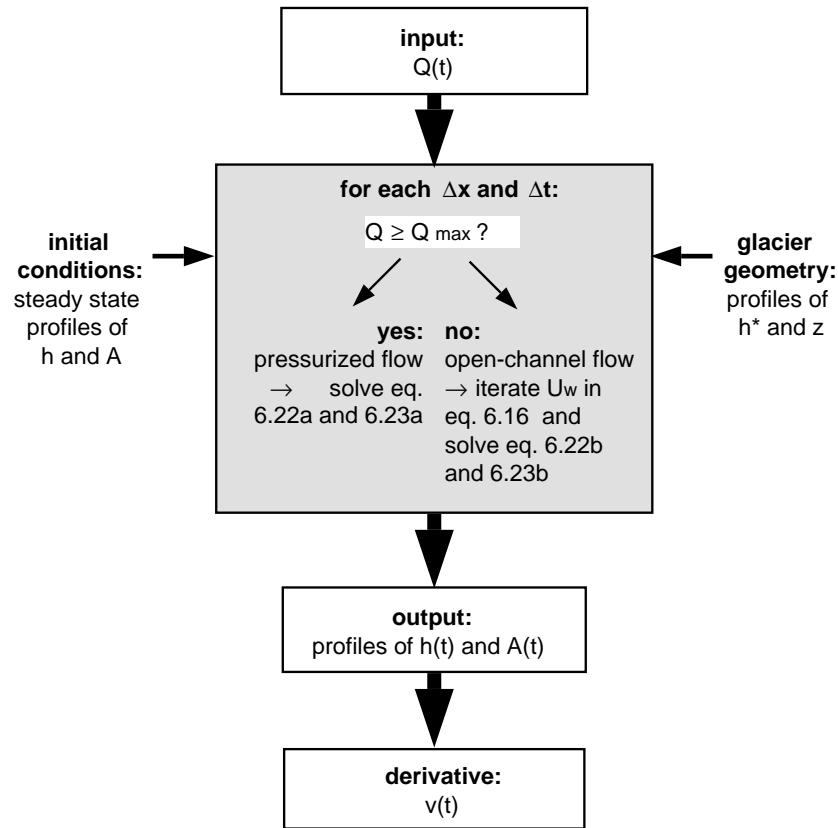
Figure 6.3: *Outline of the modeling procedure.*

and under open-channel conditions

$$\frac{\mathrm{d}A_i}{\mathrm{d}t} = C\frac{\rho_\mathrm{w}g}{\rho_\mathrm{i}L_\mathrm{f}}Q(t)\Big(\frac{\Delta z}{\Delta x}\Big)_i - 2A_iB\Big(\frac{\rho_\mathrm{w}g}{n}h^*\Big)^n \qquad (6.23\text{-b})$$

The glacier geometry in terms of bed elevation z and ice-overburden pressure h^* has to be prescribed as well as initial conditions for the distribution of hydraulic head h and conduit cross-sectional area A. Furthermore, one of the model boundaries requires a constraint from where the integration is started. Then, with a given discharge Q, the system of equations is solved for each spatial and temporal increment. From the resulting distributions of h and A, we derive the transit velocity of water v. The procedure of the model calculation is outlined in Figure 6.3.

In this study, we have implemented our model using Clarke's (1996) program code which solves similar equations. A problematic feature of this system of equations is its hybrid composition of both differential and algebraic equations (Hairer et al., 1995). This demands the employment of specially designed numerical methods to compute solutions. Here, the public domain solver ddriv3 was used, an elaboration of the program sdriv2 described by Kahaner et al. (1989). Special attention is required by the fact that the governing equations prove to be numerically stiff. An obvious source of stiffness is introduced by nonlinearities such as in Equation (6.23-a) near $Q = Q_{\max}$. A further source of stiffness is related to the interaction of differential and algebraic equations. An algebraic relation e.g. $a = b/c$ can equivalently be expressed as a differential equation $\epsilon\, \mathrm{d}a/\mathrm{d}t = b/c - a$, where ϵ is an infinitesimally small time constant. Such coexistence of very small and large time constants in the same system is a characteristic of stiffness. Additionally, special caution is required for an accurate choice of initial conditions.

Table 6.1: *Physical constants*

Physical property	Value	Unit
Gravity acceleration g	9.8	$\mathrm{m\,s^{-2}}$
Density of ice ρ_i	900	$\mathrm{kg\,m^{-3}}$
Density of water ρ_w	1000	$\mathrm{kg\,m^{-3}}$
Latent heat of melting L_f	333.5	$\mathrm{kJ\,kg^{-1}}$
Pressure melting coefficient c_t	-7.4×10^{-8}	$\mathrm{K\,J^{-1}\,m^3}$
Specific heat of water c_w	4.22×10^3	$\mathrm{J\,kg^{-1}\,K^{-1}}$

A physically implausible initial state is very likely to cause a prompt failure of the numerical integration. Here, we assumed that the system is initially in steady-state. In most applications, we used the boundary condition $h = 0$ for $x = 0$ in accordance with the observation that the water is leaving Unteraargletscher at atmospheric pressure. Then, the initial conditions for A_i and h_i can be calculated using the analytical solution for a stationary discharge through a R-channel as derived by Röthlisberger (1972).

6.5   Behavior of the model

6.5.1   Validation of steady-state profile

In a first application we examine the performance of our model and possible constraints for its spatial discretization. Röthlisberger (1972) derived an analytical solution for his steady-state theory by assuming stationary discharge in a horizontal conduit beneath ice of uniform thickness. By balancing the rates of melt-enlargement and creep-closure of an horizontal conduit, he obtained an expression for the hydraulic head gradient (Röthlisberger, 1972, equation (8)), which in our notation corresponds to

$$\frac{\mathrm{d}h}{\mathrm{d}x} = 2AB\frac{L_\mathrm{f}\rho_\mathrm{i}}{(1-\gamma)}Q^{-1}(\rho_\mathrm{w}g)^{n-1}\left(\frac{h^* - h}{n}\right)^n. \tag{6.24}$$

However, he used the Manning-Gaukler-Strickler formula (Equation (6.11)) to eliminate A whereas we adopted the Darcy-Weisbach relation (Equation (6.9)). We repeated Röthlisberger's derivation to obtain the corresponding steady-state solution

$$h(x) = h^* - \left(\left(2\pi B^5\left(\frac{L_\mathrm{f}\rho_\mathrm{i}}{1-\gamma}\right)^5(\rho_\mathrm{w}gn)^{7-5n}\frac{f^2}{g^2}Q^{-1}\right)^{\frac{1}{7}}\frac{5n-7}{7}x + h^{*\frac{7-5n}{7}}\right)^{\frac{7}{7-5n}}. \tag{6.25}$$

This expression was used to validate the model performance. The physical constants used in the computations are listed in Table 6.1. Further, it is assumed that the friction factor f as well as the material properties of ice, expressed as n and B, are constant along the conduit. Values used for these model parameters are presented in Table 6.2. Flow law parameters were adopted from Nye (1953) and the choice for f follows Spring and Hutter (1982). The value of k was determined by trial and error to achieve agreement of Röthlisberger's solution with our steady-state solution (Equation (6.25)). The values of f and k are within the narrow range of roughness coefficients which were determined for subglacial conduits by other authors (Nye,

Table 6.2: *Model parameters*

Parameter	Value	Unit
Friction factor f	0.5	-
Roughness coefficient k	15	$\mathrm{m^{1/3}\,s^{-1}}$
Flow law exponent n	3	-
Flow law coefficient B	5.3×10^{-24}	$\mathrm{Pa^{-3}\,s^{-1}}$

1976; Clarke, 1982; Spring and Hutter, 1982; Ng, 1998). Nevertheless, this roughness value is very high and by intuition one would expect an ice-walled conduit to be much smoother. This argument will be discussed in detail later (Sec. 6.8.2).
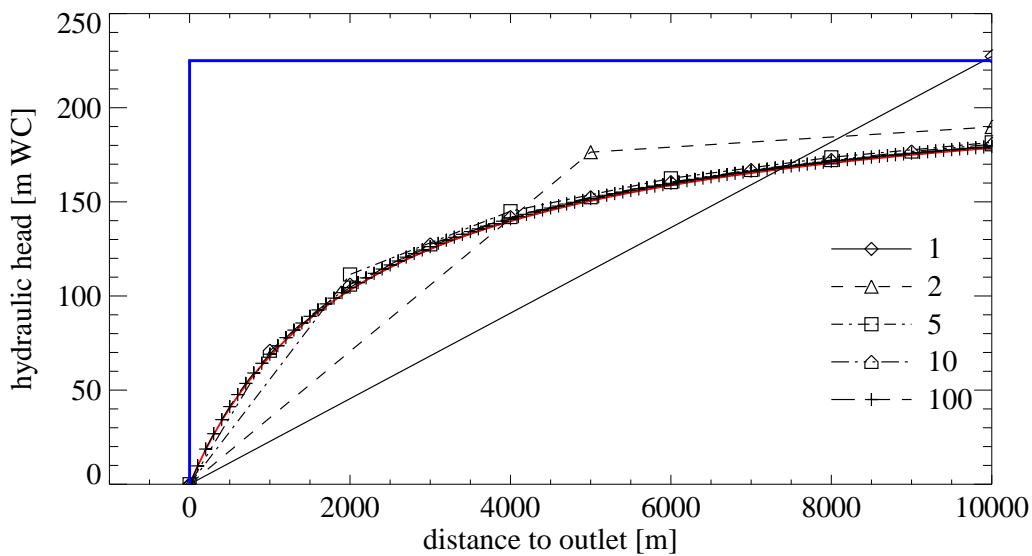

Figure 6.4: *Calculated pressure profiles of a 10 km long, horizontal conduit for different spatial resolution. The legend indicates the number of elements into which the conduit was subdivided. The red solid line represents Equation (6.25) and the thick line illustrates the ice-overburden h^*.*

We calculated simulations for a constant discharge $Q = 1\,\mathrm{m^3\,s^{-1}}$ through a $10\,\mathrm{km}$ long, horizontal conduit which is completely pressurized. The conduit is subjected to an uniform ice-overburden pressure $h^* = 225\,\mathrm{m}$ equivalent to an ice-thickness of $250\,\mathrm{m}$. In five different scenarios the conduit was represented by a linear arrangement of 1, 2, 5, 10 and 100 R_R-resistors, each having a length Δx of 10, 5, 2, 1 and $0.1\,\mathrm{km}$, respectively. The simulations were started from an uniform distribution of $A = 1\,\mathrm{m^2}$ along the conduit. Initial values of h were then calculated for this geometry and the given value of Q. Subsequently, the model was run to steady-state, which was defined to be reached when changes in the h-results were smaller than $10^{-4}\,\mathrm{m}$.

Figure 6.4 illustrates the pressure distributions along the conduit which are calculated at different spatial resolutions. They are compared to the steady-state pressure profile as calculated by the analytical solution (Equation (6.25)). This function is a hyperbola with $h = h^*$ as asymptote which is approached in up-glacier direction. However, in our example, it reaches approximately $180\,\mathrm{m}$, $45\,\mathrm{m}$ below h^*. Differences between the modeled curves and the analytical function are

systematically positive. In general, the accuracy of the model increases with increasing spatial resolution. When the conduit is represented by a single, $10\,\mathrm{km}$ long resistor, the water pressure 10 km from the outlet approaches the ice-overburden pressure, thereby exceeding the steady-state value by about $45\,\mathrm{m}$. The values calculated by the two-resistor scenario deviate by $\sim 10-15\,\mathrm{m}$ whereas a Δx of $2\,\mathrm{km}$ reproduces the analytical solution well. A choice of less than $1\,\mathrm{km}$ for Δx appears to be appropriate to mirror the analytically derived steady-state profile.

6.5.2 Response to discharge variations of different periods

Further simulations were undertaken with the same model geometry, representing a horizontal conduit under a uniformly thick glacier. The $5\,\mathrm{km}$ long conduit was subdivided into 50 R_{R}-resistors of $0.1\,\mathrm{km}$ length each. Now, we focused on the time-dependent pressure response when the conduit was exposed to a sinusoidal discharge function $Q(t)$:

$$Q(t) = \frac{Q_{\mathrm{up}} - Q_{\mathrm{low}}}{2}\left(-\cos(\omega t)\right) + \frac{Q_{\mathrm{up}} + Q_{\mathrm{low}}}{2}, \qquad (6.26)$$

where $\omega = 2\pi/T$ denotes the angular velocity corresponding to the period T. The limits Q_{up} and Q_{low} were chosen such that $Q(t)$ describes a sine between 1 and $6\,\mathrm{m^3\,s^{-1}}$.

Probably the most essential statement of Röthlisberger's steady-state theory is the prediction of an inverse relationship between discharge and pressure (cf. Equation (6.25)). In contrast, for flow through a rigid pipe, the relationship would be a direct one (Equation (6.9)). Consequently, the behavior of a R-channel would be somewhere between these two end members, depending on the state to which the conduit has developed and how close this state is from equilibrium conditions. To illuminate the phase-relationship between $Q(t)$ and $h(t)$, we have produced a set of eight scenarios by adopting the values $1, 2, 5, 10, 25, 50, 100$ and $500\,\mathrm{d}$ for the period T of the discharge variation $Q(t)$.

Figure 6.5 presents three examples of the resulting $h(t)$-variations in response to a sinusoidal $Q(t)$-input with different periods. To illustrate the course of $h(t)$, we present the pressure calculated for the location at $5\,\mathrm{km}$ distance from the terminus. Therefore, the absolute values at any other point in the conduit differ from those presented here. However, the temporal behavior is identical at any arbitrary distance.

The strong dependence of the $h(t)$-variations on the period T is evident. For $T = 1\,\mathrm{d}$, the variations of discharge and pressure are almost in phase, whereas for $T = 10\,\mathrm{d}$ and $T = 100\,\mathrm{d}$ the phase shift between peak discharge and maximum pressure increases to 0.4π and 0.67π, respectively.

The pressure regimes of these three scenarios differ substantially from each other. In the $T = 1\,\mathrm{d}$ case, the h-curve is almost symmetrical whereas with increasing T the shape becomes more asymmetrical such that in the $T = 100\,\mathrm{d}$-scenario, the curve is characterized by a steep rise and a gently declining tail. Similarly, the magnitude of the h-variation is dependent on T as well. To drive the diurnally cycling discharge in our example through the conduit, a hydraulic head ranging between 12 and $422\,\mathrm{m}$ is required. At longer periods, the minimum pressure increases simultaneously with a reduction of the maximum such that the amplitude decreases.

Furthermore, Figure 6.5 presents also the evolution of the cross-sectional area A at $5\,\mathrm{km}$ distance from the terminus for the three considered cases. In the $T = 1\,\mathrm{d}$-scenario, A varies
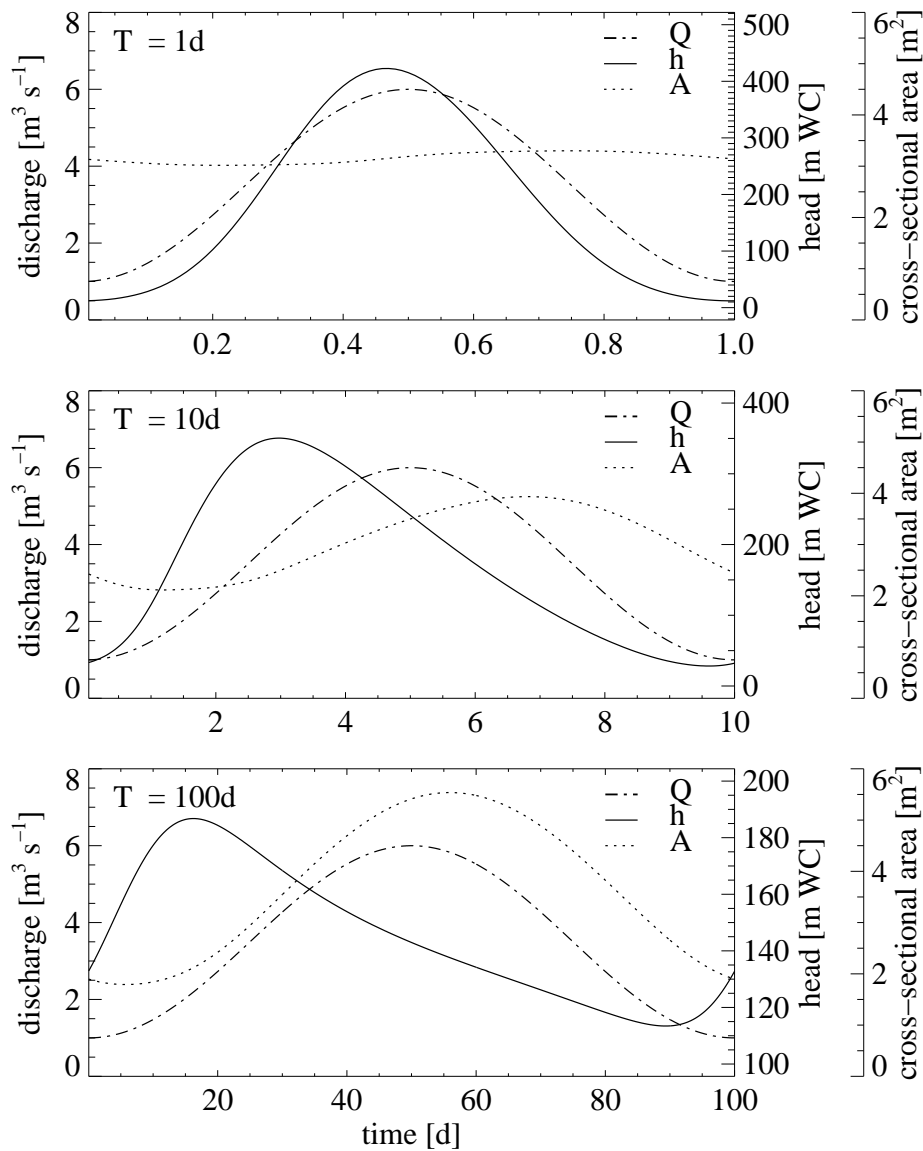
Figure 6.5: *Variations of pressure h (dashed) in a R-channel at 5 km distance from the terminus in response to a sinusoidal discharge input Q (dashed). The corresponding evolution of the cross-sectional area A is shown by the dotted line. The periods of the discharge function are 1 day (top), 10 days (center) and 100 days (bottom). Note that the pressure-axes are scaled differently.*

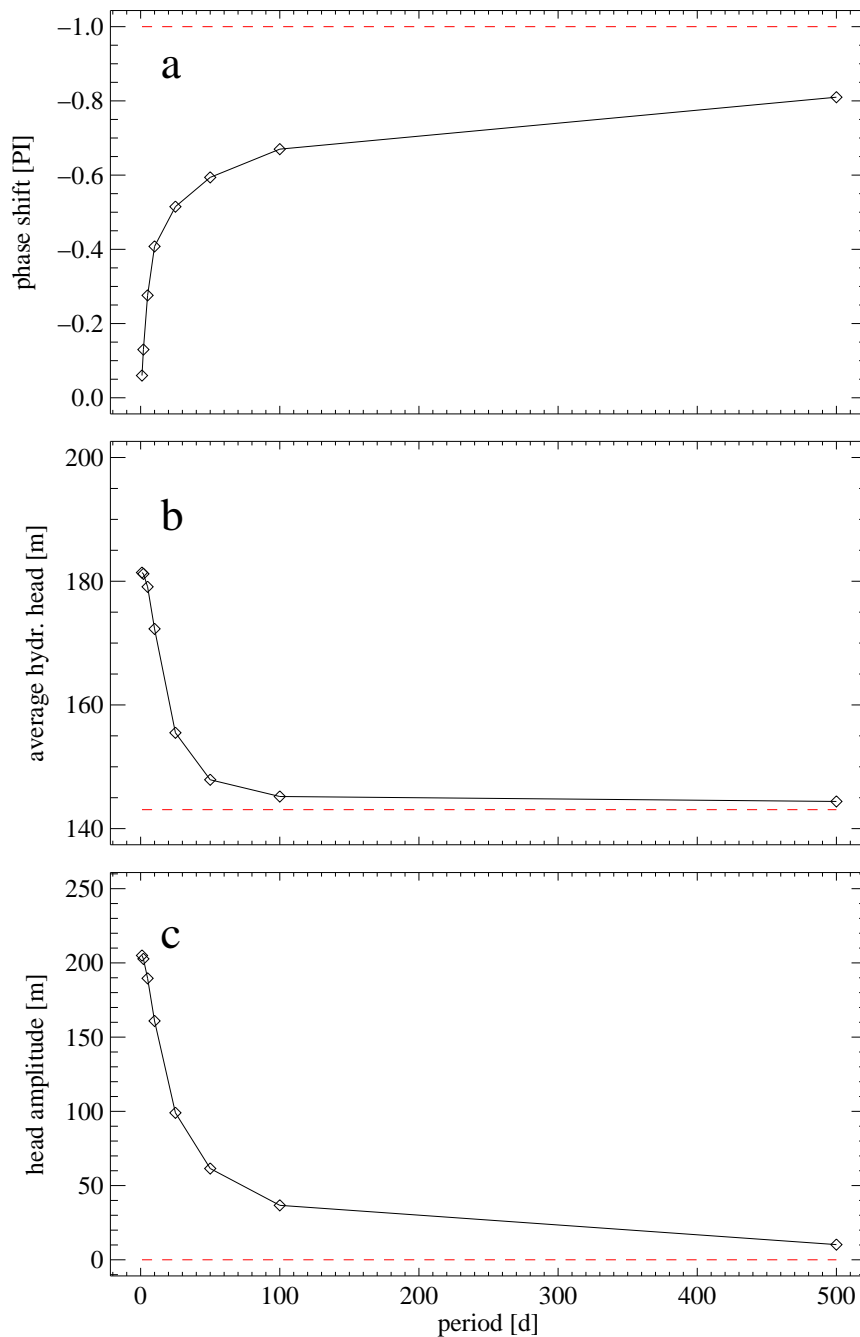Figure 6.6: *(a) Phase shift between maximum pressure at the upper end of the conduit and peak discharge as a function of the return period T. Values on the y-axis are expressed as multiples of π. (b) The hydraulic head at the same location averaged over the period as a function of T. (c) The amplitudes of the hydraulic head variation as a function of T. The dashed line represents the prediction of the steady-state theory.*

only slightly around a value of roughly $3\,\mathrm{m}^2$ and the variation follows the course of Q with a phase-shift of 0.5π. Towards longer periods of the Q-regime, the amplitude of the A-variation increases while the time lag by which it follows Q, decreases. As such, for $T = 10\,\mathrm{d}$, A varies with an amplitude of $\sim0.9\,\mathrm{m}^2$ and a phase-shift of 0.4π with respect to Q, while for $T = 100\,\mathrm{d}$, the corresponding values are $1.87\,\mathrm{m}^2$ and 0.1π, respectively.

This unequal evolution of the cross-sectional area for different periods of the discharge variation is responsible for the observed hydraulic head regime. Whereas for fast Q-variations, the conduit size cannot respond fast enough to reach a steady-state, a slowly changing discharge permits almost complete adjustment of the conduit cross-section to prevailing hydraulic conditions.

These findings are illustrated in Figures 6.6a–c where the phase shift, average pressure and pressure amplitude are presented as a function of the period T. Further, we compare these results with the values obtained from applying Equation (6.25) to the average discharge input.

Figure 6.6a shows how the phase shift increases with T. As mentioned, for small values of T, the phase shift is close to zero but increases quickly such that a value of 0.5π is reached at $T \approx 20\,\mathrm{d}$. However, the anti-phase behavior predicted by the steady state theory is not reached in our scenarios not even for $T = 500\,\mathrm{d}$.

The pressures averaged over the period (Fig. 6.6b) decrease quickly from about $180\,\mathrm{m}$ at $T = 1\,\mathrm{d}$ to approximately $145\,\mathrm{m}$ at $T = 100\,\mathrm{d}$ close to the steady-state value of $143\,\mathrm{m}$. For $T > 100\,\mathrm{d}$, the decline is very weak.

A similar picture emerges for the magnitudes of the pressure amplitude (Fig. 6.6c). From $T = 1\,\mathrm{d}$ to $T = 100\,\mathrm{d}$, the amplitude reduces by a factor of five. The decline attenuates towards longer periods and approaches the steady-state value at $T \approx 500\,\mathrm{d}$.

6.6 Model applications

6.6.1 Variations of velocity in a subglacial channel

To test the hypothesis, that changes of the conduit size can account for the observed vQ-hysteresis (Sec. 5.4.3), we applied the model to a geometry representing Unteraargletscher. With several distinct model scenarios we attempted to simulate situations as observed in the field.

The straight-line distance from the moulin where the tracer was injected to the glacier terminus where it was detected is approximately $4.5\,\mathrm{km}$. We assume, that the water is transfered from the surface directly into a main R-channel which carries the bulk of runoff from Unteraargletscher to the glacier portal. Further, it is assumed that this conduit follows the thalweg of the glacier bed. The conduit has then a length of approximately $5\,\mathrm{km}$.

In our calculation, the conduit was represented by a linear arrangement of 100 R_{R}-resistors of $50\,\mathrm{m}$ length each. The glacier geometry was imported into the model by adopting local values of the bed slope $\Delta z/\Delta x$ and the ice-overburden h^*. Since the glacier bed below the tongue of Unteraargletscher is steadily inclined, a single, constant value of $\Delta z/\Delta x = 0.012$
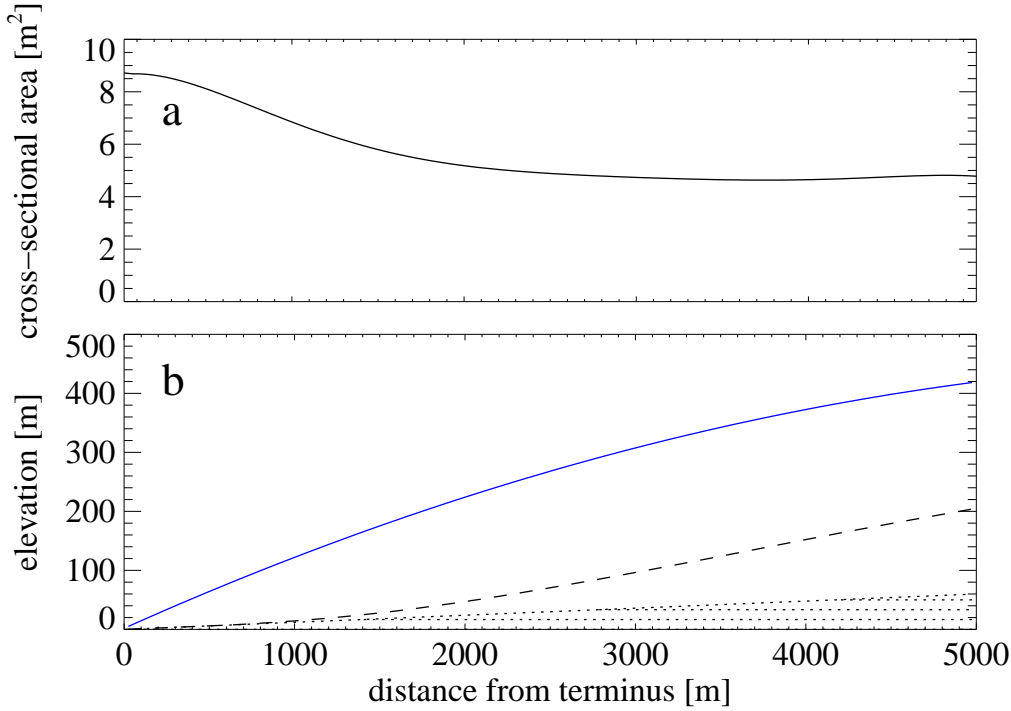
Figure 6.7: *(a) Longitudinal profile of conduit cross-sectional area determined for the Unter-aargletscher geometry and a constant discharge $Q = 10.75 \, \mathrm{m^3 \, s^{-1}}$. (b) Longitudinal profiles of steady-state water pressure (dashed), the glacier bed (dotted) and the overburden-pressure exerted by the ice (solid).*

was estimated from Figure 1.2. In a similar way, a profile of ice-thickness along the centerline of Unteraargletscher was derived and represented by a parabolic function:

$$h^*(x) = -8.44 \times 10^{-6} x^2 + 0.1082x - 1.07. \tag{6.27}$$

To study the behavior of such a conduit under typical drainage conditions, diurnal discharge cycles were prescribed by a sine function varying between 9 and $12.5 \, \mathrm{m^3 \, s^{-1}}$. As initial condition for the conduit cross-sectional area, the steady-state geometry for a constant average discharge, $Q = 10.75 \, \mathrm{m^3 \, s^{-1}}$ was derived similar as described in Section 6.5.1. The longitudinal profile of this steady-state geometry is shown in Figure 6.7a. In the upper part of the conduit, the cross-sectional area is about $5 \, \mathrm{m^2}$ but increases up to $\sim 8 \, \mathrm{m}$ towards the terminus where the glacier thins out, thereby reducing the closure rate. Figure 6.7b illustrates the distribution of bed elevation and ice overburden-pressure which were used in our calculations as well as the distribution of steady-state water pressure in the conduit which served to start the calculations.

Subsequently, we calculated variations of pressure and velocity along the channel. Therefore we implemented two fundamentally different approaches. In a first scenario, we considered a conduit with a static cross-sectional geometry as employed e.g. by Fountain (1993) and Kohler (1995) for a comparable purpose. In the remainder of this study, this channel geometry will be referred to as the "rigid pipe". Implementation of this pipe into the model was achieved by describing the equations for a corresponding resistor R_P. This requires only minor changes of the expressions described above. Since we consider identical mechanisms of water flow, the Equations (6.22-a, b) remain unchanged and the static nature of the pipe is accounted for by removing the differential equation expressing the evolution of the conduit size A (Equations (6.23-a, b)).
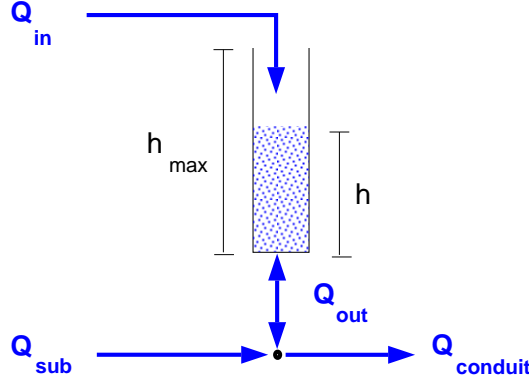
Figure 6.8: *Sketch of the moulin-model configuration.*

The second scenario was performed considering the full complexity of the model as described by the system of Equations (6.22) and (6.23). In this case, water flows through an inclined R-channel whose geometry adjusts to hydraulic conditions by the counteracting processes of melt-enlargement and creep-closure (Röthlisberger, 1972; Nye, 1976).

Further, the flow regime in both scenarios is hybrid. That means that both pressurized as well as open-channel flow occurs, depending on whether the discharge of water is sufficient to fill the conduit cross-section or not. This switching condition is examined by Equation (6.12).

6.6.2 Retardation in a tributary moulin

Retardation of water in a tributary due to inflow modulation at the junction to a main conduit could provide an alternative possibility to explain the observed vQ-hysteresis (Sec. 5.4.3). Using an appropriate model, we would like to test whether the proposed mechanism could explain the observed vQ-hysteresis.

We recall that in our tracer experiments, the dye was injected into a supraglacial stream at its entrance into a moulin. A moulin that joins a major conduit might act as a piezometer reflecting thereby the water pressure in the conduit. To consider the transit of a tracer through the combined moulin-conduit system, we describe this situation by a moulin at a certain distance from the terminus which connects subglacially into a conduit (Fig. 5.17).

Now we review this mechanism to derive an adequate formulation of the model. Figure 6.8 illustrates the configuration of the model and its individual components. Where a moulin joins a pressurized channel carrying a subglacial discharge Q_{sub}, water backs up in the moulin to a certain hydraulic head h_{moulin}. This hydraulic head determines the discharge $Q_{conduit}$ which is routed through the conduit having a resistance $R_{conduit}$ and hence $Q_{conduit} = h_{moulin}/R_{conduit}$. The water to build up h_{moulin} is obtained from the surface input into the moulin Q_{in} and partly from upwelling of excess discharge of Q_{sub} which cannot be driven through $R_{conduit}$. Considering the water balance of the moulin, we can derive the following equation to describe the temporal evolution of h_{moulin}:

$$\frac{\mathrm{d}h_{moulin}}{\mathrm{d}t} = \begin{cases} 0 & : & h_{moulin} \geq h_{max}, Q_{in} \geq Q_{out} \\ 0 & : & h_{moulin} \leq 0, Q_{in} \leq Q_{out} \\ \frac{Q_{in}-Q_{out}}{A_{moulin}} & : & \text{otherwise,} \end{cases} \qquad (6.28)$$

where $Q_{\mathrm{out}} = Q_{\mathrm{conduit}} - Q_{\mathrm{sub}}$. The maximum storage volume of the moulin is expressed by the height h_{max} and the cross-sectional area A_{moulin} and represents an upper constraint for h_{moulin}. If Q_{in}, Q_{sub} and the initial downstream geometry of the conduit are prescribed, the scenario can be simulated by treating h_{moulin} as a boundary condition at the upper end of the conduit and solving the system of equations in downstream direction. The conduit resistance is calculated as described above by Equations (6.22) and (6.23).

To determine the residence time of a tracer in the moulin, we consider the water level h_{moulin} at the time of "tracer injection" as the vertical position of the tracer $z_{\mathrm{tracer}} = z_{\mathrm{bottom}} + h_{\mathrm{moulin}}$. We calculate the velocity by which the tracer layer is lowered

$$\frac{\mathrm{d}z_{\mathrm{tracer}}}{\mathrm{d}t} = \frac{Q_{\mathrm{out}}}{A_{\mathrm{moulin}}} \tag{6.29}$$

until it reaches the bottom of the moulin ($z_{\mathrm{tracer}} = z_{\mathrm{bottom}}$), from where it is routed through the conduit.

In our scenarios, A_{moulin} is small enough such that Q_{sub} can fill the moulin volume within one time step. In this case, the moulin acts exactly like a piezometer and its delaying influence on the total discharge Q_{conduit} is negligible. For such stationary conditions, $Q_{\mathrm{out}} \approx Q_{\mathrm{in}}$. In the formulation of Equation (6.28), any head losses in the moulin or at its junction to the conduit are neglected. By using $0.5\,\mathrm{m^3\,s^{-1}}$ as a maximum estimate for Q_{in} (compare Tab. 5.2) and a minimum guess $A_{\mathrm{moulin}} = 0.1\,\mathrm{m^2}$, we obtain an estimate for the maximum velocity $v = 5\,\mathrm{m\,s^{-1}}$ by which the water would descend in the moulin. The corresponding loss of hydraulic head $\Delta h = v^2/2g$ is $1.25\,\mathrm{m}$, and we will see later (Sec. 6.7.2) that this value is less than 1% of a typical value of h_{moulin} and therefore, its omission does not affect our results significantly.

In our calculations, we assume that the moulin extends to the glacier bed, thus, $h_{\mathrm{max}} = h_{\mathrm{i}}$, the local ice-thickness. The calculations were started from a steady-state which was derived as in preceding scenarios. The corresponding steady-state value of hydraulic head at the junction of moulin and conduit was used as an initial value for h_{moulin}.

To investigate the influence of such a moulin system on the transit velocity of a tracer, the model was used to generate a number of scenarios by varying A_{moulin}. The transit time of a tracer parcel through the water column h_{moulin} is then determined by the volume of stored water $A_{\mathrm{moulin}}\, h_{\mathrm{moulin}}$ and Q_{out}.

The dynamic geometry of a R-channel might already produce vQ-hysteresis as suspected above (Sec. 5.4.3). In a combined moulin-R-channel model, the effect of the dynamic conduit geometry might interfere with that of inflow modulation, thereby complicating the determination of the retardation-effect. Since our aim is to examine the ability of inflow modulation to cause vQ-hysteresis, we use a moulin-pipe model, considering a static geometry for the conduit downstream of the moulin.

Further, a supraglacial discharge entering the moulin Q_{in} had to be defined. For this purpose, a sine function was adopted which varies on a diurnal time scale between 0.14 and $0.36\,\mathrm{m^3\,s^{-1}}$ and is shifted in phase by $0.1\,\mathrm{d}$ with respect to the discharge variations in the main conduit. Q_{sub} ranges from 9 to $12.5\,\mathrm{m^3\,s^{-1}}$, identical to the discharge described in Section 6.6.1. Besides these modifications, the model parameters were kept the same as for the previous simulations (Sec. 6.6.1). In eight scenarios, A_{moulin} was varied from 0.05 to $0.1, 0.25, 0.5, 1.0, 2.5, 5.0$ and $10.0\,\mathrm{m^2}$. The same situation but without moulin is considered as a reference, thus $A_{\mathrm{moulin}} = 0$. The depth of the moulin is $h_{\mathrm{max}} = 350\,\mathrm{m}$ at $5\,\mathrm{km}$ distance from the glacier terminus.

6.7 Results

6.7.1 Variations of velocity in a subglacial channel

Rigid pipe

The transit velocity as determined by a tracer test represents an average over the length of the flowpath. Similarly, we have calculated average values of modeled velocities along the pipe for each time step. Figure 6.9a illustrates the phase relations between discharge Q, mean velocity v and hydraulic head h for water flowing through a rigid pipe with dimensions shown in Figure 6.7. Pressure head h and cross-sectional area A are those calculated at a distance of $5\,\mathrm{km}$ from the terminus. The hydraulic head in response to the applied discharge varies sinusoidally between ~ 85 and $\sim 215\,\mathrm{m}$ and is exactly in phase with Q. This behavior is expected when we bear in mind the static geometry of the pipe. Since v is derived from Q, h and A, it follows the course of Q (and that of h) since A remains constant. The resulting velocity ranges from approximately $1.75\,\mathrm{m\,s^{-1}}$ during the discharge minimum to $2.2\,\mathrm{m\,s^{-1}}$ at peak discharge.

The distributions of hydraulic potential along the pipe in response to the discharge variations are presented in Figure 6.9b. Along a pipe of constant cross-section, the hydraulic head would decrease linearly from the upper end of the pipe to zero at the point where the flow regime switches to open-channel flow. However, since we considered a pipe with diameter that increases towards the glacier terminus (Fig. 6.7), the resulting pressure distribution is not linear. In the upper part of the pipe the head loss is approximately linear but it gradually approaches the shallower bed gradient in the lower part where open-channel flow occurs. During peak discharge, open-channel flow occurs in the lowermost $200\,\mathrm{m}$ of the pipe while it extends to the lowermost $1000\,\mathrm{m}$ during minimal discharge.

The resulting velocity profiles underline the hybrid nature of the flow regime (Fig. 6.9c). In the freely draining lower part of the pipe, the velocity depends mainly on the bed slope and only weakly on the hydraulic radius (Equation (6.11)). Therefore, v is almost constant. A noticeable jump marks the transition to pressurized flow. The transition from open-channel to pressurized flow occurs not steadily but the water level in a partly filled conduit cross-section switches suddenly to complete filling when the critical discharge Q_{max} is reached (Fig. 6.2). As such, the cross-sectional area which is occupied by water A_{w} is suddenly increased and considering the same discharge, continuity requires that the velocity drops at the transition. Where the water flow is pressurized, the velocity reflects directly the pressure gradient. Hence, initially, values increase steeply. Subsequently, the rise weakens gradually until a maximum is reached at approximately $3.8\,\mathrm{km}$ from the glacier terminus. From there, the velocity decreases slightly to reach a constant value. The differences between maximum and minimum velocities at a given site scale with the diurnal amplitude of hydraulic head and range from $\sim 0.1\,\mathrm{m\,s^{-1}}$ at the outlet to $\sim 0.7\,\mathrm{m\,s^{-1}}$ at $5\,\mathrm{km}$ distance from the terminus.

In consequence of the fact that velocity varies exactly in phase with discharge through a rigid pipe, the velocity-discharge relationship shown in Figure 6.10 is univocal. Since we considered a hybrid system where pressurized as well as open-channel flow occurred, the resulting vQ-curve is slightly bent but this effect is almost not perceptible here. The appearance of the curve in terms of slope and curvature is determined by the cross-sectional size of the drainage system and the partitioning between distinct types of flow (Fountain, 1993; Kohler, 1995). However, since drainage through a rigid pipe cannot account for the observed vQ-hysteresis, we do not further pursue this drainage configuration.
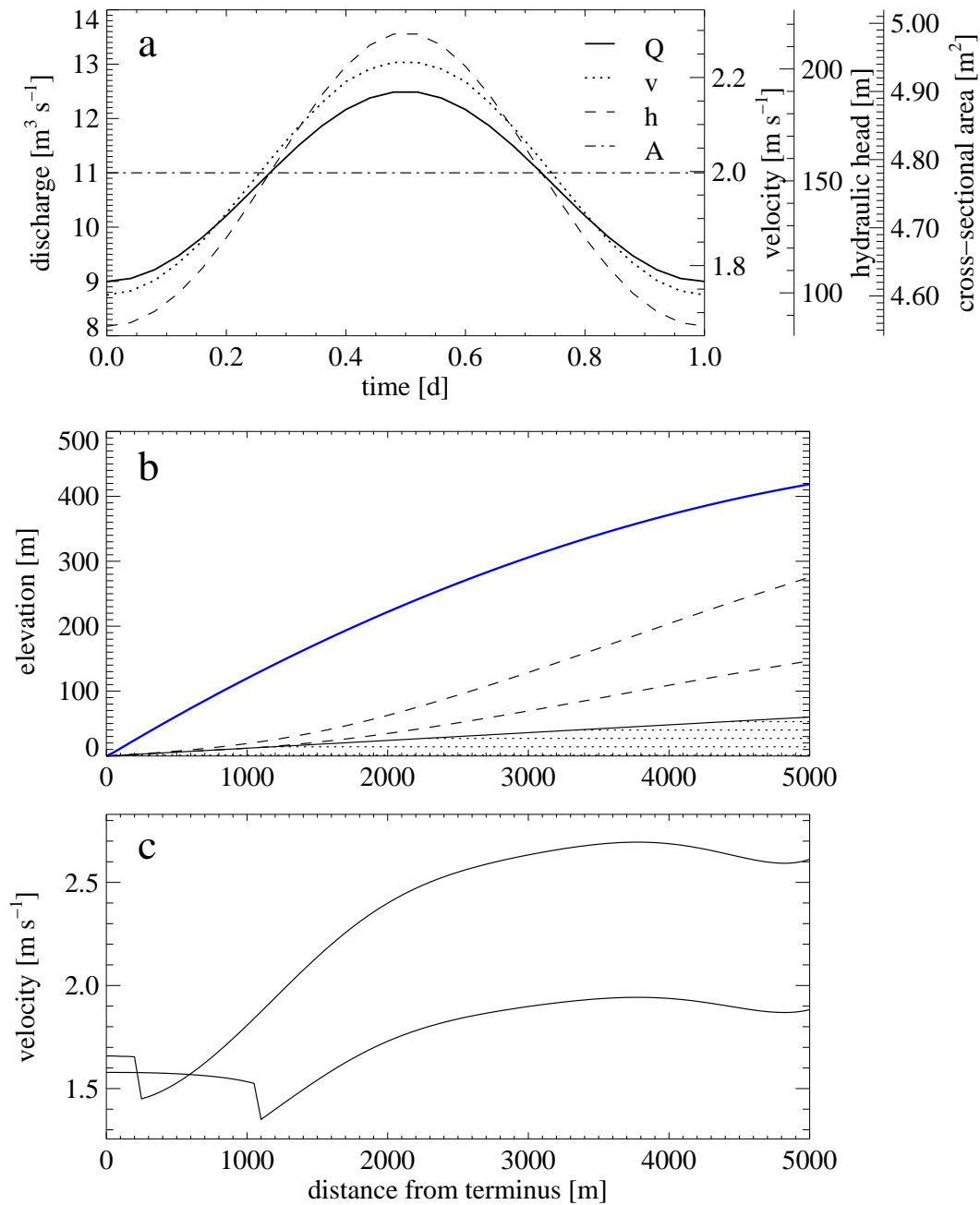
Figure 6.9: *(a) Diurnal cycles of discharge Q, mean flow velocity v, hydraulic head h and cross-sectional area A calculated for a rigid pipe. The plot shows h and A at a distance of 5 km from the terminus. (b) Longitudinal profiles of glacier bed (shaded), glacier surface (solid) and hydraulic potential (dashed). The range of hydraulic potential is illustrated by the profiles at maximum (upper profile) and minimum (lower profile) discharge. (c) Distribution of flow velocity along the rigid pipe. The two situations correspond to maximum (upper profile) and minimum (lower profile) discharge.*
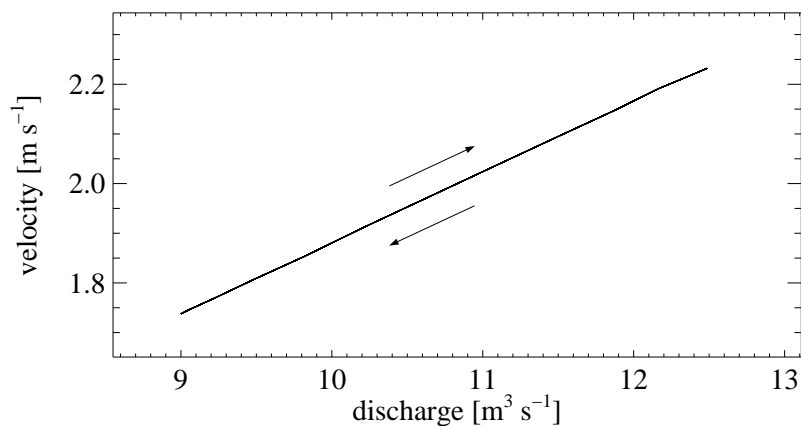
Figure 6.10: *Velocity-discharge relationship derived from modeled drainage through a rigid pipe.*

R-channel

Results obtained from modeling drainage through an inclined, hybrid R-channel are presented in the same way as for the previous scenario. Figure 6.11 shows phase relations between individual variables and distributions of both the hydraulic potential and the resulting flow velocity along the conduit. In general, findings are similar in shape and magnitude to those of the first scenario. However, the key differences arise from the dynamic nature of the conduit cross-section. Figure 6.11a illustrates the variation of the cross-sectional area A around the steady-state size of $\sim4.8\,\text{m}$. The evolution of the cross-sectional area A responds to the discharge cycle with a delay of $\sim6\,\text{h}$. This time lag causes also a phase shift between Q and h. During rising discharge, the conduit cross-section is smaller than at the falling limb of Q and thus, a lower hydraulic head is required to drive the same discharge. Therefore, maximum pressure precedes peak discharge by about $1.2\,\text{h}$ causing thereby also a comparable phase shift between velocity and discharge. The pressure distributions along the channel in Figure 6.11b resemble very much those produced by the rigid pipe model except that the freely draining fraction of the conduit is slightly longer (up to $1350\,\text{m}$). This is also the reason for the minor discrepancies between the velocity profiles in Figures 6.11c and 6.9c.

Based on the described interdependencies of Q, A and h, we understand that the resulting vQ-relationship exhibits a hysteresis in clockwise direction. As such, the transit velocity is higher when discharge is rising than on the falling limb (Fig. 6.12).

In this scenario we have thus far simulated a discharge situation which is similar to that observed during the August experiment (Fig. 5.2a). To simulate variations of velocity due to a discharge variation corresponding to the discharge situation during the September experiment (Fig. 5.2b), we adopted a discharge varying sinusoidally about a linearly increasing trend.

Results of the simulations are illustrated in Figure 6.13. The phase-relationship between discharge and pressure remains the same as in the August situation (Fig. 6.11). The magnitude and evolution of the conduit size is different in the two situations. These differences are related to the unequal amount and regime of discharge in the two scenarios. A further consequence is the higher level of pressure head which is required to drive the larger discharge in September.
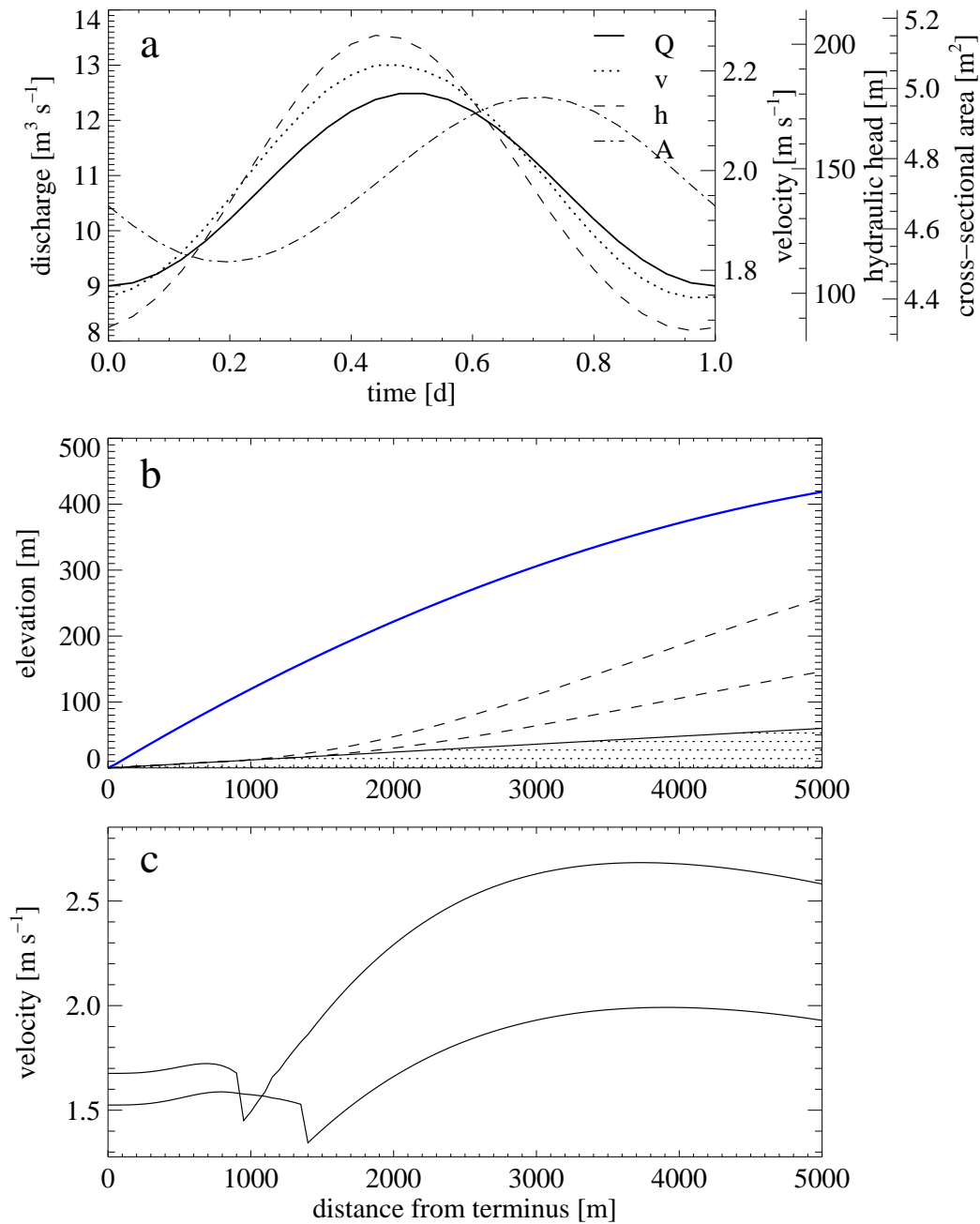
Figure 6.11: *(a) Diurnal cycles of discharge Q, mean flow velocity v, hydraulic head h and cross-sectional area A calculated for a R-channel. The plot shows h and A at a distance of 5 km from the terminus. (b) Longitudinal profiles of glacier bed (shaded), glacier surface (solid) and hydraulic potential (dashed). The range of hydraulic potential is illustrated by the profiles at maximum (upper profile) and minimum (lower profile) discharge. (c) Distribution of flow velocity along the R-channel. The two situations correspond to maximum (upper profile) and minimum (lower profile) discharge.*
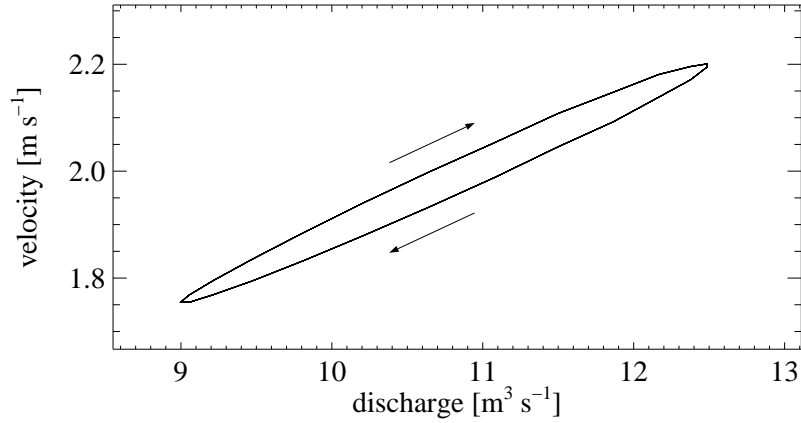
Figure 6.12: *Velocity-discharge relationship derived from drainage through a R-channel.*

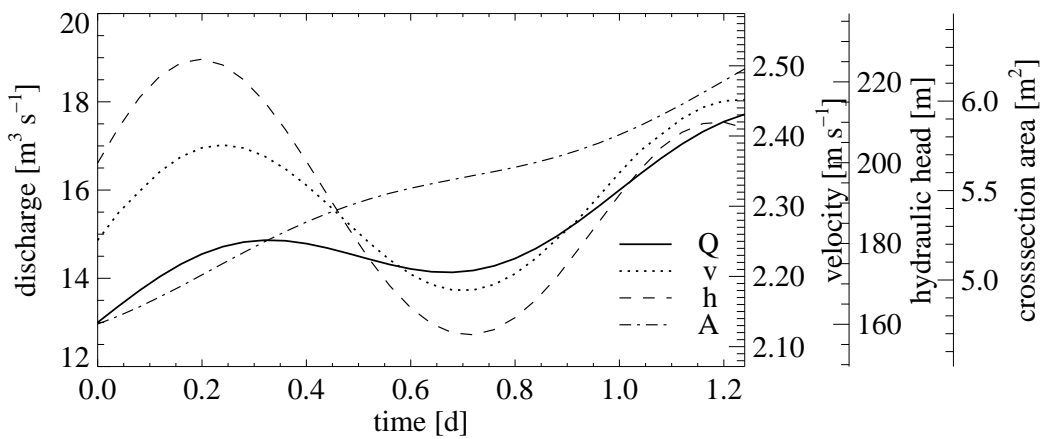

Figure 6.13: *Variations of discharge Q, mean velocity v, hydraulic head h and conduit cross-sectional area A for the September situation. The plot shows h and A at a distance of 5 km from the terminus.*
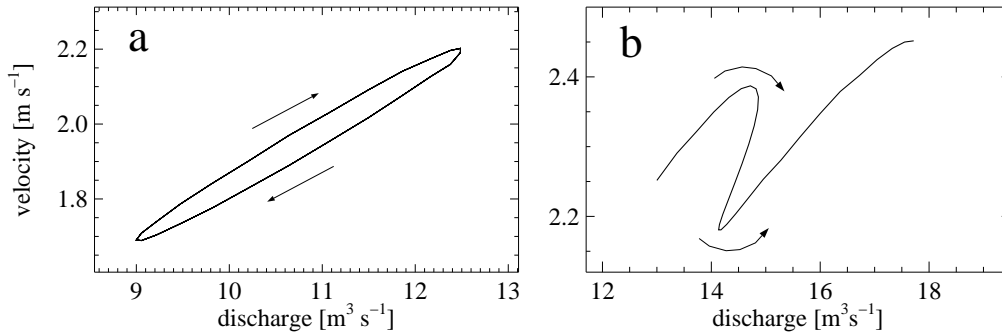
Figure 6.14: *Velocity-discharge relationships derived from scenarios representing the situation during the August (a) and September (b) experiments.*

In summary, the September scenario is dominated by an increase in discharge to which the conduit cross-sectional area A responds. In contrast, the pressure head h shows an inverse evolution and decreases as A increases although Q is rising. The resulting vQ-relationship (Fig. 6.14b) looks very different from the one obtained for the August scenario (Fig. 6.14a). This is attributed to the continuously rising discharge which does not show cyclic behavior. Due to the time lag of $\sim 6\,\mathrm{h}$ of A with respect to Q, the local maximum of A coincides with the slight decline of Q. Consequently, h and therefore v are substantially reduced but rise as soon as discharge increases again. This is expressed in the pronounced V-shape of the vQ-plot in Figure 6.14b.

6.7.2 Retardation in a tributary moulin

Figure 6.15 illustrates the effects of inflow modulation at the junction of a tributary moulin to a main conduit. As shown before, variations of hydraulic head in a rigid pipe follow directly those of discharge (Sec. 6.7.1) and therefore, the hydraulic head h_{moulin} at the junction of moulin and conduit is proportional to Q_{conduit} (Fig. 6.15a).

The supraglacial input into the moulin Q_{in} precedes Q_{sub} by $0.1\,\mathrm{d}$ but due to its small proportion of total discharge Q_{conduit}, the influence of Q_{in} on hydraulic conditions in the main channel is negligible, thus $Q_{\mathrm{conduit}} \approx Q_{\mathrm{sub}}$. However, with increasing size of the moulin cross-sectional area A_{moulin}, the transit velocity through the combined moulin-pipe system changes noticeably in magnitude and timing (Fig. 6.15b). The reduction of transit velocity of an imaginary tracer due to retardation in a moulin with $A_{\mathrm{moulin}} = 0.05\,\mathrm{m}^2$ is only weak, but Figure 6.16a demonstrates that the effect increases with size of the moulin A_{moulin}. At elevated values of h_{moulin} the retardation of tracer is enhanced since the water column in the moulin through which the tracer travels becomes longer. Consequently, the relationship between h_{moulin} and transit velocity develops gradually into a anti-correlation (Fig. 6.16b) and velocity becomes increasingly controlled by the input discharge into the moulin. Furthermore, with an increase of the water volume in the moulin, the diurnal amplitude of transit velocity is significantly attenuated (Fig. 6.16c).

As before with the R-channel model (Sec. 6.7.1), the moulin-pipe model is used to simulate the plumbing of Unteraargletscher during the tracer experiments in August and September 2000. For this purpose, we use the same parameterization of the discharge situations as used above to
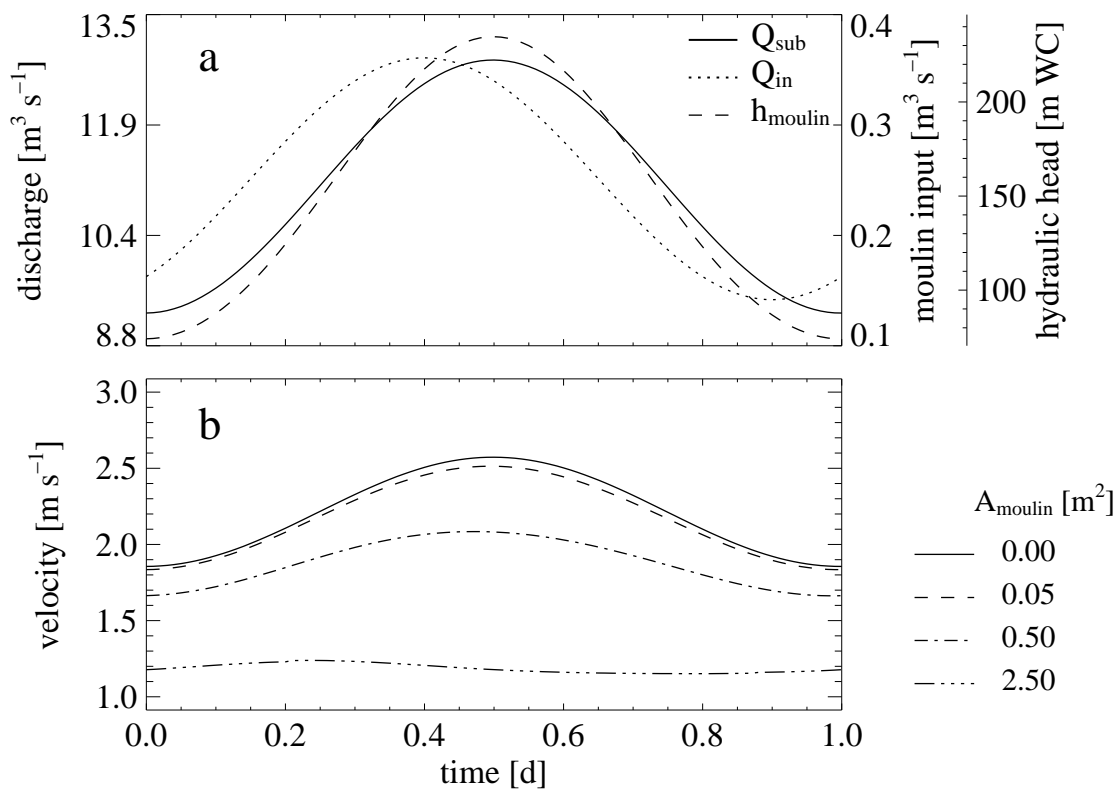
Figure 6.15: *(a) Variation of prescribed discharge in the conduit Q_{sub} (solid), the input into the moulin Q_{in} (dotted) and the hydraulic head h_{moulin} at the junction of moulin and conduit. (b) Comparison of velocity in the main conduit (solid) and transit velocity through the moulin-conduit system for several values of the moulin cross-sectional area A_{moulin}.*

Figure 6.16: *Effects of increasing infbw modulation in a tributary moulin on (a) transit velocity, (b) the phase shift between maximum velocity and peak discharge and (c) the diurnal amplitude of transit velocity. The solid line connecting diamonds represents the value corresponding to a passage through the entire system and the asterisks connected by the dashed line refer to the value in the channel solely.*

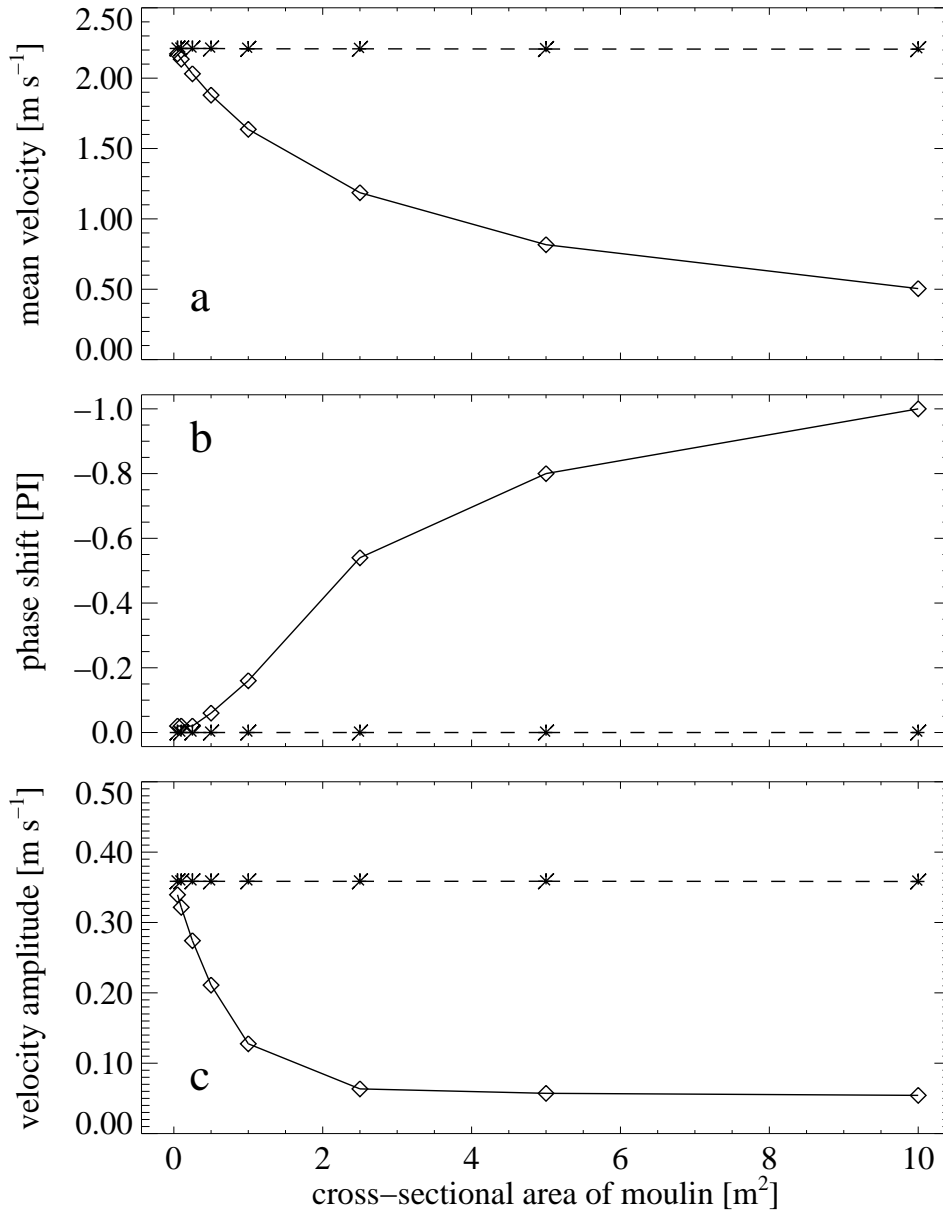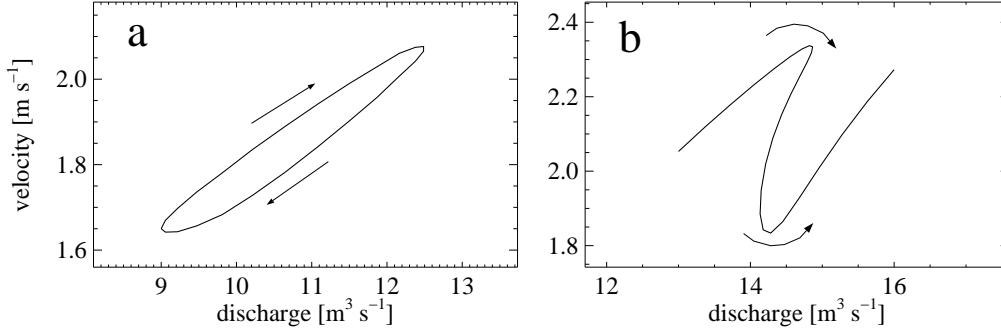Figure 6.17: *Velocity-discharge relationships derived from scenarios representing inflow modulation in a moulin with $A_{\mathrm{moulin}} = 0.25\,\mathrm{m}^2$ during the August (a) and September (b) experiments.*

derive Figure 6.14. Additionally, the input discharge into the moulin Q_{in} is expressed as a sine function reproducing the measured supraglacial discharge (Fig. 5.2). Figure 6.17 illustrates the velocity-discharge relationships obtained from the two scenarios. The size of the moulin cross-section was selected such that the observed vQ-hysteresis is approximately reproduced. In both cases, $A_{\mathrm{m}} = 0.25\,\mathrm{m}^2$ was used. The vQ-relationship of the August scenario displays clockwise hysteresis while that of the September scenario is characterized by a pronounced V-shape. Similar to the results obtained with the R-channel model (Section above), the results obtained with the moulin-pipe model exhibit vQ-hystereses which resemble those observed by the tracer experiments (Fig. 5.14).

6.8 Discussion

In this chapter we have derived a formulation to describe time dependent drainage through a subglacial channel. In a first application, we have investigated the general characteristics of this model and compared them to those derived from an analytical steady-state solution (Röthlisberger, 1972). Further, we analyzed the variations of transit velocity in response to discharge variations similar to those observed in the field (Sec. 5.2.1). Here, our aim was to simulate mechanisms which were supposed to account for the hystereses in observed vQ-relationships (Sec. 5.4.3). Considering the many assumptions which have to be made about an inaccessible environment, we prefer not to tune parameter values to obtain a good match of model results and data. Hence, we focus on elucidating the behavior of a subglacial drainage system rather than on exactly reproducing values of limited reliability.

6.8.1 R-channel model

The results of our analysis of model behavior underline clearly the necessity for a time-dependent model of subglacial water flow. Especially for discharge variations with a period of $T = 1\,\mathrm{d}$, a characteristic feature of glacial discharge, we observe substantial discrepancies between the output of our time-dependent model and the steady-state solution of Röthlisberger (1972). Nevertheless, for discharge variations with long periods, predictions of the model approach those calculated with the steady-state theory (Fig. 6.6). This contrasting behavior at different time scales is caused by the time required for a conduit to adjust its size to changing

hydraulic conditions. For long periods ($T \gg 100\,\mathrm{d}$), the evolution of the conduit cross-section occurs fast enough such that a steady-state is reached, where opening and closure rates are balanced. In contrast, for short periods, the evolution of the conduit size cannot keep up pace with the transient hydraulic conditions and a steady-state is not reached.

In response to the course of melt water production, glacial discharge displays a pronounced diurnal variation which is superimposed to a longterm trend. As seen above, the drainage system does not reach a steady-state at a time scale of one day and a time-dependent model is required to describe water flow through such a system appropriately.

Nevertheless, the use of the steady-state geometry as an initial condition for the conduit size can be justified by the steep gradient of the curves in Figure 6.6 at short periods. This indicates that most of the system adjustment takes place within the first 10 days. Therefore, the assumption that a R-channel has adjusted to a mean discharge at intermediate time scales is acceptable.

6.8.2   Choice of roughness parameters

In Section 6.5.1, we have already stated that the values for f and k which were used to describe the roughness of subglacial conduits (Röthlisberger, 1972; Nye, 1976; Clarke, 1982; Spring and Hutter, 1982; Hooke et al., 1990; Björnsson, 1998; Ng, 1998) are very high while at the same time, by intuition one would expect an ice-walled conduit to be much smoother. Further, we have also discussed that this discrepancy might be a result of our simplifying assumption of a straight conduit (Sec. 6.3.1). We visualize the flowpath as an irregularly meandering subglacial conduit. Since detailed information about the real course of such a conduit is not available, we conceptualize a simple model with one roughness parameter describing any kind of hydraulic head losses. Here, we would like to discuss to what extent physically plausible values for the friction parameter of an ice-walled conduit are consistent with a value comprising local as well as frictional losses.

With reference to Figure 6.18, we can express the total head loss ΔH by using a single loss coefficient ξ (e.g. Hager, 1995)

$$\Delta H = \xi \, \frac{v^2}{2g}, \tag{6.30}$$

where ξ describes the combination of frictional losses in the ice-walled conduit f_i and a number d of local losses ξ_loc

$$\xi = f_\mathrm{i} \, \frac{\Delta x}{4R_\mathrm{h}} + d \, \xi_\mathrm{loc}. \tag{6.31}$$

In our model formulation we lump these losses together into one effective friction factor f. Hence we can write

$$\Delta H = f \, \frac{\Delta x}{4R_\mathrm{h}} \frac{v^2}{2g}. \tag{6.32}$$

Equating this expression with Equation (6.30) and substituting Equation (6.31) yields d, the number of local losses required to explain the high value of f

$$d = (f - f_\mathrm{i}) \, \frac{\Delta x}{4R_\mathrm{h}} \frac{1}{\xi_\mathrm{loc}}. \tag{6.33}$$

By inserting typical values, we can calculate d and assess thereby how the value of our parameter f might be composed. For now, we select $f_\mathrm{i} = 0.01$ ($\simeq k = 100\,\mathrm{m^{1/3}\,s^{-1}}$) and we will
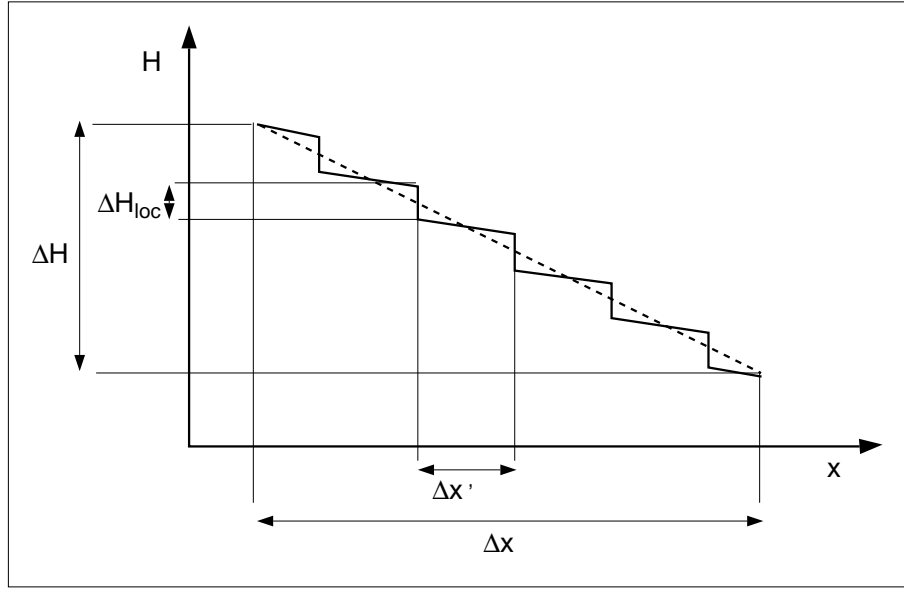
Figure 6.18: *The total hydraulic head loss ΔH over a distance Δx expressed as a combination of frictional losses along $\Delta x'$ and local losses ΔH_{loc} (solid line). Alternatively, the dashed line shows the same ΔH but expressed as a continuous head loss which is described by a single, effective loss coefficient.*

discuss this choice below. Above, we visualized the conduit beneath Unteraargletscher as meandering and being intersected by crevasses (Sec. 6.1). From the wide range of loss coefficients for bends, we choose $\xi_{\mathrm{loc}} = 1$ for simplicity. This value corresponds to a sharp bend of the conduit. Further, we use $\Delta x = 5000\,\mathrm{m}$, the length of our modeled conduit and $R_{\mathrm{h}} = 0.63\,\mathrm{m}$. The latter value is the hydraulic radius of a circular conduit with a cross-sectional area of $5\,\mathrm{m}^2$. If we assign a value of 0.01 for f_{i} and 0.5 for f, we obtain $d = 972$. One might also argue, that the roughness of a subglacial conduit is a composite of a smooth ice roof and a rough boulder-strewn bottom. If the sediments at the bottom comprise not more than 30% of the conduit perimeter and we assign $f_{\mathrm{bottom}}{=}0.25$ ($\simeq k_{\mathrm{bottom}}{=}20\,\mathrm{m}^{1/3}\,\mathrm{s}^{-1}$) to the bottom part, the combination yields a value $f_{\mathrm{com}}{=}0.02$ ($k_{\mathrm{com}}{=}70\,\mathrm{m}^{1/3}\,\mathrm{s}^{-1}$). In this case $d = 952$.

Further, we can try to assess the consequences for the choice of f related to the fact that the real course of the conduit is unknown. Below, we will discuss the discrepancy between measured and modeled transit velocities. It appears that the modeled values systematically overestimate the measurements by at least a factor of 3 (Sec. 6.8.3). Although we cannot attribute this difference directly to differences in path length, it is obvious, that the real flowpath must be longer than the straight-line distance as assumed in the model. Hence, as a rough estimate we assume that the real length of the conduit is double its straight-line length. Then, we insert $\Delta x_{\mathrm{real}}{=}2\,\Delta x$ into Equation (6.31) while Equation (6.32) remains unchanged. Then

$$d = (f - 2\,f_{\mathrm{i}})\,\frac{\Delta x}{4R_{\mathrm{h}}}\,\frac{1}{\xi_{\mathrm{loc}}}.$$

and the resulting values of d are 952 and 912 for the 0.01 and 0.02 estimates for f_{i} and f_{com}, respectively.

Although we have considered different situations, enveloped by a smooth, ice-walled conduit having a circular cross-section and following a straight line on the one hand and a meandering conduit at the bed having a composite roughness on the other hand, the number of local losses

required to explain the high value of a lumped losses parameter ($f = 0.5$), is in a narrow range from 972 to 912. Along a straight-line length of $5000\,\mathrm{m}$, this corresponds to one local loss about every $5\,\mathrm{m}$, a value which appears to be plausible for a meandering conduit.

Further, we discuss our selection of f_i and the formerly introduced assumption of f being constant. An ice-walled conduit might be appropriately described as hydraulically smooth. In this case, the Colebrook-White equation (e.g. Hager, 1995) simplifies to

$$f^{-1/2} = -2\lg\left(\frac{2.51}{\mathrm{Re}\,f^{1/2}}\right), \tag{6.34}$$

where $\mathrm{Re} = 4vR_\mathrm{h}/\nu$ is the Reynolds-number with $\nu = 1.79 \times 10^{-6}\,\mathrm{m^2\,s^{-1}}$ being the kinematic viscosity of water. In the different scenarios which were considered by our model, Reynolds-numbers range from 4.3×10^5 to 3.7×10^6. Using Equation (6.34) yields values for f_i varying between 0.009 and 0.013. Hence, $f_\mathrm{i} = 0.01$ is an appropriate choice for our purpose to assess the composition of our effective loss parameter f.

While local losses are independent of Reynolds-numbers, frictional losses vary with Re. Although this dependence attenuates for high values of Re, we have seen that in our scenarios f_i varies with Re. Hence, the assumption of a single, constant value introduces an error of $\pm 20\%$. However, using our considerations above, we can determine the portion of the total head loss which occurs locally $(d\xi_\mathrm{loc})/\xi$. For the range of values determined for d, we find that local losses contribute 92-98% to the total loss. With maximal 8% of the loss depending on the Reynolds-number, the maximum inaccuracy due to the assumption of a constant f amounts to $8\% \times \pm 20\% = \pm 1.6\%$ and is therefore negligible.

6.8.3 Velocity variations due to a dynamic geometry

If we compare the results of our calculations to the measurements, it appears that the magnitudes of modeled velocity exceed systematically the values derived from the tracer experiments. This shortcoming is mainly associated with the fact that the real length of the flow path in nature is unknown and the straight-line assumption for the calculation of velocity represents a minimum estimate. Consequently, any modeled transit velocity overestimates the measured data. Further possible sources of discrepancy are attributed to the assumption of a circular conduit cross-section and the choice of roughness (Equations (6.9) and (6.11)) and flow law parameters (Equation (6.6)).

Table 6.3 summarizes the results of a sensitivity study which was carried out to illuminate the effects of parameter uncertainties on the model results in terms of water pressure and transit velocity. The roughness parameters k and f were varied in a range which appears plausible for the roughness of a proglacial stream (Röthlisberger, 1972). The flow law coefficient B was changed to values representing each a slightly softer and a slightly stiffer ice. For the case of softer ice, we adopted a value determined by Gudmundsson (1994, 1999) from comparing measured and modeled surface velocities in the confluence area of Unteraargletscher. The value of B used by Bauder (2001) in his flow model of entire Unteraargletscher is also smaller than the one used by us. However, we have to bear in mind, that both authors have neglected basal motion in their model formulation and therefore they had to overestimate ice-deformation to achieve agreement between measured and modeled surface velocities. Therefore, we regard this value as a minimum estimate for our parameter B. We prefer to use a value determined

Table 6.3: *Sensitivity of model results to uncertainties in conduit roughness k [$\mathrm{m}^{1/3}\mathrm{s}^{-1}$], f [-] and flow law coefficient B [$\mathrm{Pa}^{-3}\mathrm{s}^{-1}$].*

Description	Parameter value	Pressure head range [m]	Velocity range [$\mathrm{m\,s}^{-1}$]
reference	$k = 15 \quad f = 0.5$ $B = 5.3 \times 10^{-24}$	85–203	1.7–2.2
enhanced roughness	$k = 10 \quad f = 1.1$	97–233	1.3–1.6
reduced roughness	$k = 20 \quad f = 0.3$	76–189	2.1–2.6
softer ice	$B = 6.8 \times 10^{-24}$	104–244	1.8–2.3
stiffer ice	$B = 2.4 \times 10^{-24}$	65–168	1.6–2.1

by Nye (1953) using measured closure-rates of glacier tunnels. The value for stiffer ice was adopted from Paterson (1994).

It turns out that an enhanced conduit roughness increases the resistance of the conduit and therefore, the hydraulic gradient required to drive the flow increases but the transit velocity is reduced. Further, a softer ice would permit enhanced closure rates. Hence, a smaller conduit would require an enhanced hydraulic head to drive the flow thereby increasing the velocity. Thus, changes in channel roughness and ice-stiffness which affect the water pressure in a similar way have contrary effects on transit velocity. This finding demonstrates that without further constraints on parameter values, fitting the model to measured data would not provide a gain of information.

In conclusion, the modeling work supports the hypothesis that the dynamic geometry of a R-channel could account for hysteresis in the vQ-relationships derived from tracer experiments (Chapter 5). In contrast, such hysteretic behavior cannot be explained by routing an identical discharge through a static pipe.

6.8.4   Velocity variations due to inflow modulation

In analogy to the discussion of consequences of a dynamic conduit geometry, we now consider the results of the moulin model with respect to variations of transit velocity (Fig. 6.17). We should recall here, that in this model we described the conduit as a rigid pipe. Since this pipe has the same steady-state geometry as used in the preceding scenarios and the model was applied to an identical discharge variation, the velocities in the conduit itself are similar to those obtained from the pipe model (Fig. 6.9). Additional variations of transit velocity through the entire system are caused by retardation of the water flow in a moulin. Consequently, the magnitude of transit velocity is reduced. The retardation depends directly on the volume of the moulin, expressed by the parameter A_{moulin} which is unknown. The idea of a moulin being a vertical slot of uniform cross-section is certainly a strong oversimplification of the natural phenomenon. However, the equations for an inclined moulin look identical to those of a vertical one if an effective cross-section $A_{\mathrm{eff}} = A_{\mathrm{inc}}/\cos\Phi$ is used instead of A_{moulin}. Here, the angle Φ denotes the deviation from vertical and A_{inc} is the cross-sectional area of the inclined moulin. Thus, A_{moulin} can be understood as an effective cross-sectional area averaged over the depth of the moulin.

Figure 6.16b shows clearly that a phase shift between transit velocity through a moulin-conduit system and main discharge can be produced by retardation of water in a moulin. Further, the effect depends on the magnitude of A_{moulin}. In consequence, the model enables any phase shift between 0 and $-\pi$ independent of the considered period of discharge variation. In contrast, the phase shift between discharge and velocity in a dynamic conduit is strongly dependent of the period. Finally, we conclude that inflow modulation at the junction of a tributary moulin to a main conduit is a valid mechanism to explain vQ-hysteresis.

Chapter 7

Modeling variations of tracer dispersion

In Chapter 6 we have validated the hypotheses that the dynamic geometry of a R-channel as well as hydraulic damming at the junction of a moulin and a conduit can both account for hysteresis in the vQ-relationship. Based on the interdependence of discharge, conduit size and transit velocity in a Röthlisberger-channel, we suggested a positive relationship between conduit size and dispersion coefficient to explain the observed hysteresis in the velocity-dispersion relationship (Sec. 5.4.3). Alternatively, for the case of transit velocities being controlled by hydraulic damming, we postulated that increasing retardation in a moulin causes higher dispersion coefficients (Sec. 5.4.3). However, the model which was used in Chapter 6 considers only the variations in transit velocity but does not account for tracer dispersion. Thus, we have to develop an independent approach to test whether the variations of tracer dispersion are consistent with the interpretations drawn from the velocity variations. For this purpose, numerical tracer tests were performed to study systematically the influence of geometry changes on tracer dispersion. Therefore, a model is adopted which was used by Hauns (1999) and Hauns et al. (1998) to investigate the retardation of water flow in karst conduits of different geometries. Numerical tracer experiments are performed by propagating a scalar field representing the tracer with the velocity field through a simplified flow geometry. Hauns et al. (1998) have validated the model with accompanying laboratory experiments. In this study, we adapt this model to several idealized conduits which differ in size, shape or roughness. With each conduit scenario, tracer return curves were generated for different hydraulic conditions.

7.1 Turbulent flow field

The Navier-Stokes equations describe laminar flow of an incompressible and isothermal fluid. The set of governing equations comprises an expression for conservation of mass:

$$\nabla \cdot \mathbf{v} = 0 \tag{7.1}$$

and one for conservation of momentum:

$$\frac{\partial}{\partial t}\rho\mathbf{v} + \nabla \cdot (\rho\mathbf{v} \otimes \mathbf{v}) = -\nabla p + \Delta(\mu\mathbf{v}) + \mathbf{B}. \tag{7.2}$$

Here $\mathbf{v}$ is the fluid velocity, ρ denotes the fluid density, p and t are pressure and time, respectively. Further, $\mathbf{B}$ is a body force and μ is molecular viscosity.

However, flow through subglacial conduits is considered to be turbulent (Röthlisberger, 1972; Weertman, 1972). Nevertheless, the Navier-Stokes equations are valid for turbulent flow as well since turbulent flow can be considered also as a very complex unsteady laminar flow. However, it is not feasible to solve the Navier-Stokes equations accurately for high Reynolds-numbers. Therefore, we have to resort to turbulence modeling. The fundamental procedure in turbulence modeling is to split the field quantities each into a mean and a fluctuating part:

$$
\begin{aligned}
\Phi &= \overline{\Phi} + \Phi' \\
\Psi &= \overline{\Psi} + \Psi',
\end{aligned}
\tag{7.3}
$$

where Φ and Ψ denote two arbitrary field quantities. Equation 7.3 is subject to the following conditions:

1. $\overline{\overline{\Phi}} = \overline{\Phi}$ and $\overline{\Phi'} = 0$

2. $\overline{\overline{\Phi}\Psi} = \overline{\Phi}\,\overline{\Psi}$

3. $\overline{\overline{\Phi}\Psi'} = 0$

4. $\overline{\Phi\Psi} = \overline{\Phi}\,\overline{\Psi} + \overline{\Phi'\Psi'}$.

Applying this method to the Navier-Stokes equations, the continuity equation becomes:

$$
\nabla \cdot \overline{\mathbf{v}} = 0
\tag{7.4}
$$

and the momentum equation is written:

$$
\frac{\partial}{\partial t}\rho\overline{\mathbf{v}} + \nabla \cdot (\rho\overline{\mathbf{v}} \otimes \overline{\mathbf{v}}) = -\nabla\overline{p} + \Delta(\mu\overline{\mathbf{v}}) - \nabla \cdot (\rho\overline{\mathbf{v}' \otimes \mathbf{v}'}),
\tag{7.5}
$$

where the body force was dropped for clarity. The additional turbulent flux term $\nabla \cdot (\rho\overline{\mathbf{v}' \otimes \mathbf{v}'})$ has the dimension of a stress and is also known as Reynolds-stress. This term cannot be calculated explicitly and is therefore parameterized by the k-ϵ-approach which introduces a turbulent viscosity $\mu_T = c_\mu \rho \frac{k^2}{\epsilon}$ to describe the Reynolds-stress

$$
\nabla \cdot (\rho\overline{\mathbf{v}' \otimes \mathbf{v}'}) = \mu_T(\nabla\mathbf{v} + \nabla\mathbf{v}^T).
\tag{7.6}
$$

Here, k is the turbulent kinetic energy and ϵ represents the turbulence dissipation rate, c_μ is a constant. Empirical expressions or values for k, ϵ and c_μ were adopted from CFX (1996).

7.2 Model description

The approach consists in describing the three-dimensional velocity field of turbulent discharge through a given geometry. Subsequently, tracer transit is simulated by a scalar volume which is propagated through this flow field by advection and diffusion. For the numerical tracer experiments, we used the commercial package CFX-4.3 of AEA Technology which provides a complete environment to solve turbulent flow problems.
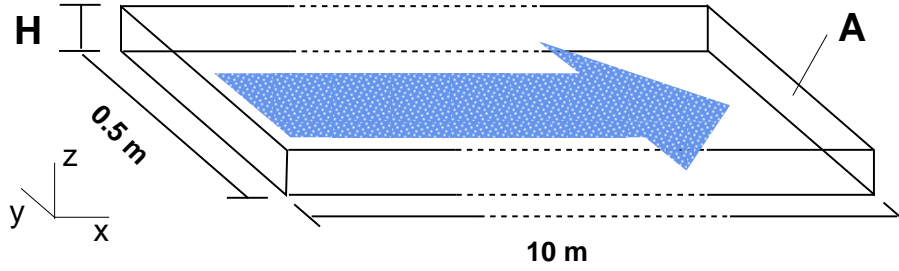
Figure 7.1: *The idealized conduit geometry through which numerical tracer tests were performed. Water flow is in x-direction.*

7.2.1 Numerics

The set of equations for the turbulent velocity-field was discretized using a finite volumes and solved using finite differences. Therefore, the flow geometry was subdivided into a grid of rectangular volumes using the CFX mesh-generator. Each equation was integrated over each control volume to obtain a discrete equation which connects the variable at the center of the control volume to its neighbors. All terms were discretized in space using a hybrid differencing scheme, whereby upwind differencing was used for advection terms where advection dominates diffusion and central differencing otherwise. In an upwind scheme, the value of the variable is taken from the upstream neighbor, whereas in central differencing the mean value between two neighbors is assigned to the variable. These procedures are used as the default by CFX-4.3 CFX (1996).

7.2.2 Model geometry

The procedure was applied to an idealized conduit which was represented by a rectangular geometry (Fig. 7.1). Numerical integration of the model equations requires boundary conditions at the margins of the geometry. Where the water flow is constrained by a solid boundary, a no-slip condition for velocity was applied. The amount and direction of water discharge is defined by adequate boundary conditions at the inlet and outlet cross-section. Inflow of water was represented by a constant two-dimensional velocity field pointing into the model region whereas a no-pressure condition was prescribed at the outlet plane. Since the considered model geometries here are horizontal, the water flow is driven only by the pressure gradient which is required to match the mass flow condition at the inlet.

7.2.3 Tracer transport

In the stationary velocity field which is then obtained, transport of a conservative tracer is simulated by an advective-diffusive propagation of a scalar Θ representing the tracer concentration:

$$\frac{\partial}{\partial t}\Theta = -\nabla \cdot (\mathbf{v}\,\Theta + D_m\nabla\Theta), \tag{7.7}$$

where D_m represents the coefficient of molecular diffusion. Although the diffusion process is irrelevant for the tracer transport since hydrodynamic dispersion is several orders of magnitude larger, a non-zero value for D_m is required by the solver to obtain a stable solution (CFX,
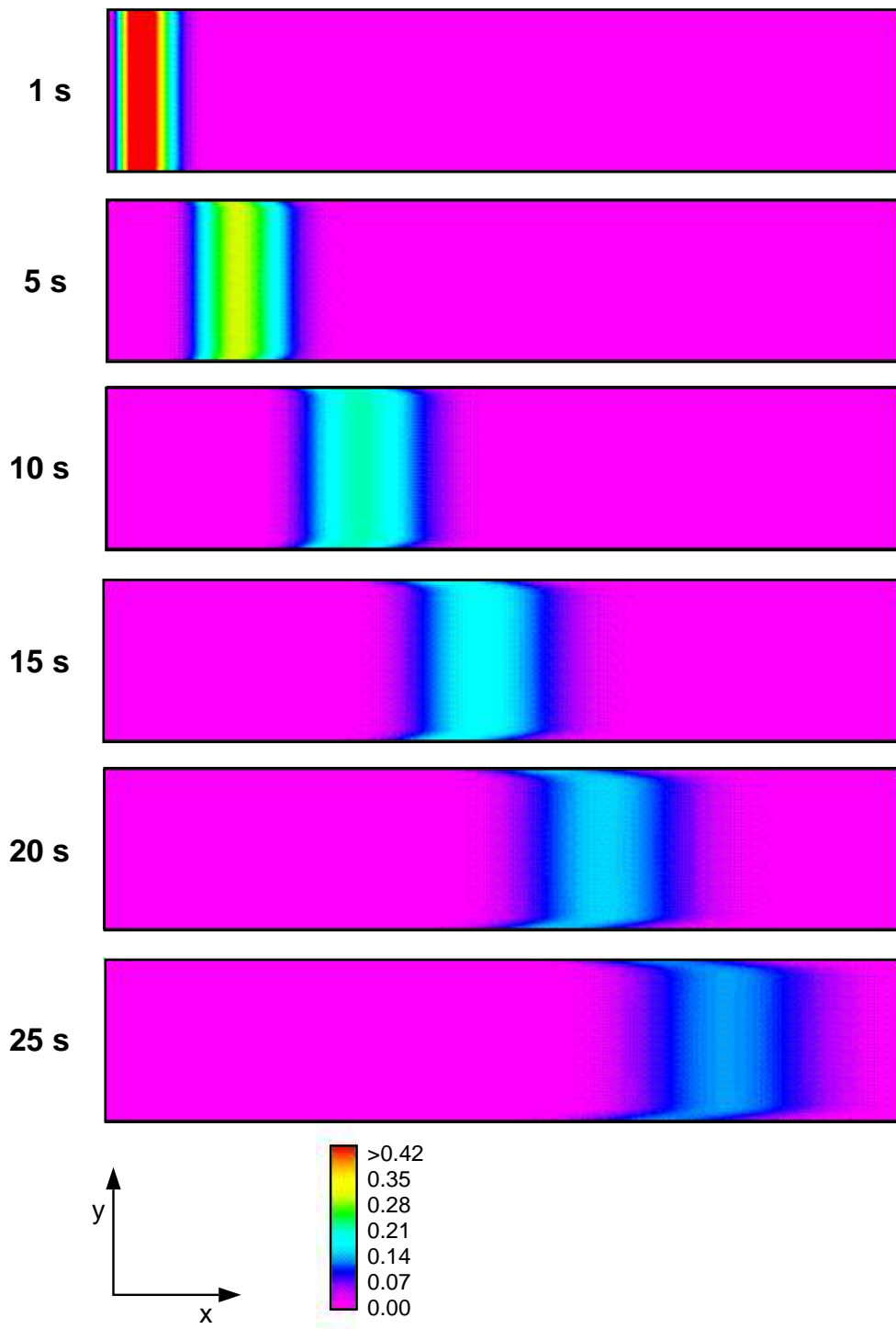
Figure 7.2: *Illustration of simulated tracer distribution in the xy-plane at half height of the conduit at different time steps after injection. Flow is in x-direction and the color bar denotes the tracer concentration relative to its input value.*

Figure 7.3: *A black-box procedure F transforms an input I to a system output O.*

1996). Therefore, a very small value of $10^{-13} \, \mathrm{m^2 \, s^{-1}}$ was used. As such, the approach is valid only if the tracer's influence on the fluid density is negligible. This is typically the case in the experiments at Unteraargletscher where maximum observed dye tracer concentrations were lower than $20 \, \mathrm{ppm}$. Tracer breakthrough curves were obtained by recording the scalar flux through the outlet plane.

Figure 7.2 shows an example of how the tracer cloud propagates through the conduit. During transit, the initially compact field becomes increasingly dispersed concurrent with a decrease of maximum concentration. Further, there is a backwards bending of the concentration contours noticeable. It increases with travel time and reflects the retarding influence of the conduit walls.

7.2.4 Extending the length scale

The explicit modeling of turbulent flow and tracer transport is restricted to length scales on the order of $10^0 - 10^1 \, \mathrm{m}$ since for longer dimensions the computational effort becomes excessive. However, natural tracer tests are typically performed over length scales of $10^2 - 10^3 \, \mathrm{m}$. This has to be taken into account since roughness elements can cause significant tracer retardation at the meter scale. However, at the $10^2 - 10^3 \, \mathrm{m}$ scale roughness might rather contribute to dispersion as the retardation effect is repeated regularly (Hauns et al., 2001). Therefore, an additional approach is required to investigate the behavior of the considered conduits at a scale representative of our field situation. Here, a simple black box model is applied. This approach entails that once the transfer function of a simulated conduit segment is determined, scenarios for conduits of any desired length can be generated by multiple concatenation of such transfer functions (Box et al., 1994).

Convolution

The transfer-function F is a convolution operator which describes the transformation of an input signal I into a system output O, even though the exact physical process of that transformation remains unknown or is ignored (Fig. 7.3). In the problem considered here, the tracer is conservative, therefore the system can be considered as a single-degree-of-freedom system with the temporal distribution of concentration $\frac{\partial}{\partial t}\Theta$ as the only degree of freedom. Then, the convolution can be performed in the time domain by Duhamel's Integral (expressed in discretized form):

$$O_m = \sum_{n=0}^{m} F_n I_{m-n}. \tag{7.8}$$

Here, the subscript m denotes the considered time step and n represents the time steps between 0 and m.
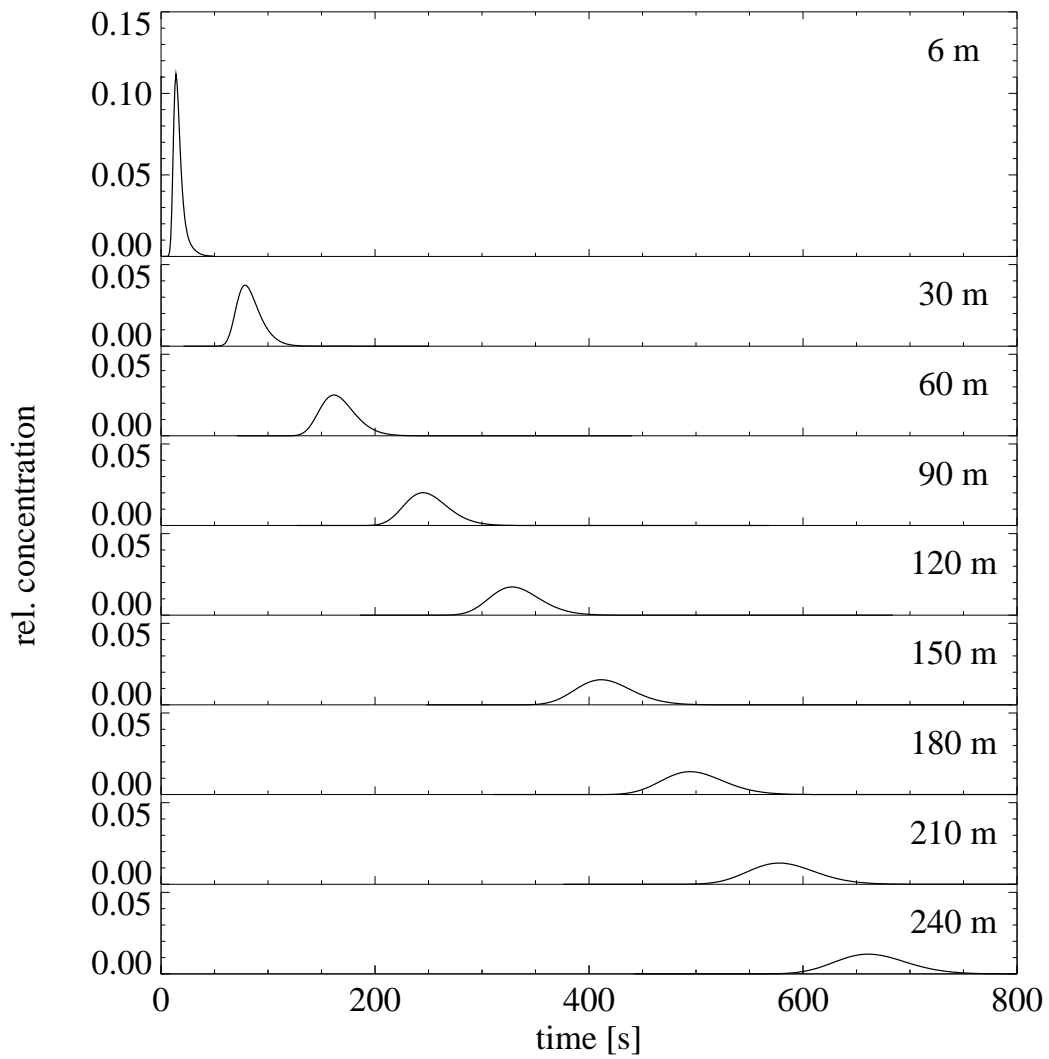
Figure 7.4: *The evolution of concentration-time curves along the conduit with increasing distance from the point of tracer injection. Tracer return curves are shown at 6, 30, 60, 90, 120, 150, 180, 210 and 240 m, respectively. Tracer concentration is shown relative to its input value.*
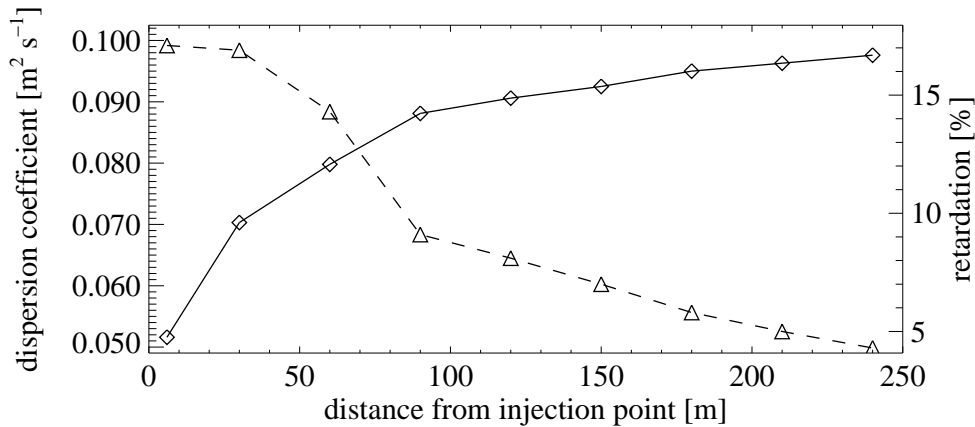
Figure 7.5: *The evolution of dispersion coefficient (solid) and retardation (dashed) of the tracer breakthrough curves shown in Figure 7.4 with increasing distance from the injection site. Retardation is quantified by the portion of the tracer mass, which is not accounted for by the advection-dispersion model (cf. Sec. 5.2.3).*

Deconvolution

With the knowledge of the system output function O in response to a known input signal I, the transfer function F can be obtained by deconvolution:

$$F_m = \frac{1}{I_0}(O_m - \sum_{n=1}^{m}(F_{m-n}I_n)). \tag{7.9}$$

Although, this is an efficient method to determine the transfer function, it suffers in many cases from numerical instability (Box et al., 1994). However, in this application, the input function consists of a simple, rectangular pulse and the procedure proofed to be non-problematic. Once F is obtained, its convolution with any input function is very robust.

7.2.5 Model performance

Once the hydraulic solution was found, transport of tracer through the stationary flow field was simulated. To initiate the tracer transport, the scalar-field used to represent the tracer was set equal to 1 at the inlet cross-section during 2 seconds. The scalar-tracer field was recorded at the outlet cross-section and its time series is analogue to a tracer return curve. From this return curve, we constructed the corresponding transfer-function by deconvolution and used this subsequently to derive return curves for a 240 m long flow path.

Figure 7.4 illustrates how the shape of a return curve evolves with increasing length of the conduit. Tracer concentration was logged at several sections along the flow path. The first breakthrough curve displays an asymmetrical shape which is characterized by a steep rise and a long-lasting decline, indicative of pronounced retardation. With increasing length of the conduit, the asymmetry of the return curve decreases gradually, peak concentrations decline and curves become broader. This evolution was quantified by using the advection-dispersion model as described in Chapter 4 and Section 5.2.3. Figure 7.5 shows how the dispersion coefficient

Table 7.1: *Different tracer tests performed to study the effect of conduit size on tracer dispersion. Discharge Q was routed through the conduit of cross-sectional area A with a mean flow velocity v_0.*

no.	Q [l/s]	v_0 [m/s]	A [m^2]
c1	10.	0.173	0.0576
c2	15.	0.261	0.0576
c3	20.	0.347	0.0576
c4	34.6	0.600	0.0576
c5	15.	0.221	0.0677
c6	20.	0.295	0.0677
c7	23.5	0.347	0.0677
c8	40.6	0.600	0.0677
c9	25.	0.200	0.125
c10	43.4	0.347	0.125
c11	75.	0.600	0.125

Table 7.2: *Different tracer tests performed to study the effects of conduit shape on tracer dispersion.*

no.	H [m]	W [m]	R_h [m]
r1	0.5	0.5	0.125
r2	0.25	1.0	0.100
r3	0.125	2.0	0.058
r4	0.0625	4.0	0.031

increases with the length of the flow path concurrent with a decrease of retardation. This observation demonstrates how tracer retardation at short spatial scales contributes to hydrodynamic dispersion at larger spatial scales.

7.3   Experiments

To study systematically the influence on tracer dispersion in different scenarios, the conduit geometry was altered in size, width to height ratio and roughness. To characterize the dispersive behavior of each of these scenarios, we derived velocity-dispersion relationships by using a number of different flow velocities.

In a first experiment, the height H of the conduit geometry was varied to generate conduits with different cross-sectional areas A. Table 7.1 lists details of individual experiments.

Another set of tracer tests was designed to study the influence of the cross-sectional shape. Since the flow velocity is zero at the conduit walls, the flow field and therefore also the tracer transport is affected by the fraction of water that is in contact with the wall. This influence can be examined by systematically varying the hydraulic radius $R_{\mathrm{h}} = A/U$, where A is the cross-sectional area that is occupied by the water and U is the wetted perimeter of the conduit. The mean flow velocity $v_0 = 0.3\,\mathrm{m\,s^{-1}}$ was kept constant in the four cases performed. Details are presented in Table 7.2.
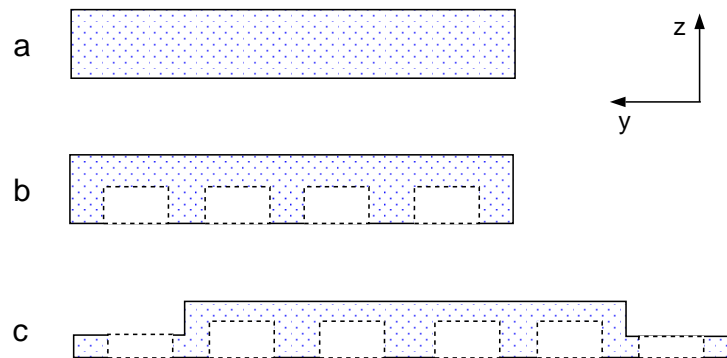
Figure 7.6: *Cross-sectional profiles of the three conduits which were used to study the effect of roughness on tracer dispersion. Water flow is into the page.*
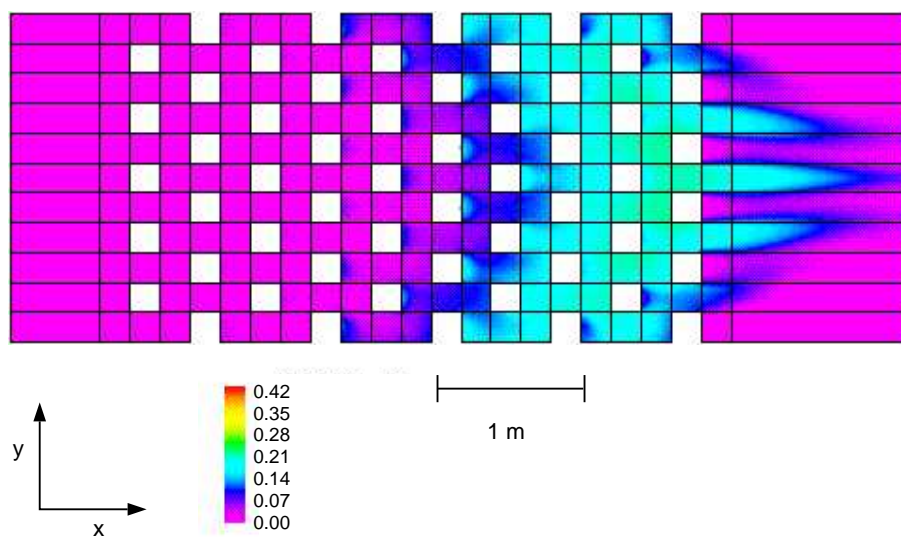

Figure 7.7: *Tracer distribution in the xy-plane at* $0.04\,\mathrm{m}$ *height of the conduit shown in Figure 7.6c. The situation represents a snapshot at* $20\,\mathrm{s}$ *after introduction of the tracer. Water flow is in x-direction. The color bar denotes tracer concentration relative to its input value. Location of the obstacles is indicated by the white squares.*
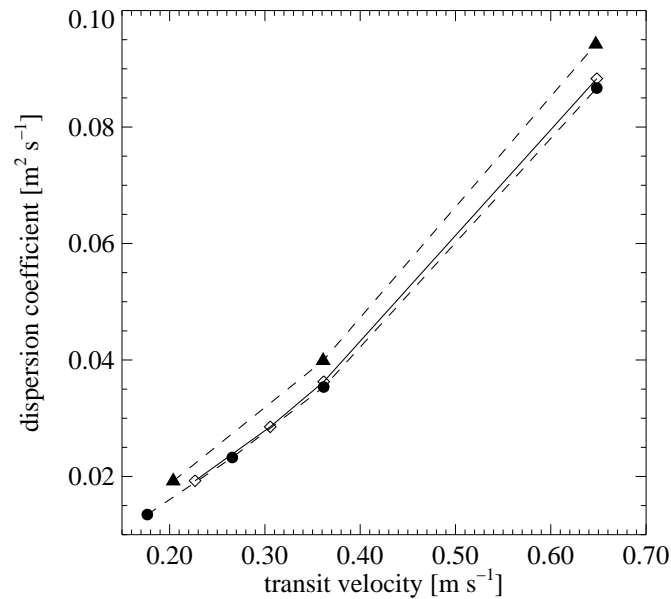
Figure 7.8: *Velocity-dispersion relationships for three conduits of different cross-sectional area. Solid circles connected with a dashed line denote the small conduit, open diamonds on a solid line mark the medium size and solid triangles again connected with dashes represent the large conduit.*

A third set of return curves was generated to investigate the effect of changes in roughness on tracer dispersion. A mean flow velocity $v_0 = 0.3\,\mathrm{m\,s^{-1}}$ was kept constant throughout these experiments. Roughness was introduced into the conduit by distributing rectangular obstacles at the bottom of the conduit (Fig. 7.6). The obstacles are $0.2 \times 0.2 \times 0.1\,\mathrm{m}$ in size and are meant to represent roughness elements typical for a glacial stream. Roughness enhances turbulence in the flow-field thereby affecting the transport of a tracer. Figure 7.7 illustrates how the tracer is retarded in the flow-reversals at the lee side of the obstacles.

Before introducing obstacles, a reference experiment was conducted (Scenario 'a' in Fig. 7.6). A second test consisted of the same configuration but containing obstacles (Fig. 7.6b). In a third scenario, the influence of the bottom roughness was increased. This was achieved by broadening the conduit and to conserve the cross-sectional area, the ceiling was shaped asymmetrically (Fig. 7.6c).

7.4 Results

Results of the 11 experiments performed to study the interdependence of tracer dispersion and cross-sectional area are presented in Figure 7.8. Velocity-dispersion relationships are shown for each of the three different conduit sizes. The curves feature a positive relationship between transit velocity and the dispersion coefficient with the slope of the curves increasing towards higher velocity. The dependence of dispersion coefficients on cross-sectional area is expressed by different curves described for differently sized conduits. It reveals that a larger conduit yields systematically higher dispersion coefficients than a smaller one.

Results from varying the hydraulic radius at constant flow velocity and constant cross-sectional area are shown in Figure 7.9. We can perform an extrapolation of the graph with two additional
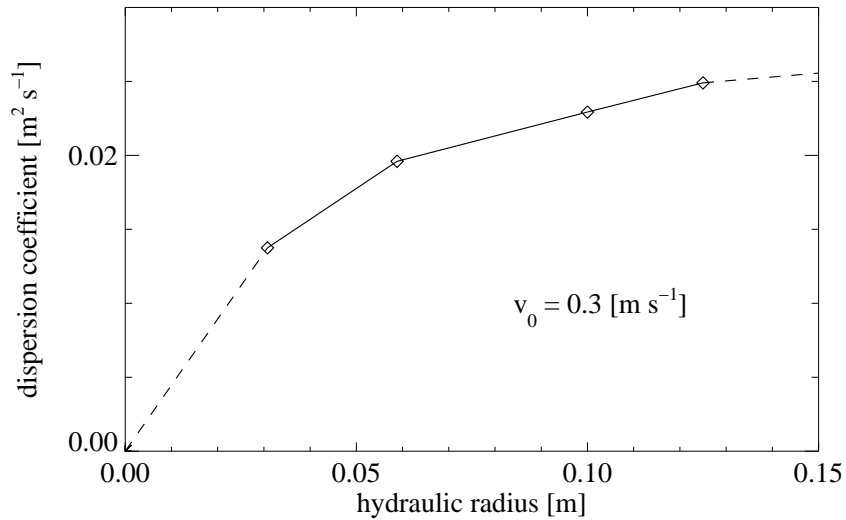
Figure 7.9: *Effect of the hydraulic radius on dispersion. The flow velocity was kept constant in all scenarios. The dashed lines denote extrapolations of the relationship based on data from Hauns et al. (2001). See text for details.*

Table 7.3: *Dispersion coefficients obtained from varying the influence of roughness in the conduit geometry.*

scenario	R_h [m]	D [m^2 s^{-1}]	remarks
a	0.0706	0.01717	no additional roughness
b	0.0706	0.05906	additional roughness
c	0.0614	0.09783	enhanced influence of roughness

points. First, we consider the trivial case $D = 0$ for $R_h = 0$ and second, we adopt a value determined by Hauns et al. (2001) for a perfectly homogeneous velocity field. This condition is realized for an infinitely high and wide conduit. Therefore $R_{\mathrm{h}} \rightarrow \infty$ and it was found $D_{\infty} = 0.045\,\mathrm{m}^2\,\mathrm{s}^{-1}$ for $v = 0.3\,\mathrm{m}\,\mathrm{s}^{-1}$. The figure demonstrates that with increasing hydraulic radius, dispersion approaches asymptotically D_{∞}.

Table 7.3 lists results of the three experiments performed to investigate the effect of roughness on tracer dispersion. Comparison of Scenarios 'a' and 'b' shows that introduction of obstacles into the conduit causes a substantial increase of the dispersion coefficient. If the influence of roughness is further increased as considered in Scenario 'c', the dispersion coefficient increases even more, although the hydraulic radius of this conduit is reduced with respect to that of Scenario 'a' or 'b'.

7.5   Discussion

In this chapter, we performed numerical tracer tests to study systematically the effect of changes of the conduit geometry on tracer dispersion. The results of our experiments indicate a positive relationship between the dispersion coefficient D and cross-sectional area of the conduit A.

Such a relationship was postulated in Chapter 5 where variations of tracer dispersion were discussed in relation to variations of transit velocity.

However, the dependence of D on A as illustrated in Figure 7.8 is not very strong. In these examples the increase in size was accomplished by heightening a rectangular conduit of constant width. This involves a change of the perimeter and thereby the influence of the conduit-wall is altered. Here, the influence of the conduit-wall was expressed in terms of hydraulic radius $R_{\rm h}$. Figure 7.9 reveals that an increase of hydraulic radius at constant cross-sectional area also increases the dispersion coefficient. However, this effect is relevant only for hydraulic radii below the meter scale. Towards larger values of $R_{\rm h}$, the increase of D is attenuated and the dispersion coefficient approaches a maximum value. This indicates that the increase of dispersion coefficients in Figure 7.8 would also approach an upper limit since an increase of the cross-sectional area is accompanied by an increase of $R_{\rm h}$. Results of simulating the conduit evolution in Chapter 6 suggest a cross-sectional area of the subglacial channel beneath Unteraargletscher on the order of $10^0\,{\rm m}^2$. On this scale, the effect on tracer dispersion from changes in conduit size alone would be very weak.

In contrast, a positive relationship between A and D was reported by Taylor (1954), but his experiments were conducted using pipes of a few centimeters in diameter. As discussed above, the increase of D attenuates towards larger values of $R_{\rm h}$.

Further, it is shown by our experiments that the dispersion coefficient is strongly affected by changes in roughness (Table 7.3) such that increased roughness generates enhanced dispersion. If conduit-increase entails a roughness increase, the tracer dispersion would be enhanced at the same time. And if further roughness recedes after the termination of conduit-increase, the dispersion coefficient would decrease to a lower level. This argumentation provides a possibility to interpret the observed velocity-dispersion hystereses using the R-channel model.

For our numerical tracer tests, we assumed a constant size and roughness along a straight, rectangular conduit which is certainly a strong simplification of the investigated flow path on Unteraargletscher. Instead, the conduit in nature might be curved with size and roughness changing along its length thereby causing significantly higher dispersion coefficients than those obtained from our idealized experiments. A roughness change as required by our interpretation might be accomplished by either a nonuniform conduit growth or by erosion and sedimentation of subglacial sediments at the bottom of the conduit.

If hydraulic damming occurs, the effects on tracer dispersion are well comprehensible. We recall that water flow occurs at a lower speed in the moulin and at a higher one in the conduit and that the measured transit velocity represents an average value over the entire system. Let us consider two identical transit velocities, one is obtained from a drainage system where water flows homogeneously with a constant velocity and the other one is affected by hydraulic damming, such that the retardation in the moulin must be compensated by a higher flow velocity in the conduit. Figure 7.8 demonstrates that higher flow velocities coincide with enhanced dispersion. Therefore, the case which is more affected by hydraulic damming would yield a higher dispersion coefficient due to a higher flow velocity in the conduit. This conclusion confirms the positive relationship between tracer dispersion and retardation in a moulin which was suggested in Chapter 5 from field experiments.

Finally, as already indicated by the analysis of velocity variations (Chap. 6), we can conclude that a dynamic conduit geometry and hydraulic damming in a moulin are both equally valid mechanisms to explain the observed behavior of tracer dispersion.

Chapter 8

Synthesis

8.1 Concluding discussion

In this thesis, the drainage of water through and from Unteraargletscher was studied with particular emphasis on the internal plumbing and its behavior with time. Valuable insight into an otherwise inaccessible system was obtained by tracer experiments which were designed appropriately to take particularities of a subglacial drainage system into account.

Tracer injections into a moulin of Unteraargletscher were repeated in quick succession over a number of diurnal discharge cycles to characterize the instantaneous state of the drainage system. Results are within the range found in previous comparable studies (Collins, 1982; Burkimsher, 1983; Nienow et al., 1996c). It is generally accepted to associate high velocities in combination with low dispersion coefficients with a hydraulically efficient, channelized drainage system (e.g. Behrens et al., 1975; Lang et al., 1979; Collins, 1982; Burkimsher, 1983; Seaberg et al., 1988; Hock and Hooke, 1993; Fountain, 1993; Nienow et al., 1996b; Nienow et al., 1998; Wagnon et al., 1998; Hock et al., 1999; Hasnain et al., 2001). On the other hand, transit velocities lower than $0.2\,\mathrm{m\,s^{-1}}$ were occasionally interpreted as typical for a less efficient, distributed drainage system (Hubbard and Nienow, 1997; Hasnain et al., 2001). However, our results exhibit a pronounced diurnal variation of transit velocity and tracer dispersion with minimum values of transit velocity below this limit. Since all tests were performed in the same flow path, there is little doubt that these variations reflect changing hydraulic conditions in this particular channel rather than morphological switching between distributed and channelized drainage configurations.

This finding underlines the major difficulty to detect a possible evolution of the drainage system based on single tracer tests conducted at coarse temporal intervals. Single tests represent only random situations within a pronounced diurnal range. Therefore, different transport parameters derived from single tracer injections can be caused both by different hydraulic conditions and by different morphologies of the drainage system. Hence, to deduce extensive morphological changes in the drainage system based on single tracer tests (e.g. Hasnain et al., 2001) is of limited value. Instead, the inference of a drainage system evolution is much better defined if the range of transit velocities over a diurnal discharge cycle is taken into account and therefore, the obtained interpretation is more reliable.

Observed values of the dispersion coefficient are within the wide range described in previous studies of subglacial drainage systems (e.g. Behrens et al., 1975; Seaberg et al., 1988; Willis et

al., 1990; Hock and Hooke, 1993; Hubbard and Nienow, 1997; Nienow et al., 1998). Only a few authors show the quality of their parameter estimation and discuss the reliability of the applied transport model (Seaberg et al., 1988; Willis et al., 1990; Hock and Hooke, 1993; Fountain, 1993). However, a reliable estimate of transport parameters requires a careful inversion of the obtained tracer return curve by an adequate transport model. In this study, it is shown that reliable parameter values can be obtained by fitting a simple advection-dispersion model to the rising limb of an asymmetric tracer return curve. As such, only the part of the data which is adequately described by the model is evaluated. This approach was validated by comparison with the mobile-immobile model which accounts for storage-retardation processes.

Our experiments reveal a pronounced, clockwise velocity-discharge hysteresis thereby inhibiting the application of known methods to infer hydraulic conditions of the flow path. All of the previously established methods (Fountain, 1993; Kohler, 1995; Seaberg et al., 1988; Hock and Hooke, 1993) are based on the assumption that there exists a unique functional relationship between velocity and discharge. Hysteretic behavior was observed by Nienow et al. (1996b) who reports also the occurrence of counterclockwise vQ-hysteresis. Such behavior has been interpreted to result from a two-component drainage configuration where discharge in the tributary conduit varies out of phase with that in the main conduit (Collins, 1995; Nienow et al., 1996b). However, the only attempt to date to simulate velocity-discharge hysteresis (Nienow et al., 1996b) is described by purely empirical relations and suffers from equifinality.

In this thesis, two mechanisms were identified which can account for hystereses in the velocity-discharge relationships. Such complex velocity-discharge relationships can be produced by a dynamic conduit geometry as proposed for a Röthlisberger-channel or by hydraulic damming at the junction of a two conduits carrying different discharges. With a physically based model of subglacial water flow, each hypothesis was tested. The results suggest that both mechanisms provide equally valid explanations.

The analysis of diurnal variations of the dispersion coefficient were used as an additional approach to validate the explanation derived from variations of transit velocity. Similarly, a pronounced hysteresis in the velocity-dispersion relationship renders conventional interpretation techniques inapplicable. Usually, a linear relationship between dispersion and velocity is assumed (e.g. Behrens et al., 1975; Brugman, 1986; Seaberg et al., 1988; Willis et al., 1990; Nienow et al., 1998) and the factor of proportionality, named "dispersivity" is calculated which should provide an independent measure of the dispersive behavior of the considered system. However, this interpretation is valid only in the case of a strictly linear velocity-dispersion relationship (Kinzelbach, 1992). This condition is obviously not fulfilled by the dataset which was obtained in this study. Instead, the influence of changes in conduit size or roughness on tracer dispersion was investigated using a numerical model of tracer transport through an idealized geometry. Results suggest that a dynamical conduit geometry can account for the observed velocity-dispersion relationship, especially, if the evolution of the conduit involves also changes in its roughness. Further, the effect of hydraulic damming on tracer dispersion is found to provide an equivalent explanation for the observed behavior.

In conclusion, hysteresis in velocity-discharge and in velocity-dispersion relationships can be equally caused by a dynamic conduit geometry or by hydraulic damming in a tributary. Since either of the mechanisms is highly plausible and neither of them can be excluded, a combination of both is probably the most realistic configuration in nature.

This conception of multicomponent water transfer through the interior of a glacier has important implications for the interpretation of tracer experiments conducted in glacial drainage systems.

The transit time of water entering a moulin is affected by englacial storage as well as subglacial routing processes and therefore both mechanisms have to be considered when hydraulic parameters are to be inferred from tracer tests. Especially, if tracer tests are performed to investigate subglacial drainage conditions, the influence of hydraulic damming on tracer transit has to be taken into account.

Our analysis of the water balance at Unteraargletscher provides evidence for englacial or subglacial storage which is related to the structure of the drainage system. Comparison of meltwater input and proglacial discharge revealed that a significant amount of water was temporarily stored in or beneath the glacier which was subsequently released during a reconfiguration of the subglacial drainage system.

8.2 Outlook

Tracer experiments represent undoubtedly a valuable approach to infer characteristics of subglacial drainage systems. However, in this study it is demonstrated that the inference of hydraulic conditions at the glacier bed is complicated if the tracer passes through a multi-component system. The reliability of such an inference will be significantly increased if a subglacial channel could be investigated in isolation. This can be achieved by an injection of tracer directly into the channel, for instance through a borehole. The problem of locating a subglacial conduit was tackled by Sharp et al. (1993) who mapped the hydraulic potential of Haut Glacier d'Arolla.. Based on these results, a dense set of boreholes has been drilled across the region where a preferential drainage axis was predicted (Hubbard et al., 1995).

Furthermore, informations on the moulin geometry or measurements of the water level in the moulin concurrent with the tracer tests will help to constrain the representation of the moulin in a two-component model. Knowledge about the geometry can be obtained by descents into moulins (e.g. Reynaud, 1987). A record of water pressure in the moulin could be used to constrain the representation of head losses.

Predictions of the numerical subglacial drainage model can be tested experimentally to enhance the reliability of the interpretation. Such predictions include for instance the velocity distribution along the channel or the length of the channel section where open-channel flow occurs. A possibility to validate these predictions is provided by simultaneous tracer injections into the same conduit but at different locations along the flow path. Therefore, different tracers have to be used which can be detected separately.

Relating the melt water supply from the glacier surface to the pressure distribution at the bed is a prerequisite to understanding the temporal evolution of basal conditions of a glacier. An extension of the numerical subglacial drainage model to the entire glacier bed could elucidate this relationship. Therefore, interactions between subglacial channels, a porous sediment bed and a linked cavity system have to be considered. The ability of such a system to temporarily store and suddenly release water is demonstrated by the findings described in Chapter 3. Flowers and Clarke (2000, in press) have presented a multicomponent model of glacier hydrology and used it to interpret subglacial hydraulic release events. The model describes the glacial drainage system by coupling glacier surface runoff, englacial water storage and transport and subglacial drainage. To understand the distribution of subglacial water pressure beneath an alpine glacier whose drainage is conduit-dominated, a model of subglacial conduit flow is required. However,

a model coupling water flow through a Röthlisberger-conduit and distributed drainage at the glacier bed is not yet available.

The use of active tracing techniques in geomorphology (e.g. Schmidt and Ergenzinger, 1992; Ergenzinger et al., 1989) is an innovative development which could significantly increase the amount of information gained from tracer tests. Active tracers consist of small sensors which take measurements during their passage through the system. The data is either transmitted directly by radio-telemetry to the observer or it is read out after the tracer is recovered. However, the requirements on such a tracer to survive the passage through a subglacial drainage system are challenging and the problem of data retrieval is not yet solved. Future technological advancements might enable records of water pressure or flow velocity along a subglacial channel which would considerably improve our present understanding of subglacial hydrology.

Appendix A

Results of individual tracer tests

A.1   Advection-dispersion model results

The following figures illustrate the individual tracer return curves (black) resulting from dye injections into the drainage system of Unteraargletscher in August and September 2000. Further, the results of fitting the advection-dispersion model (red) to the data are shown for comparison. The integral under the fitted curve (shaded area) corresponds to the value of m_{model} (Sec. 5.2.3). The coefficient of determination r^2 refers to the fit of the model to the rising limb of the data.
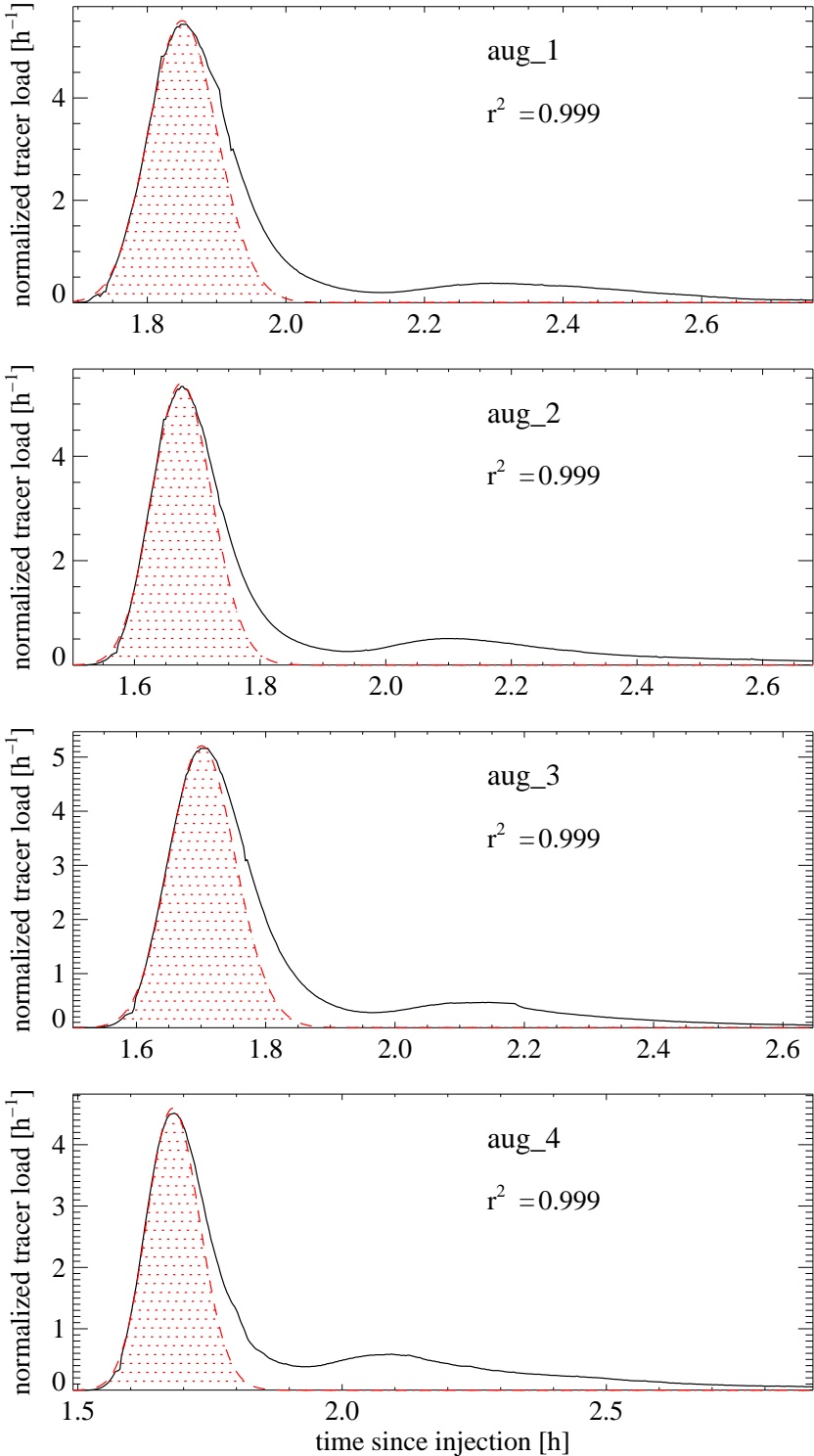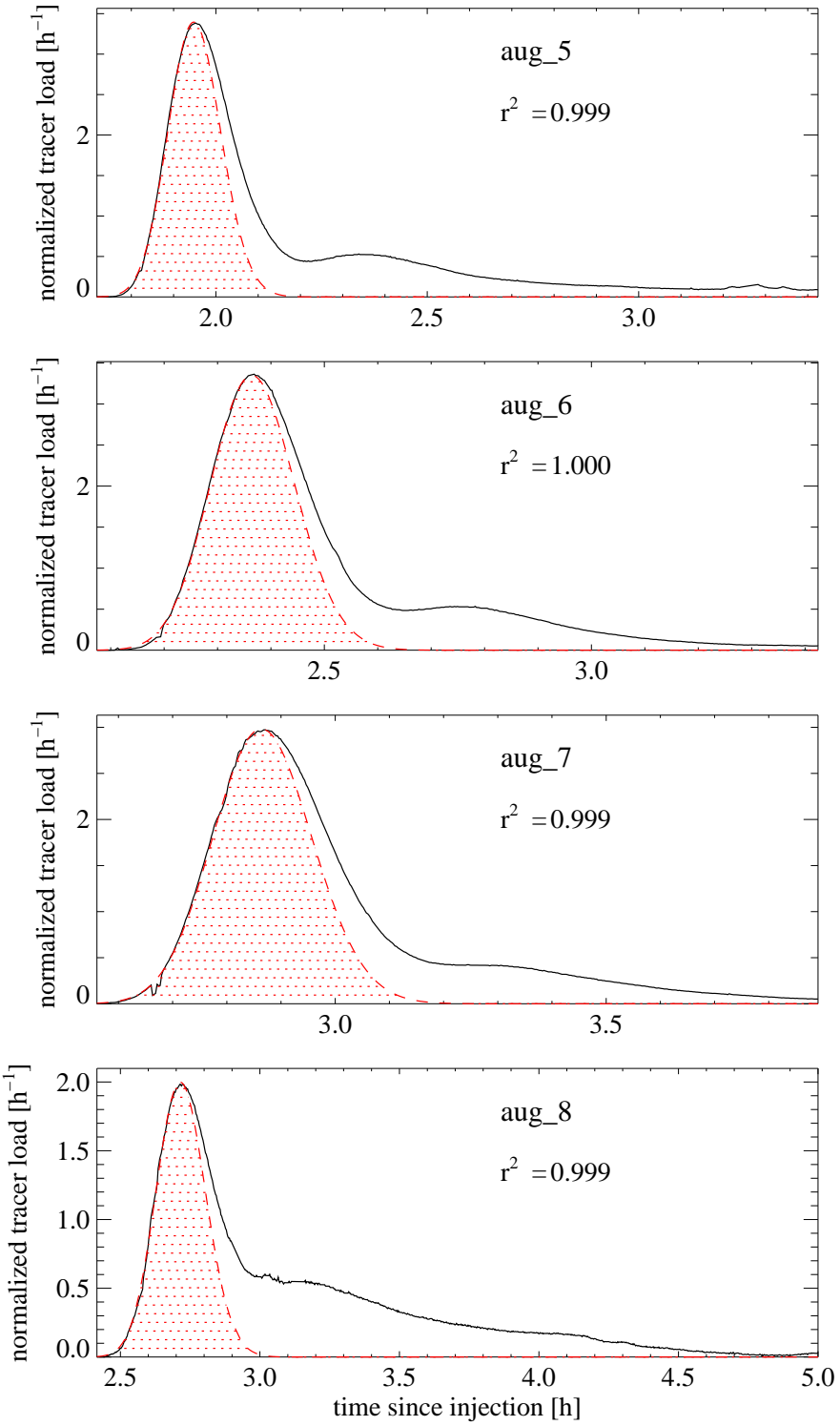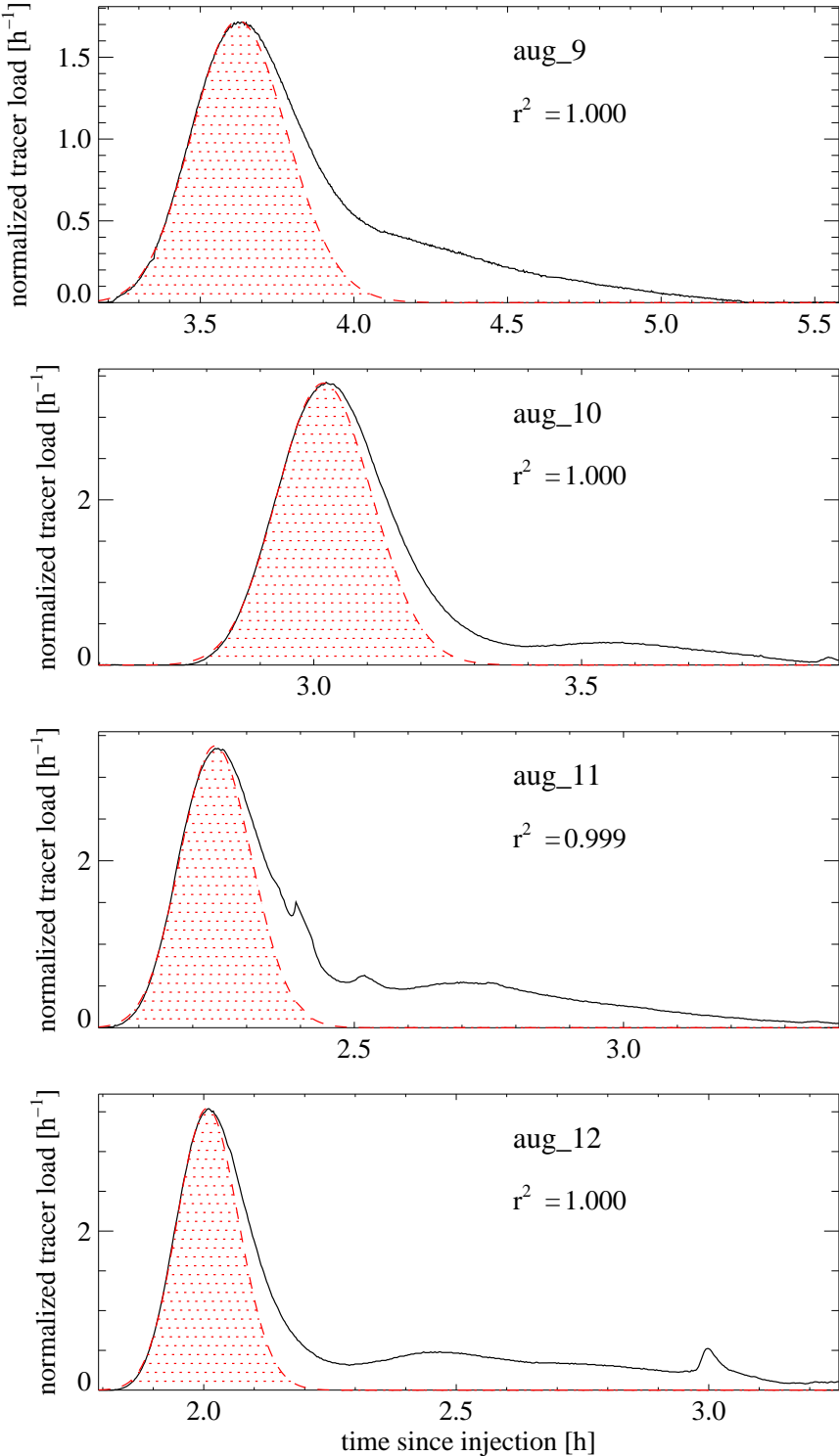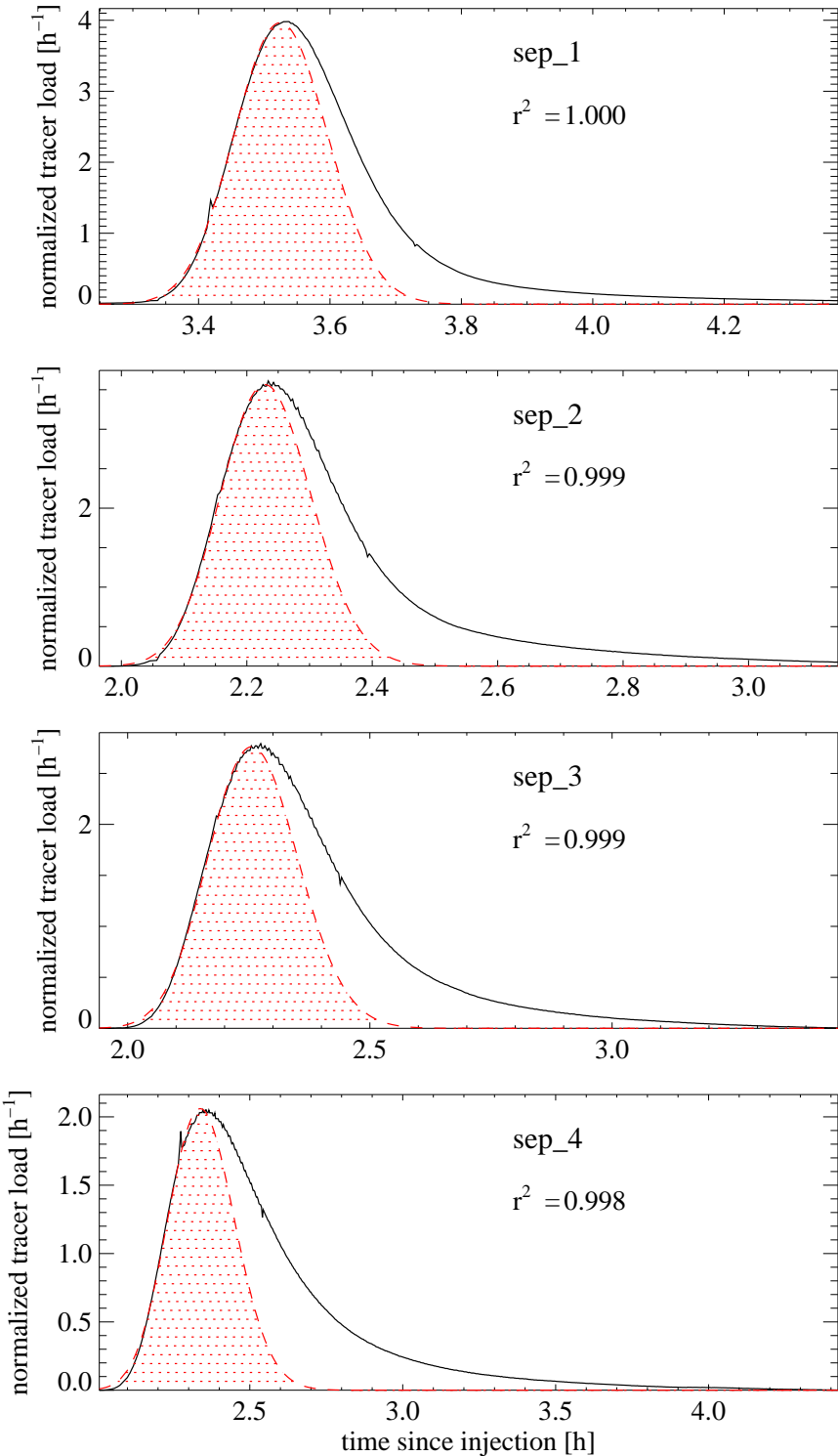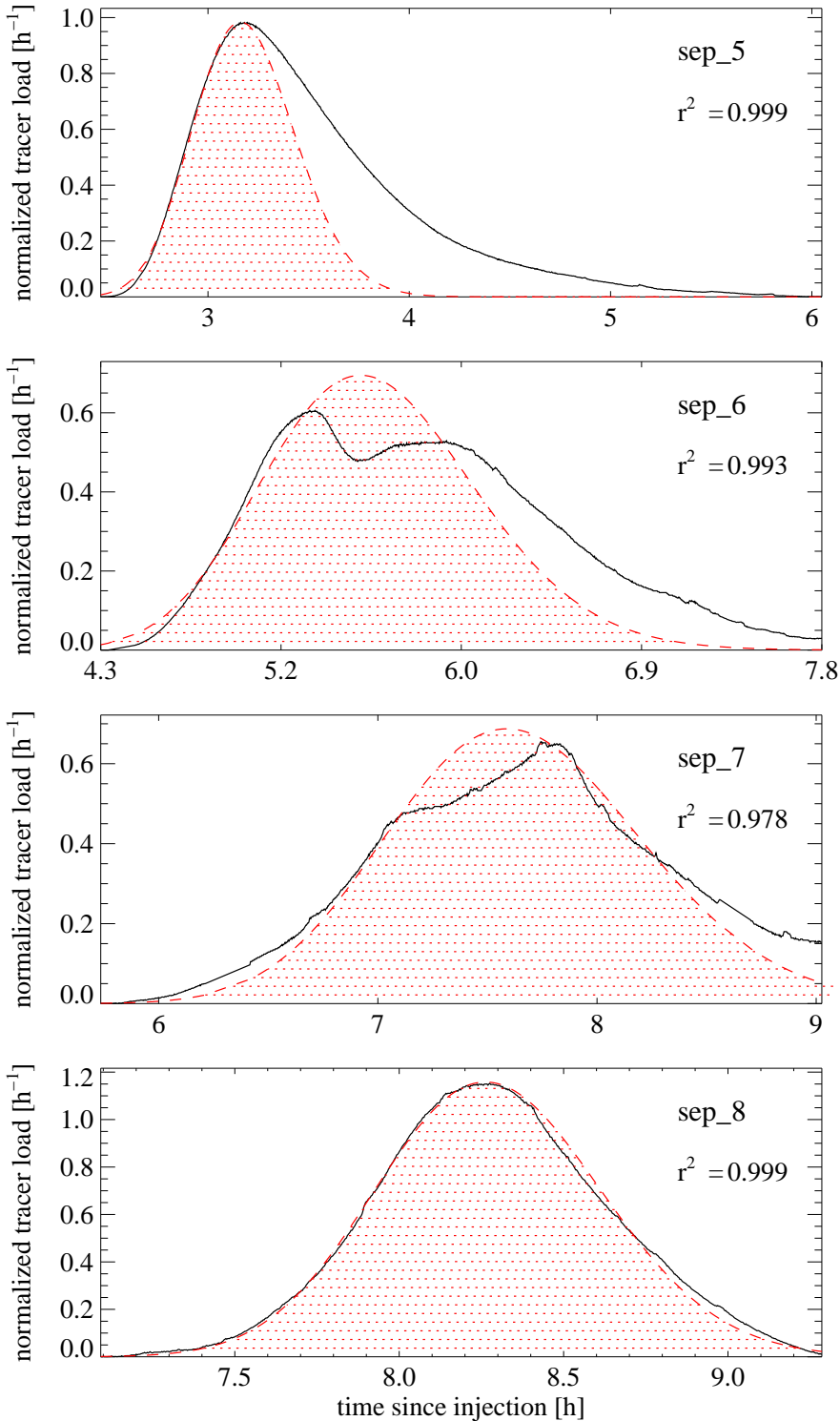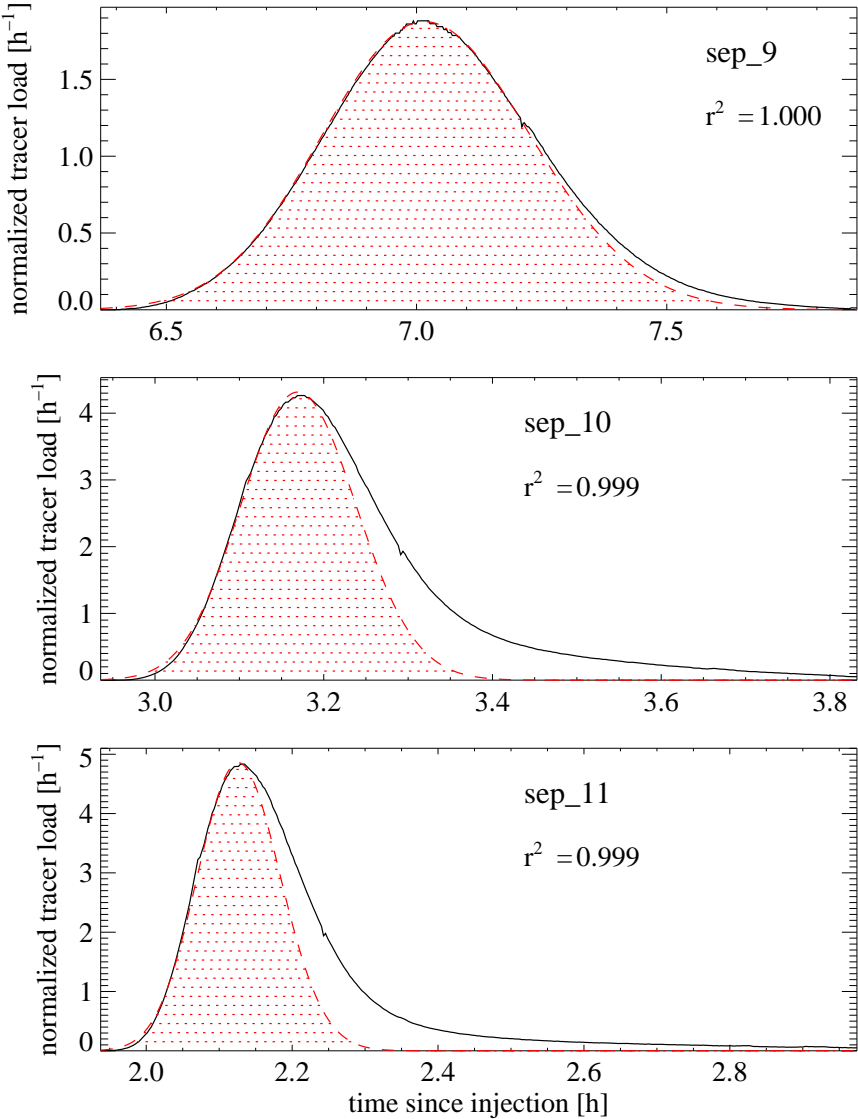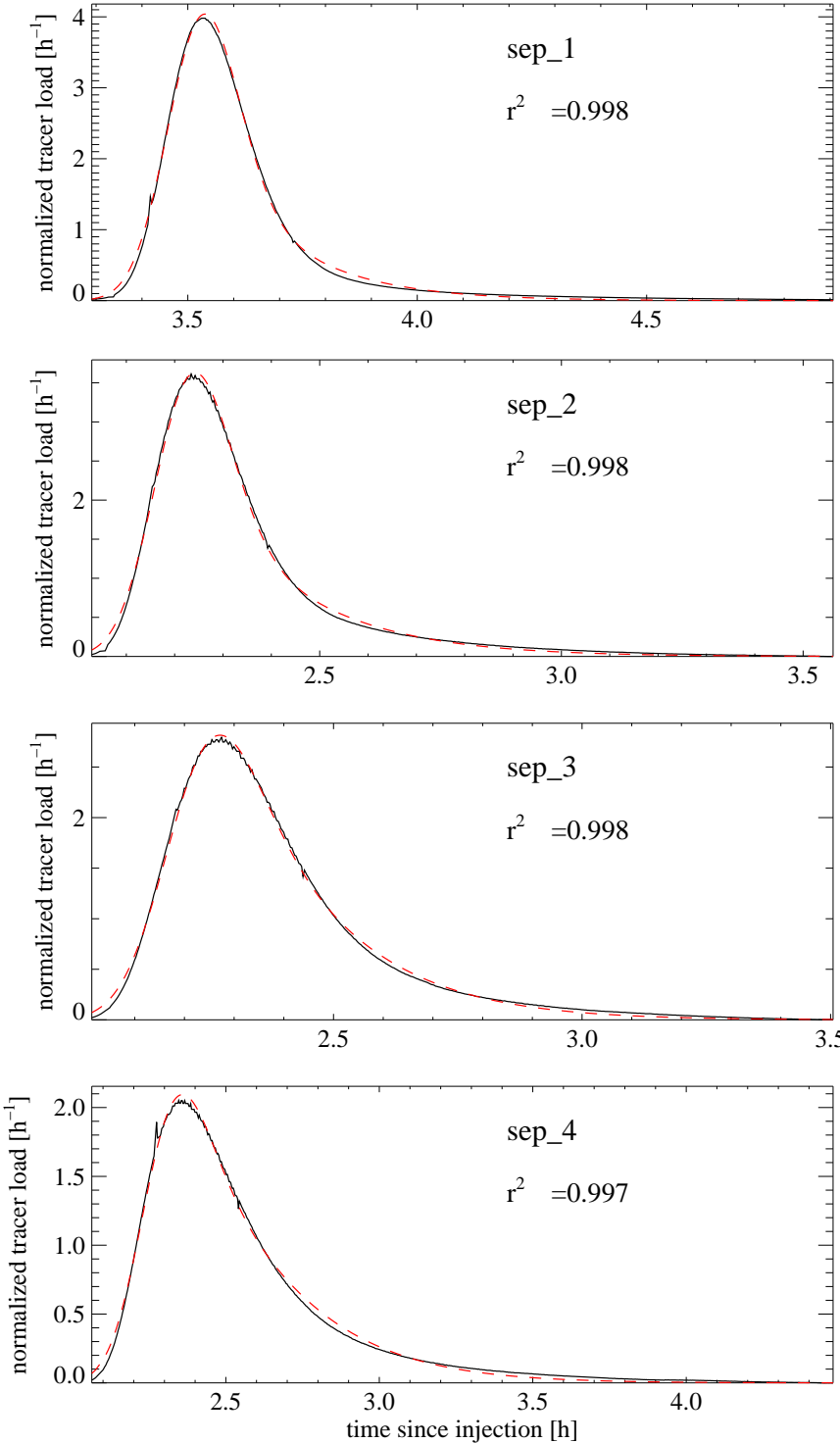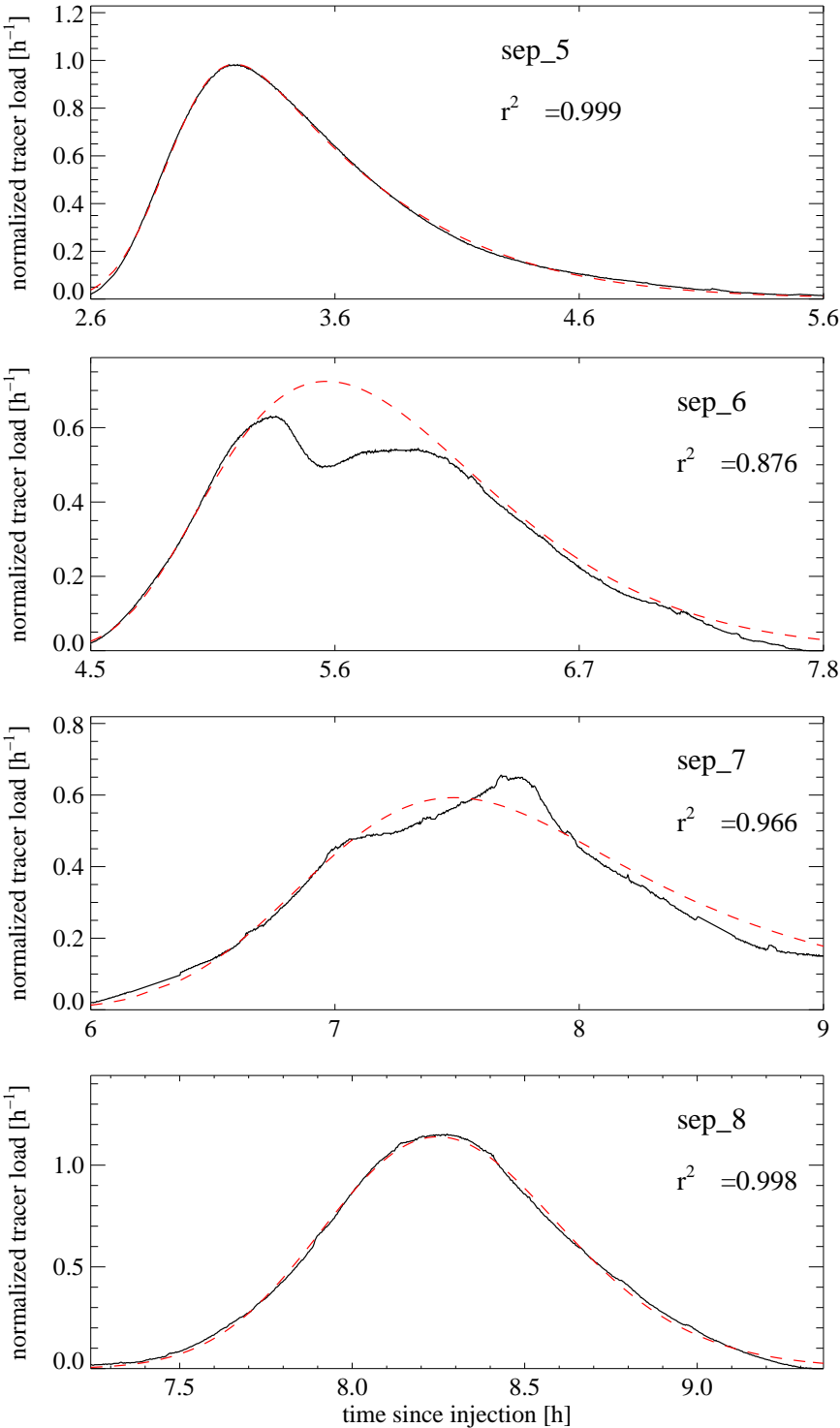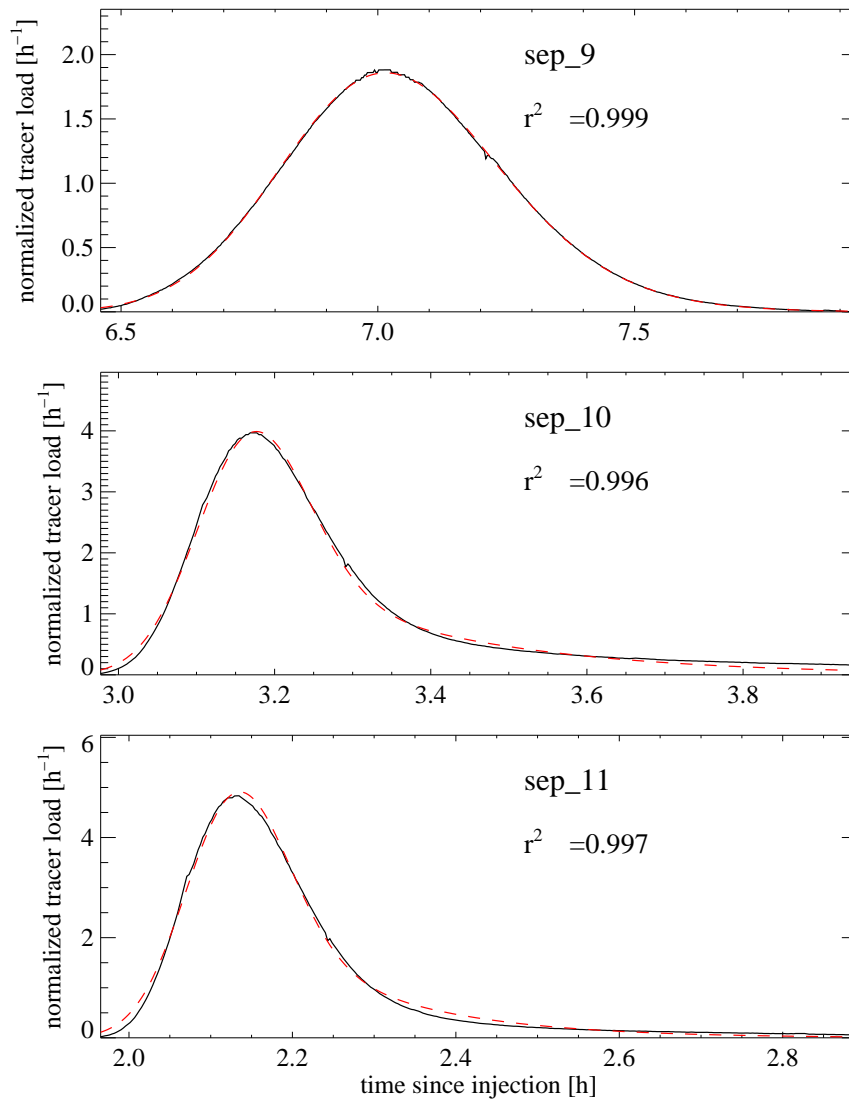
A.2 Mobile-immobile model results

The following figures illustrate the results from fitting the mobile-immobile model (red) to individual tracer return curves (black). The coefficient of determination r^2 refers to the fit of the model to the entire curve.

Bibliography

Agassiz, L. (1840). *Etudes sur les glaciers*, volume 1. Jent & Gassmann, Neuchâtel.

Agassiz, L. (1847). *Système glaciaire ou recherches sur les glaciers, leur mécanisme, leur ancienne extension et le rôle qu'ils ont joué dans l'histoire de la terre. Premiére partie: Nouvelles études et expériences sur les glaciers actuels, leur structure, leur progression et leur action physique sur le sol par.* V. Masson, Paris. 2 vols.

Alley, R. B. (1989a). Water-pressure coupling of sliding and bed deformation: II. Velocity-depth profiles. *Journal of Glaciology*, 35(119):119–129.

Alley, R. B. (1989b). Water-pressure coupling of sliding and bed deformaton: I. Water system. *Journal of Glaciology*, 35(119):108–118.

Alley, R. B. (1992). How can low-pressure channels and deforming tills coexist subglacially? *Journal of Glaciology*, 38(128):200–207.

Alley, R. B., Blankenship, D. D., Bentley, C. R., and Rooney, S. T. (1987). Till beneath Ice Stream B 3. till deformation: Evidence and implications. *Journal of Geophysical Research*, 92(B9):8921–8929.

Ambach, W., Behrens, H., Bergmann, H., and Moser, H. (1972). Markierungsversuche am inneren Abfluss-System des Hintereisferners (Ötztaler Alpen). *Zeitschrift für Gletscherkunde und Glazialgeologie*, 8(1–2):137–145.

Ambach, W., Blumthaler, M., Eisner, H., Kirchlechner, P., Schneider, H., Behrens, H., Moser, H., and Oerter, H. (1978). Untersuchungen der Wassertafel am Kesselwandferner (Ötztaler Alpen) an einem 30 m tiefen Firnschacht. *Zeitschrift für Gletscherkunde und Glazialgeologie*, 14:61–71.

Ambach, W., Blumthaler, M., and Kirchlechner, P. (1981). Application of the gravity flow theory to the percolation of melt water through firn. *Journal of Glaciology*, 27(95):67–75.

Ambach, W. and Eisner, H. (1979). Ein Tracerexperiment zum Schmelzwasserabfluss in der Wassertafel eines temperierten Gletschers. *Zeitschrift für Gletscherkunde und Glazialgeologie*, 15(2):229–234.

Ambach, W. and Jochum, O. (1973). Zur Dispersion im offenen Gerinne: Einfluss von Randzonen bei Gebirgsbächen. *Zeitschrift für Gletscherkunde und Glazialgeologie*, 9(1–2):181–188.

Anderson, S. P., Fernald, K. M. H., Anderson, R. S., and Humphrey, N. F. (1999). Physical and chemical characterization of a spring flood event, Bench Glacier, Alaska, U.S.A.: evidence for water storage. *Journal of Glaciology*, 45(150):177–189.

Baker, D., Escher-Vetter, H., Moser, H., Oerter, H., and Reinwarth, O. (1982). A glacier discharge model based on results from field studies of energy balance, water storage and flow. In *Hydrological aspects of alpine and high mountain areas*, volume 138, pages 103–112. International Association of Hydrological Sciences. Proceedings of the Exeter Symposium, July 1982.

Barrett, A. P. and Collins, D. N. (1997). Interaction between water pressure in the basal drainage system and discharge from an Alpine glacier before and during a rainfall-induced subglacial hydrological event. *Annals of Glaciology*, 24:288–292.

Bauder, A. (2001). *Bestimmung der Massenbilanz von Gletschern mit Fernerkundungsmethoden und Fliessmodellierungen: Eine Sensitivitätsstudie auf dem Unteraargletscher (Diss. ETH 14110)*. PhD thesis, ETH Zürich.

Behrens, H., Bergmann, H., Moser, H., Ambach, W., and Jochum, O. (1975). On the water channels of the internal drainage system of the Hintereisferner, Ötztal Alps, Austria. *Journal of Glaciology*, 14(72):375–382.

Behrens, H., Bergmann, H., Moser, H., Rauert, W., Stichler, W., Ambach, W., Eisner, H., and Pessl, K. (1971). Study of the discharge of Alpine glaciers by means of environmental isotopes and dye tracers. *Zeitschrift für Gletscherkunde und Glazialgeologie*, 7(1-2):79–102.

Behrens, H., Moser, H., Oerter, H., Bergmann, H., Ambach, W., Eisner, H., Kirchlechner, P., and Schneider, H. (1979). Neue Ergebnisse zur Bewegung des Schmelzwassers im Firnkörper des Akkumulationsgebietes eines Alpengletschers (Kesselwandferner, Ötztaler Alpen). *Zeitschrift für Gletscherkunde und Glazialgeologie*, 15:219–228.

Beven, K. J. (2001). *Rainfall-runoff modelling: the primer*. John Wiley & Sons Ltd.

Bindschadler, R. A. (1983). The importance of pressurized subglacial water in separation and sliding at the glacier bed. *Journal of Glaciology*, 29(101):3–19.

Björnsson, H. (1998). Hydrological characteristics of the drainage system beneath a surging glacier. *Nature*, 395:771–774.

Boulton, G. S. (1974). Processes and patterns of glacial erosion. In *Glacial Geomorphology*, pages 41–87. Binghampton, New York.

Boulton, G. S., Dent, D. L., and Morris, E. M. (1974). Subglacial shearing and crushing, and the role of water pressures in tills from South-East Iceland. *Geografiska Annaler*, 56A(3-4):135–145.

Boulton, G. S. and Hindmarsh, R. C. A. (1987). Sediment deformation beneath glaciers: Rheology and geological consequences. *Journal of Geophysical Research*, 92(B9):9059–9082.

Boulton, G. S. and Jones, A. S. (1979). Stability of temperate ice caps and ice sheets resting on beds of deformable sediment. *Journal of Glaciology*, 24(90):29–44.

Box, G., Jenkins, G., and Reinsel, G. (1994). *Time series analysis: forecasting and control*. Englewood Cliffs: Prentice Hall. 3rd ed.

Braithwaite, R. J. (1995). Positive degree-day factors for ablation on the Greenland ice sheet studied by energy-balance modeling. *Journal of Glaciology*, 41(137):153–160.

Brandt, R. and Warren, S. (1993). Solar-heating rates and temperature profiles in Antarctic snow and ice. *Journal of Glaciology*, 39(131):99–110.

Braun, L. N. (1996). Gletscherabflüsse unter verschiedenen klimatischen Bedingungen. In *Klimaänderung und Wasserwirtschaft*, volume 56b, pages 269–292. Institut für Wasserwesen, Universität der Bundeswehr, München. Symposium im Europäischen Patentamt 27./28. Nov. 1995.

Braun, L. N. and Aellen, M. (1990). Modelling discharge of glacierized basins assisted by direct measurements of glacier mass balance. In Lang, H. and Musky, A., editors, *Hydrology of mountainous regions*, volume 193, pages 99–106. International Association of Hydrological Sciences. I. Proceedings of two Lausanne Symposia.

Brugman, M. (1986). *Water flow at the base of a surging glacier*. PhD thesis, Cal. Tech., Pasadena, U. S. A.

Burkimsher, M. (1983). Investigations of glacier hydrological systems using dye tracer techniques: observations at Pasterzengletscher, Austria. *Journal of Glaciology*, 29(103):403–416.

Campbell (1994). *S247 Conductivity and Temperature Probe, User Guide*. Campbell Scientific Ltd.

CFX (1996). *CFX 4.1, Flow solver user guide*. AEA Technology.

Chow, V. T. (1988). *Open-channel hydraulics*. McGraw-Hill, Boston.

Clarke, G. C. K. (1996). Lumped-elements analysis of subglacial hydraulic circuits. *Journal of Geophysical Research*, 101(B8):17547–17559.

Clarke, G. K. C. (1982). Glacier outburst floods from "Hazard Lake", Yukon Territory, and the problem of flood magnitude prediction. *Journal of Glaciology*, 28(98):3–21.

Clarke, G. K. C. (1987). Subglacial till: a physical framework for its properties and processes. *Journal of Geophysical Research*, 92(B9):9023–9036.

Colbeck, S. and Davidson, G. (1973). Water percolation through homogeneous snow. In *Proceedings of the Banff Symposium*, pages 242–257. IAHS. Nr.107.

Collins, D. N. (1979). Quantitative determination of the subglacial hydrology of two Alpine glaciers. *Journal of Glaciology*, 23(89):347–362.

Collins, D. N. (1982). Flow-routing of meltwater in an alpine glacier as indicated by dye tracer tests. *Beiträge zur Geologie der Schweiz-Hydrologie*, 28(2):523–534.

Collins, D. N. (1988). Suspended sediment and solute delivery to meltwaters beneath an alpine glacier. Mitteilung 94, Versuchsanstalt für Wasserbau, Hydrologie und Glaziologie der ETH Zürich, Gloriastrasse 37-39, ETH-Zentrum, CH-8092 Zürich. in *Schnee, Eis und Wasser alpiner Gletscher* pp. 147–162.

Collins, D. N. (1995). Diurnal variations of flow-through velocity and transit time of meltwater traversing moulin-conduit systems in an alpine glacier. In *Biochemistry of Seasonally Snow-Covered Catchments*, volume 228, pages 363–369. IAHS. Proceedings of the Boulder Symposium.

Collins, D. N. (1998). Outburst and rainfall-induced peak runoff events in highly glacierized Alpine basins. *Hydrological Processes*, 12:2369–2381.

Cutler, P. (1998). Modelling the evolution of subglacial tunnels due to varying water input. *Journal of Glaciology*, 44(148):485–497.

Elliston, G. R. (1973). Water movement through the Gornergletscher. In *Hydrology of Glaciers*, volume 95, pages 79–84. International Association of Scientific Hydrology.

Ergenzinger, P., Schmidt, K. H., and Busskamp, R. (1989). The Pebble Transmitter System (PETS) - first results of a technique for studying coarse material erosion, transport and deposition . *Zeitschrift für Geomorphology*, 33(4):503–508.

Escher-Vetter, H. and Reinwarth, O. (1994). Two decades of runoff measurements (1974 to 1993) at the Pegelstation Vernagtbach/ Ötztal Alps. *Zeitschrift für Gletscherkunde und Glazialgeologie*, 30:53–98.

Fischer, M. (1982). Abflussmessungen mit Tracern nach dem Verdünnungsverfahren. *Beiträge zur Geologie der Schweiz - Hydrologie*, 28(2):447–458.

Fischer, U. H. and Clarke, G. K. C. (2001). Review of subglacial hydro-mechanical coupling: Trapridge Glacier, Yukon Territory, Canada. *Quaternary International*, 86(1):29–43.

Fischer, U. H., Clarke, G. K. C., and Blatter, H. (1999). Evidence for temporally-varying "sticky spots" at the base of Trapridge Glacier. *Journal of Glaciology*, 45(150):352–360.

Fischer, U. H., Porter, P. R., Schuler, T., Evans, A. J., and Gudmundsson, G. H. (2001). Hydraulic and mechanical properties of glacial sediments beneath Unteraargletscher, Switzerland: implications for glacier basal motion. *Hydrological Processes*, 15:3525–3540.

Flotron, A. (father and son; 1924 to date). Jährliche Berichte über die Ergebnisse der Gletschermessungen im Auftrag der Kraftwerke Oberhasli. Annual reports.

Flowers, G. E. and Clarke, G. K. C. (2000). An integrated modelling approach to understanding subglacial release events. *Annals of Glaciology*, 31:222–228.

Flowers, G. E. and Clarke, G. K. C. (2002). A multicomponent coupled model of glacier hydrology: 1. Theory and synthetic examples. *Journal of Geophysical Research*. in press.

Forel, F. A. (1898). Circulation des eaux dans le Glacier du Rhône. *Spelunca, Bulletin de la Societé de Spéléologie*, 4(16):156–158.

Fountain, A. and Tangborn, W. (1985). Overview of contemporary techniques. In *Techniques for prediction of runoff from glacierized areas*, volume 149, pages 27–41. International Association of Hydrological Sciences.

Fountain, A. G. (1989). The storage of water in, and hydraulic characteristics of, the firn of South Cascade Glacier, Washington State U.S.A. *Annals of Glaciology*, 13:69–75.

Fountain, A. G. (1993). Geometry and flow conditions of subglacial water at South Cascade Glacier, Washington State, U.S.A; an analysis of tracer injections. *Journal of Glaciology*, 39(131):143–156.

Fountain, A. G. (1994). Borehole water-level variations and implications for the subglacial hydraulics of South Cascade Glacier, Washington State, U.S.A. *Journal of Glaciology*, 40(135):293–304.

Fountain, A. G. and Walder, J. S. (1998). Water flow through temperate glaciers. *Reviews of Geophysics*, 36(3):299–328.

Fowler, A. C. (1987). Sliding with cavity formation. *Journal of Glaciology*, 33(115):225–257.

Funk, M., Gudmundsson, G. H., and Hermann, F. (1994). Geometry of the glacier bed of the Unteraarglacier, Bernese Alps, Switzerland. *Zeitschrift für Gletscherkunde und Glazialgeologie*, 30:1–8.

Goethe, J. W. (1829). Naturwissenschaftliche Schriften: Zur Geologie. In *K. Richter and H. Göpfert and N. Miller and G. Sauder and E. Zehm (Ed.), Goethe: Sämtliche Werke nach Epochen seines Schaffens*, volume 18, pages 364–385. Carl Hanser Verlag München, 1992.

Gordon, S., Sharp, M., Hubbard, B., Smart, C., Ketterling, B., and Willis, I. (1998). Seasonal reorganisation of subglacial drainage inferred from measurements in boreholes. *Hydrological Processes*, 12:105–133.

Grust, K., Käss, W., and Nienow, P. (2001). Lithium chloride as a tracer in glacier hydrology. submitted to IAHG.

Gudmundsson, G. H. (1994). Converging glacier flow — a case study: the Unteraarglacier. Mitteilung 131, Versuchsanstalt für Wasserbau, Hydrologie und Glaziologie der ETH Zürich, Gloriastrasse 37-39, ETH-Zentrum, CH-8092 Zürich. pp. 120.

Gudmundsson, G. H. (1996). New observations of uplift events on Unteraarglacier. *Eos Trans. AGU*, 77(46):F212. Fall Meet. Suppl.

Gudmundsson, G. H. (1999). A three-dimensional numerical model of the confluence area of Unteraargletscher, Bernese Alps, Switzerland. *Journal of Glaciology*, 45(150):219–230.

Haeberli, W. (1983). Frequency and characteristics of glacier floods in the Swiss Alps. *Annals of Glaciology*, 4:85–90.

Hagen, J. O., Wold, B., Liestøl, O., Østrem, G., and Sollid, J. (1983). Subglacial processes at Bondhusbreen, Norway: Preliminary results. *Annals of Glaciology*, 4:91–98.

Hager, W. (1995). *Abwasserhydraulik: Theorie und Praxis*. Springer-Verlag, Berlin.

Hairer, E., Lubich, C., and Roche, M. (1995). *The Numerical Solution of Differential-Algebraic Systems by Runge-Kutta Methods*. Springer-Verlag, New York.

Hallet, B. and Anderson, R. (1980). Detailed glacial geomorphology of a proglacial bedrock area at Castleguard Glacier, Alberta, Canada. *Zeitschrift für Gletscherkunde und Glazialgeologie*, 16:171–184.

Hantz, D. and Lliboutry, L. (1983). Waterways, ice permeability at depth and water pressures at Glacier d'Argentière, French Alps. *Journal of Glaciology*, 29(102):227–239.

Hasnain, S., Jose, P., Ahmad, S., and Negi, D. (2001). Character of the subglacial drainage system in the ablation area of Dokriani Glacier, India, as revealed by dye-tracer studies. *Journal of Hydrology*, 248:216–223.

Hauns, M. (1999). *Modeling tracer and particle transport under turbulent flow conditions in karst conduit structures*. PhD thesis, Centre d'Hydrogéologie, Université de Neuchâtel.

Hauns, M., Jeannin, P.-Y., and Atteia, O. (2001). Dispersion, retardation and scale effect in tracer breakthrough curves in karst conduits. *Journal of Hydrology*, 241:177–193.

Hauns, M., Jeannin, P.-Y., and Hermann, F. (1998). Tracer transport in karst underground rivers: tailing effect from channel geometry. *Bulletin d'Hydrogéologie*, 16:123–142.

Hay, J. and Fitzharris, B. (1988). A comparison of the energy-balance and bulk-aerodynamic approaches for estimating glacier melt. *Journal of Glaciology*, 34(117):145–153.

Hock, R. (1998). Modelling of glacier melt and discharge. Technical Report 70, Zürcher Geographische Schriften, ETH Zürich.

Hock, R. (1999). A distributed temperature-index ice- and snowmelt model including potential direct solar radiation. *Journal of Glaciology*, 45(149):101–111.

Hock, R. and Hooke, R. L. (1993). Evolution of the internal drainage system in the lower part of the ablation area of Storglaciären, Sweden. *Geological Society of America Bulletin*, 105(4):537–546.

Hock, R., Iken, A., and Wangler, A. (1999). Tracer experiments and borehole observations in the overdeepening of Aletschgletscher, Switzerland. *Annals of Glaciology*, 28:253–260.

Hodge, S. M. (1979). Direct measurement of basal water pressures: Progress and problems. *Journal of Glaciology*, 23(89):309–319.

Hoinkes, H. and Rudolph, R. (1962). Variations in the mass balance of Hintereisferner (Oetztal Alps), 1952–1961, and their relation to variations of climatic elements. In *IASH Publications*, volume 58, pages 16–28. International Association of Scientific Hydrology.

Holmlund, P. (1988). Internal geometry and evolution of moulins, Storglaciären, Sweden. *Journal of Glaciology*, 34(117):242–248.

Hooke, R. L. (1984). On the role of mechanical energy in maintaining subglacial water conduits at atmospheric pressure. *Journal of Glaciology*, 30(105):180–187.

Hooke, R. L. (1989). Englacial and subglacial hydrology: a qualitative review. *Arctic and Alpine Research*, 21(3):221–233.

Hooke, R. L., Calla, P., Holmlund, P., Nilsson, M., and Stroeven, A. (1989). A 3 year record of seasonal variations in surface velocity, Storglaciären, Sweden. *Journal of Glaciology*, 35(120):235–247.

Hooke, R. L., Laumann, T., and Kohler, J. (1990). Subglacial water pressures and the shape of subglacial conduits. *Journal of Glaciology*, 36(122):67–71.

Hooke, R. L., Miller, S. B., and Kohler, J. (1988). Character of the englacial and subglacial drainage system in the upper part of the ablation area of Storglaciären, Sweden. *Journal of Glaciology*, 34(117):228–231.

Hubbard, B. and Nienow, P. (1997). Alpine subglacial hydrology. *Quaternary Science Reviews*, 16:939–955.

Hubbard, B., Sharp, M., Willis, I. C., Nielsen, M. K., and Smart, C. C. (1995). Borehole water-level variations and the structure of the subglacial hydrological system of Haut Glacier d'Arolla, Valais, Switzerland. *Journal of Glaciology*, 41(139):572–583.

Hugi, F. J. (1830). *Naturhistorische Alpenreise*. Amiet-Lutiger, Solothurn.

Hugi, F. J. (1842). *Über das Wesen der Gletscher*. J. G. Cotta'scher Verlag, Stuttgart und Tübingen.

Humphrey, N., Raymond, C. F., and Harrison, W. (1986). Discharges of turbid water during mini-surges of Variegated Glacier, Alaska, U.S.A. *Journal of Glaciology*, 32(111):195–207.

Humphrey, N. F. and Raymond, C. F. (1994). Hydrology, erosion and sediment production in a surging glacier: Variegated Glacier, Alaska, 1982-83. *Journal of Glaciology*, 40(136):539–552.

IAHS (ICSI)–UNEP–UNESCO (1999). Glacier Mass Balance Bulletin No. 5, 1996–1997. Technical report, WGMS.

Iken, A. (1972). Measurements of water pressure in moulins as part of a movement study of the White Glacier, Axel Heiberg Island, Northwest Territories, Canada. *Journal of Glaciology*, 11(61):53–58.

Iken, A. and Bindschadler, R. A. (1986). Combined measurements of subglacial water pressure and surface velocity of Findelengletscher, Switzerland: Conclusions about drainage system and sliding mechanism. *Journal of Glaciology*, 32(110):101–119.

Iken, A., Röthlisberger, H., Flotron, A., and Haeberli, W. (1983). The uplift of the Unteraargletscher at the beginning of the melt season – a consequence of water storage at the bed? *Journal of Glaciology*, 29(101):28–47.

Iverson, N. R., Hanson, B., Hooke, R. L., and Jansson, P. (1995). Flow mechanism of glaciers on soft beds. *Science*, 267(5194):80–81.

Jansson, P., Kohler, J., and Pohjola, V. (1996). Characteristics of basal ice at Engabreen, northern Norway. *Annals of Glaciology*, 22:114–120.

Jury, W. A. and Roth, K. (1990). *Transfer functions and solute movement through soils: Theory and applications*. Birkenhäuser Verlag, Basel.

Kahaner, D., Moler, C., and Nash, S. (1989). *Numerical methods and Software*. Prentice-Hall, Englewood Cliffs, N.J.

Kamb, B. (1987). Glacier surge mechanism based on linked cavity configuration of the basal water conduit system. *Journal of Geophysical Research*, 92(B9):9083–9100.

Kamb, B. and Engelhardt, H. (1987). Waves of accelerated motion in a glacier approaching surge: the mini-surges of Variegated Glacier, Alaska, U.S.A. *Journal of Glaciology*, 33(113):27–46.

Kamb, B., Raymond, C. F., Harrison, W. D., Engelhardt, H., Echelmeyer, K. A., Humphrey, N., Brugman, M. M., and Pfeffer, T. (1985). Glacier surge mechanism: 1982-1983 surge of Variegated Glacier, Alaska. *Science*, 227:469–479.

Käss, W. (1998). *Tracing Technique in Geohydrology*. A.A. Balkema, Rotterdam/Brookefield.

Kavanaugh, J. L. and Clarke, G. K. C. (2001). Abrupt glacier motion and reorganisation of basal shear stress following the establishment of a connected drainage system. *Journal of Glaciology*, 47(158):472–480.

Kinzelbach, W. (1992). *Numerische Methoden zur Modellierung des Transports von Schadstoffen im Grundwasser*. R. Oldenburg Verlag, München, Wien.

Kite, G. (1994). Measuring glacier outflow using a computerized conductivity system. *Journal of Glaciology*, 40(134):93–96.

Knecht, H. and Süsstrunk, A. (1952). Bericht über die seismischen Sondierungen der schweizerischen Gletscherkommission auf dem Unteraargletscher, 1936 - 1950. Bericht No. 512.

Kohler, J. (1995). Determining the extent of pressurized flow beneath Storglaciären, Sweden, using results of tracer experiments and measurements of input and output discharge. *Journal of Glaciology*, 41(138):217–231.

Kondratyev, K. F. (1965). *Radiative heat exchange in the atmosphere*. Pergamon Press, Oxford, London.

Kreft, A. and Zuber, A. (1978). On the physical meaning of the dispersion equation and its solutions for different initial and boundary conditions. *Chem. Eng. Sci.*, 33:1471–1480.

Labhart, T. (1992). *Geologie der Schweiz*. Ott Verlag, Thun.

Lang, H. (1966). Hydrometeorologische Ergebnisse aus Abflussmessungen im Bereich des Hintereisferners in den Jahren 1957–1959. *Archiv für Meteorologie, Geophysik und Bioklimatologie*, 14:280–302.

Lang, H. (1981). Is evaporation an important component in high alpine hydrology? *Nordic Hydrology*, 12:217–224.

Lang, H. and Braun, L. N. (1990). On the information content of air temperature in the context of snow melt estimation. In Molnar, L., editor, *Hydrology of mountainous areas*, volume 190, pages 347–354. International Association of Hydrological Sciences. Proceedings of the Štrbské Pleso Symposium, Czechoslovakia, 1988.

Lang, H., Leibundgut, C., and Festel, E. (1979). Results from tracer experiments on the water flow through the Aletschgletscher. *Zeitschrift für Gletscherkunde und Glazialgeologie*, 16(2):209–218.

Lang, H., Schädler, B., and Davidson, G. (1977). Hydroglaciological investigations on the Ewigschneefeld – Grosser Aletschgletscher. *Zeitschrift für Gletscherkunde und Glazialgeologie*, 12:109–124.

Lang, H. and Schönbächler, M. (1967). Heat balance studies and runoff at the Aletschgletscher, 1965. Technical report, Versuchsanstalt für Wasserbau, Hydrologie und Glaziologie der ETH Zürich.

Liestøl, O. (1956). Glacier dammed lakes in Norway. *Norsk Geografisk Tidsskrift*, 15:122–149.

Lliboutry, L. (1971). Permeability, brine content and temperature of temperate ice. *Journal of Glaciology*, 10:15–30.

Lliboutry, L. (1996). Temperate ice permeability, stability of water veins and percolation of internal meltwater. *Journal of Glaciology*, 42(141):201–211.

Lliboutry, L. A. (1964). *Traité de Glaciologie*, volume I. Masson, Paris.

Lliboutry, L. A. (1968). General theory of subglacial cavitation and sliding of temperate glaciers. *Journal of Glaciology*, 7(49):21–58.

Lliboutry, L. A. (1983). Modifications to the theory of intraglacial waterways for the case of subglacial ones. *Journal of Glaciology*, 29(102):216–226.

L+T (1993). Digitales Höhenmodell DHM25. Bundesamt für Landestopographie, Wabern, Switzerland. Produktinformation.

Lütschg, O. (1926). Über Niederschlag und Abfluß im Hochgebirge, Sonderdarstellung des Mattmarkgebietes. Verbandsschrift Nr. 14, Schweizerischer Wasserwirtschaftsverband – Veröffentlichung der Hydrologischen Abteilung der Schweizerischen Meteorologischen Zentralanstalt in Zürich.

Mader, M. and Kaser, G. (1994). Application of a linear reservoir model to the discharge of a glacierized basin in the Silvretta mountains. *Zeitschrift für Gletscherkunde und Glazialgeologie*, 30:125–140.

Mair, D., Nienow, P., Willis, I., and Sharp, M. (2001). Spatial patterns of glacier motion during a high-velocity event: Haut Glacier d'Arolla, Switzerland. *Journal of Glaciology*, 47(156):9–20.

Marquardt, D. (1963). An algorithm for least-squares estimation of nonlinear parameters. *J. Soc. Ind. Appl. Math.*, 11:431–441.

Mathews, W. H. (1964). Water pressure under a glacier. *Journal of Glaciology*, 5:235–240.

Meier, M. F. (1973). Hydraulics and hydrology of glaciers. In *The Role of Snow and Ice in Hydrology*, volume 107, pages 353–369. International Association of Hydrological Sciences.

Melvold, K., Schuler, T., and Lappegard, G. (2002). Groundwater intrusions in a mine beneath Høganesbreen, Svalbard: assessing the possibility of evacuating water subglacially. *Annals of Glaciology*, 37. in press.

Mercanton, P. L. (1916). Vermessungen am Rhonegletscher, Mensurations au Glacier du Rhône, 1874–1915. *Neue Denkschriften der Schweizerischen Naturforschenden Gesellschaft*, 52.

Morris, E. (1989). Turbulent transfer over snow and ice. *Journal of Hydrology*, 105:205–223.

Ng, F. (1998). *Mathematical modelling of subglacial drainage and erosion.* PhD thesis, St Catherin's College, Oxford.

Ng, F. (2000). Canals under sediment-based ice-sheets. *Annals of Glaciology*, 30:146–152.

Nienow, P. (1993). *Dye tracer investigations of glacier hydrological systems.* PhD thesis, St Johns College, Cambridge.

Nienow, P. W., Sharp, M., and Willis, I. C. (1996a). Sampling-rate effects on the properties of dye breakthrough curves from glaciers. *Journal of Glaciology*, 42(140):184–193.

Nienow, P. W., Sharp, M., and Willis, I. C. (1996b). Temporal switching between englacial and subglacial drainage pathways: dye tracer evidence from Haut Glacier d'Arolla, Switzerland. *Geografiska Annaler*, 78A:51–60.

Nienow, P. W., Sharp, M., and Willis, I. C. (1996c). Velocity-discharge relationships derived from dye tracer experiments in glacial meltwaters: implications for subglacial flow conditions. *Hydrological Processes*, 10:1411–1426.

Nienow, P. W., Sharp, M., and Willis, I. C. (1998). Seasonal changes in the morphology of the subglacial drainage system, Haut Glacier d'Arolla, Switzerland. *Earth Surface Processes and Landforms*, 23:825–843.

Nye, J. F. (1953). The flow law of ice from measurements in glacier tunnels, laboratory experiments and the Jungfraufirn borehole experiment. *Proceedings of the Royal Society of London, Ser A*, 219(1193):477–489.

Nye, J. F. (1973). Water at the bed of a glacier. In *Proceedings of the Cambridge Symposium 1969*, pages 189–194. IASH. Nr.95.

Nye, J. F. (1976). Water flow in glaciers: jökulhlaups, tunnels and veins. *Journal of Glaciology*, 17(76):181–207.

Nye, J. F. and Frank, F. C. (1973). Hydrology of the intergranular veins in a temperate glacier. In *Symposium on the Hydrology of Glaciers*, pages 157–161. Proceedings of the symposium held at Cambridge, England, 7–13 September 1969, IAHS Publication No. 95.

Oerter, H., Behrens, H., Hibsch, G., Rauert, W., and Stichler, W. (1980). Combined environmental isotope and electrical conductivity investigations at the runoff of Vernagtferner (Oetztal Alps, Austria). *Data of Glaciological Studies (Moscow)*, 39:86–92.

Oerter, H. and Moser, H. (1982). Water storage and drainage within the firn of a temperate glacier (Vernagtferner, Oetztal Alps, Austria). In *Hydrological Aspects of Alpine and High-Mountain Areas*, volume 138, pages 71–81. International Association of Hydrological Sciences.

Ohmura, A. (2001). Physical basis for the temperature-based melt-index method. *Journal of Applied Meteorology*, 40:753–761.

Paterson, W. S. B. (1994). *The Physics of Glaciers*. Pergamon, New York, third edition.

Pohjola, V. A. (1994). TV-video observations of englacial voids in Storglaciären, Sweden. *Journal of Glaciology*, 40(135):231–240.

Raymond, C. F. (1987). How do glaciers surge? A review. *Journal of Geophysical Research*, 92(B9):9121–9134.

Raymond, C. F. and Harrison, W. D. (1975). Some observations on the behaviour of the liquid and gas phases in temperate glacier ice. *Journal of Glaciology*, 14(71):213–233.

Reynaud, L. (1987). The November 1986 survey of the Grand Moulin on the Mer de Glace, Mont Blanc Massif, France. *Journal of Glaciology*, 33(113):130–131.

Robin, G. (1974). Depth of water filled crevasses that are closely spaced. *Journal of Glaciology*, 13(69):543.

Röthlisberger, H. (1972). Water pressure in intra– and subglacial channels. *Journal of Glaciology*, 11(62):177–203.

Röthlisberger, H. (1981). Eislawinen und Ausbrüche von Gletscherseen. In *P. Kasser (Ed.), Gletscher und Klima - glaciers et climat, Jahrbuch der Schweizerischen Naturforschenden Gesellschaft, wissenschaftlicher Teil 1978*, pages 170–212. Birkhäuser Verlag Basel, Boston, Stuttgart.

Röthlisberger, H. and Lang, H. (1987). Glacial Hydrology. In *A.M. Gurnell and M.J. Clark (Ed.), Glacio-Fluvial Sediment Transfer - An Alpine Perspective*, pages 207–284. John Wiley and Sons, Chichester, New York, Toronto, Singapore.

Sambeth, U. and Frey, P. (1987a). Auswertung der Geoelektrischen Messungen im unteren Gebiet der Zunge des Unteraargletschers. Technical Report Ref. Nr. 87107, Peter Frey, Geolog. Expertisen, Zug.

Sambeth, U. and Frey, P. (1987b). Geophysikalische Messungen zur Abklärung des Aufbaus des Unteraargletschers, der unterliegenden Sedimente und der Felsoberkante. Technical Report Ref Nr. 87102, Peter Frey, Geolog. Expertisen, Zug.

Sauty, J.-P. and Kinzelbach, W. (1988). On the identification of the parameters of groundwater mass transport. In *Groundwater flow and quality modelling*, pages 33–56. E. Custodio, A. Gurgui and L. P. Lobo Ferreira.

Schmidt, K. H. and Ergenzinger, P. (1992). Bedload entrainment, travel lengths, step lengths, rest periods– studied with passive (iron, magnetic) and active (radio) tracer techniques. *Earth Surface Processes and Landforms*, 17(2):147–165.

Schneider, T. (1999). Water movement in the firn of Storglaciären, Sweden. *Journal of Glaciology*, 45(150):286–294.

Schneider, T. (2001). *Hydrological processes in firn on Storglaciären, Sweden*. PhD thesis, Stockholm University.

Schommer, P. (1977). Wasserspiegelmessungen im Firn des Ewigschneefeldes (Schweizer Alpen) 1976. *Zeitschrift für Gletscherkunde und Glazialgeologie*, 12(2):125–141.

Schuler, T. and Fischer, U. H. (2002). Elucidating changes in the degree of tracer dispersion in a subglacial channel. *Annals of Glaciology*, 37. in press.

Schuler, T., Fischer, U. H., Sterr, R., Hock, R., and Gudmundsson, G. H. (2002). Comparison of modeled water input and measured discharge prior to a release event: Unteraargletscher, Bernese Alps, Switzerland. *Nordic Hydrology*, 33(1):27–46.

Seaberg, S. Z., Seaberg, J. Z., Hooke, R. L., and Wiberg, D. W. (1988). Character of the englacial and subglacial drainage system in the lower part of the ablation area of Storglaciären, Sweden, as revealed by dye-trace studies. *Journal of Glaciology*, 34(117):217–227.

Sharp, M., Gemmel, J., and Tison, J.-L. (1989). Structure and stability of the former subglacial drainage system of the Glacier de Tsanfleuron, Switzerland. *Earth Surface Processes and Landforms*, 14:119–134.

Sharp, M. J., Richards, K., Willis, I., Arnold, N., Nienow, P., Larson, W., and Tison, J.-L. (1993). Geometry, bed topography and drainage system structure of the Haut Glacier d'Arolla, Switzerland. *Earth Surface Processes and Landforms*, 18:557–572.

Shreve, R. L. (1972). Movement of water in glaciers. *Journal of Glaciology*, 11(62):205–214.

Shreve, R. L. (1985). Esker characteristics in terms of glacier physics, Katahdin esker system, Maine. *Geological Society of America Bulletin*, 96:639–646.

Smart, C. (1983). The hydrology of the Castleguard Karst, Columbia Icefields, Alberta, Canada. *Arctic and Alpine Research*, 15(4):471–487.

Smart, C. (1986). Some observations on subglacial ground-water flow. *Journal of Glaciology*, 32(111):232–234.

Smart, C. (1990). Comments on: "Character of the englacial and subglacial drainage system in the lower part of the ablation area of Storglaciären, Sweden, as revealed by dye-trace studies". *Journal of Glaciology*, 36(122):126–128.

Smart, C. and Zabo, L. (1997). Some developments in fluorometric tracing of ground water. In *Beck & Stephenson (Eds.): Engineering Geology and Hydrogeology of Karst Terranes*, pages 213–217. Balkema, Rotterdam.

Smart, P. and Laidlaw, I. (1977). An evaluation of some fluorescent dyes for water tracing. *Water Resources Research*, 13(1):15–33.

Spring, U. (1980). Intraglazialer Wasserabfluss: Theorie und Modellrechnung. Mitteilung 48, Versuchsanstalt für Wasserbau, Hydrologie und Glaziologie der ETH Zürich, Gloriastrasse 37-39, ETH-Zentrum, CH-8092 Zürich.

Spring, U. and Hutter, K. (1981). Numerical studies of Jökulhlaups. *Cold Regions Science and Technology*, 4:221–244.

Spring, U. and Hutter, K. (1982). Conduit flow of a fluid through its solid phase and its application to intraglacial channel flow. *International Journal of Engineering Sciences*, 20:327–363.

Stenborg, T. (1969). Studies of the internal drainage of glaciers. *Geografiska Annaler*, 51A:13–41.

Stenborg, T. (1973). Some viewpoints on the internal drainage of glaciers. In *Hydrology of Glaciers*, volume 95, pages 117–129. International Association of Hydrological Sciences.

Sterr, R. (2000). Modellierung der Schmelze, Anwendung des Erweiterten Temperatur-Index-Modells auf den Unteraargletscher. Diploma Thesis, University of Innsbruck, Austria.

Stone, D. B. and Clarke, G. K. C. (1993). Estimation of subglacial hydraulic properties from induced changes in basal water pressure: a theoretical framework for borehole response tests. *Journal of Glaciology*, 39(132):327–340.

Stone, D. B. and Clarke, G. K. C. (1996). In situ measurements of basal water quality and pressure as an indicator of the character of subglacial drainage systems. *Hydrological Processes*, 10(4):615–628.

Taylor, G. (1954). The dispersion of matter in turbulent flow through a pipe. *Proceedings of the Royal Society of London*, A223:446–468.

Toride, N., Leij, F., and van Genuchten, M. T. (1999). The CXTFIT code for estimating transport parameters from laboratory or field tracer experiments, version 2.1. Technical Report 137, U.S. Salinity Laboratory, U.S. Department of Agriculture, Riverside, California.

Tranter, M., Brown, G. H., Hodson, A., and Gurnell, A. (1996). Hydrochemistry as an indicator of subglacial drainage structure: a comparison of alpine and sub-polar environments. *Hydrological Processes*, 10:541–556.

Tronov, M. V. (1962). On the role of summer snowfall in glacier variations. In *IASH Publications*, volume 58, pages 262–269. International Association of Scientific Hydrology.

Turner (1997). *Model 10-AU-005-CE Fluorometer, User's Manual*. Turner Designs, 845 W. Maude Ave., Sunnyvale, CA 94086, USA.

van Genuchten, M. T. and Wagenet, R. J. (1989). Two-site/ two-region models for pesticide transport and degradation: theoretical developement and analytical solutions. *SSSAJ*, 53:1303–1310.

van Genuchten, M. T. and Wierenga, P. (1976). Mass transfer studies in sorbing porous media, I, Analytical solutions. *SSSAJ*, 40:473–481.

Vivian, R. and Bocquet, G. (1973). Subglacial cavitation phenomena under the Glacier d'Argentière. *Journal of Glaciology*, 12(66):439–451.

Wagnon, P., Ribstein, P., Schuler, T., and Francou, B. (1998). Flow separation on Zongo Glacier, Cordillera Real, Bolivia. *Hydrological Processes*, 12:1911–1926.

Walder, J. and Hallet, B. (1979). Geometry of former subglacial water channels and cavities. *Journal of Glaciology*, 23:335–346.

Walder, J. S. (1982). Stability of sheet flow of water beneath temperate glaciers and implications for glacier surging. *Journal of Glaciology*, 28(99):273–293.

Walder, J. S. (1986). Hydraulics of subglacial cavities. *Journal of Glaciology*, 32(112):439–445.

Walder, J. S. and Fowler, A. (1994). Channelized subglacial drainage over a deformable bed. *Journal of Glaciology*, 40(134):3–15.

Warren, S. (1982). Optical properties of snow. *Reviews of Geophysics and Space Physics*, 20(1):67–89.

Weertman, J. (1957). On the sliding of glaciers. *Journal of Glaciology*, 3(21):33–38.

Weertman, J. (1972). General theory of water flow at the base of a glacier or ice sheet. *Reviews of Geophysics and Space Physics*, 10(1):287–333.

Weertman, J. (1974). Depth of water-filled crevasses that are closely spaced. *Journal of Glaciology*, 13(69):544. (correspondence).

Weertman, J. (1983). Basal water film, basal water pressure, and velocity of traveling waves on glaciers. *Journal of Glaciology*, 29(101):20–27.

Willis, I. C., Sharp, M. J., and Richards, K. S. (1990). Configuration of the drainage system of Midtalsbreen, Norway, as indicated by dye-tracing experiments. *Journal of Glaciology*, 36(122):89–101.

Zumbühl, H. and Holzhauser, H. (1988). Alpengletscher in der Kleinen Eiszeit. *Die Alpen*, 64(3):130–322. 3. Quartal, Sonderheft zum 125. jährigen Jubiläum des SAC.

Zumbühl, H. and Holzhauser, H. (1990). Alpengletscher in der Kleinen Eiszeit. *Geographica Bernensia*. Band G 31. Ergänzungsband zu 'Die Alpen 64(3)'.

Acknowledgements

Numerous people have contributed to the successful completion of this thesis in different ways. I would like to express my gratitude to all of them.

First of all, sincere thanks goes to my supervisor, Urs Fischer. He initiated this project and provided continuous support during all stages of this work. His efforts in numerous discussions and arduous field campaigns are gratefully appreciated. Equally, I treasure his merits in enhancing my English writing skills and guiding me through the many difficulties encountered during the research work. Furthermore, I like to remember many pleasant ski-tours, dinners and other spare-time activities which contributed a lot to the nice time I enjoyed in Zürich. Thank you so much for everything!

My "Doktorvater" Prof. Dr. Hans-Erwin Minor provided working facilities at the Laboratory of Hydraulics, Hydrology and Glaciology (VAW) and supported the project financially.

The thesis is embedded in the project "Flow dynamics of Unteraargletscher" which was initiated and promoted by G. Hilmar Gudmundsson. He accompanied my research with many helpful comments and discussions.

Ludwig Braun has accompanied my career as a glaciologist since 1996 when I did an internship at the Bavarian Academy of Sciences. He encouraged me to do a PhD and later, he was willing to serve as a referee of my thesis.

The four people mentioned above thoroughly scrutinized this thesis and their valuable comments on earlier drafts significantly improved the quality of my dissertation.

I am deeply grateful for a generous scholarship provided by Dr. Berz of the MunichRe insurance company. This helped me to survive the one year period after my "Diplomarbeit" when the PhD-project was prepared.

This project was financed by ETH grant 0-20527-98. When the project funding ran out but my thesis was still far from being what it is now, Martin Funk found means to extend my salary. His support is greatly acknowledged!

The major part of my work was carried out in my office at the section of glaciology at VAW. My PhD-colleagues Gudfinna Adalgeirsdottir, Andreas Bauder, Christian Hauck, Jakob Helbing, Gwendolyn Leysinger-Vieli, Martin Lüthi, Antoine Pralong, Melanie Raymond, Marie Rousselot, Aurel Schwerzmann, Stephan Suter, Andreas Vieli and This Wegmann (in alphabetical order) contributed to make the work environment a pleasant and creative one. Thank you very much for all the computer support and endless discussions about science and life in general!

Bruno Nedela contributed with drawings and put me from science back to other realities when necessary. I enjoyed the times when he explained me his personal views of mountaineering, life, the universe and everything.

Curriculum vitae

Name	Thomas Schuler
Adresse	Stapferstr. 33
	8006 Zürich
Date of birth	19. March 1971
In	Bühl/ Baden
Citizenship	German

1999-2002	PhD-thesis "Investigation of water drainage through an alpine glacier by tracer experiments and numerical modeling" at Laboratory of Hydraulics, Hydrology and Glaciology (VAW), Swiss Federal Institute of Technology Zürich (ETHZ)
1997	Diploma degree in hydrology, thesis: "Hydrologie eines randtropischen Gletschers, Fallstudie Glaciar Zongo, Cordillera Real, Bolivien" at the Institute for Hydrology, ALU
1992-1997	Studies in hydrology at Albert-Ludwigs-Universität in Freiburg im Breisgau (ALU)
1991-1992	Civil service at Loretto-Hospital, Freiburg im Breisgau
1990	Abitur
1981-1990	Friedrich-Gymnasium in Freiburg im Breisgau
1977-1981	Primary school in Wittnau/ Sölden